POLYIONIC NANOCLAYS AS TAILORABLE HYBRID ORGANIC-INORGANIC PLATFORMS

A Dissertation

Presented to

The Doctoral Program Committee

At the University of Missouri-Columbia

In Partial Fulfillment

Of the Requirements for the Degree

Doctor of Philosophy

By

Nathaniel E. Larm

Dr. Gary A. Baker, Dissertation Supervisor

July 2021

The undersigned, appointed by the dean of the Graduate School,

have examined the dissertation entitled

POLYIONIC NANOCLAYS AS TAILORABLE HYBRID ORGANIC-INORGANIC PLATFORMS

presented by Nathaniel E. Larm,

a candidate for the degree of Doctor of Philosophy,

and hereby certify that, in their opinion, it is worthy of acceptance.

Professor Gary A. Baker

Professor C. Michael Greenlief

Professor Silvia S. Jurisson

Professor Luis Polo-Parada

Acknowledgements

I wish to thank my research advisor, Dr. Gary A. Baker, whose passion for knowledge and desire to relentlessly challenge himself is (fortunately) contagious. I am fortunate that this amazing mentor has become a close friend over the years, and I anticipate many collaborations in our future. I would also like the thank the various members of the Baker group, both past and present, for our often fruitful and always entertaining conversations. Specifically, I would like to thank Laxmi Adhikari, Piyuni Ishtaweera, Angira Roy, and Jason Thon.

My deepest gratitude goes out to my parents, Daniel and Tina Larm, for their love and constant encouragement throughout my pursuits in higher education. Their devotion to family, along with the sacrifices they have made for my betterment, has allowed me to reach this point in my life, and I am eternally grateful.

Finally, I wish to thank my wife, Bryanne Cornine, for her tireless love and support through the years. I dedicate this document to her, as she stood by my side throughout its conception, work, and creation.

Table of Contents

List of Figures and Schemes

***Figure 3-14**: (Left) A HR-TEM image showing a R = 5, x = 0.5 bimetallic Au_xAg_{1-x}NP and (right) the corresponding EDS spectrum confirming the presence of both gold and silver within the nanostructure. Copper is typically observed when using copper TEM grids, but the presence of silicon is more likely attributed to a small amount of contamination on the TEM grid, as no glassware or silicon-containing reagents were used in the preparation of these bimetallic NPs.*

***Figure 3-15**: TEM images and related size histograms for borohydride-capped Au_xAg_{1-x}NPs for (A, B) x = 0.6; (C, D) x = 0.3; and (E, F) x = 0.0 (i.e., AgNPs). The borohydride-to-metal molar ratio (R value) is 2 for these samples.*

***Figure 3-16**: Representative TEM images and size distribution histograms for R = 5 Au_xAg_{1-x}NPs where (A, B) x = 1.0 and (C, D) x = 0.3. Note the apparent formation of metal networks and particle ripening (sizes of metal networks were ignored during particle size analysis).*

***Figure 3-17**: Representative TEM images and size distribution histograms for R = 10 Au_xAg_{1-x}NPs, for (A, B) x = 1.0 and (C, D) x = 0.3. Note the occasional large nanoparticle or aggregation of nanoparticles, particularly in panel C.*

***Figure 3-18**: Plots depicting the pseudo-first-order kinetics of 4-NP reduction and associated catalytic rates (k_{app}) using 5 d-old borohydride-stabilized Au_xAg_{1-x}NP nanocatalysts (R = 2, 5, and 10, top to bottom). Excluded x values for a particular R value indicate the observation of colloidal precipitation after aging for 5 d.*

***Figure 3-19**: (A) Turnover frequency (TOF) and (B) TOF per U.S. dollar (USD), expressed as functions of the overall nanoparticle composition, for borohydride-stabilized Au_xAg_{1-x}NPs applied as nanocatalysts for 4-NP reduction. Panel (B) illustrates the economic viability of replacing Au with Ag in this catalytic system by way of a monotonic increase in the TOF per USD. Economic performance is based on current representative vendor prices for the metal precursors used, as mentioned in the Supplementary Information for this Chapter.*

***Figure 3-20**: Assessment of the recyclability of the R = 2, x = 0.3 bimetallic Au_xAg_{1-x}NPs. Top) Absorbance spectra (blue, left axis) and rate plots (red, right axis) for each cycle versus time, with considerable slowing of the reaction rate observed in later cycles. The duration of time between cycles when the cuvette was mixed outside of the instrument has been removed for clarity. Bottom) The k_{app} (blue, left axis) and TOF (red, right axis) values for each cycle, showing exponential decay in activity with sequential cycles.*

***Scheme 4-1:** Proposed PINC Synthetic Routes*

***Figure 4-1**: Characterization of the [mpim]I silane IL and PINC. A) and B) respective ^1H NMR spectra; C) XRPD pattern of [mpim]I PINC; D) FTIR spectrum of [mpim]I PINC; E) TGA thermogram of [mpim]I PINC; F) photographs of i) [mpim]I silane IL below ethyl acetate and ii) [mpim]I PINC.*

***Figure 4-2**: [1]H-NMR spectrum of butylimidazolium iodide silane IL. Peak assignments show the presence of residual solvent (chloroform) and possibly water (at 1.8 ppm). The following shifts are identified (500MHz; $CDCl_3$): 10.18 (1H, s, N-C**H**-N), 7.45 and 7.40 (1H each, s, CH_2-N-C**H**-C**H**), 4.35 (4H, t, C**H**$_2$-N-CH-N-C**H**$_2$), 3.56 (9H, s, C**H**$_3$-O-Si), 2.03 (2H, m, CH_3-CH_2-C**H**$_2$), 1.91 (2H, m, Si-C**H**$_2$), 1.39 (2H, m, CH_3-C**H**$_2$), 0.96 (3H, t, C**H**$_3$), 0.64 (2H, t, Si-CH_2-C**H**$_2$).*

***Figure 4-3**: [1]H-NMR spectrum of the butylimidazolium iodide PINC. Interlocking of the longer alkyl chain branching from the imidazolium ring dissuades delamination of the PINC in water, resulting in broader peaks than those observed in the methylimidazolium iodide PINC. This broadening also reduces peak resolution, producing a significant hurdle for integration. Peak assignments show the presence of residual solvent (ethanol). The following shifts are identified (600MHz; D_2O): 7.49 (2H, s, CH_2-N-C**H**-C**H**), 4.19 (4H, m, C**H**$_2$-N-CH-N-C**H**$_2$), 1.96 (2H, m, Si-CH_2-C**H**$_2$), 1.87 (2H, m, CH_3-CH_2-C**H**$_2$), 1.33 (3H, m, CH_3-C**H**$_2$), 0.94 (3H, s, C**H**$_3$), 0.93 (2H, s, clay-C**H**$_2$). The proton located at the N-C**H**-N location experiences rapid exchange with D_2O, resulting in its absence from the spectrum.*

***Figure 4-4**: XRPD diffractogram for the butylimidazolium iodide PINC. Sharp peaks are present at 32°, 45°, and 57° 2Θ, corresponding to the (200), (220), and (222) reflections in NaCl, respectively. All other reflections are indicative of a 2:1 phyllosilicate clay, with peak broadening attributed to the large organic moiety [(1-butyl-(3-propyl)imidazolium] present on the lamella surface.*

***Figure 4-5**: [1]H-NMR spectrum of octylimidazolium iodide silane IL. Peak assignments show the presence of residual solvent (chloroform) and possibly water (at 1.8 ppm). The following shifts are identified (500 MHz; $CDCl_3$): 10.03 (1H, s, N-C**H**-N), 7.69 and 7.42 (1H each, s, CH_2-N-C**H**-C**H**), 4.34 (4H, m, C**H**$_2$-N-CH-N-C**H**$_2$), 3.54 (9H, s, C**H**$_3$-O-Si), 2.01 (2H, m, Si-…-N-CH_2-C**H**$_2$), 1.90 (2H, m, Si-C**H**$_2$), 1.26 (10H, m, CH_3-C**H**$_2$-C**H**$_2$-C**H**$_2$-C**H**$_2$-C**H**$_2$), 0.84 (3H, t, C**H**$_3$), 0.63 (2H, t, Si-CH_2-C**H**$_2$). Peaks marked with a green asterisk (*) are unidentified but may belong to a degradant of octyimidazole.*

***Figure 4-6**: XRPD diffractogram for the octylimidazolium iodide PINC. Sharp peaks are present at 27°, 32°, 45°, 54°, 57°, and 66° 2Θ, corresponding to the (111), (200), (220), (311), (222), and (400) reflections in NaCl, respectively. All other reflections are indicative of a 2:1 phyllosilicate clay, with peak broadening attributed to the large organic moiety [(1-octyl-(3-propyl)imidazolium] present on the lamella surface. It is possible that the absence of the (001) reflection in the PINC, typically found near 8° 2 Θ, is indicative of a large interlayer spacing in the lamellar structure resulting from steric hinderances caused by the large octyl chain.*

***Figure 4-7**: Transmission FTIR spectra of the [m-, [b, and [opim]I PINCs. Magneso-silicate peaks are observed at ~520 cm^{-1} for Mg–O, 1015-1020 cm^{-1} for Si–O–Si, 1165-1170 cm^{-1} for Si–C, 3430-3450 cm^{-1} for O–H, and 3700 cm^{-1} for MgO–H. Organic*

moieties display characteristic peaks at 1380-1480 cm^{-1} for C–N, 1560-1575 cm^{-1} for C–C, 2930-2960 cm^{-1} for alkyl C–H, and 3000-3150 cm^{-1} for ring C–H.

***Figure 4-8**: TGA thermogram (top) and 1st derivative plot (bottom) for the methylimidazolium and butylimidazolium iodide PINCs. For [mpim]I PINC, the following mass losses are noted: 9% loss before 200 °C attributed to gradual release and evaporation of water, EtOH, and MeOH; 31% mass loss from 250 to 450 °C attributed to degradation of the methylimidazolium functionality; 8% mass loss from 475 to 600 °C attributed to degradation of the propyl chain. For the [bpim]I PINC, the following mass losses are noted: 6% loss before 200 °C attributed to gradual release and evaporation of water, EtOH, and MeOH; 30% mass loss from 225 to 375 °C attributed to degradation of the butylimidazolium functionality; 20% mass loss from 375 to 600 °C attributed to degradation of the propyl chain. For [opim]I PINC, the following mass losses are noted: 7% loss before 200 °C attributed to gradual release and evaporation of water, EtOH, and MeOH; 21% mass loss from 250 to 450 °C attributed to degradation of the octylimidazolium functionality; 10% mass loss from 475 to 600 °C attributed to degradation of the propyl chain. Note that the disproportionate mass losses observed for the organic components in [opim]I PINC are tentatively attributed to residual NaCl (presence evident in XRPD).*

***Figure 4-9**: A TGA profile for [mpim]Cl PINC which was, prior to analysis, cleaned repeatedly with ethanol and thoroughly dried to remove as much solvent and interlamellar salt and reactants as possible. Using a heating rate of 10 °C min^{-1}, the white sample was heated from room temperature to 100 °C, where it remained for 1 h, and then continued to 800 °C, where it remained for 1 h. Subtracting the wt% after drying at 100 °C for 1 h (95.4 wt%) and after run completion (37.7 wt%) yields a total mass loss due to degradation of organic moieties (i.e., the covalently-bound IL) of 57.7 wt%. Using the molecular weight of the [mpim]Cl IL moiety (159.64 g mol^{-1}), we calculate an IL loading of 3.8 mmol g^{-1}. We note that the presence of residual salt and char, the latter of which can be seen in the "post-TGA" picture, can cause error in this estimation.*

***Figure 4-10**: Characterization of [mpim]Cl silane IL/PINC and [mpim][Tf_2N] PINC. A) and B) [mpim]Cl silane IL and PINC ^{1}H-NMR spectra. Green asterisks (*) denote impurities tentatively attributed to degraded methyl imidazole. C) Scheme showing the anion exchange between [mpim]Cl PINC and [mpim][Tf_2N]. D) PXRD diffractograms for both [mpim]Cl and [mpim][Tf_2N] PINCs, with red asterisks (*) denoting the NaCl (200), (220), and (222) impurity peaks. The higher diffraction angle for the (001) peak in [mpim][Tf_2N] PINC when compared to [mpim]Cl PINC is attributed to the hydration of Cl^-, which expands the interlayer region. E) FTIR spectra, with the denoted ν_aS=O (1350 cm^{-1}), ν_aC–F (peak at 1147 cm^{-1} and shoulder at 1230 cm^{-1}), and ν_aS–N–S (1060 cm^{-1}) bands arising from the $[Tf_2N]^-$ anion. F) TGA thermogram (solid lines) and first derivative plot (dashed lines) for each analyte from panel E, with characteristic mass losses from Tf_2N^- in the corresponding [mpim][Tf_2N] PINC. The legend in panel E also applies to panel F.*

***Figure 4-11**: (Left) SEM and (right) TEM images of [mpim]Cl PINC. The stacked PINCs in the SEM image allude to a layered structure, and the TEM image presents an average platelet size of 59.2 ± 26.8 nm (the smallest and largest measured platelets are 12 and 176 nm, respectively).*

***Figure 4-12**: Solid-state ^{29}Si NMR spectrum for [mpim]Cl PINC. We additionally provide structure representation for each condensation degree, where "Im" represents the imidazolium group and "R" represents either Mg or Si atoms. The area % for each peak is based on the deconvoluted data, which inherently possesses a maximum error of 5%.*

***Figure 4-13**: Aqueous anion exchange of Cl^- for Tf_2N^- (top left) to form an insoluble SIL precipitate [mpim][Tf_2N] PINC, and $AuCl_4^-$ (bottom) to form a sediment of [mpim][$AuCl_4$] PINC, followed by sonication and reduction via sodium borohydride ($NaBH_4$) to create sub-5 nm AuNPs supported on the PINC substrate (top right; image is from the 1.0 mM PINC@AuNPs solution and consists of 2.5 ± 0.7 nm AuNPs).*

***Figure 4-14**: Stability analysis showing A) the UV–vis spectra showing PINC@AuNP (1.0 mM Au sample, diluted to 0.25 mM for measurement) stability and B) the corresponding normalized spectra. A very slight red shift (~2 nm) was observed in the spectra for samples aged for 21 and 60 d, indicating slight growth in the AuNPs over time.*

***Figure 4-15**: Top) Schematic of the catalyzed reduction of 4-NP to 4-AP using PINC@AuNPs and $NaBH_4$. Bottom left shows the decrease in absorbance at 400 nm over time, corresponding to loss of the 4-nitrophenolate anion intermediate. At bottom right is a plot of $\ln(A_0/A_t)$ vs. time, extracting the slope (k_{app}). Notably, the 0.1 and 0.2 mol% Au reactions appear to be bilinear in nature, and as a result their respective k_{app} values were calculated as an average of the two slopes. The turnover frequency (TOF) of the 0.1 mol% Au reaction is calculated to be 25,000 h^{-1}, which, at the time of publication, is faster than any other Au catalyst reported in literature. All PINC@AuNPs used in these reductions were aged for 1 d prior to use.*

***Figure 4-16**: A) Rate plot and B) spectra showing the reduction of 4-NP to 4-AP using $NaBH_4$ and 2-month-old PINC@AuNPs as the catalyst. The apparent rates indicated in A) show good agreement with those obtained from 1-day-old PINC@AuNPs, indicating good catalyst stability.*

***Figure 4-17**: Rate plots showing the change in the apparent rate (k_{app}) imposed by recycling A) 10-day-old PINC@AuNPs and B) 2-month-old PINC@AuNPs for the catalyzed reduction of 4-NP. Both reductions were performed using 0.5 mol% Au to 4-NP. Notably, extra $NaBH_4$ was not added until cycles 6 and 7, resulting in a noticeable increase in the apparent rate. Rate retardations of 26% and 30% were observed for the 10-day-old and 2-month-old PINC@AuNPs after 7 cycles, respectively, attributed in part to the large increases to both ionic character and product concentration in the latter cycles.*

***Figure 4-18**: A) UV–vis spectroscopic analysis of PINC@AuNPs synthesized using several Au concentrations (all diluted to 0.25 mM for measurement) as well as the spectrum of a reconstituted aliquot of previously lyophilized 21.9 mM PINC@AuNPs. A red shift in the LSPR is evident as [Au] increases, indicating an increase particle size. Further, the reconstituted PINC@AuNPs solution is nearly identical to its parent solution, indicating that dry storage followed by aqueous dispersion prior to use is an attractive feature of these supported AuNPs. B) and C) TEM images of 1.0 and 21.9 mM PINC@AuNPs, showing Au-free areas in the former image and possible particle aggregation in the latter. The average particle sizes for each sample are below 5 nm.*

***Figure 4-19**: Histograms representing TEM size analysis of A) 1.0 mM PINC@AuNPs and B) 21.9 mM PINC@AuNPs. As observed in the corresponding UV–vis spectral analysis, particles produced at the lower Au concentration are smaller on average, with no observed particles with diameters larger than 5 nm. Conversely, particles synthesized using a Au concentration of 21.9 mM are about 64% larger, indicating slight aggregation. Both solutions primarily consist of particles smaller than 5 nm in diameter, and no particles with diameters larger than 10 nm were observed.*

***Figure 5-1**: Bimetallic [mpim]Cl PINC@Au_xAg_{1-x}NPs colloids ([metal] = 0.25 mM) at the 1 d (top) and 7 d (bottom) time points. Solutions are ordered based on their x value; from left to right, x = 1.0 (AuNPs) to x = 0.0 (AgNPs).*

***Figure 5-2**: UV–vis spectroscopic assessment of the LSPR band for [mpim]Cl PINC@Au_xAg_{1-x}NPs colloids after 7 d of aging, where (A) shows the full spectra and (B) is more focused to show spectral differences between x values. The legend in panel A also applies to panel B. In panel C, we show the LSPR max (λ_{max}) for each x value, where closed circles represent defined peaks and open circles represent an estimation of the LSPR due to the presence of a broad shoulder.*

***Figure 5-3**: UV–vis spectroscopic stability assessment of [mpim]Cl PINC@Au_xAg_{1-x}NPs. The legend in panel A applies to all panels. The [mpim]Cl PINC@AgNPs in panel K exhibit a large plasmon growth after storage for 1 d, necessitating the use of an inset to properly show the plasmon band. LSPR band evolution is more pronounced for colloids containing higher ratios of Ag, and most samples experience particle ripening across a 1-month time frame.*

***Figure 5-4**: Representative TEM images and particle size histograms of the x = 0.7 (top panels) and x = 0.3 (bottom panels) bimetallic [mpim]Cl PINC@Au_xAg_{1-x}NPs solutions.*

***Figure 5-5**: EDS spectrum for the x = 0.7 intermetallic sample confirming the presence of Au and Ag in a 76.5 : 23.5 atom% ratio, respectively. The inset is expanded to show the area of interest (Au and Ag).*

***Figure 5-6**: Rate plots illustrating the catalytic conversion of 4-NP to 4-AP in the presence of [mpim]Cl PINC@Au_xAg_{1-x}NPs and $NaBH_4$. The rate kinetics are determined by plotting $ln(A_t/A_0)$ vs. time, and panels A and B represent colloids aged for 3 d and 7 d, respectively. The legend in A applies to both plots. All colloids where x = 1.0–0.3 fall intermediate*

within the cyan and magenta plots. For ease of viewing, we exclude the first 5 s of the reaction from these plots due to copious bubble formation. Dashed lines indicate the linear portions used to calculate k_{app}.

***Figure 5-7**: Plots illustrating the catalytic conversion of 4-NP to 4-AP in the presence of [mpim]Cl PINC@Au_xAg_{1-x}NPs and $NaBH_4$. Panels A and B illustrate the decrease in solution absorbance at 400 nm (400 nm is the characteristic peak of the 4-nitrophenolate intermediate) when utilizing PINC@NPs aged for 3 and 7 d, respectively, as measured using UV–vis spectrometry. The legend in A applies to both panels.*

***Figure 5-8**: UV–vis spectra illustrating the much slower catalytic conversion of 4-NP to 4-AP when using PINC@AgNPs aged for 3 d. The top panel and bottom panel display the 4-NP conversion by monitoring absorbance at 400 nm and the $ln(A_0/A_t)$ rate plot, respectively, with the x = 0.1 sample provided for comparison purposes. The legend in A applies to both panels.*

***Figure 5-9**: Panel A shows the correlation between TOF and x value in the [mpim]Cl PINC@Au_xAg_{1-x}NPs after aging for either 3 or 7 d when using 0.5 mol% metal to 4-NP (excluding t_{ind} from the TOF calculation). Notably, the PINC@$Au_{0.7}Ag_{0.3}$NPs possess the highest yet recorded TOF for noble metal nanocatalysts at roughly 33,000 h^{-1}. Panel B provides the TOF per $US (based on the metal salt precursors) versus the x value for each [mpim]Cl PINC@Au_xAg_{1-x}NPs solution, while panel C provides a similar assessment using the values of pure metal. Metal salt prices were obtained from Millipore Sigma for one-gram bottles of the respective metal precursors ($HAuCl_4 \cdot 3H_2O$, cat. no. 520918, $US 141.00 for 1 g; $AgNO_3$, cat. no. 204390, $US 26.50 for 1 g), while market metal prices ($US 56.23 per g for Au, $US 0.83 per g for Ag) were obtained from https://www.nasdaq.com/market-activity/commodities/gc%3Acmx (accessed on March 22, 2021).*

***Figure 5-10**: Plot comparing the TOF values observed for free, borohydride-stabilized AuAgNPs and those generated in situ and supported directly on the [mpim]Cl PINCs. A distinct synergistic effect arising from the PINC support leads to an extreme enhancement in nanocatalytic activity, particularly at higher Au mole fractions. The R value represents the borohydride-to-metal (i.e., Au + Ag) molar ratio; for PINC-supported AuAgNPs, R = 10.*

***Figure 5-11**: Rate plot showing recycling of the PINC@$Au_{0.7}Ag_{0.3}$NPs catalyst performed by restarting the 4-NP reduction reaction. Relative k_{app} and TOF values are color-coded to their respective rate plots. Cycle four expresses a TOF value of 30,190 h^{-1}, the highest value observed for this study, alluding to the capabilities of this catalyst when utilized under conditions which suppress the induction period (e.g., inert gas flow). The trailing kinetics in cycles 2 and 3 are caused by bubble formation in the light pathway.*

***Figure 5-12**: Rate plot showing recycling of the PINC@AgNPs catalyst performed by restarting the 4-NP reduction reaction. Relative k_{app} and TOF values are color-coded to their respective rate plots. The induction time decreases with each iterative cycle and is absent for cycles 4–8, which are also cycles with the fastest TOF values.*

***Figure 5-22**: UV–vis spectra for 50 mM aqueous CR, 50 mM aqueous MB, a mixture of the dyes, the artificially summed spectra for each neat dye solution, and the mixture of dyes in the presence of PINC. Dashed black vertical lines track the shifting λ_{max} for CR and MB. The inset photograph displays the initial CR/MB dye solution prior to the addition of PINC (left cuvette) and after adding PINC and allowing the solution to rest for 48 h (right cuvette), resulting in a colorless solution.*

List of Tables

Abbreviations

4-AP	4-aminophenol
4-NP	4-nitrophenol
[bpim]	1-butyl-3-(trimethoxysilylpropyl)imidazolium
EtOH	Ethanol
FTIR	Fourier-transform infrared spectroscop
IL	Ionic liquid
[mpim]	1-methyl-3-(trimethoxysilylpropyl)imidazolium
NMR	Nuclear magnetic resonance
[opim]	1-octyl-3-(trimethoxysilylpropyl)imidazolium
PINC	Polyionic nanoclay
SEM	Scanning electron microscopy
SIL	Supported ionic liquid
TEM	Transmission electron microscopy
Tf_2N	Bis(trifluoromethylsulfonyl)imide
TGA	Thermogravimetric analysis
UV–vis	Ultraviolet–visible

Abstract

We disclose the synthesis, characterization, and application of an imidazolium-based hybrid inorganic-organic layered magnesium phyllo(organo)silicate nanosheets, coined polyionic nanoclays (PINCs), as an emergent class of supported ionic liquids which boast extremely high ionic density (3.8 mmol g^{-1} for the 1-methyl-3-propylimidazolium chloride PINC, or roughly two-thirds the ion loading in the analogous free-flowing ionic liquid) and exchangeability (i.e., tailorability) of the associated cation and counteranion. The aqueously dispersing imidazolium PINCs are employed as nanocatalyst supports for monometallic gold and silver nanoparticles (PINC@Au- and AgNPs) and their bimetallic intermediates using sodium borohydride as a reducing agent, and the resulting heterogeneous catalysts are applied for the model reduction of 4-nitrophenol to 4-aminophenol to achieve the highest reaction turnover frequency yet reported in the literature (over 33,000 h^{-1} for nanoparticles comprising a 70:30 molar ratio of Au:Ag). Remarkably, the turnover for PINC@AuNPs is a 4000% increase over the corresponding unsupported borohydride-stabilized AuNPs (600 h^{-1}), indicating an intense synergistic effect imparted by the PINC support. Additionally, aqueous anionic dye sequestration is demonstrated using Congo Red as a model dye system, accomplishing a maximum adsorption capacity of over 2,600 mg dye per g of PINC when maintained at 50 °C. The exceptional performance of these PINCs for the herein applications suggest an auspicious future for PINCs in catalysis, ion exchange, energy storage, separations, (bio)sensing, imaging, and the construction of nanoscale assemblies.

Chapter 1: The Prospective Union of Functional Nanoclays and Supported Ionic Liquids

Clay applications, which range from pottery and art preparation to dwelling construction and stain removal, were ubiquitous during the development of worldwide human civilization. In modern times, these applications extend to commercial products (e.g., toothpaste, anti-caking agents, ceramics) and specialized systems such as separations,[1] medicine,[2] nanocomposites,[3] and catalysis.[4] Typical nanoclays are minerals comprising layered tetrahedral silicate sheets and octahedral metal oxides and are differentiated by their specific ratio of silicate to metal oxide layers, sequestering them into groups of 2:1 or 1:1 phyllosilicates. For example, talc is a naturally occurring 2:1 phyllosilicate with the chemical structure $Si_4Mg_3O_{10}(OH)_2$ and is formed by metamorphism of magnesium-rich rocks in the presence of water and carbon dioxide.[5] Kaolinite, a 1:1 phyllosilicate with the chemical structure $Si_2Al_2O_5(OH)_4$, is another common mineral which is formed when allophane (an amorphous clay-like mineraloid) is subjected to high pressure, heat, and excess water. Such natural clays are ubiquitous in soil and rock deposits, and talc alone accounted for USD 2.63 billion of the global market in 2018 (with an expected compound annual growth rate of 4.42%).[6] With such a large economic footprint for natural nanoclays, impetus exists in the development of synthetic and functionalized nanoclays to expand and innovate their applications.

First popularized by Stephen Mann and Sandra Burkett in 1997,[7] functional 2:1 phyllosilicate nanoclays with the structure $R_4Si_4Mg_3O_8(OH)_2$ (comprising surface functional groups "R") were prepared by co-condensation of a functional silane and Mg^{2+}.

In this study, Mann demonstrates a simple method for the ethanolic preparation of aminoclay, a functional nanoclay with pendant propylamine groups appended to the silicate layer. The synthesis combines (3-aminopropyl)triethoxysilane and magnesium chloride at room temperature in an ethanolic environment and exploits the buffering capacity of the ammonium proton to achieve a solution pH of ~11, promoting slow condensation of brucite ($MgOH_2$) and co-condensation of the silanes on the brucite surface. The resulting two-dimensional, layered structure does not disperse in the reaction medium (ethanol) yet is dispersible in water, revealing an interesting property of aminoclay: surface protonation below the pK_a of the primary ammonium proton (~10.6[8]) results in exfoliation of individual cationic sheets (Figure 1-1). Aqueous dispersions of aminoclay can be applied as dispersible platforms for nanoparticles, and their cationic nature promotes application as antibacterial and antifungal agents and as inorganic components in hybrid composite materials opposite enzymes and deoxyribonucleic acid. Indeed, the aqueous dispersibility of aminoclay allows for many applications unsuited for talc or other, non-charged functional nanoclays.

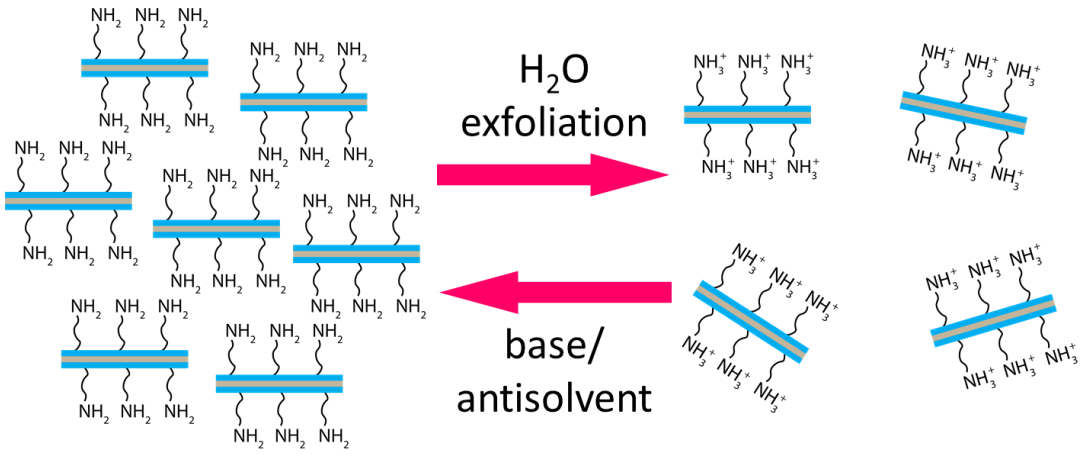

Figure 1-1*: Illustration of the delamination and precipitation of aminoclay under aqueous and basic/non-aqueous conditions, respectively.*

Characterization of aminoclay (and other functional nanoclays) typically relies on FTIR, XRD, and ^{29}Si NMR for the backbone, ^{1}H NMR and FTIR for the surface functional groups, and TGA, TEM/SEM, DLS, and AFM for the overall structure and composition. Of note, siloxane impurities within the tetrahedral layers are evident in ^{29}Si NMR and can greatly affect surface coverage, dispersibility, and crystallinity.[9]

Although their application is diverse, aminoclay is typically limited to protic media (essentially just water) below pH 10 to ensure exfoliation. Outside of these conditions, aminoclay precipitates into laminate structures of stacked clay. Fortunately, Mann's approach toward nanoclay synthesis provides near limitless pathways toward other two-dimensional functional materials. In this vein, supported ionic liquids (SILs, Figure 1-2) are functional materials which are frequently applied for similar purposes as aminoclay, such as nanoparticle stabilization,[10] catalysis,[11-12] and separation/sequestration of gases, heavy metals, and contaminants.[13] These materials encompass any substrate coated in covalently or ionically bound permanently charged organic moieties (e.g., onium and organic acids) and impart the properties (and interface) of the bulk ionic liquid contained within a thin layer. In the case of physiosorbed ions, washing of the SIL typically results in desorption and degradation of the SIL thin layer. Covalently bound ions, however, are stable under normal washing conditions and can be recycled, much like the surface of the functional nanoclays produced by Mann. Indeed, two-dimensional SILs appended to clays,[14] octosilicate,[15] and aluminum oxide[16] exist in the literature, although their preparation is limited to only top-down synthetic methods (i.e., condensation of the organic moiety onto a pre-prepared two-dimensional substrate). The top-down process has several inherent issues, such as incomplete surface modification (typically less than 85% of

theoretical surface coverage), an increase in substrate thickness (a 2:1 phyllosilicate would become a 2:2:1 phyllosilicate due to the addition of a second silane appendage to the 2:1 structure), and difficulty purifying the product from the IL precursor solution. A bottom-up, aminoclay-like approach toward a two-dimensional nanoclay SIL is of great importance to help close this gap in the literature.

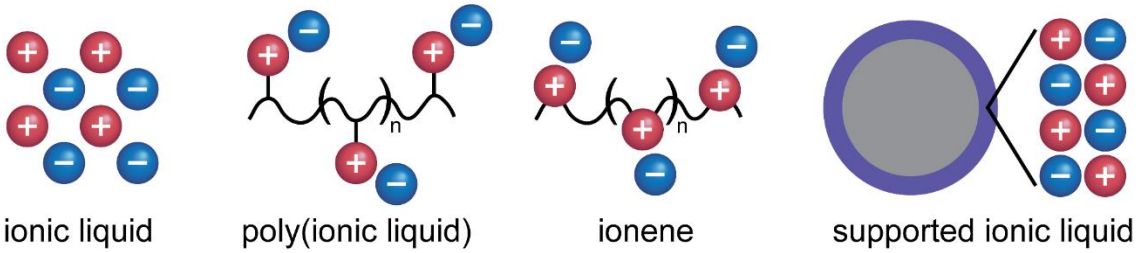

***Figure 1-2**: Visual comparison between bulk ionic liquid, polyionic polymers, and supported ionic liquids.*

Our group reported the first bottom-up preparation of a permanently charged functionalized polyionic nanoclay (PINC) and their initial application as a support material for noble metal nanocatalysts.[17] This material began as a concept to produce an aminoclay-like material with more diverse applicability, including dispersion in polar organic solvents, and quickly grew as we found that the support not only stabilized nanoparticles, but also greatly enhanced their catalytic capabilities far beyond anything we anticipated. Within this document, we provide a brief background of the model reaction used to assess noble metal nanoparticles: 4-nitrophenol (4-NP) reduction to 4-aminophenol (4-AP).[18] This discussion serves as an introduction to the reaction and our manner of calculating reaction rates and turnover frequency (TOF) as a comparator between nanocatalysts. Next, we summarize the synthesis of traditional borohydride-stabilized bimetallic gold and silver

nanoparticles (AuAgNPs) as a typical free nanocatalyst and demonstrate the 4-NP reduction reaction.[19] By free, we specifically refer to the fact that these nanocatalysts are not supported by a substrate. This study also serves as an introduction to the typical formation of nanoparticles and acts as a direct comparator for the nanoparticles prepared in the presence of the PINC substrate. The following chapter includes our introduction to PINCs, including the synthesis, characterization, and application of the imidazolium-based PINC for anion exchange and nanoparticle stabilization.[17] We also provide the first demonstration of 4-NP reduction, including a brief comparison between free and PINC-appended AuNPs. Following this is an additional PINC study demonstrating the stabilization of bimetallic imidazolium PINC@AuAgNPs and a more in-depth comparison between PINC appended and free NPs. In addition, this study includes our first non-nanoparticle PINC application: anionic dye sequestration. The final chapter concludes my work regarding PINCs and alludes to future work, including the preparation of other onium PINCs, alcohol oxidation using PINC@NPs, and further dye-sequestration applications.

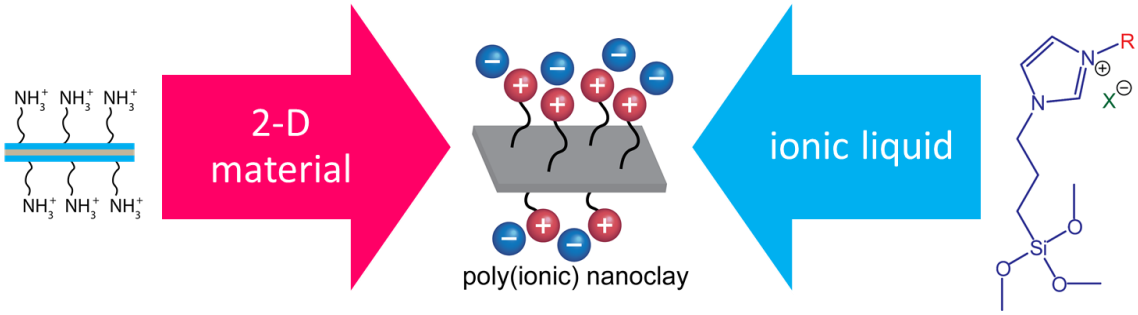

***Figure 1-3**: Illustration demonstrating the merging of ionic liquid-functionalized silanes and the aminoclay synthesis route to prepare two-dimensional polyionic nanoclays (PINCs).*

References

1. Ding, X.; Henrichs, S. M., Adsorption and Desorption of Proteins and Polyamino Acids by Clay Minerals and Marine Sediments. *Mar. Chem.* **2002,** *77* (4), 225-237.

2. Viseras, C.; Cerezo, P.; Sanchez, R.; Salcedo, I.; Aguzzi, C., Current Challenges in Clay Minerals for Drug Delivery. *Appl. Clay Sci.* **2010,** *48* (3), 291-295.

3. Balazs, A. C.; Emrick, T.; Russell, T. P., Nanoparticle Polymer Composites: Where Two Small Worlds Meet. *Science* **2006,** *314* (5802), 1107.

4. Miao, S.; Liu, Z.; Han, B.; Huang, J.; Sun, Z.; Zhang, J.; Jiang, T., Ru Nanoparticles Immobilized on Montmorillonite by Ionic Liquids: A Highly Efficient Heterogeneous Catalyst for the Hydrogenation of Benzene. *Angew. Chem. Int. Ed.* **2006,** *45* (2), 266-269.

5. Wan, Y.; Wang, X.; Chou, I. M.; Hu, W.; Zhang, Y.; Wang, X., An Experimental Study of the Formation of Talc through $CaMg(CO_3)_2$–SiO_2–H_2O Interaction at 100–200 °C and Vapor-Saturation Pressures. *Geofluids* **2017,** *2017*, 3942826.

6. Intelligence, M. Talc Market - Growth, Trends, Covid-19 Impact, and Forecasts (2021 - 2026). https://www.mordorintelligence.com/industry-reports/talc-market. *Accessed June 15, 2021.*

7. Burkett, S. L.; Press, A.; Mann, S., Synthesis, Characterization, and Reactivity of Layered Inorganic−Organic Nanocomposites Based on 2:1 Trioctahedral Phyllosilicates. *Chem. Mater.* **1997,** *9* (5), 1071-1073.

8. Farooq, W.; Lee, Y.-C.; Han, J.-I.; Darpito, C. H.; Choi, M.; Yang, J.-W., Efficient Microalgae Harvesting by Organo-Building Blocks of Nanoclays. *Green Chem.* **2013,** *15* (3), 749-755.

9. Bruneau, M.; Brendle, J.; Bennici, S.; Limousy, L.; Pluchon, S., Talc-Like Hybrids: Influence of the Synthesis. *New J. Chem.* **2020,** *44* (25), 10326-10333.

10. Manojkumar, K.; Sivaramakrishna, A.; Vijayakrishna, K., A Short Review on Stable Metal Nanoparticles Using Ionic Liquids, Supported Ionic Liquids, and Poly(Ionic Liquids). *J. Nanopart. Res.* **2016,** *18* (4), 103.

11. Monge-Marcet, A.; Pleixats, R.; Cattoen, X.; Wong Chi Man, M., Imidazolium-Derived Organosilicas for Catalytic Applications. *Catal. Sci. Techol.* **2011,** *1* (9), 1544-1563.

12. Boris, V. R.; Irina, G. T., Supported Ionic Liquids in Catalysis. *Russ. Chem. Rev.* **2017,** *86* (5), 444.

13. Riisagera, A.; Fehrmanna, R.; Haumannb, M.; Wasserscheidb, P., Supported Ionic Liquids: Versatile Reaction and Separation Media. *Top. Catal.* **2006,** *40* (1), 91-102.

14. Ha, J. U.; Xanthos, M., Functionalization of Nanoclays with Ionic Liquids for Polypropylene Composites. *Polym. Compos.* **2009,** *30* (5), 534-542.

15. Takahashi, N.; Hata, H.; Kuroda, K., Anion Exchangeable Layered Silicates Modified with Ionic Liquids on the Interlayer Surface. *Chem. Mater.* **2010,** *22* (11), 3340-3348.

16. Bauer, T.; Stepic, R.; Wolf, P.; Kollhoff, F.; Karawacka, W.; Wick, C. R.; Haumann, M.; Wasserscheid, P.; Smith, D. M.; Smith, A.-S.; Libuda, J., Dynamic Equilibria in Supported Ionic Liquid Phase (SILP) Catalysis: *In Situ* IR Spectroscopy Identifies $[Ru(Co)_XCl_y]N$ Species in Water Gas Shift Catalysis. *Catal. Sci. Techol.* **2018,** *8* (1), 344-357.

17. Larm, N. E.; Adhikari, L.; McKee, S.; Baker, G. A., Polyionic Nanoclays: Tailorable Hybrid Organic–Inorganic Catalytic Platforms. *Chem. Mater.* **2021,** *33* (10), 3585-3592.

18. Larm, N. E.; Bhawawet, N.; Thon, J. A.; Baker, G. A., Best Practices for Reporting Nanocatalytic Performance: Lessons Learned from Nitroarene Reduction as a Model Reaction. *New J. Chem.* **2019,** *43* (46), 17932-17936.

19. Larm, N. E.; Thon, J. A.; Vazmitsel, Y.; Atwood, J. L.; Baker, G. A., Borohydride Stabilized Gold–Silver Bimetallic Nanocatalysts for Highly Efficient 4-Nitrophenol Reduction. *Nanoscale Adv.* **2019,** *1* (12), 4665-4668.

Chapter 2: 4-Nitrophenol Reduction – Best Practices for Reporting the Well-Known Model Reaction[†]

[†] This Chapter is based upon a published manuscript in *New Journal of Chemistry* and is adapted with permission. Nathaniel E. Larm, Nakara Bhawawet, Jason A. Thon, Gary A. Baker, *New J. Chem.,* **2019,** *43,* 17932-17936.

The intrinsic catalytic activity of gold nanoparticles (AuNPs) has led to their use as catalysts in a variety of reactions, such as alcohol oxidation,[1] hydrogenation,[2] CO oxidation,[3] and Suzuki-Miyaura cross-coupling reaction[4] to name a few. As the demand for these versatile catalysts rises, it becomes apparent that there exist relatively few model tests to assess their catalytic efficacy in a comparative manner. Instead, interest lies in producing AuNPs possessing novel sizes, shapes, and surface chemistries, properties that are known to affect their performance as catalyts.[5-6] The catalytic activities of these novel AuNPs for the above reactions are frequently compared,[5, 7-9] but without using a well-understood model reaction, reliability in these comparisons can be uncertain.

One of the most widely used reactions to screen noble metal NPs is nitroarene reduction.[10-11] Indeed, this method is widely used to test a variety of supported AuNPs (MgO,[12] aminoclay,[13] titania,[14] graphene,[15] graphene oxide[16]) and unsupported AuNPs,[17-19] as well as Au nanoclusters (AuNCs)[20] and other noble metal NPs (Ag,[21] Pt,[22] Pd[23]), bimetallic NPs,[13, 24] and non-noble metal NPs (Ni,[25-26] Cu,[25, 27] Co,[25] Fe[25]). In particular, the aqueous reduction of 4-nitrophenol (4-NP) to 4-aminophenol (4-AP) by borohydride (BH_4^-) in the presence of a noble metal catalyst is commonly used due to the ease with which it is performed (aqueous medium, ambient pressure and temperature, UV–vis

detection method, common and cheap reagents).[10, 28-33] The reaction is monitored through an intermediate (4-nitrophenolate) peak, which strongly absorbs at 400 nm and decays as the reaction proceeds. This becomes visually evident when the UV–vis spectra are plotted as illustrated in Figure 2-1A, where the absorption at 400 nm at reaction start (t_0) drops to baseline at reaction completion (t_f). The red plot in Figure 2-1B shows a typical absorption spectrum at 400 nm as a function of time alongside the corresponding pseudo-first-order rate plot (represented by $\ln(A_0/A_t)$ *versus* time) in blue. Notably, an induction period (t_{ind}) of null spectroscopic change, attributed to a back-reaction wherein dissolved oxygen converts 4-AP to 4-nitrophenolate,[34] is observed prior to the start of analysis. Following t_{ind} is a linear portion in the rate plot where the slope equals the apparent rate (k_{app}), a widely reported value in literature when comparing catalytic activities of AuNPs.[35-39]

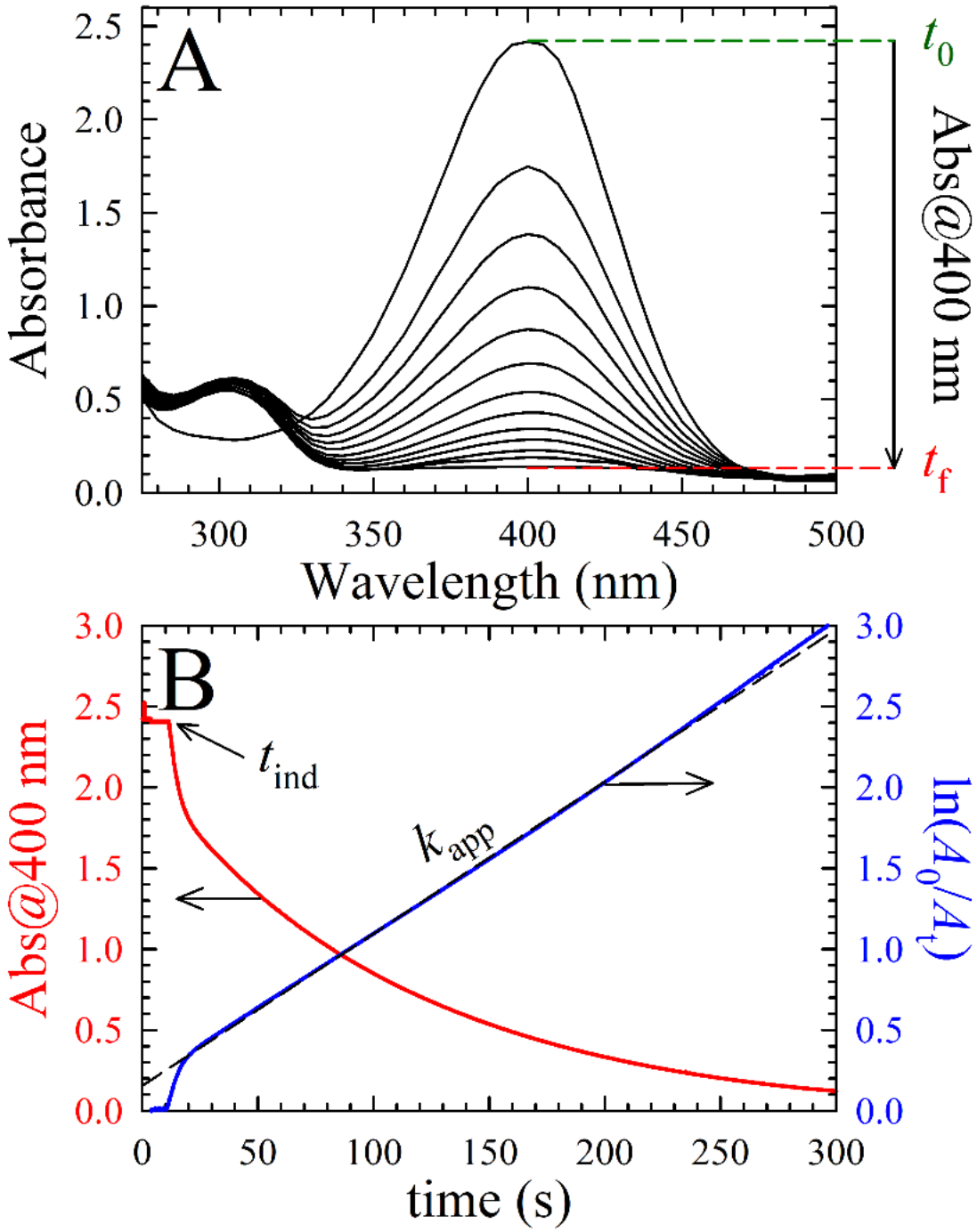

***Figure 2-1**: A) Typical spectra of 4-nitrophenolate (λ_{max} = 400 nm) as it converts to 4-AP over time (t_0–t_f) in the presence of AuNP catalyst. B) Example time-dependent absorption (red) and rate plot (blue). A black arrow on the absorption spectrum marks the induction period (t_{ind}), here lasting about 10 s. The k_{app} can be determined from the slope of the linear section of the rate plot, shown here as a dashed line.*

While many researchers report k_{app} values for this reaction, occasionally the catalyst loading with regards to 4-NP (mol% Au) is absent in experimental descriptions. Specifically, here mol% Au incorporates moles of Au metal, not moles of NPs. These poor reporting practices are problematic, as the observed k_{app} shows direct correlation with mol% Au.[40] Further, researchers often report comparisons between k_{app} values of their AuNPs and others from literature without mentioning that the mol% Au was incongruent between studies. This oversight makes the relationship between mol% Au and k_{app} an elemental and severely lacking aspect of this model reaction. To better understand this relationship, we prepared AuNPs using ascorbic acid (AA; AA-AuNPs) as a dual-role reducing and capping agent via a previously reported method[19] (experimental details can be found in Table 2-1 with UV–vis characterization in Figure 2-2). These AuNPs were chosen due to their simple and highly reproducible synthesis, making comparisons between AA-AuNP solutions prepared in different laboratories reliable. The solution of AA-AuNPs was used for the model reduction of 4-NP to 4-AP (triplicate runs) using a range of catalyst loadings and the resulting k_{app} was determined in each case (Figure 2-3 and Table 2-2). For reproducibility, this process was repeated independently by three researchers. As can be seen in Figure 2-4, mol% Au and k_{app} are proportional (assuming negligible activity in the absence of catalyst), indicating that k_{app} for this reaction can be tailored by simply changing mol% Au. This relationship, which is only rarely discussed in the literature,[40] reinforces the importance of transparency regarding reaction conditions and establishes that AuNP systems cannot be directly compared using k_{app} unless identical mol% Au values are used.

Table 2-1: *Volumes of AA-AuNP solution used to prepare the specified catalyst loadings (mol% Au, relative to 4-NP) for testing nanocatalytic 4-NP reduction and the resulting molar amounts of the reaction constituents.*

mol% Au	Vol. AA-AuNP soln. (mL)	4-NP (mol)	$NaBH_4$ (mol)	Au (mol)
1.25%	0.021	4.20×10^{-7}	9.00×10^{-5}	5.25×10^{-9}
2.50%	0.042	4.20×10^{-7}	9.00×10^{-5}	1.05×10^{-8}
5.00%	0.084	4.20×10^{-7}	9.00×10^{-5}	2.10×10^{-8}
7.50%	0.126	4.20×10^{-7}	9.00×10^{-5}	3.15×10^{-8}
10.0%	0.168	4.20×10^{-7}	9.00×10^{-5}	4.20×10^{-8}
12.5%	0.210	4.20×10^{-7}	9.00×10^{-5}	5.25×10^{-8}
15.0%	0.252	4.20×10^{-7}	9.00×10^{-5}	6.30×10^{-8}
17.5%	0.294	4.20×10^{-7}	9.00×10^{-5}	7.35×10^{-8}
20.0%	0.336	4.20×10^{-7}	9.00×10^{-5}	8.40×10^{-8}
22.5%	0.378	4.20×10^{-7}	9.00×10^{-5}	9.45×10^{-8}
25.0%	0.420	4.20×10^{-7}	9.00×10^{-5}	1.05×10^{-7}
27.5%	0.462	4.20×10^{-7}	9.00×10^{-5}	1.16×10^{-7}
30.0%	0.504	4.20×10^{-7}	9.00×10^{-5}	1.26×10^{-7}

Table 2-2: *Apparent catalytic rates and turnover frequencies as functions of mol% Au for the AA-AuNP-catalyzed reduction of 4-NP. Errors are listed parenthetically and represent standard deviations for three separate measurements made by each of three researchers (#1–3).*

mol% Au	k_{app} (s^{-1}) (#1)	k_{app} (s^{-1}) (#2)	k_{app} (s^{-1}) (#3)	TOF (h^{-1}) (#1)	TOF (h^{-1}) (#2)	TOF (h^{-1}) (#3)
1.25%	$9.83(0.65) \times 10^{-4}$	$9.46(0.15) \times 10^{-4}$	$1.13(0.18) \times 10^{-3}$	90(6)	87(14)	104(16)
2.50%	$2.00(0.20) \times 10^{-3}$	$1.93(0.18) \times 10^{-3}$	$1.99(0.27) \times 10^{-3}$	92(9)	89(8)	91(12)
5.00%	$3.68(0.15) \times 10^{-3}$	$3.38(0.33) \times 10^{-3}$	$3.95(0.53) \times 10^{-3}$	84(3)	77(7)	91(12)
7.50%	$5.54(0.20) \times 10^{-3}$	$5.36(0.13) \times 10^{-3}$	$6.08(0.24) \times 10^{-3}$	84(3)	82(2)	93(4)
10.0%	$7.01(0.31) \times 10^{-3}$	$6.87(0.17) \times 10^{-3}$	$8.90(0.24) \times 10^{-3}$	80(3)	78(2)	101(3)
12.5%	$8.95(0.69) \times 10^{-3}$	$1.01(0.01) \times 10^{-2}$	$1.10(0.04) \times 10^{-2}$	82(6)	92(1)	100(4)
15.0%	$1.02(0.01) \times 10^{-2}$	$1.28(0.08) \times 10^{-2}$	$1.56(0.07) \times 10^{-2}$	77(1)	97(6)	118(5)
17.5%	$1.21(0.10) \times 10^{-2}$	$1.49(0.02) \times 10^{-2}$	$1.70(0.09) \times 10^{-2}$	79(6)	97(2)	111(6)
20.0%	$1.52(0.12) \times 10^{-2}$	$1.70(0.04) \times 10^{-2}$	$1.50(0.09) \times 10^{-2}$	87(7)	97(2)	86(5)
22.5%	$1.74(0.07) \times 10^{-2}$	$2.24(0.14) \times 10^{-2}$	$1.88(0.33) \times 10^{-2}$	85(4)	110(7)	92(6)
25.0%	$2.04(0.16) \times 10^{-2}$	$2.29(0.05) \times 10^{-2}$	$2.04(0.09) \times 10^{-2}$	93(7)	104(2)	93(4)
27.5%	$2.15(0.16) \times 10^{-2}$	$2.41(0.03) \times 10^{-2}$	$2.54(0.08) \times 10^{-2}$	90(7)	100(1)	106(3)
30.0%	$2.33(0.11) \times 10^{-2}$	$2.50(0.04) \times 10^{-2}$	$2.76(0.16) \times 10^{-2}$	98(4)	94(2)	104(6)

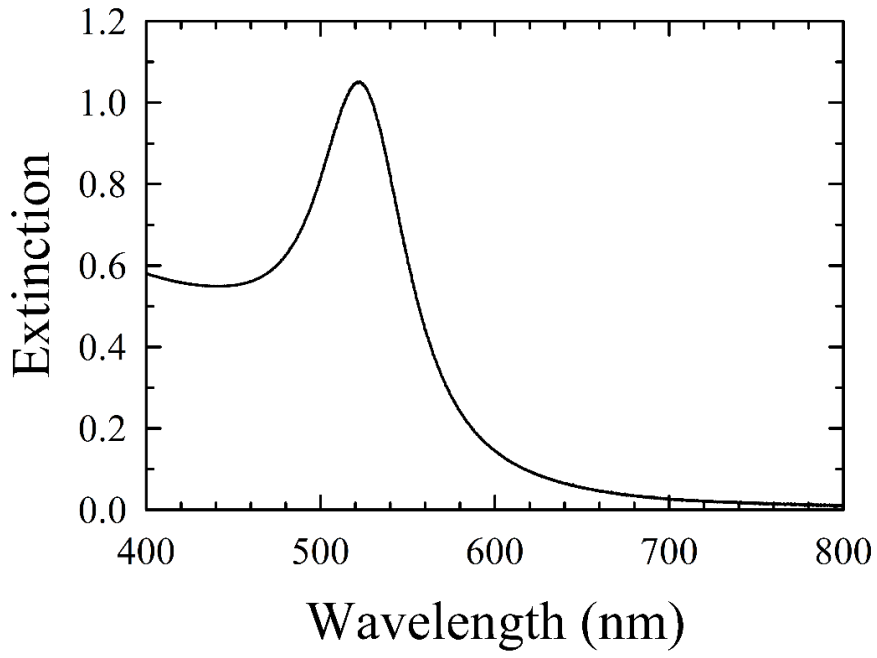

***Figure 2-2**: A typical UV–vis spectrum of AA-AuNPs. The position of the localized surface plasmon resonance (LSPR) band at 522 nm corresponds to a mean particle size of 33 ± 9 nm.*

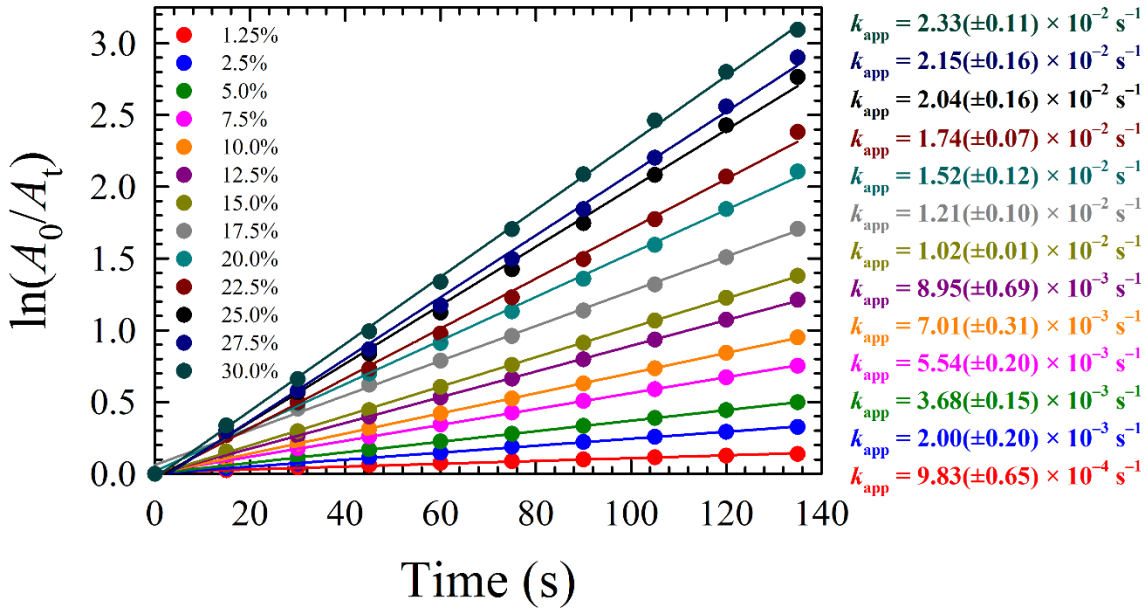

***Figure 2-3**: Representative kinetic plots for AA-AuNP-catalyzed 4-NP reduction showing the range of catalyst loadings examined. The apparent rates shown were obtained from the slopes of the linear regressions for each catalytic run shown.*

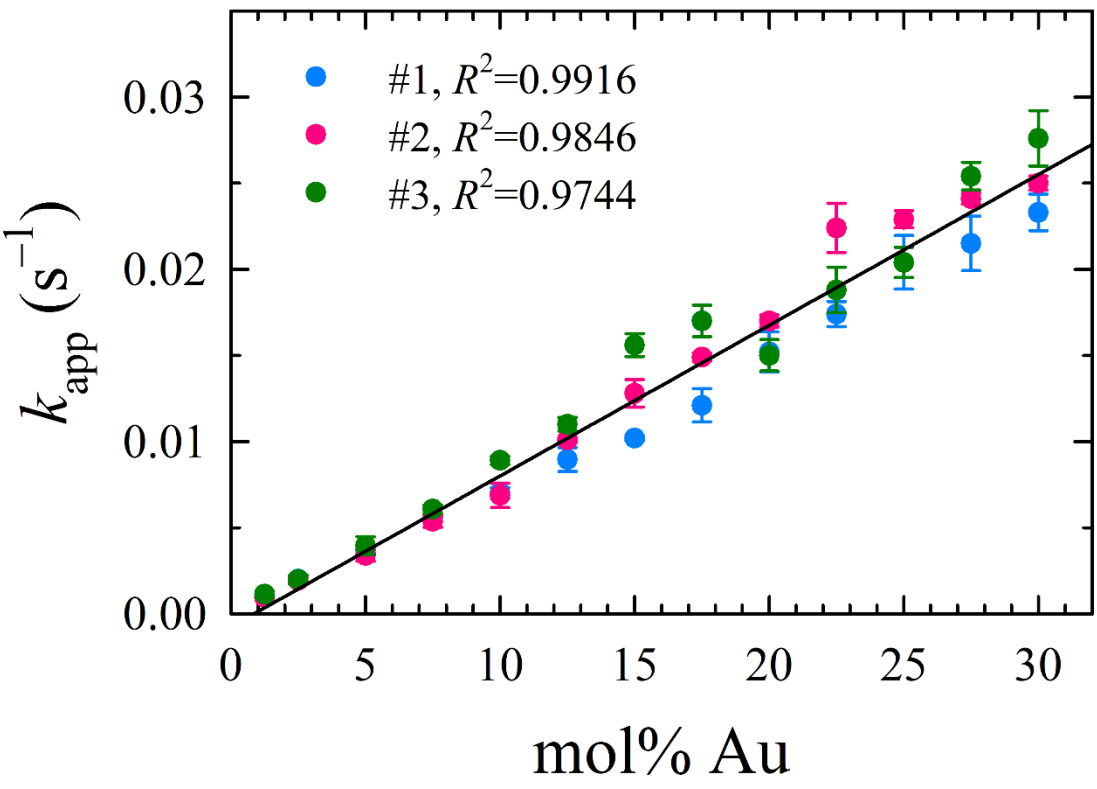

***Figure 2-4**: Plot showing the linear relationship between k_{app} and mol% Au to 4-NP when using AA-AuNPs as catalysts as determined in triplicate by three researchers (#1–3) working independently.*

Occasionally, the mol% Au cannot be universal between studies due to experimental limitations (e.g., very low or high catalyst activity, poor solubility or limited availability of catalyst).[37, 41-42] For these instances, and indeed as a standard in reporting of this model reaction moving forward, we look to use a simple calculation to replace k_{app}. Turnover frequency (TOF), a value from enzymology representing the conversion of substrate to product per amount of catalyst in a period of time, should be reported alongside k_{app} in nanoparticle catalysis.[36, 43] TOF can be calculated as follows for this reaction:

$$\mathbf{TOF} = \frac{\boldsymbol{n}_{\mathbf{4\text{-}NP}}}{(\boldsymbol{n}_{\mathbf{Au}})(\boldsymbol{t}_{\mathbf{rxn}})} \times \frac{\mathbf{completion\ \%}}{\mathbf{100}} \quad (1)$$

where $n_{4\text{-NP}}$ and n_{Au} are the moles of 4-NP and catalyst, respectively, and t_{rxn} is the time in hours from initial mixing to reaction completion (note that t_{rxn} in this calculation includes the induction period, indicating that AuNP surface restructuring hinders apparent catalytic performance). The percent reaction completion is included as a correction to exclude unreacted substrate from the calculation. Incorporating the amounts of 4-NP and Au used for the reaction allows TOF to be used to compare the catalytic activities of different AuNP systems regardless of the mol% Au used, making it an indiscriminate method for determining catalytic activity. It does, however, have a limitation: the value t_{rxn} does not currently have a universal criterion dictating when the reaction is considered "complete."[8] To tackle this problem, we synthesized data to model a typical catalyzed 4-NP reduction and examined the effect of t_{rxn} on TOF. Using a k_{app} value of 0.015 s^{-1} and an initial 4-NP concentration (C_0) of 0.14 mM we simulated a pseudo-first-order reaction and rate plot (Figure 2-5A, blue and red lines, respectively).

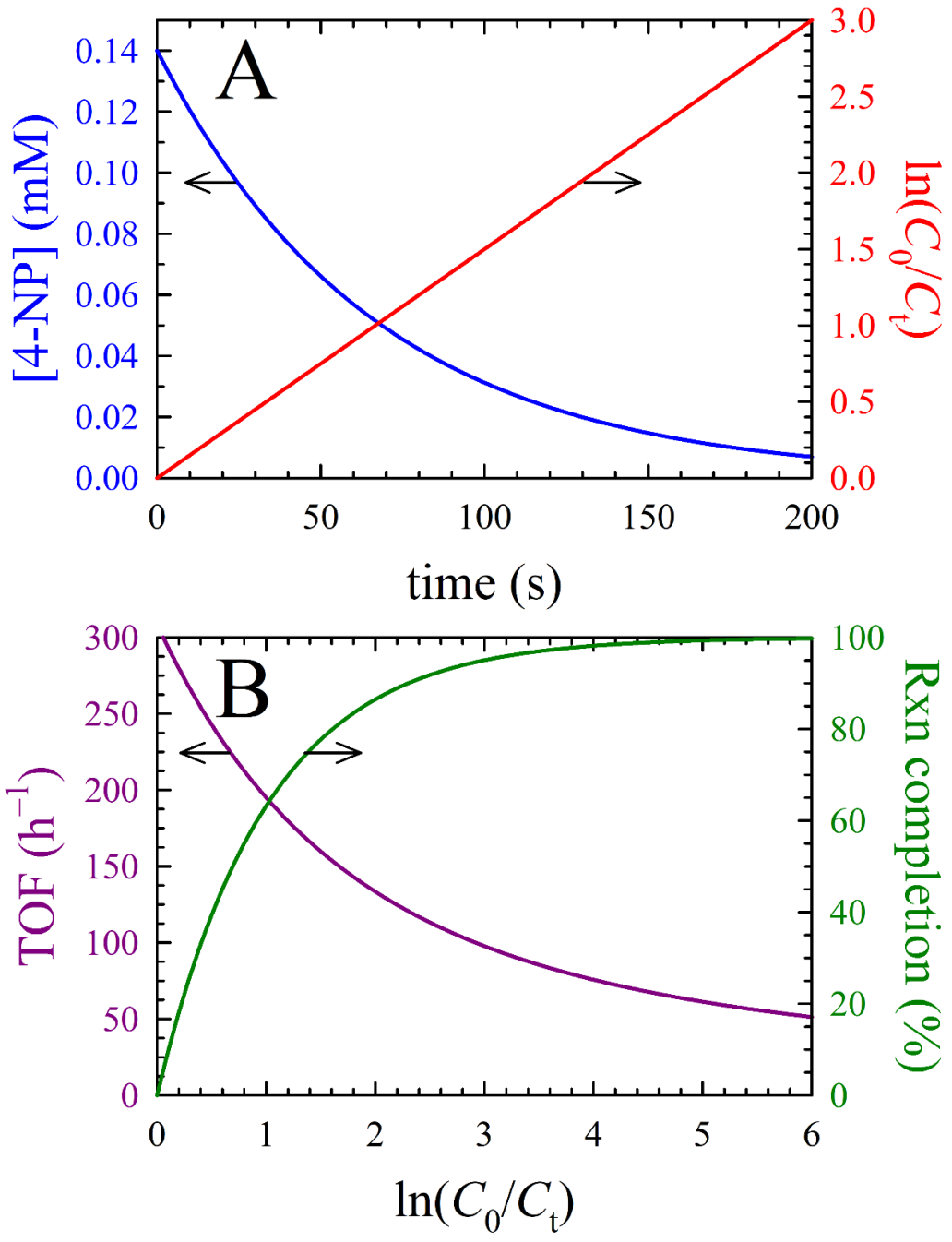

***Figure 2-5**: A) In blue, a plot of [4-NP] versus time using synthesized data (t_{ind} = 0, $[4\text{-NP}]_0$ = 0.14 mM, k_{app} = 0.015 s^{-1}). In red, the corresponding pseudo-first-order rate plot. B) Relationship between % reaction completion (conversion of 4-NP to 4-AP) and the calculated TOF using Eq. 1 and the synthesized data above at each value of $\ln(C_0/C_t)$. Note that $\ln(C_0/C_t)$ is equal to $\ln(A_0/A_t)$, as concentration and absorbance are proportional.*

Note that we assume an induction period (t_{ind}) of 0 s to simplify the calculations and use $\ln(C_0/C_t)$ for the rate plot instead of $\ln(A_0/A_t)$ since concentration and absorbance are proportional. We calculated values for TOF using Eq. 1 and the t_{rxn} value and reaction completion % that correspond to each $\ln(C_0/C_t)$ value (Figure 2-5B, purple line). As the $\ln(C_0/C_t)$ value numerically represents the reaction progress, we also plotted their relationship in green as a visual reference. It is easily observed in Figure 2-5B that the calculated TOF is highly dependent on reaction completion %: the reliability of residual substrate conversion is hampered by UV–vis limitations at higher $\ln(C_0/C_t)$, whereas lower $\ln(C_0/C_t)$ values produce inflated TOFs which observe greater penalty from long t_{ind}. As such, a standard value of $\ln(C_0/C_t)$, or $\ln(A_0/A_t)$, must be established to make TOF a comparable value between studies. We assert that a $\ln(C_0/C_t)$ value of 3 (95% reaction completion), being located between these two limitations, should be universally used. This standard value should prolong the overall measurement time to enhance reproducibility while simultaneously avoiding instrument sensitivity limitations during late-stage reaction progress.

Using this standard, we determined the TOF at $\ln(A_0/A_t) = 3$ for each mol% Au using the data from Figure 2-4 and compiled the results in Figure 2-6 and Table 2-2. As expected, the calculated TOF is consistent across all mol% Au values for this AuNP system, with an average value of 92.4 and %RSD of 10.7%, alluding to the robust nature of the AA-AuNP synthesis while also confirming that TOF is a better comparison metric than k_{app} when catalyst loading is not consistent.

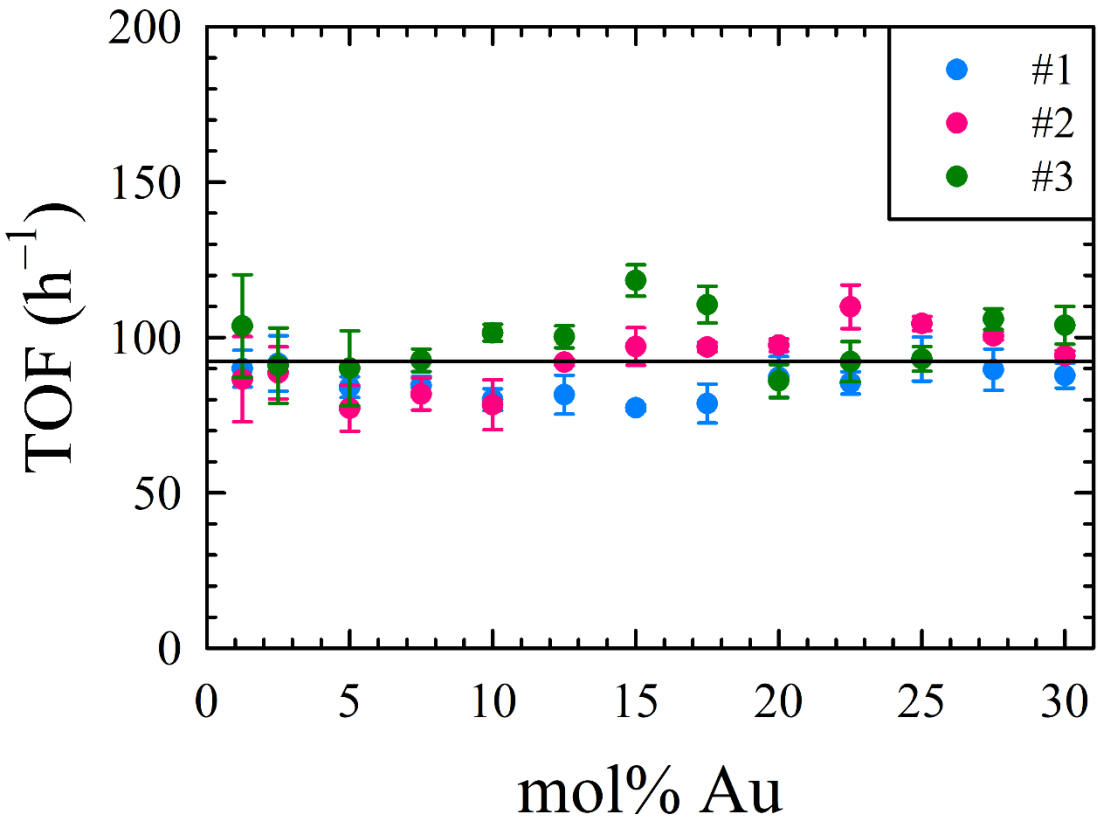

***Figure 2-6**: Plot showing the variability in TOF with respect to mol% Au when using Eq. 1 at a reaction completion criterion of $\ln(A_0/A_t) = 3$ (95% completion) for each researcher (#1–3). The solid black line at 92.4 h^{-1} represents the average TOF.*

In summary, we propose new standards for reporting the model reaction of 4-NP reduction when using AuNPs as catalysts. A commonly reported value for this reaction, k_{app}, has been shown to scale linearly with respect to mol% Au, making it a tailorable quantity which must be explicitly defined by the experimental parameters before comparisons can be made to other AuNP systems. As a replacement, we recommend that researchers report TOF, a value which incorporates the quantities of substrate and catalyst used in the reaction as well as reaction time. Further, we propose that a reaction completion of 95% (corresponding to a $\ln(A_0/A_t)$ value of 3) allows for reliable calculation of TOF by avoiding

instrument sensitivity limitations from low precursor concentration. It is our assertion that these guidelines can help alleviate confusion and inaccurate reporting with regards to this frequently used model reaction. In addition, these guidelines should be applicable to other catalytic systems as well, in particular those using metal nanoparticles.

Chapter 2 Supplementary Information

Chemicals and Reagents. Ultrapure Millipore water purified to a resistivity of 18.2 MΩ cm at 25 °C was used throughout. Tetrachloroauric acid trihydrate ($HAuCl_4 \cdot 3H_2O$, ≥99.9%, 520918), L-ascorbic acid (AA, Fluka, ≥99.9998%, 05878), sodium borohydride ($NaBH_4$, 99.99%, 480886), and 4-nitrophenol (4-NP, ≥99%, 241326) were purchased from Millipore Sigma (St. Louis, MO) and were used as received.

Characterization. UV–vis spectroscopy was performed on a Cary 50 Bio UV–vis spectrophotometer using Fisherbrand™ disposable poly(methyl methacrylate) (PMMA) cuvettes (10 mm path length, 14-955-130, Fisher Scientific, Pittsburgh, PA).

Gold Nanocatalyst Synthesis. The following procedure was followed independently by each of three researchers performing the nanocatalysis experiments discussed herein. This method was found to yield ascorbic acid-capped gold nanoparticles (AA-AuNPs) with highly reproducible optical properties and catalytic performances for 4-NP reduction. Additionally, the synthetic route is simple to follow and convenient (*i.e.*, no heating and only three components are needed, one being water), endorsing these AuNPs as valuable nanocatalysts for benchmarking the performance of future nanocatalysts for this model reaction. In a typical synthesis of AA-capped AuNPs, 18 mL of Millipore water were added to a 100-mL round bottom flask that had previously been cleaned with *aqua regia*, exhaustively rinsed with Millipore water, and then equipped with a Teflon®-coated stir bar. 1.0 mL of 5.0 mM $HAuCl_4 \cdot 3H_2O$ was pipetted into the water in the flask and the solution stirred for 1 min at 750 rpm before adding 1.0 mL of 17.0 mM AA to initiate reduction of the gold. The solution immediately became red, indicating the successful formation of AA-

AuNPs. AA-AuNPs solutions were stored at room temperature and aged protected from light for 1 day prior to benchmarking AA-AuNP nanocatalytic behavior.

4-Nitrophenol Reduction. The activity of AA-AuNPs for catalyzing the reduction of 4-nitrophenol (4-NP) to 4-aminophenol (4-AP) under the action of $NaBH_4$ was assessed for different catalyst levels spanning the range of 1.25 to 30.0 mol% Au (Table 2-1). It should be noted that each researcher (n = 3) independently prepared the stock solutions from which they conducted catalytic studies in order to truly evaluate the reproducibility through the whole of this model reaction: this also includes the individual synthesis of the AA-AuNP catalyst by each experimenter.

To assess the catalytic activity of the AA-AuNPs toward 4-NP reduction, 0.9 mL of freshly prepared aqueous 0.1 M $NaBH_4$ was firstly added to 2.1 mL of 0.2 mM aqueous 4-NP solution (prepared the same day) in a standard, disposable PMMA cuvette, to yield a deep-yellow solution indicative of 4-nitrophenolate formation. In practice, for the preparation of the 0.1 M $NaBH_4$ stock, 10 mL of Millipore water and 37.8 mg of $NaBH_4$ initially contained in separate glass vials were combined just prior to analysis, then held on ice for up to 15–20 min for repetitive measurements, after which the stock was discarded and a fresh one made as needed. To initiate catalysis, the desired volume of AA-AuNP (nanocatalyst) solution was rapidly injected into the solution containing 4-NP and $NaBH_4$ (see Table 2-1), the cuvette swiftly capped, cautiously inverted three times to mix (being careful to minimize bubble formation), then placed into the cell holder of a Cary Bio 50 spectrophotometer, followed by triggering the Cary WinUV software to collect kinetic data. The lag between AA-AuNP injection and commencement of spectrophotometric assay was reliably 3–5 s. Reaction progress was monitored by tracking the loss in solution

absorbance at 400 nm. Reaction evolution was accompanied by a conspicuous color change from bright yellow to colorless. Assuming pseudo-first-order kinetics (a reasonable assumption, given that $[NaBH_4]/[4\text{-NP}] = 214$), the apparent rate constant (k_{app}) values for catalytic profiles were calculated from the linear correlations of $\ln(A_0/A_t)$ versus time graphs. Catalytic experiments were performed in triplicate by each researcher at every mol% Au listed in Table 2-2. Turnover frequencies (TOFs) were calculated using eqn. (1) from the main text using, for consistency, the time required to attain a $\ln(A_0/A_t)$ value of 3.0 for t_{rxn}, which corresponds to 95% completion of 4-NP reduction.

References

1. Gopi, E.; Gravel, E.; Doris, E., Direct Aerobic Oxidation of Alcohols into Esters Catalyzed by Carbon Nanotube–Gold Nanohybrids. *Nanoscale Adv.* **2019,** *1,* 1181-1185.

2. Mitsudome, T.; Kaneda, K., Gold Nanoparticle Catalysts for Selective Hydrogenations. *Green Chem.* **2013,** *15* (10), 2636-2654.

3. Tian, C.; Zhu, X.; Abney, C. W.; Liu, X.; Foo, G. S.; Wu, Z.; Li, M.; Meyer, H. M.; Brown, S.; Mahurin, S. M.; Wu, S.; Yang, S.-Z.; Liu, J.; Dai, S., Toward the Design of a Hierarchical Perovskite Support: Ultra-Sintering-Resistant Gold Nanocatalysts for Co Oxidation. *ACS Catal.* **2017,** *7* (5), 3388-3393.

4. Han, J.; Liu, Y.; Guo, R., Facile Synthesis of Highly Stable Gold Nanoparticles and Their Unexpected Excellent Catalytic Activity for Suzuki−Miyaura Cross-Coupling Reaction in Water. *J. Am. Chem. Soc.* **2009,** *131* (6), 2060-2061.

5. An, K.; Somorjai, G. A., Size and Shape Control of Metal Nanoparticles for Reaction Selectivity in Catalysis. *ChemCatChem* **2012,** *4* (10), 1512-1524.

6. Sau, T. K.; Pal, A.; Pal, T., Size Regime Dependent Catalysis by Gold Nanoparticles for the Reduction of Eosin. *J. Phys. Chem. B* **2001,** *105* (38), 9266-9272.

7. Daniel, M.-C.; Astruc, D., Gold Nanoparticles: Assembly, Supramolecular Chemistry, Quantum-Size-Related Properties, and Applications toward Biology, Catalysis, and Nanotechnology. *Chem. Rev.* **2004,** *104* (1), 293-346.

8. Deraedt, C.; Salmon, L.; Gatard, S.; Ciganda, R.; Hernandez, R.; Ruiz, J.; Astruc, D., Sodium Borohydride Stabilizes Very Active Gold Nanoparticle Catalysts. *Chem. Commun.* **2014,** *50* (91), 14194-14196.

9. Hu, H.; Xin, J. H.; Hu, H.; Wang, X.; Miao, D.; Liu, Y., Synthesis and Stabilization of Metal Nanocatalysts for Reduction Reactions – a Review. *J. Mater. Chem. A* **2015,** *3* (21), 11157-11182.

10. Aditya, T.; Pal, A.; Pal, T., Nitroarene Reduction: A Trusted Model Reaction to Test Nanoparticle Catalysts. *Chem. Commun.* **2015,** *51* (46), 9410-9431.

11. Pradhan, N.; Pal, A.; Pal, T., Silver Nanoparticle Catalyzed Reduction of Aromatic Nitro Compounds. *Colloids Surf., A* **2002,** *196* (2), 247-257.

12. Layek, K.; Kantam, M. L.; Shirai, M.; Nishio-Hamane, D.; Sasaki, T.; Maheswaran, H., Gold Nanoparticles Stabilized on Nanocrystalline Magnesium Oxide as an Active Catalyst for Reduction of Nitroarenes in Aqueous Medium at Room Temperature. *Green Chem.* **2012,** *14* (11), 3164-3174.

13. Ravula, S.; Essner, J. B.; La, W. A.; Polo-Parada, L.; Kargupta, R.; Hull, G. J.; Sengupta, S.; Baker, G. A., Sunlight-Assisted Route to Antimicrobial Plasmonic Aminoclay Catalysts. *Nanoscale* **2015,** *7* (1), 86-91.

14. Fountoulaki, S.; Daikopoulou, V.; Gkizis, P. L.; Tamiolakis, I.; Armatas, G. S.; Lykakis, I. N., Mechanistic Studies of the Reduction of Nitroarenes by Nabh4 or Hydrosilanes Catalyzed by Supported Gold Nanoparticles. *ACS Catal.* **2014,** *4* (10), 3504-3511.

15. Chen, X.; Cai, Z.; Chen, X.; Oyama, M., Aupd Bimetallic Nanoparticles Decorated on Graphene Nanosheets: Their Green Synthesis, Growth Mechanism and High Catalytic Ability in 4-Nitrophenol Reduction. *J. Mater. Chem. A* **2014,** *2* (16), 5668-5674.

16. Zhang, Y.; Liu, S.; Lu, W.; Wang, L.; Tian, J.; Sun, X., *In Situ* Green Synthesis of Au Nanostructures on Graphene Oxide and Their Application for Catalytic Reduction of 4-Nitrophenol. *Catal. Sci. Techol.* **2011,** *1* (7), 1142-1144.

17. Ansar, S. M.; Kitchens, C. L., Impact of Gold Nanoparticle Stabilizing Ligands on the Colloidal Catalytic Reduction of 4-Nitrophenol. *ACS Catal.* **2016,** *6* (8), 5553-5560.

18. Essner, J. B.; Laber, C. H.; Baker, G. A., Carbon Dot Reduced Bimetallic Nanoparticles: Size and Surface Plasmon Resonance Tunability for Enhanced Catalytic Applications. *J. Mater. Chem. A* **2015,** *3* (31), 16354-16360.

19. Larm, N. E.; Essner, J. B.; Pokpas, K.; Canon, J. A.; Jahed, N.; Iwuoha, E. I.; Baker, G. A., Room-Temperature Turkevich Method: Formation of Gold Nanoparticles at the Speed of Mixing Using Cyclic Oxocarbon Reducing Agents. *J. Phys. Chem. C* **2018,** *122* (9), 5105-5118.

20. Yamamoto, H.; Yano, H.; Kouchi, H.; Obora, Y.; Arakawa, R.; Kawasaki, H., N,N-Dimethylformamide-Stabilized Gold Nanoclusters as a Catalyst for the Reduction of 4-Nitrophenol. *Nanoscale* **2012,** *4* (14), 4148-4154.

21. Esumi, K.; Isono, R.; Yoshimura, T., Preparation of PAMAM− and PPI−Metal (Silver, Platinum, and Palladium) Nanocomposites and Their Catalytic Activities for Reduction of 4-Nitrophenol. *Langmuir* **2004,** *20* (1), 237-243.

22. Pandey, S.; Mishra, S. B., Catalytic Reduction of P-Nitrophenol by Using Platinum Nanoparticles Stabilised by Guar Gum. *Carbohyd. Polym.* **2014,** *113*, 525-531.

23. Johnson, J. A.; Makis, J. J.; Marvin, K. A.; Rodenbusch, S. E.; Stevenson, K. J., Size-Dependent Hydrogenation of P-Nitrophenol with Pd Nanoparticles Synthesized with

Poly(Amido)Amine Dendrimer Templates. *J. Phys. Chem. C* **2013,** *117* (44), 22644-22651.

24. Wu, W.; Lei, M.; Yang, S.; Zhou, L.; Liu, L.; Xiao, X.; Jiang, C.; Roy, V. A. L., A One-Pot Route to the Synthesis of Alloyed Cu/Ag Bimetallic Nanoparticles with Different Mass Ratios for Catalytic Reduction of 4-Nitrophenol. *J. Mater. Chem. A* **2015,** *3* (7), 3450-3455.

25. Formenti, D.; Ferretti, F.; Scharnagl, F. K.; Beller, M., Reduction of Nitro Compounds Using 3D-Non-Noble Metal Catalysts. *Chem. Rev.* **2018,** *119* (4), 2611-2680.

26. Wang, A.; Yin, H.; Lu, H.; Xue, J.; Ren, M.; Jiang, T., Catalytic Activity of Nickel Nanoparticles in Hydrogenation of P-Nitrophenol to P-Aminophenol. *Catal. Commun.* **2009,** *10* (15), 2060-2064.

27. Deka, P.; Deka, R. C.; Bharali, P., *In Situ* Generated Copper Nanoparticle Catalyzed Reduction of 4-Nitrophenol. *New J. Chem.* **2014,** *38* (4), 1789-1793.

28. Gu, S.; Wunder, S.; Lu, Y.; Ballauff, M.; Fenger, R.; Rademann, K.; Jaquet, B.; Zaccone, A., Kinetic Analysis of the Catalytic Reduction of 4-Nitrophenol by Metallic Nanoparticles. *J. Phys. Chem. C* **2014,** *118* (32), 18618-18625.

29. Hervés, P.; Pérez-Lorenzo, M.; Liz-Marzán, L. M.; Dzubiella, J.; Lu, Y.; Ballauff, M., Catalysis by Metallic Nanoparticles in Aqueous Solution: Model Reactions. *Chem. Soc. Rev.* **2012,** *41* (17), 5577-5587.

30. Kadam, H. K.; Tilve, S. G., Advancement in Methodologies for Reduction of Nitroarenes. *RSC Adv.* **2015,** *5* (101), 83391-83407.

31. Wunder, S.; Lu, Y.; Albrecht, M.; Ballauff, M., Catalytic Activity of Faceted Gold Nanoparticles Studied by a Model Reaction: Evidence for Substrate-Induced Surface Restructuring. *ACS Catal.* **2011,** *1* (8), 908-916.

32. Wunder, S.; Polzer, F.; Lu, Y.; Mei, Y.; Ballauff, M., Kinetic Analysis of Catalytic Reduction of 4-Nitrophenol by Metallic Nanoparticles Immobilized in Spherical Polyelectrolyte Brushes. *J. Phys. Chem. C* **2010,** *114* (19), 8814-8820.

33. Zhao, P.; Feng, X.; Huang, D.; Yang, G.; Astruc, D., Basic Concepts and Recent Advances in Nitrophenol Reduction by Gold- and Other Transition Metal Nanoparticles. *Coord. Chem. Rev.* **2015,** *287*, 114-136.

34. Menumerov, E.; Hughes, R. A.; Neretina, S., Catalytic Reduction of 4-Nitrophenol: A Quantitative Assessment of the Role of Dissolved Oxygen in Determining the Induction Time. *Nano Lett.* **2016,** *16* (12), 7791-7797.

35. Gangula, A.; Podila, R.; M, R.; Karanam, L.; Janardhana, C.; Rao, A. M., Catalytic Reduction of 4-Nitrophenol Using Biogenic Gold and Silver Nanoparticles Derived from Breynia Rhamnoides. *Langmuir* **2011,** *27* (24), 15268-15274.

36. Kästner, C.; Thünemann, A. F., Catalytic Reduction of 4-Nitrophenol Using Silver Nanoparticles with Adjustable Activity. *Langmuir* **2016,** *32* (29), 7383-7391.

37. Ma, T.; Yang, W.; Liu, S.; Zhang, H.; Liang, F., A Comparison Reduction of 4-Nitrophenol by Gold Nanospheres and Gold Nanostars. *Catalysts* **2017,** *7* (2), 38.

38. Seo, Y. S.; Ahn, E.-Y.; Park, J.; Kim, T. Y.; Hong, J. E.; Kim, K.; Park, Y.; Park, Y., Catalytic Reduction of 4-Nitrophenol with Gold Nanoparticles Synthesized by Caffeic Acid. *Nanoscale Res. Lett.* **2017,** *12* (1), 7-7.

39. Zhou, W.; Fang, Y.; Ren, J.; Dong, S., DNA-Templated Silver and Silver-Based Bimetallic Clusters with Remarkable and Sequence-Related Catalytic Activity toward 4-Nitrophenol Reduction. *Chem. Commun.* **2019,** *55* (3), 373-376.

40. Saha, S.; Pal, A.; Kundu, S.; Basu, S.; Pal, T., Photochemical Green Synthesis of Calcium-Alginate-Stabilized Ag and Au Nanoparticles and Their Catalytic Application to 4-Nitrophenol Reduction. *Langmuir* **2010,** *26* (4), 2885-2893.

41. Juárez, J.; Cambón, A.; Goy-López, S.; Topete, A.; Taboada, P.; Mosquera, V., Obtention of Metallic Nanowires by Protein Biotemplating and Their Catalytic Application. *J. Phys. Chem. Lett.* **2010,** *1* (18), 2680-2687.

42. Liu, R.; Liu, J.; Kong, W.; Huang, H.; Han, X.; Zhang, X.; Liu, Y.; Kang, Z., Adsorption Dominant Catalytic Activity of a Carbon Dots Stabilized Gold Nanoparticles System. *Dalton T.* **2014,** *43* (28), 10920-10929.

43. Chang, Y.-C.; Chen, D.-H., Catalytic Reduction of 4-Nitrophenol by Magnetically Recoverable Au Nanocatalyst. *J. Hazard. Mater.* **2009,** *165* (1), 664-669.

Chapter 3: Preparation of Unsupported, Borohydride-Stabilized Gold and Silver Bimetallic Nanocatalysts[†]

[†] This Chapter is based upon a published manuscript in *Nanoscale Advances* and is adapted with permission. Nathaniel E. Larm, Jason A. Thon, Yahor Vazmitsel, Jerry L. Atwood, and Gary A. Baker, *Nanoscale Adv.*, **2019,** *1*, 4665-4668.

Noble metal nanoparticles (NPs) are promising catalysts for a variety of organic reactions such as 4-nitroarene reduction using sodium borohydride,[1-5] aerobic oxidation of alkyl benzenes to benzaldehydes,[6-8] and alkylation of primary amines to secondary amines in the presence of an alcohol.[9-11] It is well known that the catalytic potential of noble metal NPs relies heavily on their size, shape, crystallinity, dispersity, and surface chemistry.[9, 12] In this regard, strong stabilizing ligands typically hinder catalytic activity by creating a diffusion barrier between reactants and the NP surface, with tightly-bound surfactants leading to slower diffusion of reactants and poor catalytic activity.[13] This flaw was turned into a feature by Astruc and co-workers in 2014 when they reported the synthesis of gold nanoparticles (AuNPs) stabilized by $NaBH_4$ for the catalytic reduction of 4-nitrophenol (4-NP) to 4-aminophenol (4-AP) in the presence of $NaBH_4$,[14] providing an intriguing circumstance where BH_4^- participated in the catalytic system as both the catalyst surfactant and as one of the reactants. Their catalyst preparation used clever manipulation of the concentration of $NaBH_4$, a common reducing agent[15] but seldom-utilized stabilizing ligand, to produce AuNPs possessing the highest activity for this reaction yet reported.

Bimetallic NPs provide an interesting opportunity to expand the current catalog of nanocatalysts. In particular, bimetallic gold/silver nanoparticles (AuAgNPs) provide a cheap alternative to monometallic AuNP catalysts while generally possessing higher catalytic activity for the reduction of nitroarenes.[16-22] Herein, we investigate a slightly modified Astruc method for the synthesis of monometallic AuNPs and AgNPs as well as bimetallic Au_xAg_{1-x}NPs (where *x* ranges from 0.9 to 0.1 in 0.1 increments) using $NaBH_4$ as the sole reducing/stabilizing agent. Three distinct molar ratios of reducing agent to metal (denoted herein as R values; specifically, R = 2, 5, and 10) were used to create sets of monometallic/bimetallic NP solutions as shown in Tables 3-1–3-3. These colloidal NP solutions were then used as catalysts in the reduction of 4-NP to 4-AP in the presence of $NaBH_4$, which resulted in the highest observed catalytic activity for this reaction when using noble metal NPs at room temperature.

Table 3-1: *R = 2 sample preparation for Au_xAg_{1-x}NPs reduced and stabilized by $NaBH_4$.*

Stocks	[stock] (mM)	*x*	water (mL)	$HAuCl_4$ stock (mL)	$AgNO_3$ stock (mL)	$NaBH_4$ stock (mL)
$HAuCl_4$	5.0	1.0	18.0	1.0	0.0	1.0
$AgNO_3$	5.0	0.9	18.0	0.9	0.1	1.0
$NaBH_4$	10.0	0.8	18.0	0.8	0.2	1.0
		0.7	18.0	0.7	0.3	1.0
		0.6	18.0	0.6	0.4	1.0
		0.5	18.0	0.5	0.5	1.0
		0.4	18.0	0.4	0.6	1.0
		0.3	18.0	0.3	0.7	1.0
		0.2	18.0	0.2	0.8	1.0
		0.1	18.0	0.1	0.9	1.0
		0.0	18.0	0.0	1.0	1.0

Table 3-2: *R = 5 sample preparation for Au_xAg_{1-x}NPs reduced and stabilized by $NaBH_4$.*

Stocks	[stock] (mM)	*x*	Water (mL)	$HAuCl_4$ stock (mL)	$AgNO_3$ stock (mL)	$NaBH_4$ stock (mL)
$HAuCl_4$	5.0	1.0	18.0	1.0	0.0	1.0
$AgNO_3$	5.0	0.9	18.0	0.9	0.1	1.0
$NaBH_4$	25.0	0.8	18.0	0.8	0.2	1.0
		0.7	18.0	0.7	0.3	1.0
		0.6	18.0	0.6	0.4	1.0
		0.5	18.0	0.5	0.5	1.0
		0.4	18.0	0.4	0.6	1.0
		0.3	18.0	0.3	0.7	1.0
		0.2	18.0	0.2	0.8	1.0
		0.1	18.0	0.1	0.9	1.0
		0.0	18.0	0.0	1.0	1.0

Table 3-3: *R = 10 sample preparation for Au_xAg_{1-x}NPs reduced and stabilized by $NaBH_4$.*

Stocks	[stock] (mM)	*x*	Water (mL)	$HAuCl_4$ stock (mL)	$AgNO_3$ stock (mL)	$NaBH_4$ stock (mL)
$HAuCl_4$	5.0	1.0	18.0	1.0	0.0	1.0
$AgNO_3$	5.0	0.9	18.0	0.9	0.1	1.0
$NaBH_4$	50.0	0.8	18.0	0.8	0.2	1.0
		0.7	18.0	0.7	0.3	1.0
		0.6	18.0	0.6	0.4	1.0
		0.5	18.0	0.5	0.5	1.0
		0.4	18.0	0.4	0.6	1.0
		0.3	18.0	0.3	0.7	1.0
		0.2	18.0	0.2	0.8	1.0
		0.1	18.0	0.1	0.9	1.0
		0.0	18.0	0.0	1.0	1.0

The Au_xAg_{1-x}NP colloids were initially screened using UV–vis spectrophotometry (Figures 3-1 through 3-12), monitoring for changes in their localized surface plasmon resonance (LSPR) band over time as an indication of colloid stability. The LSPR bands of the as-synthesized monometallic solutions

indicate the formation of small AuNPs ($LSPR_{max}$ of ~510 nm) and AgNPs ($LSPR_{max}$ of ~410 nm) in the x = 1.0 and 0.0 solutions, respectively, while the bimetallic solutions possess intermediate LSPR bands. Within 5 d of synthesis, aggregation in the form of a black precipitate was observed in the R = 5 AgNPs as well as all samples containing more than 50 mol% Ag ($x \leq 0.5$) from the R = 10 sample set. After aging for 20 d, the solutions of AgNPs from the R = 2, 5, and 10 sample sets, bimetallic x = 0.1 Au_xAg_{1-x}NPs from the R = 5 sample set, and bimetallic x = 0.1, 0.2, 0.3, and 0.4 Au_xAg_{1-x}NPs from the R = 10 sample set also possessed such aggregates. This aggregation is attributed to a decrease in surface potential imparted by electron injection into the NP by BH_4^-, resulting in destabilization of the colloidal dispersion.[3] All other samples showed colloidal stability through 20 d, with some broadening and red-shifting of the LSPR band in each AuNP spectrum.

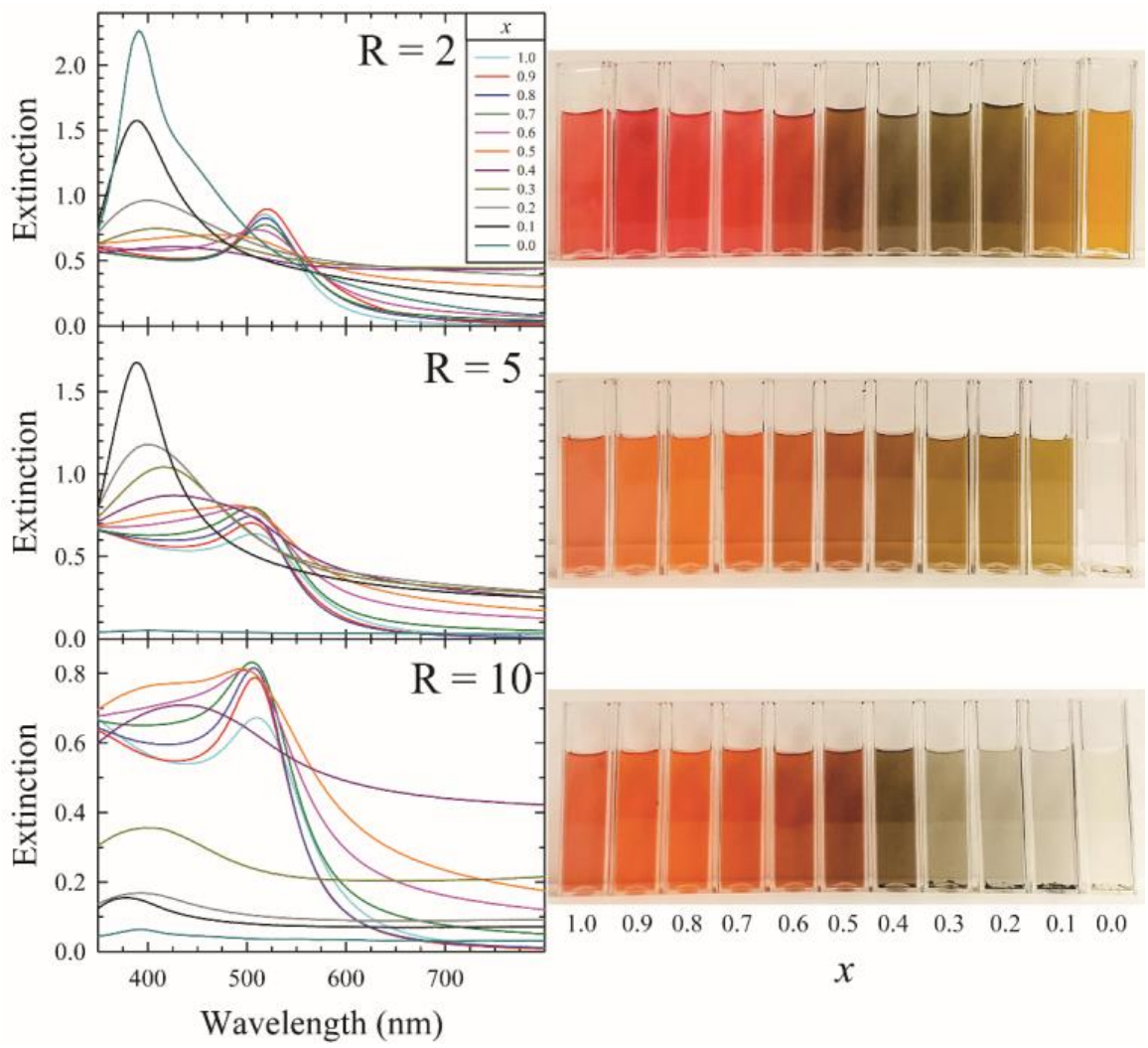

***Figure 3-1**: UV–vis spectra of borohydride-capped Au_xAg_{1-x}NPs alongside images of the samples aged for 5 d. The R values provided in the left panels denote the number of equivalents of $NaBH_4$ per metal atom employed in the synthesis. Colloidal instability in the form of black precipitates affiliated with sample decoloration is observed for very low x values (high silver content) in the R = 5 (x = 0.0) and R = 10 (x ≤ 0.3) sample sets.*

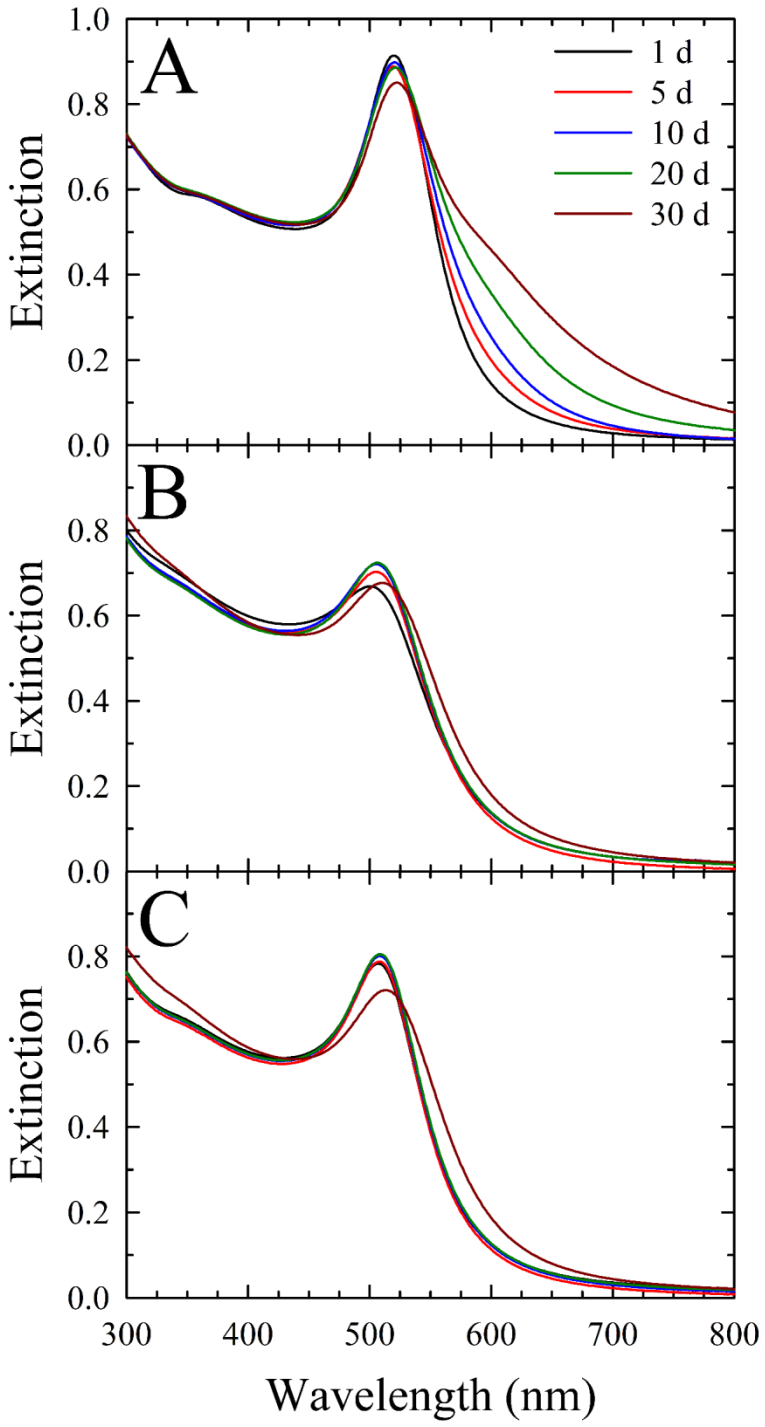

***Figure 3-2**: Stability of AuNPs (Au_xAg_{1-x}NPs for x = 1.0) over 30 days of storage as monitored using UV–vis spectrophotometry. Panels A, B, and C correspond to R values of 2, 5, and 10, respectively. The legend in panel A applies to all panels.*

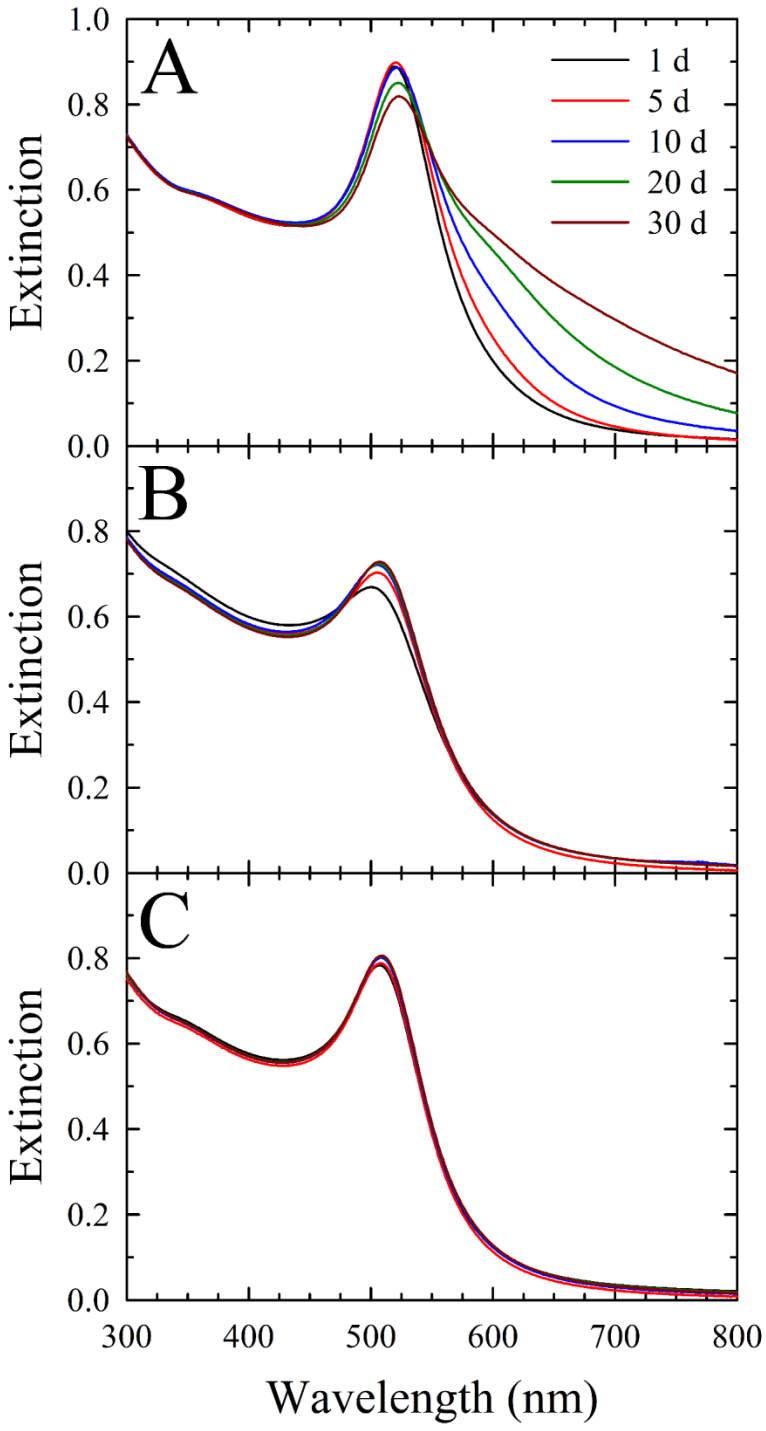

***Figure 3-3**: Stability of Au_xAg_{1-x}NPs (x = 0.9) over 30 days of storage as followed by UV–vis spectrophotometry. Panels A, B, and C correspond to R values of 2, 5, and 10, respectively. The legend in panel A applies to all panels.*

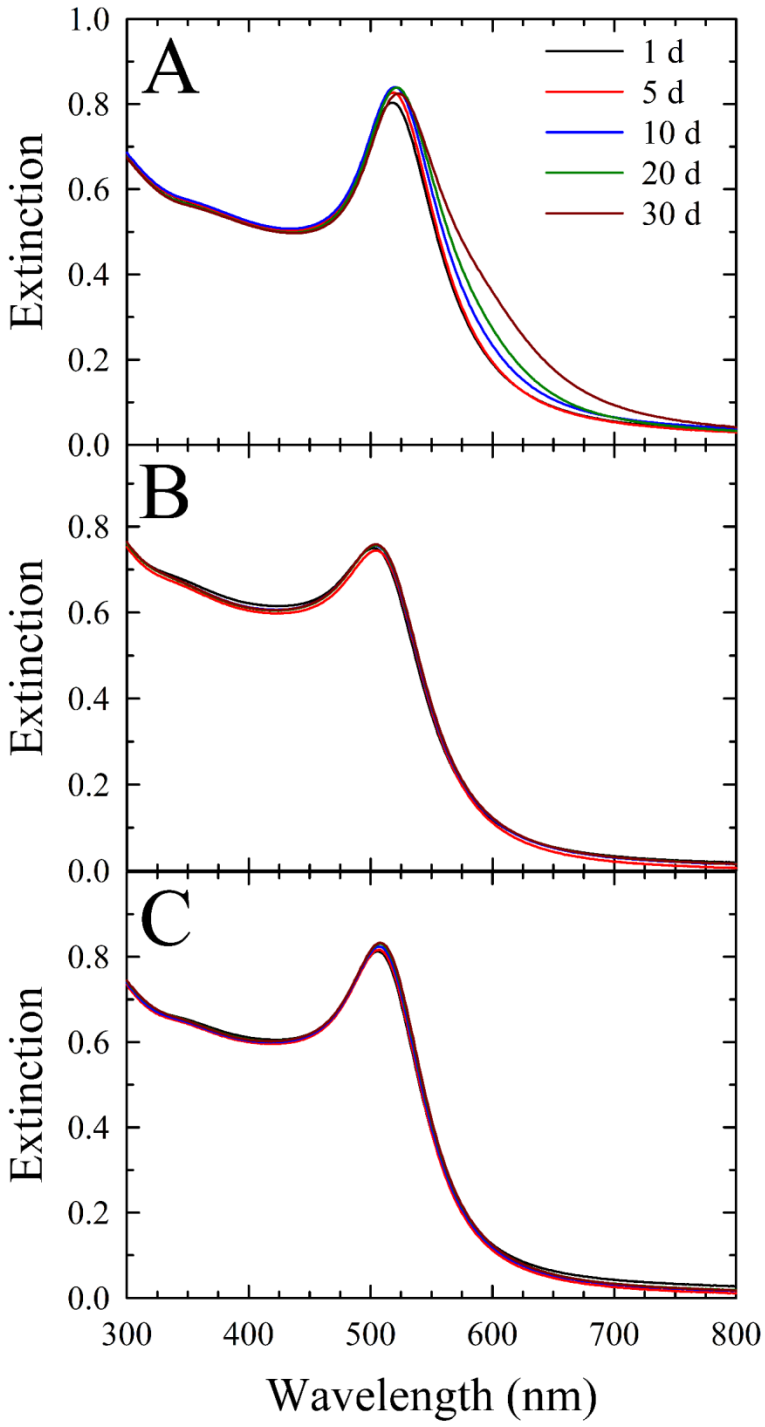

***Figure 3-4**: Stability of Au_xAg_{1-x}NPs (x = 0.8) over 30 days of storage, interrogated using UV–vis spectrophotometry. Panels A, B, and C correspond to R values of 2, 5, and 10, respectively. The legend in panel A applies to all panels.*

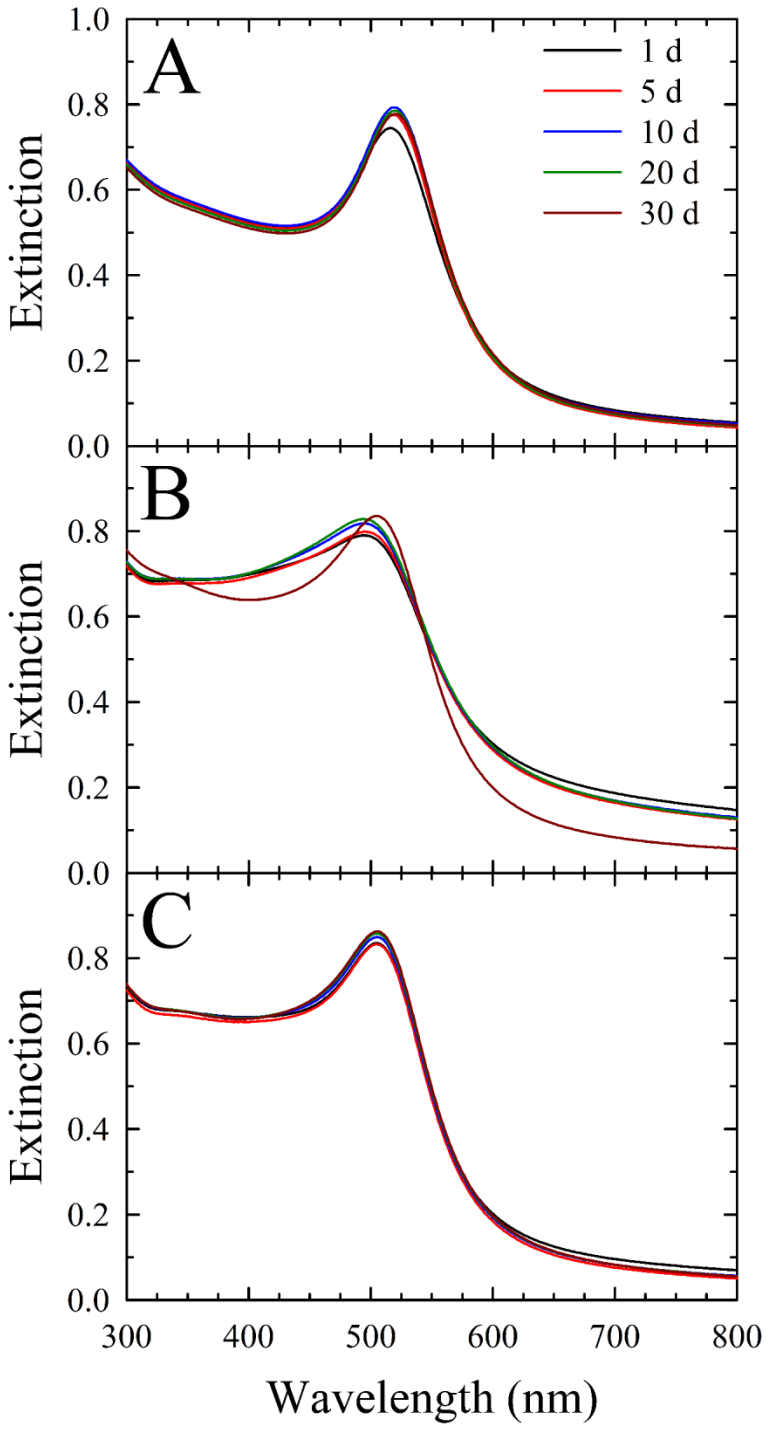

***Figure 3-5**: Stability of Au_xAg_{1-x}NPs (x = 0.7) over 30 days of storage as monitored using UV–vis spectrophotometry. Panels A, B, and C correspond to R values of 2, 5, and 10, respectively. The legend in panel A applies to all panels.*

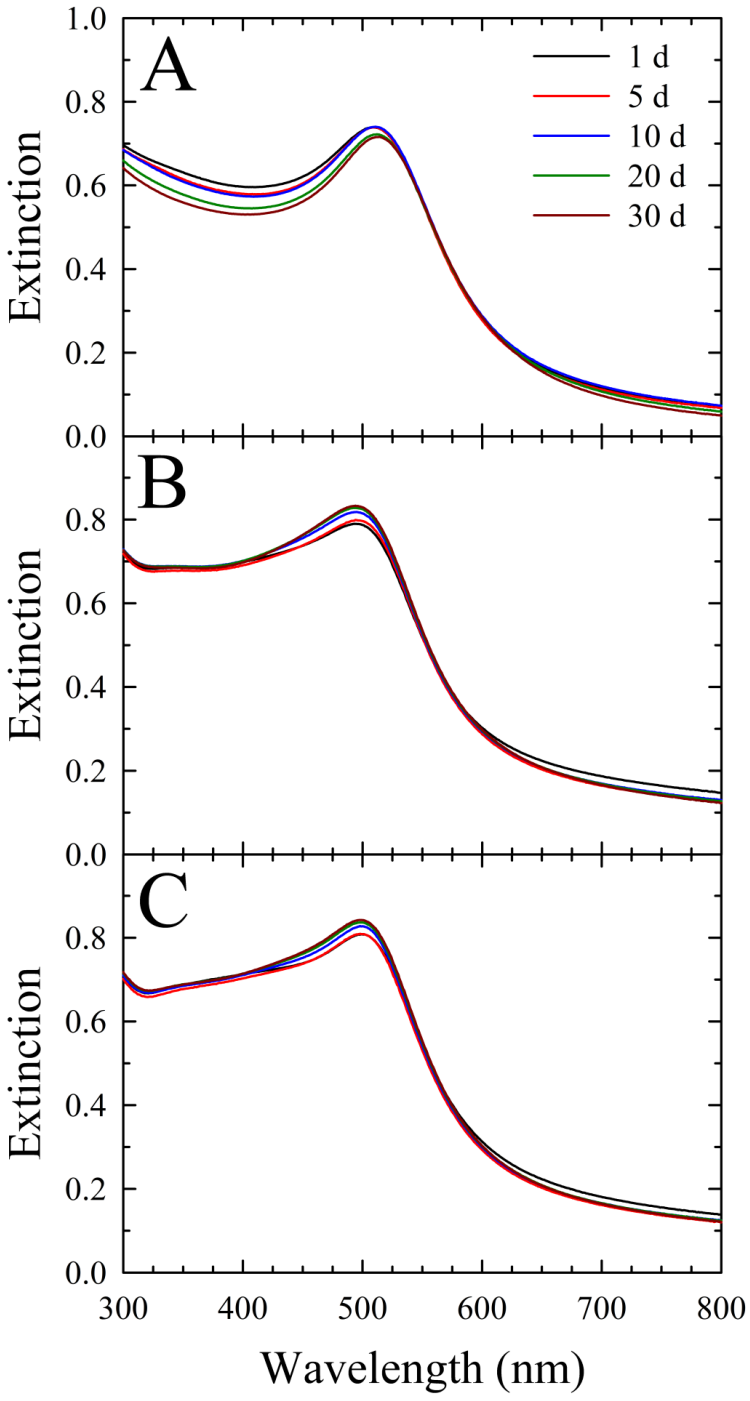

***Figure 3-6**: Stability of Au_xAg_{1-x}NPs (x = 0.6) over 30 days of storage as measured using UV–vis spectrophotometry. Panels A, B, and C correspond to R values of 2, 5, and 10, respectively. The legend in panel A applies to all panels.*

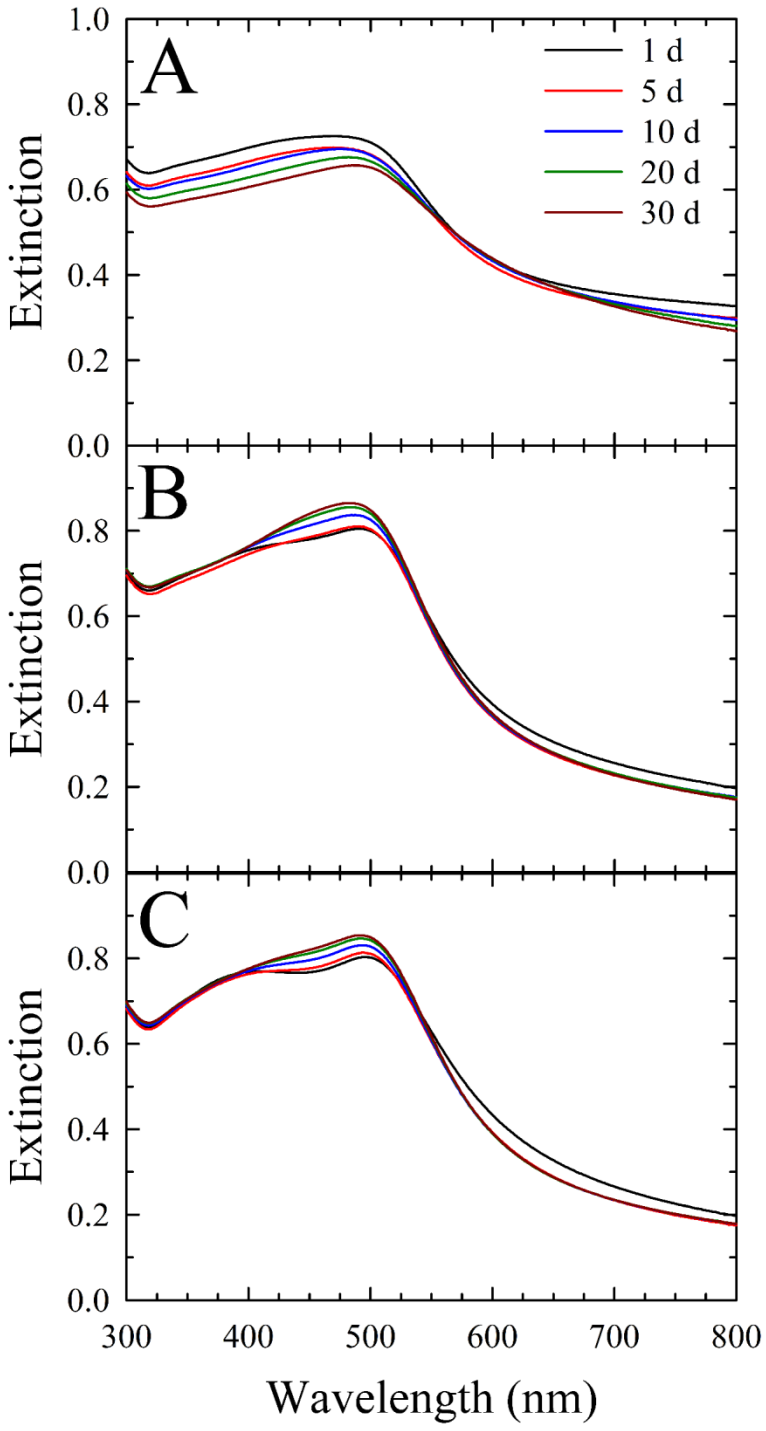

***Figure 3-7**: Stability of Au_xAg_{1-x}NPs (x = 0.5) over 30 days of storage, tracked using UV–vis spectrophotometry. Panels A, B, and C correspond to R values of 2, 5, and 10, respectively. The legend in panel A applies to all panels.*

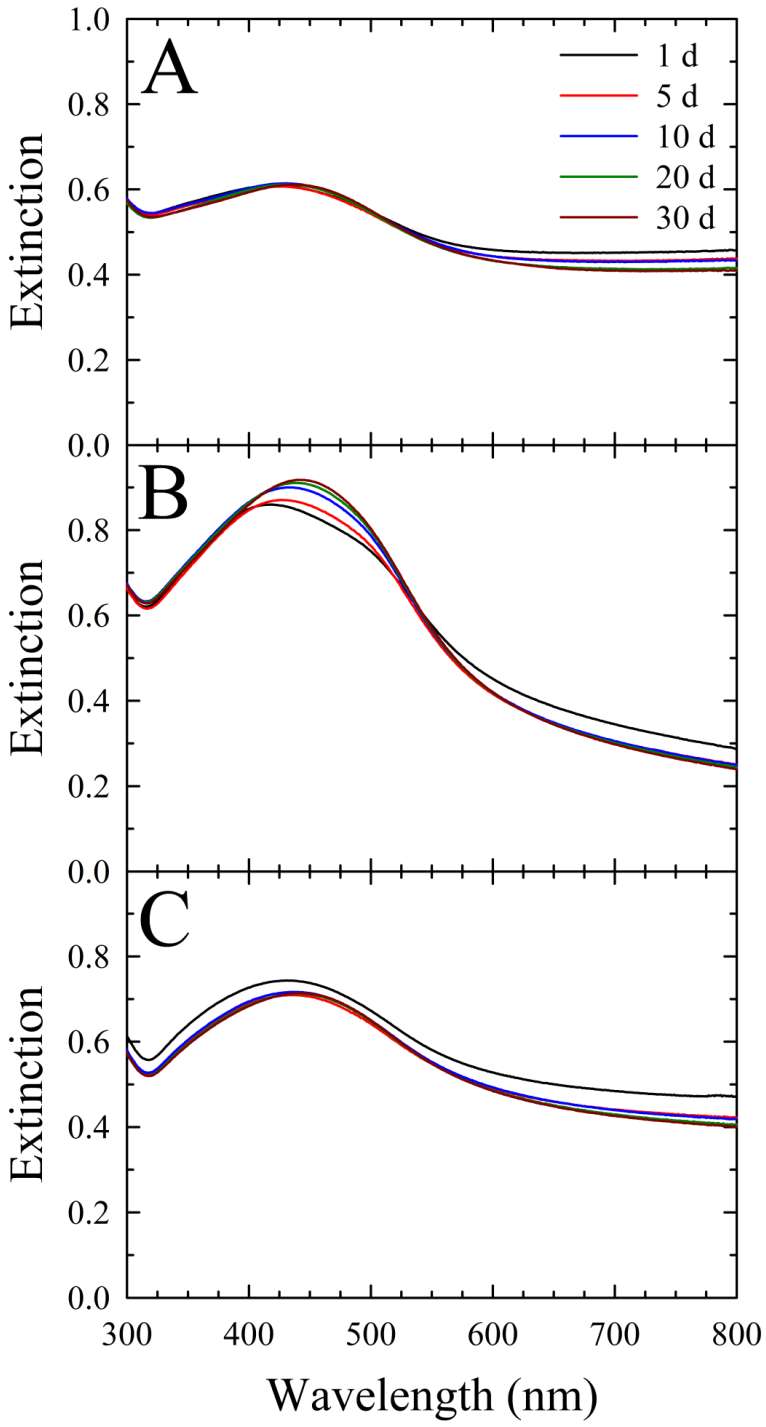

***Figure 3-8**: Stability of Au_xAg_{1-x}NPs (x = 0.4) over 30 days of storage, followed by UV–vis spectrophotometry. Panels A, B, and C correspond to R values of 2, 5, and 10, respectively. The legend in panel A applies to all panels.*

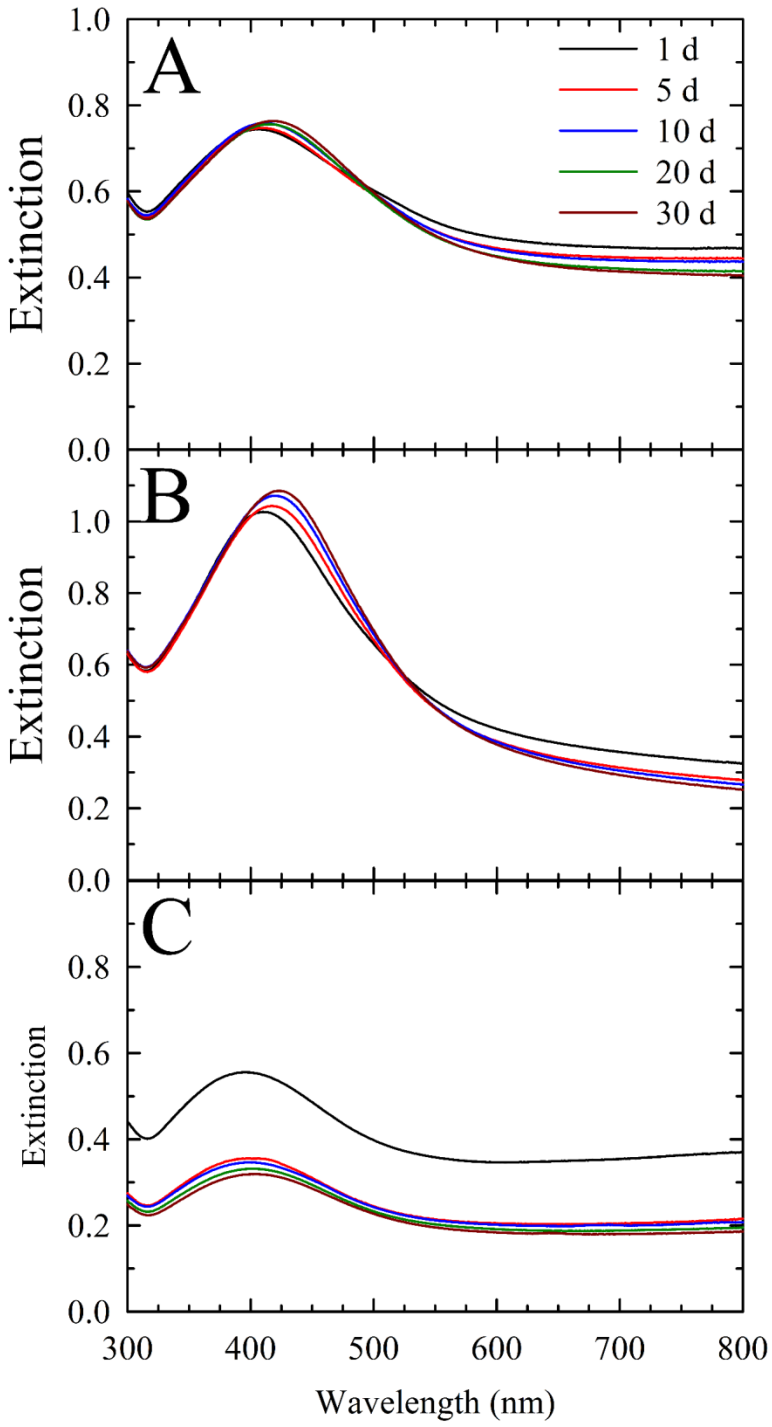

***Figure 3-9**: Stability of Au_xAg_{1-x}NPs (x = 0.3) followed over 30 days of storage using UV–vis spectrophotometry. Panels A, B, and C correspond to R values of 2, 5, and 10, respectively. The legend in panel A applies to all panels.*

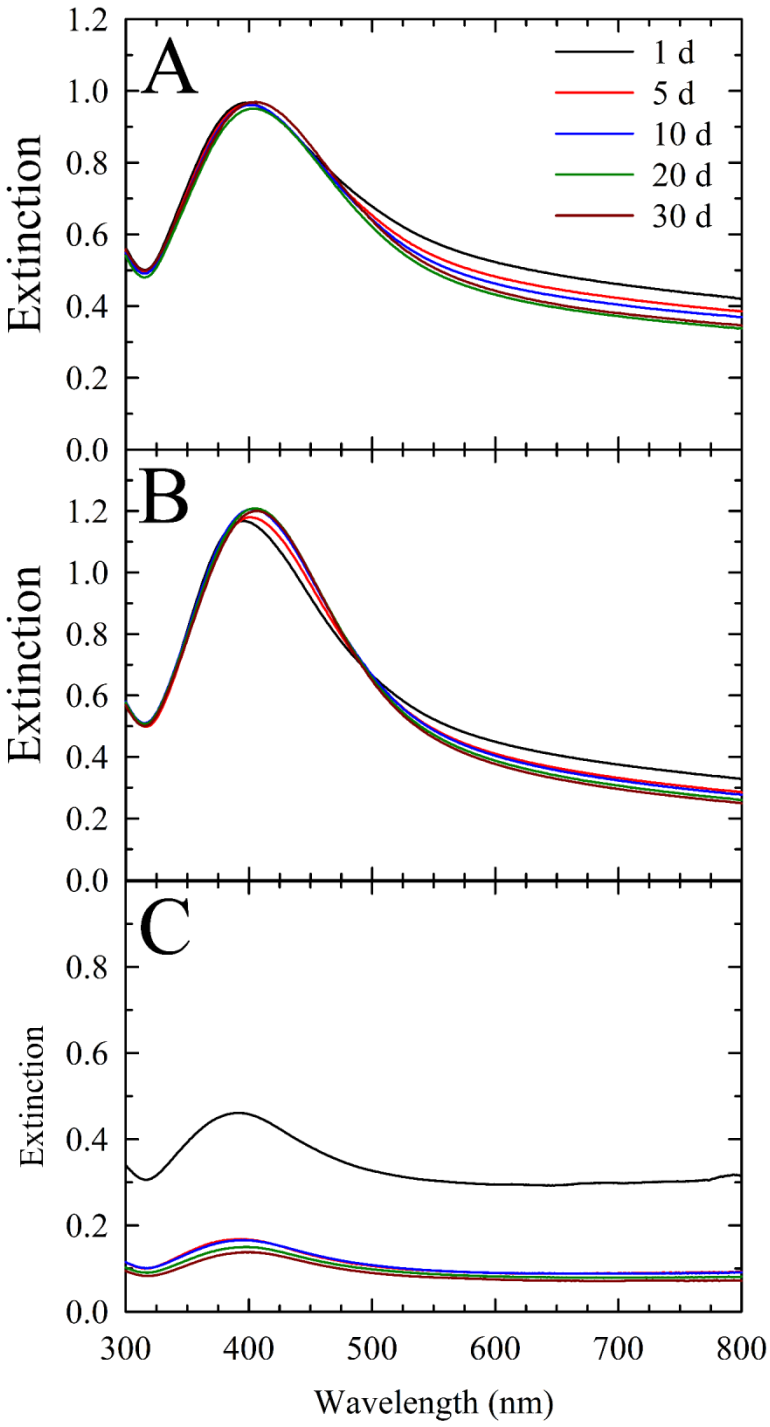

***Figure 3-10**: Stability of Au_xAg_{1-x}NPs (x = 0.2) evaluated over 30 days of storage with UV–vis spectrophotometry. Panels A, B, and C correspond to R values of 2, 5, and 10, respectively. The legend in panel A applies to all panels.*

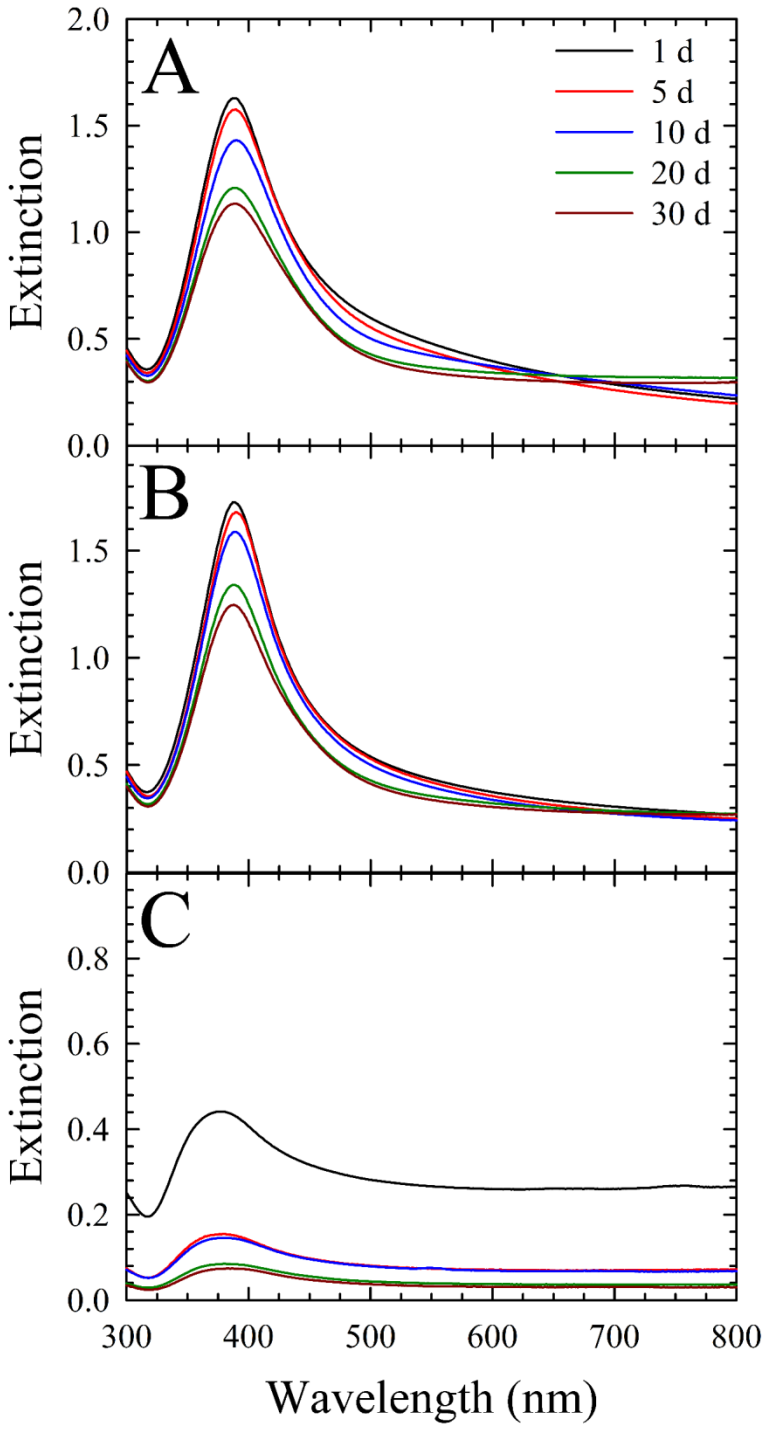

***Figure 3-11**: Stability of Au_xAg_{1-x}NPs (x = 0.1) investigated over 30 days of storage with UV–vis spectrophotometry. Panels A, B, and C correspond to R values of 2, 5, and 10, respectively. The legend in panel A applies to all panels.*

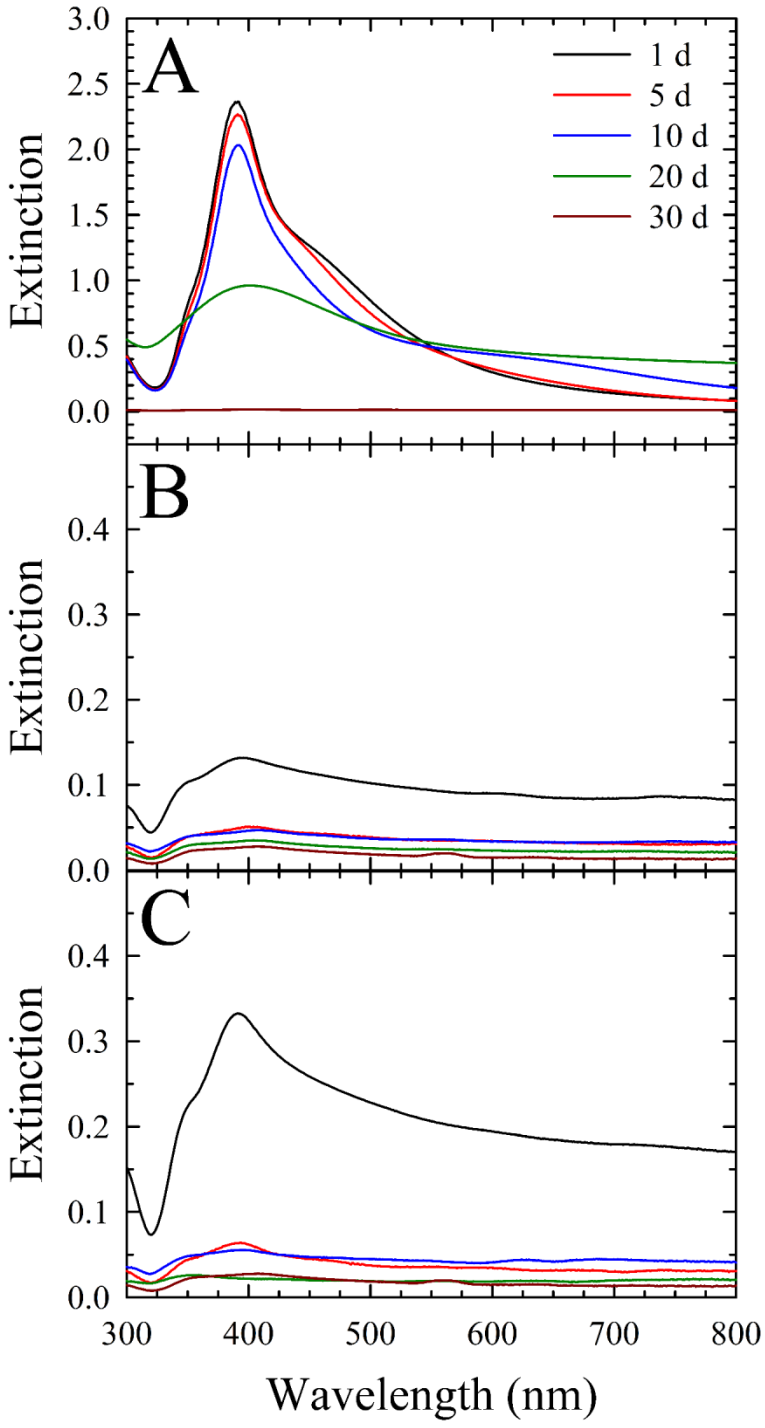

***Figure 3-12**: Stability of AgNPs (Au_xAg_{1-x}NPs for x = 0.0), monitored over 30 days of storage using UV–vis spectrophotometry. Panels A, B, and C correspond to R values of 2, 5, and 10, respectively. The legend in panel A applies to all panels.*

Aging from 20 to 30 d resulted in interesting plasmon behavior. For instance, spectra measured of AuNPs from the R = 2 sample set alluded to the aforementioned particle growth throughout the 20-d time frame, but suddenly exhibited a much narrower peak than was previously observed in any spectra of that same sample collected to that point (Figure 3-2), suggesting the formation of more monodisperse NPs. Indeed, AuNP solutions from each R value sample set demonstrated red-shifting of the LSPR. We attribute this to long-term instability of borohydride-capped NPs. Bubbles were also observed in these aged solutions, indicative of H_2 gas production from the hydrolysis of the borohydride to borohydroxides of the form $[BH_y(OH)_{4-y}]^-$.

A comparison of the UV–vis spectrum of a 1:1 v:v mixture of AuNPs and AgNPs and that of our x = 0.5 bimetallic NPs is shown in Figure 3-13. The latter sample exhibits peak broadening and a decrease in peak intensity when compared to the spectra from the monometallic samples, alluding to the formation of intermetallic structures. Further, energy-dispersive X-ray spectroscopy (EDS) spot analysis was used to interrogate the atomic composition of our bimetallic NPs from the R = 5, x = 0.5 solution. The proportions of Au and Ag were determined to be 36.7 and 63.3 atom%, respectively, as calculated from the EDS spectrum (Figure 3-14). We attribute the discrepancy between the as-prepared (50:50) and as-measured (37:63) atom ratios to low X-ray counts and the high relative error of the EDS measurement (~30%), a consequence of the small NP size. We propose that these bimetallic NPs comprise a pseudo-random composition that is primarily governed by the relative

concentrations of available metal atoms in solution, although the small NP sizes thwarted our attempts to elucidate the exact atomic composition *via* EDS mapping.

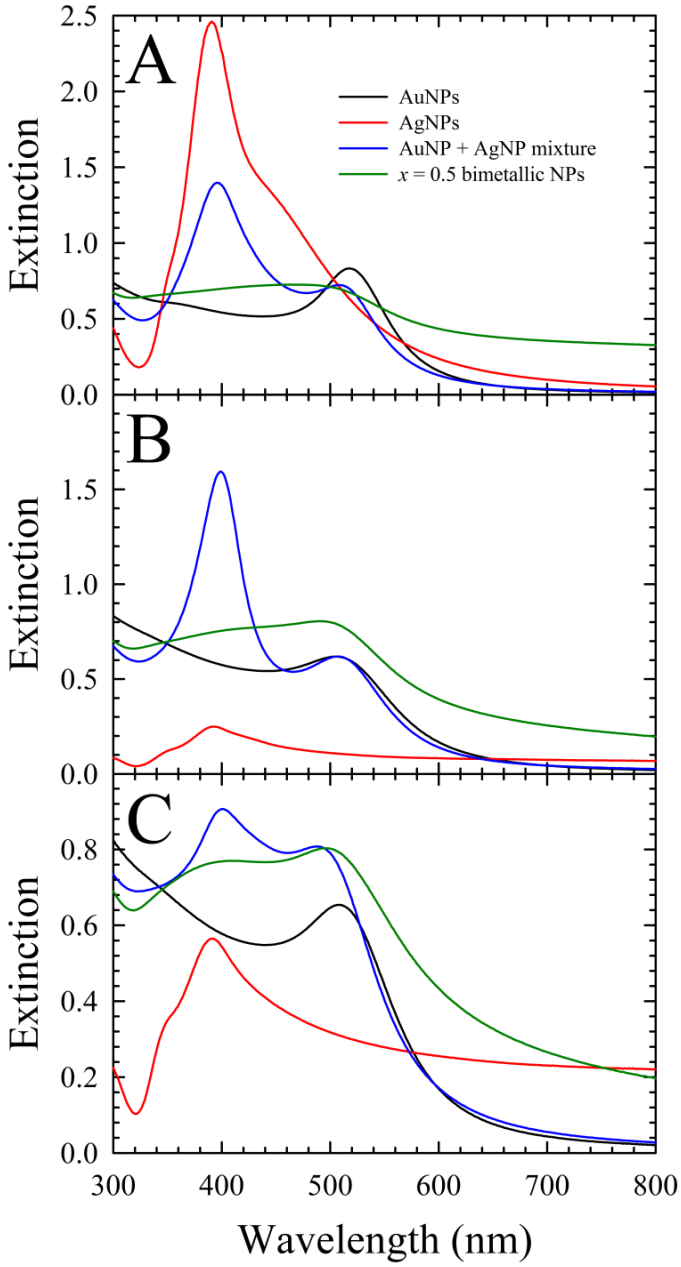

***Figure 3-13**: Comparison of AuNPs, AgNPs, a 1:1 AuNP:AgNP mixture, and bimetallic Au_xAg_{1-x}NPs (x = 0.5). Shown are A) R = 2, B) R = 5, and C) R = 10, where R equals the molar ratio of $NaBH_4$ to metal. The total metal (Au + Ag) concentration is 0.25 mM for all samples.*

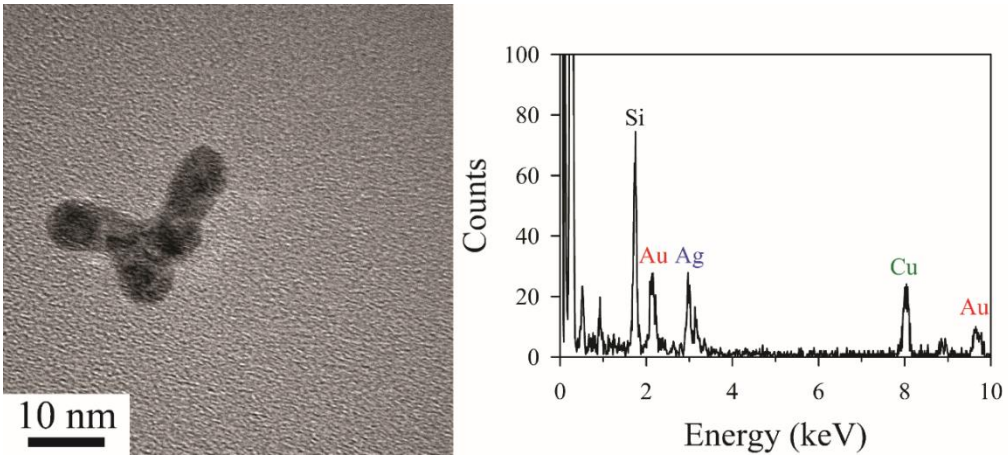

***Figure 3-14**: (Left) A high resolution TEM image showing a R = 5, x = 0.5 bimetallic Au_xAg_{1-x}NP and (right) the corresponding EDS spectrum confirming the presence of both gold and silver within the nanostructure. Copper is typically observed when using copper TEM grids, but the presence of silicon is more likely attributed to a small amount of contamination on the TEM grid, as no glassware or silicon-containing reagents were used in the preparation of these bimetallic NPs.*

Transmission electron microscopy (TEM) images were acquired for the following Au_xAg_{1-x}NPs samples after aging for 5 d: R = 2, x = 0.6, 0.3, 0.0 (Figure 3-15); R = 5, x = 1.0, 3.0 (Figure 3-16); and R = 10, x = 0.7, 0.5 (Figure 3-17). The representative images and respective histograms indicate narrow size distributions and mostly sub-10 nm particle sizes for all but the R = 2 AgNPs, an anomaly which we are tentatively attributing to the instability of borohydride-capped AgNPs, as the solutions of AgNPs when R = 5 or 10 contained black precipitate at this time point. Further, the TEM images suggest the formation of metal networks either in solution or upon drying on the grid, making NP size assessment difficult (at least 300 NP were counted, with some level of inaccuracy as the branching metal networks were ignored). Notably, these networks were also observed by Astruc *et al.*[14] The smallest observed NPs were produced by the R = 2, x = 0.3 Au_xAg_{1-x}NPs solution, with an average size of 4.6 ± 2.4 nm.

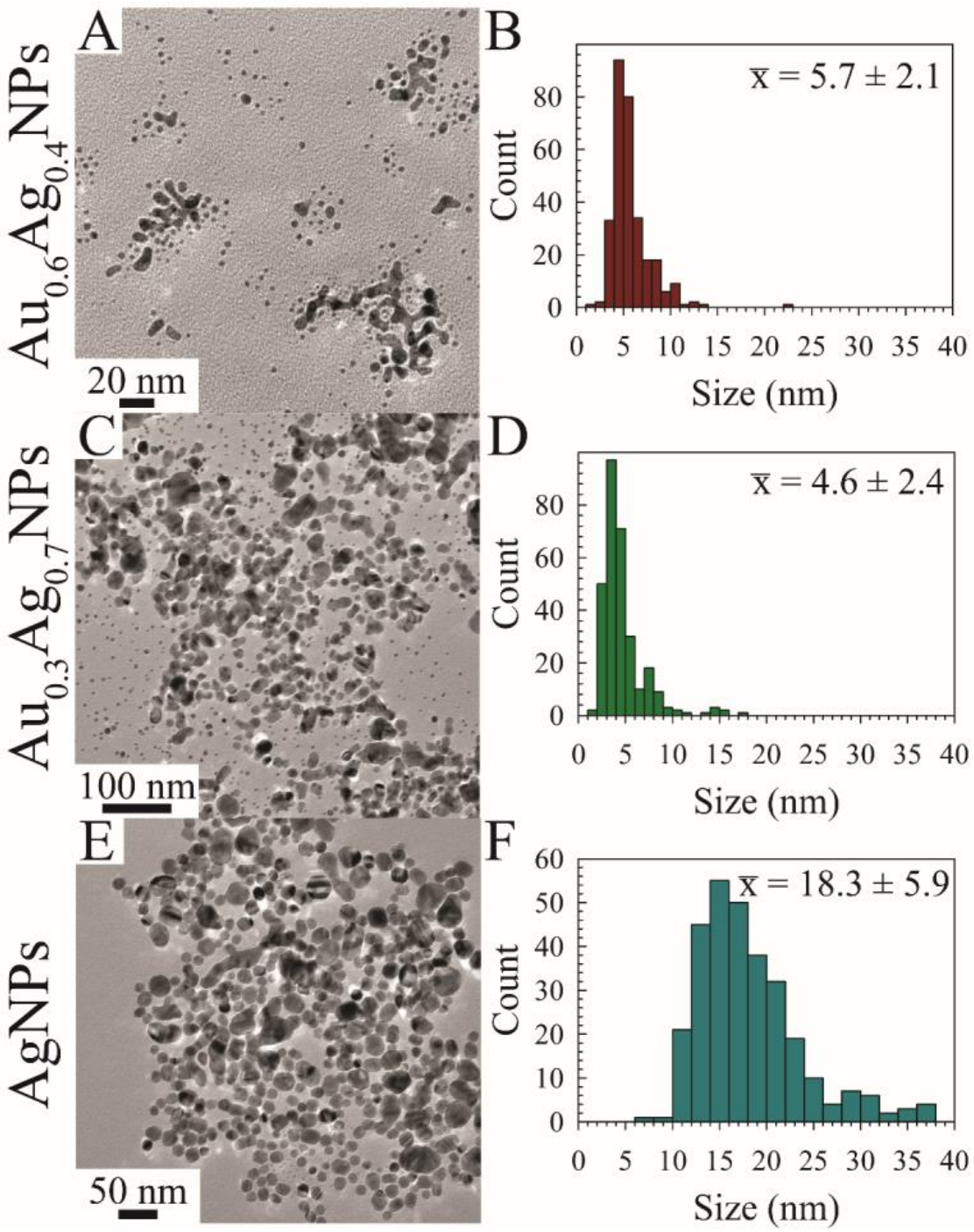

***Figure 3-15**: TEM images and related size histograms for borohydride-capped Au_xAg_{1-x}NPs for (A, B) x = 0.6; (C, D) x = 0.3; and (E, F) x = 0.0 (i.e., AgNPs). The borohydride-to-metal molar ratio (R value) is 2 for these samples.*

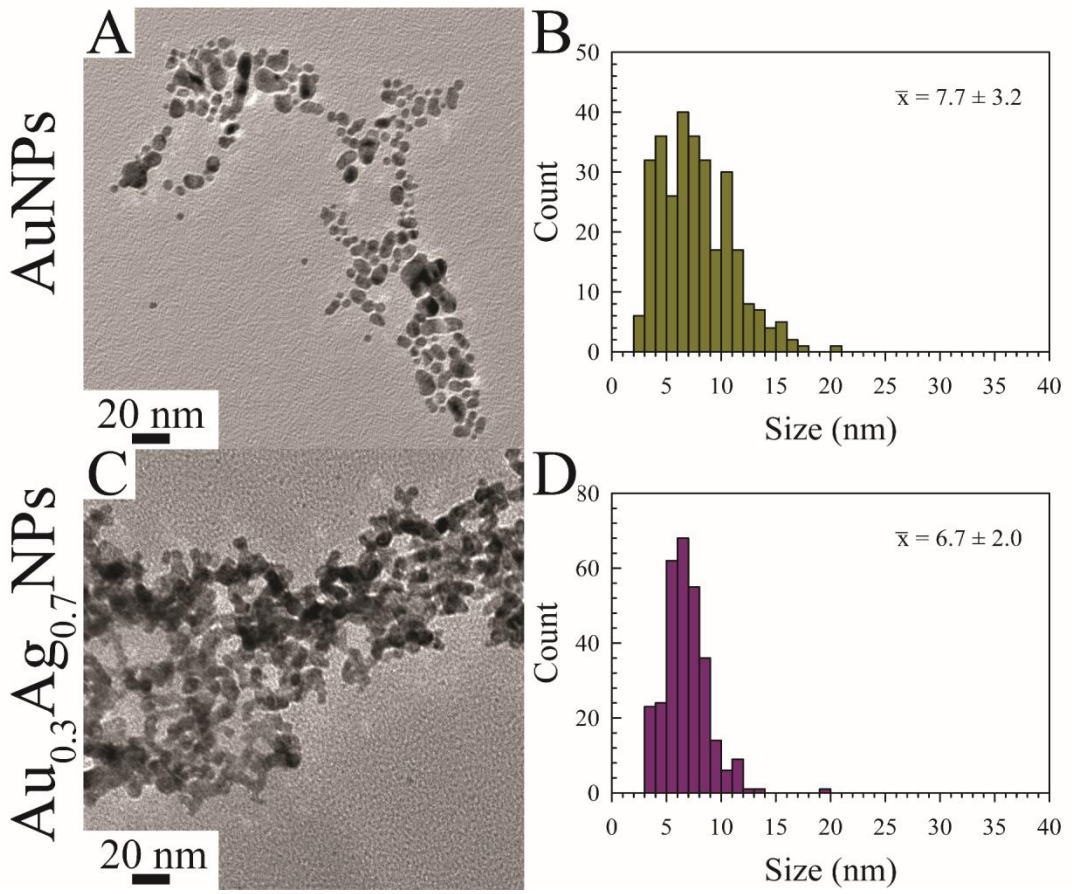

***Figure 3-16**: Representative TEM images and size distribution histograms for R = 5 Au_xAg_{1-x}NPs where (A, B) x = 1.0 and (C, D) x = 0.3. Note the apparent formation of metal networks and particle ripening (sizes of metal networks were ignored during particle size analysis).*

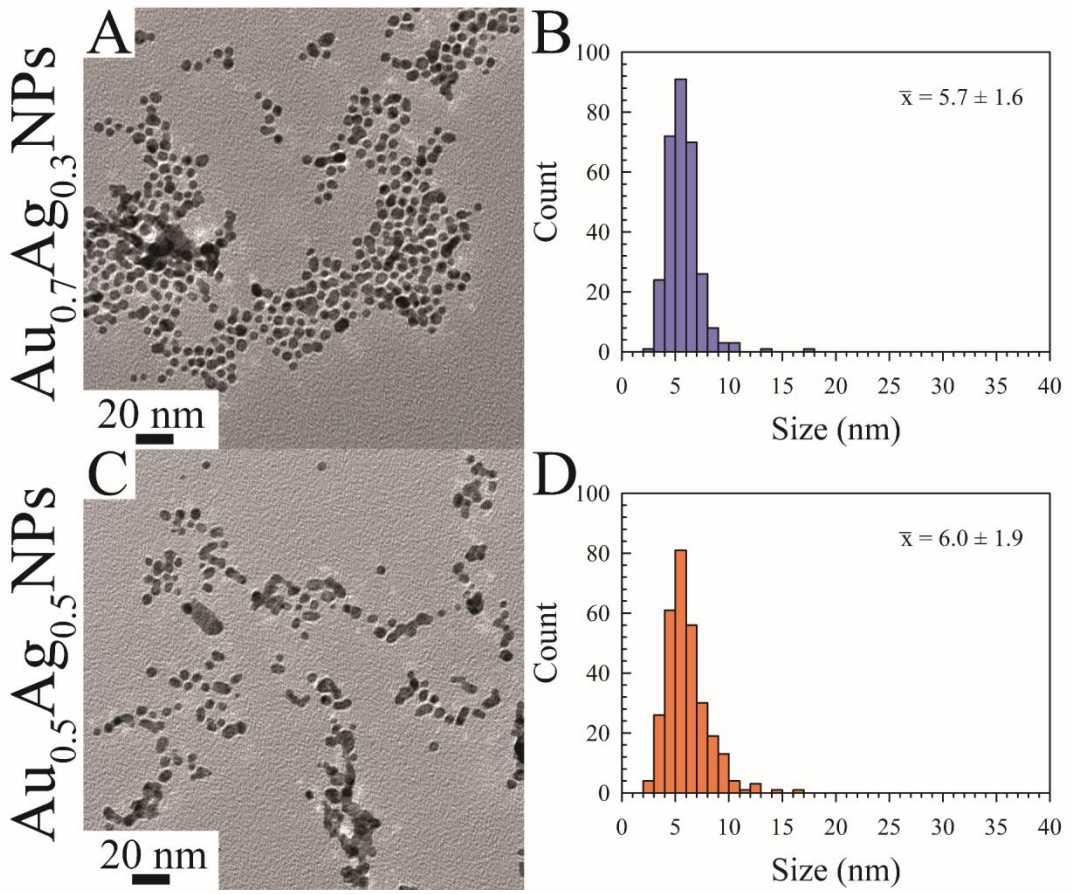

***Figure 3-17**: Representative TEM images and size distribution histograms for R = 10 Au_xAg_{1-x}NPs, for (A, B) x = 1.0 and (C, D) x = 0.3. Note the occasional large nanoparticle or aggregation of nanoparticles, particularly in panel C.*

The catalytic activity of 5 d-old Au_xAg_{1-x}NPs was measured through the model reduction of 4-nitrophenol (4-NP) to 4-aminophenol (4-AP) in the presence of sodium borohydride ($NaBH_4$), with experimental details provided in the ESI. Briefly, 2.1 mL of aqueous 0.2 mM 4-NP and 0.9 mL of aqueous 0.1 M $NaBH_4$ was added to a poly(methyl methacrylate) (PMMA) cuvette, resulting in a yellow solution of 4-nitrophenolate (λ_{max} = 400 nm). To this, 34 μL of the aqueous 0.25 mM metal catalyst solution (that is, [Au] + [Ag] = 0.25 mM) was added (catalyst loading

of 2.0 mol% metal to 4-NP, which was kept constant throughout), and the cuvette was capped, inverted to mix, and placed in the UV–vis spectrometer to begin measuring solution absorbance at 400 nm, similar to techniques used in previous publications.[23] Notably, samples containing black precipitate were not assessed for catalytic performance due to inaccuracies in calculating the remaining concentration of dispersed NPs. In the presence of excess $NaBH_4$, the reaction proceeds *via* pseudo-first-order kinetics and a linear relationship between $\ln(A_0/A_t)$ *versus* time can be established, the slope of which equals the catalytic rate (k_{app}). These plots and the resulting k_{app} values are shown in Figure 3-18. While it is common during 4-NP reduction to observe an initial induction period wherein dissolved oxygen back-reacts with 4-AP,[24] such a delay is only observed during the slower reactions when using AuNPs and AgNPs. We propose that the faster kinetics imparted by our bimetallic NPs greatly shorten this induction period, limiting it to the time required to invert our cuvette for mixing. The reactions were considered complete when the decrease in absorbance at 400 nm slowed substantially (corresponding to a $\ln(A_0/A_t)$ value of 3 and equating to 95.0% reaction completion), or after 5 min had passed. Generally, bimetallic Au_xAg_{1-x}NPs with medium-to-high silver contents (*i.e.*, $x \leq 0.7$) demonstrated higher catalytic rates within a given R value sample set.

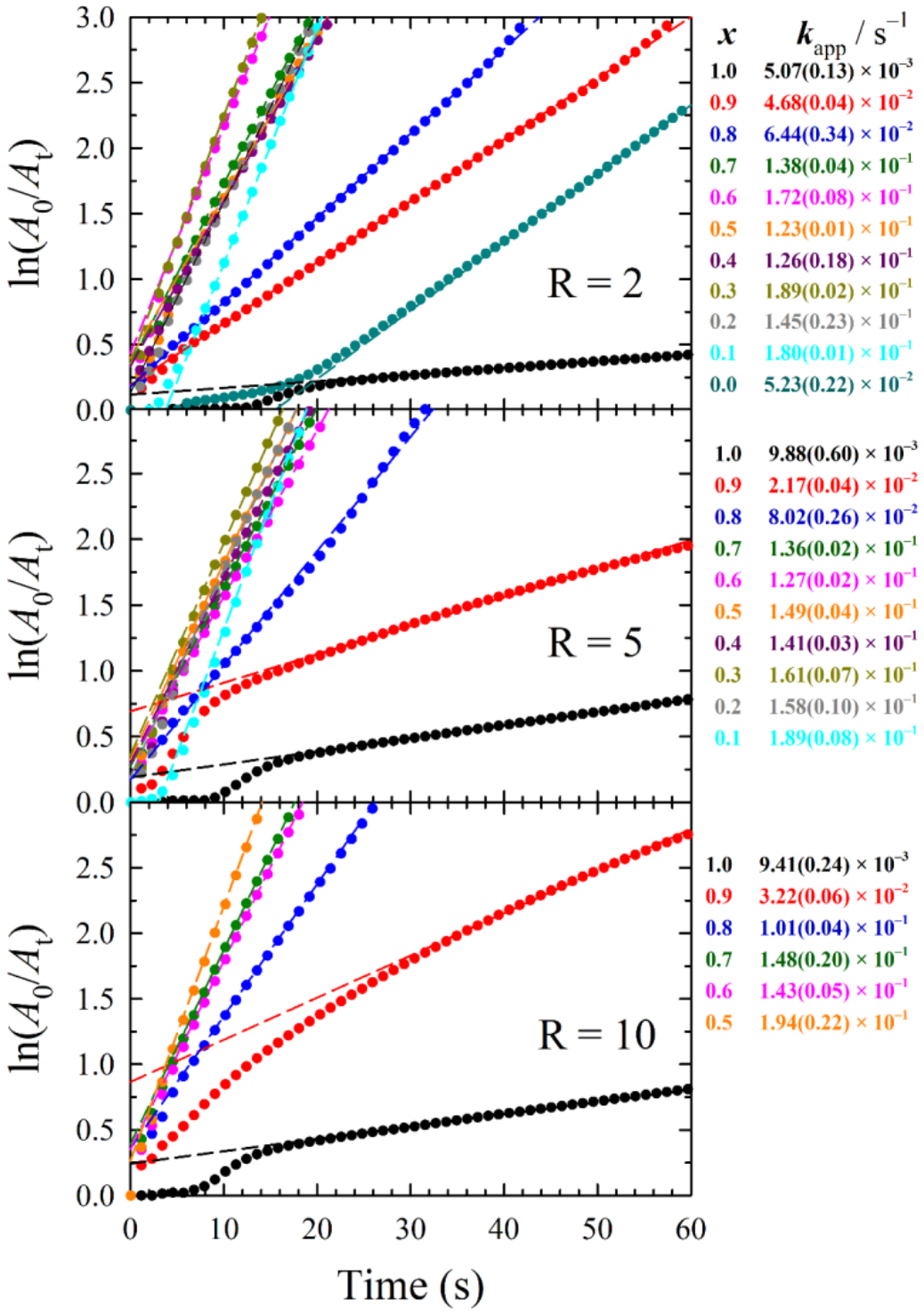

***Figure 3-18**: Plots depicting the pseudo-first-order kinetics of 4-NP reduction and associated catalytic rates (k_{app}) using 5 d-old borohydride-stabilized Au_xAg_{1-x}NP nanocatalysts (R = 2, 5, and 10, top to bottom). Excluded x values for a particular R value indicate the observation of colloidal precipitation after aging for 5 d.*

Turnover frequency (TOF) is often preferred over k_{app} when reporting comparative catalytic activity of NPs due to the former's incorporation of the molar ratio of catalyst to substrate. More specifically, this value is calculated by dividing the moles of substrate ($n_{4\text{–NP}}$) by the product of moles of catalyst (n_m) and the reaction time (t_{rxn}) in hours, then correcting for reaction completion, as per eqn. (1).

$$\mathbf{TOF} = \frac{\boldsymbol{n}_{\mathbf{4\text{-NP}}}}{(\boldsymbol{n}_{\mathbf{m}})(\boldsymbol{t}_{\mathbf{rxn}})} \times \frac{\mathbf{completion\ \%}}{\mathbf{100}} \quad (1)$$

Herein, we used 2.0 mol% metal to 4-NP and define the reaction time as the time to attain $\ln(A_0/A_t) = 3$ (95% reaction completion). This reaction completion % has the benefit of incorporating most of the reaction progress while simultaneously negating instrument sensitivity concerns arising when the [4-nitrophenolate] becomes very small. Under these parameters, the $x = 0.3$ Au_xAg_{1-x}NPs from the R = 2 sample set demonstrated the highest catalytic activity, with a calculated TOF of 12,160 h^{-1} (Figure 3-19, Table 3-4). Notably, several of our bimetallic NPs at each R value outperformed the previously-reported best-in-class AuNP catalyst (TOF = 9,000 h^{-1}),[14] despite our use of more stringent reaction completion conditions (the reference reported a completion time corresponding to a $\ln(A_0/A_t) = 2$, or 86% completion, and did not correct for this in their calculation of TOF). To our knowledge, these Au_xAg_{1-x}NPs possess the highest catalytic activity for this system yet reported in literature. The proposed reason for such a pronounced increase in TOF when using bimetallic NPs is two-fold: first, a size regulating effect is evident for solutions of mixed metals, resulting in populations of smaller NPs and a potential

increase in the number of surface atoms available for catalysis. Second, the presence of guest metals within an ordered crystalline structure results in disharmonious, defect-laden surfaces, increasing the number of active sites for catalytic activity and surface rearrangement of stabilizing ligands. Further study is required to fully appreciate and quantify the amount of catalytic enhancement imparted, in general, when incorporating bimetallic systems.

Table 3-4: *Turnover frequency (TOF/h^{-1}) of Au_xAg_{1-x}NPs.*

x	R = 2	R = 5	R = 10
1.0	605 ± 10	620 ± 40	590 ± 10
0.9	2,926 ± 50	1,310 ± 50	2,460 ± 70
0.8	4,010 ± 200	5,400 ± 330	6,500 ± 230
0.7	8,830 ± 480	8,600 ± 170	9,690 ± 1240
0.6	11,500 ± 740	7,980 ± 40	9,160 ± 660
0.5	8,180 ± 50	9,500 ± 240	12,070 ± 1,370
0.4	7,930 ± 1,190	8,840 ± 60	[a]
0.3	12,160 ± 230	10,450 ± 390	[a]
0.2	8,590 ± 1,100	9,600 ± 830	[a]
0.1	8,280 ± 210	9,000 ± 410	[a]
0.0	2,370 ± 70	[a]	[a]

[a] Catalytic activity was not assessed for these samples due to the presence of black precipitate, evidence of NP aggregation.

A recyclability assessment was performed using the R = 2, x = 0.3 sample (Table 3-5 and Figure 3-20). The initial catalytic cycle was performed as specified above, and, once the reaction was complete, the cuvette was spiked with 84 μL of 5.0 mM 4-NP and 90 μL of 0.1 M $NaBH_4$ to restart the reaction. This recycling procedure was performed five sequential times using the same cuvette and catalysis solution. Unfortunately, we find that the TOF experiences an exponential decay in each sequential cycle, dropping from an initial value of 12,260 h^{-1} to 1,570 h^{-1} after six cycles. This is, however, not surprising as the high surface energy of nanoscale

colloids invariably results in instability, aggregation, and eventual loss of catalytic activity. Indeed, in practice nanocatalysts are typically protected against colloidal aggregation and oxidation by coating with a suitable polymer (*e.g.*, poly(*N*-vinyl-2-pyrrolidone) PVP), deposition on a solid inorganic support, or encapsulation within a porous scaffold to yield superior stability, durability, and recoverability relative to the free nanocatalyst.[25-27] Nonetheless, the final TOF observed after six catalytic cycles for our *unsupported* catalysts remains high compared to typical nitroarene reduction nanocatalysts reported in the literature.[14]

Table 3-5: *Apparent catalytic rate (k_{app}/s^{-1}) and turnover frequency (TOF/h^{-1}) for the recyclability study performed using the R = 2, x = 0.3 bimetallic Au_xAg_{1-x}NPs.*

Cycle	k_{app} (s^{-1})	TOF (h^{-1})
1	1.87×10^{-1}	12,260
2 (1st recycle)	9.77×10^{-2}	6,030
3 (2nd recycle)	7.22×10^{-2}	4,490
4 (3rd recycle)	4.17×10^{-2}	2,880
5 (4th recycle)	3.30×10^{-2}	2,120
6 (5th recycle)	2.68×10^{-2}	1,570

As a metric to compare the price and activity of our bimetallic NPs, we prepared a plot of TOF per USD (h^{-1} $\$^{-1}$) *versus* the *x* value for Au_xAg_{1-x}NPs (Figure 3-19B). Our aim is to show that not only are these bimetallic NPs the best catalysts for this system yet reported, but they are much more cost effective than the monometallic AuNPs typically utilized. Indeed, higher Ag concentrations (lower *x* values) possessed higher activity per $, with a special note of the very high activity and lowered cost of the $x = 0.1$ Au_xAg_{1-x}NPs.

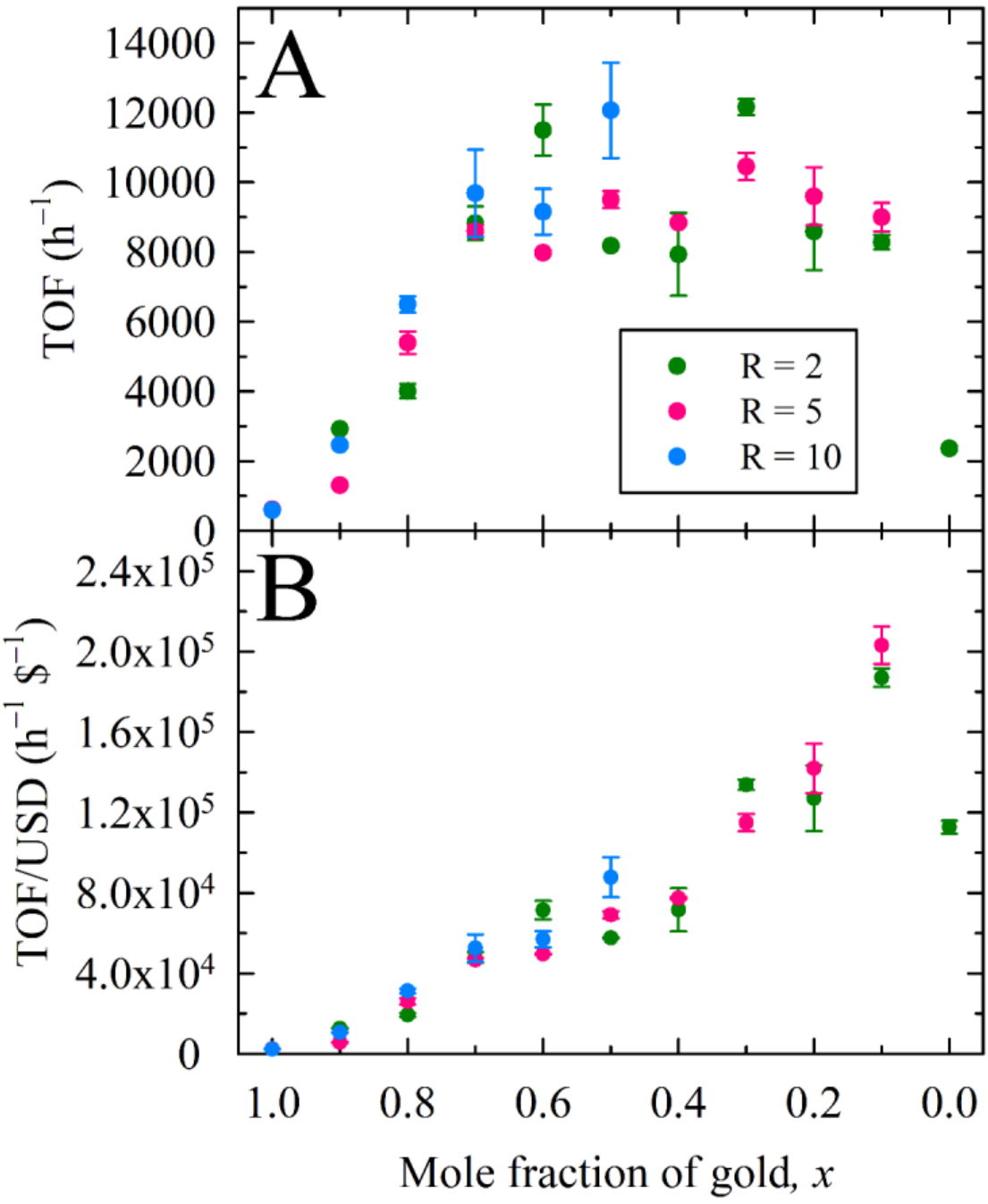

***Figure 3-19**: (A) Turnover frequency (TOF) and (B) TOF per U.S. dollar (USD), expressed as functions of the overall nanoparticle composition, for borohydride-stabilized Au_xAg_{1-x}NPs applied as nanocatalysts for 4-NP reduction. Panel (B) illustrates the economic viability of replacing Au with Ag in this catalytic system by way of a monotonic increase in the TOF per USD. Economic performance is based on current representative vendor prices for the metal precursors used, as mentioned in the Supplementary Information for this Chapter.*

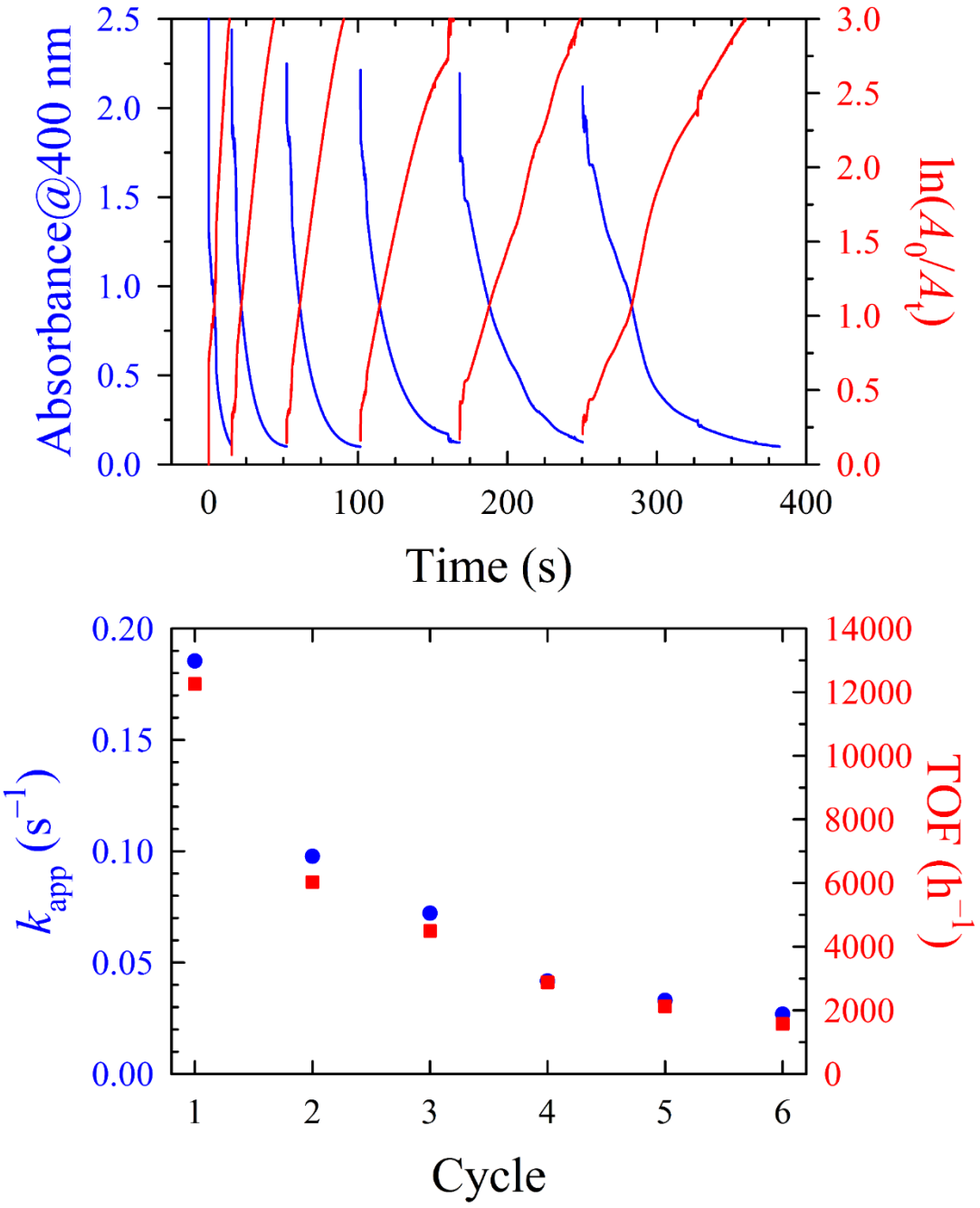

***Figure 3-20**: Assessment of the recyclability of the R = 2, x = 0.3 bimetallic Au_xAg_{1-x}NPs. Top) Absorbance spectra (blue, left axis) and rate plots (red, right axis) for each cycle versus time, with considerable slowing of the reaction rate observed in later cycles. The duration of time between cycles when the cuvette was mixed outside of the instrument has been removed for clarity. Bottom) The k_{app} (blue, left axis) and TOF (red, right axis) values for each cycle, showing exponential decay in activity with sequential cycles.*

In summary, we report a method for synthesizing bimetallic Au_xAg_{1-x}NPs capped with $NaBH_4$ which possess higher catalytic activity for the reduction of 4-NP to 4-AP than their corresponding monometallic counterparts when utilizing the same total moles of metal. With TOF values up to 12,160 h^{-1}, these nanoparticles have, to our knowledge, exhibited the fastest rates recorded in literature for the NP-catalyzed reduction of 4-NP to 4-AP. Further, this research sheds light on the use of Ag as a substitute for Au in catalytic systems to alleviate financial limitations of traditional monometallic catalysts.

Chapter 3 Supplementary Information

Materials. Ultrapure Millipore water purified to a resistivity of 18.2 MΩ cm was used throughout. Tetrachloroauric acid trihydrate ($HAuCl_4 \cdot 3\ H_2O$, ≥99.9%, 520918), silver nitrate ($AgNO_3$, 99.9999%, 204390), sodium borohydride ($NaBH_4$, 99.99%, 480886), and 4-nitrophenol (4-NP, ≥99%, 241326) were all acquired from Millipore Sigma (St. Louis, MO) and used as received.

Characterization. UV–vis spectroscopy was performed using a Cary 50 Bio UV–vis spectrometer with disposable, 1-cm path length poly(methyl methacrylate) (PMMA) cuvettes. Transmission electron microscopy (TEM) images of 5-day-old NPs deposited on carbon-coated copper grids (Ted Pella, Inc.; 01814-F, support films, carbon type-B, 400 mesh) were obtained using an FEI Technai (F20) microscope operating at 200 keV. At least 300 particles were analyzed using ImageJ software to generate NP size histograms.

Nanocatalyst Synthesis. 18.0 mL of ultrapure H_2O was added to each of thirty-three 50-mL polypropylene centrifuge tubes. The appropriate volume of 5.0 mM $HAuCl_4 \cdot 3H_2O$ was added to each tube according to the experimental parameters given in Tables 3-1–3-3. 10.0, 25.0, and 50.0 mM $NaBH_4$ solutions were prepared immediately before use. Two 1000-μL autopipettors were used to rapidly and simultaneously inject the appropriate amounts of 5.0 mM $AgNO_3$ and $NaBH_4$ stock to the $HAuCl_4$ solution under vortex mixing, achieving a BH_4^- to metal molar ratio of 2.0, 5.0, or 10.0 based on the sample set in Tables 3-1–3-3. The resulting solutions, which immediately turned a shade of red to yellow depending on the metal ratio, were vortexed for an additional 20 s to mix. UV–vis absorption spectroscopy was used to follow the colloidal stability of the nanoparticles during aging

for 1, 5, 10, 20, and 30 d. All solutions were kept at room temperature and stored protected from light during aging.

Nitroarene Reduction. The catalytic activity for 4-nitrophenol (4-NP) reduction to 4-aminophenol (4-AP) using $NaBH_4$ was assessed for each sample that did not visibly show black aggregates after aging for 5 d. First, 2.1 mL of 0.20 mM 4-NP and 0.9 mL of fresh 0.1 M $NaBH_4$ were combined in a clean 4-mL PMMA cuvette and placed in the UV–vis spectrometer set to scan at 400 nm. To initiate a catalytic run, 0.034 mL of a given nanoparticle solution (0.25 mM metal) was added, followed by rapid capping and inversion of the cuvette to mix before placing it in the spectrometer. The reaction was assumed to have completed when the absorbance at 400 nm was at 5% of the starting value. For a large excess of borohydride ($NaBH_4$:4-NP ratio of 214 was used throughout), the pseudo-first-order kinetics yield a linear plot of $\ln(A_0/A_t)$ *versus* time, where A_0 and A_t are the initial and time-dependent absorbance, respectively, with the slope equaling the apparent rate (k_{app}). All kinetic studies were performed in triplicate.

Evaluation of Economics. At the time of this writing, 1 g of $AgNO_3$ costs $24.70 (99.9999% trace metals basis, 204390) whereas 1 g of $HAuCl_4 \cdot 3H_2O$ runs $127.00 (99.9% trace metals basis, 520918) from Millipore Sigma. Notably, the TOF/USD ratio increased over 85-fold between $x = 1.0$ and $x = 0.1$ for Au_xAg_{1-x} NPs made for R = 5. Error bars were derived from the uncertainty in the TOF and do not account for price variability.

References

1. Zhao, S.; Das, A.; Zhang, H.; Jin, R.; Song, Y.; Jin, R., Mechanistic Insights from Atomically Precise Gold Nanocluster-Catalyzed Reduction of 4-Nitrophenol. *Pro. Nat. Sci.-Mater.* **2016,** *26* (5), 483-486.

2. Li, G.; Jin, R., Atomically Precise Gold Nanoclusters as New Model Catalysts. *Acc. Chem. Res.* **2013,** *46* (8), 1749-1758.

3. Ciganda, R.; Li, N.; Deraedt, C.; Gatard, S.; Zhao, P.; Salmon, L.; Hernández, R.; Ruiz, J.; Astruc, D., Gold Nanoparticles as Electron Reservoir Redox Catalysts for 4-Nitrophenol Reduction: A Strong Stereoelectronic Ligand Influence. *Chem. Commun.* **2014,** *50* (70), 10126-10129.

4. Seo, Y. S.; Ahn, E.-Y.; Park, J.; Kim, T. Y.; Hong, J. E.; Kim, K.; Park, Y.; Park, Y., Catalytic Reduction of 4-Nitrophenol with Gold Nanoparticles Synthesized by Caffeic Acid. *Nanoscale Res. Lett.* **2017,** *12* (1), 7-7.

5. Aditya, T.; Pal, A.; Pal, T., Nitroarene Reduction: A Trusted Model Reaction to Test Nanoparticle Catalysts. *Chem. Commun.* **2015,** *51* (46), 9410-9431.

6. Biradar, A. V.; Asefa, T., Nanosized Gold-Catalyzed Selective Oxidation of Alkyl-Substituted Benzenes and N-Alkanes. *Appl. Catal. A: Gen.* **2012,** *435-436*, 19-26.

7. Hashmi, A. S. K.; Hutchings, G. J., Gold Catalysis. *Angew. Chem. Int. Ed.* **2006,** *45* (47), 7896-7936.

8. Guan, B.; Xing, D.; Cai, G.; Wan, X.; Yu, N.; Fang, Z.; Yang, L.; Shi, Z., Highly Selective Aerobic Oxidation of Alcohol Catalyzed by a Gold(I) Complex with an Anionic Ligand. *J. Am. Chem. Soc.* **2005,** *127* (51), 18004-18005.

9. Lin, H.; Xia-Bing, L.; Ji, N.; Yong-Mei, L.; Yong, C.; He-Yong, H.; Kang-Nian, F., Efficient and Clean Gold-Catalyzed One-Pot Selective N-Alkylation of Amines with Alcohols. *Chem.–Eur. J.* **2010,** *16* (47), 13965-13969.

10. Saidi, O.; Blacker, A. J.; Lamb, G. W.; Marsden, S. P.; Taylor, J. E.; Williams, J. M. J., Borrowing Hydrogen in Water and Ionic Liquids: Iridium-Catalyzed Alkylation of Amines with Alcohols. *Org. Process Res. Dev.* **2010,** *14* (4), 1046-1049.

11. Shimizu, K.; Nishimura, M.; Satsuma, A., Γ-Alumina-Supported Silver Cluster for N-Benzylation of Anilines with Alcohols. *ChemCatChem* **2009,** *1* (4), 497-503.

12. Gamler, J. T. L.; Ashberry, H. M.; Skrabalak, S. E.; Koczkur, K. M., Random Alloyed Versus Intermetallic Nanoparticles: A Comparison of Electrocatalytic Performance. *Adv. Mater.* **2018,** *30* (40), 1801563.

13. Campisi, S.; Schiavoni, M.; Chan-Thaw, C.; Villa, A., Untangling the Role of the Capping Agent in Nanocatalysis: Recent Advances and Perspectives. *Catalysts* **2016,** *6* (12), 185.

14. Deraedt, C.; Salmon, L.; Gatard, S.; Ciganda, R.; Hernandez, R.; Ruiz, J.; Astruc, D., Sodium Borohydride Stabilizes Very Active Gold Nanoparticle Catalysts. *Chem. Commun.* **2014,** *50* (91), 14194-14196.

15. Dasog, M.; Hou, W.; Scott, R. W. J., Controlled Growth and Catalytic Activity of Gold Monolayer Protected Clusters in Presence of Borohydride Salts. *Chem. Commun.* **2011,** *47* (30), 8569-8571.

16. Ferrando, R.; Jellinek, J.; Johnston, R. L., Nanoalloys: From Theory to Applications of Alloy Clusters and Nanoparticles. *Chem. Rev.* **2008,** *108* (3), 845-910.

17. Ravula, S.; Essner, J. B.; La, W. A.; Polo-Parada, L.; Kargupta, R.; Hull, G. J.; Sengupta, S.; Baker, G. A., Sunlight-Assisted Route to Antimicrobial Plasmonic Aminoclay Catalysts. *Nanoscale* **2015,** *7* (1), 86-91.

18. Harak, E. W.; Koczkur, K. M.; Harak, D. W.; Patton, P.; Skrabalak, S. E., Designing Efficient Catalysts through Bimetallic Architecture: Rh@Pt Nanocubes as a Case Study. *ChemNanoMat* **2017,** *3* (11), 815-821.

19. Skrabalak, S. E.; Chen, J.; Neretina, S.; Qin, D., Beyond the Gold Standard: Bimetallic Nanomaterials Bring New Properties and Functions. *Part. Part. Syst. Char.* **2018,** *35* (5), 1800111.

20. Essner, J. B.; Laber, C. H.; Baker, G. A., Carbon Dot Reduced Bimetallic Nanoparticles: Size and Surface Plasmon Resonance Tunability for Enhanced Catalytic Applications. *J. Mater. Chem. A* **2015,** *3* (31), 16354-16360.

21. Wang, X.; Chen, S.; Reggiano, G.; Thota, S.; Wang, Y.; Kerns, P.; Suib, S. L.; Zhao, J., Au–Cu–M (M = Pt, Pd, Ag) Nanorods with Enhanced Catalytic Efficiency by Galvanic Replacement Reaction. *Chem. Commun.* **2019,** *55* (9), 1249-1252.

22. Larm, N. E.; Madugula, D.; Lee, M. W.; Baker, G. A., Polyhedral Borane-Capped Coinage Metal Nanoparticles as High-Performing Catalysts for 4-Nitrophenol Reduction. *Chem. Commun.* **2019,** ***55***, 7990-7993.

23. Larm, N. E.; Essner, J. B.; Pokpas, K.; Canon, J. A.; Jahed, N.; Iwuoha, E. I.; Baker, G. A., Room-Temperature Turkevich Method: Formation of Gold Nanoparticles at the Speed of Mixing Using Cyclic Oxocarbon Reducing Agents. *J. Phys. Chem. C* **2018,** *122* (9), 5105-5118.

24. Menumerov, E.; Hughes, R. A.; Neretina, S., Catalytic Reduction of 4-Nitrophenol: A Quantitative Assessment of the Role of Dissolved Oxygen in Determining the Induction Time. *Nano Lett.* **2016,** *16* (12), 7791-7797.

25. Zhang, K.; Suh, J. M.; Choi, J.-W.; Jang, H. W.; Shokouhimehr, M.; Varma, R. S., Recent Advances in the Nanocatalyst-Assisted Nabh4 Reduction of Nitroaromatics in Water. *ACS Omega* **2019,** *4* (1), 483-495.

26. Hu, H.; Xin, J. H.; Hu, H.; Wang, X.; Miao, D.; Liu, Y., Synthesis and Stabilization of Metal Nanocatalysts for Reduction Reactions – a Review. *J. Mater. Chem. A* **2015,** *3* (21), 11157-11182.

27. Wang, D.; Astruc, D., The Recent Development of Efficient Earth-Abundant Transition-Metal Nanocatalysts. *Chem. Soc. Rev.* **2017,** *46* (3), 816-854.

Chapter 4: The First Preparation of Polyionic Nanoclays (PINCs) and Their Application in Heterogeneous Catalysis[†]

[†] This Chapter is based upon a published manuscript in *Chemistry of Materials* and is adapted with permission. Nathaniel E. Larm, Laxmi Adhikari, Samantha McKee, and Gary A. Baker, *Chem. Mater.,* **2021,** *33,* 3585-3592.

Ionic liquids (ILs) have amassed considerable academic and industrial attention as alternatives to traditional solvents for a wide range of applications including liquid-liquid separations,[1-2] catalysis,[3-7] and nanoparticle synthesis.[8-10] Further, nanofilm layers of IL dispersed on solid substrates, coined supported ionic liquids (SILs), have received significant attention over the last decade as alternatives to bulk IL, as evidenced by numerous analytical reviews,[11-14] research articles,[15-16] and at least one book.[17] Because these SILs mimic the physicochemical properties of bulk IL in a nanoscale layer on a solid support, they impart several inherent benefits over bulk IL such as (i) an increase in diffusivity of analytes within the SIL nanofilm, alleviating the retardation of reaction rates observed in viscous IL solution, (ii) a greater affinity for continuous flow (rather than batch) applications, increasing product throughput, and (iii) an inclusion of a tailorable solid support, promoting simple separation and recovery of the SIL. These features incentivize the investigation and development of SILs and allude to the reasoning behind their successful inclusion in academic and industrial applications.

When preparing SILs, selection of a support (two- or three-dimensional) and synthesis direction (top-down or bottom-up) is vital, as the substrate has extensive control over surface area, solid-state packing efficiency, and dispersibility of the SIL composite in solvents. Current literature reports lean heavily toward top-down methods of IL dispersion

onto porous three-dimensional (e.g., mesoporous silica[18]) and lamellar two-dimensional (e.g., aluminum oxide,[19] clay,[20-21] octosilicate[22]) substrates by exploiting physisorption (van der Waals forces and hydrogen bonding interactions) or chemisorption (covalent bonding) between the cation of the IL and the substrate surface. Despite the simplified appearance of these top-down approaches and the access they provide to both two- and three-dimensional supports, the top-down methodology imparts several distinct drawbacks: (i) pre-treatment of the substrate is often required prior to IL modification, (ii) the IL and substrate must be solvent-compatible, (iii) heterogenous surfaces can result from incomplete IL deposition, and (iv) the product requires separation/purification from excess IL and unmodified substrate. To alleviate these problems, bottom-up procedures toward three-dimensional SILs have been developed wherein a cation-functionalized trialkoxysilane undergoes acid or base catalyzed, surfactant-assisted sol–gel co-condensation, followed by surfactant extraction to obtain a SIL composite.[11, 18] We note, however, the absence of a similar literature method toward two-dimensional SIL synthesis. While the inherent size-tunability of pores within three-dimensional structures can aid separations, two-dimensional substrates intrinsically possess more accessible and less size-restricted surface areas, increasing diffusion rates during continuous-flow reactions and increasing SIL efficiency over a broader range of catalytic and separations applications. Herein, we address the lack of a bottom-up approach to two-dimensional SILs.

Reports from Burkett et al.[23] have demonstrated a bottom-up synthesis of organo-functionalized phyllosilicate nanoclays using specialized trimethoxysilane precursors (i.e., the synthesis of amine- and thiol-functionalized nanoclays have been known for decades, and aminoclay is a common, well-studied material[24-25]). Thus, it stands to reason that a

trimethoxysilane functionalized with an organocation moiety can be used as a nanoclay precursor, allowing us to extend well-established nanoclay synthesis techniques into the realm of SILs. In this regard, the first reported bottom-up approach for the synthesis of two-dimensional, imidazolium-functionalized, phyllosilicate nanoclay-based SILs (coined polyionic nanoclays, or PINCs, due to their ionic liquid surface functionality) is presented herein. Scheme 4-1 illustrates the two synthetic routes investigated to make PINCs. Initially (Route 1), we proposed alkylation of a propylimidazole-functionalized nanoclay to yield the desired PINC; however, the negligible delamination of the imidazole nanoclay in any tested solvent limits alkylation to only the exposed surfaces of nanoclay stacks. Route 2 illustrates the successful method toward alkylimidazolium-functionalized silane IL synthesis,[26] followed by nanoclay formation in the presence of Mg^{2+} and under basic conditions. We recommend this route for preparing PINCs, resulting in aminoclay analogues with complete surface functionalization.

Experimentally, 2.00 grams (6.89 mmol) of (3-iodopropyl)trimethoxysilane was combined with 0.51 grams (6.26 mmol) of 1-methylimidazole in a clean, dry 15-mL round bottom flask. The mixture was stirred at room temperature and protected from light for 7 d. The resulting yellow liquid was rinsed with ethyl acetate under vigorous stirring three times to extract excess reactants, followed by rotary evaporation at 30 °C for 2 h to obtain a viscous yellow liquid (yield of 0.74 g, or 2.00 mmol based on the proposed formula weight of 371.9 g mol^{-1}), which was identified via ^{1}H NMR to be 1-methyl-3-(trimethoxysilylpropyl)imidazolium iodide ([mpim]I silane, Figure 4-1A). This method was also used to synthesize 1-butyl-3-(trimethoxysilylpropyl)imidazolium iodide ([bpim]I silane) and 1-octyl-3-(trimethoxysilylpropyl)imidazolium iodide ([opim]I silane) by

replacing 1-methylimidazole with similar molar quantities of 1-butyl- or 1-octylimizadole, respectively. In this regard, 1-butylimidazole was purchased while 1-octylimidazole was produced by dissolving 5.0 g of imidazole and 14.2 g of 1-bromooctane in 50 mL of absolute EtOH, followed by slow addition of 1.8 g of sodium hydride while stirring to deprotonate the imidazole. This solution of 1-bromooctane was stirred for 1 day and distilled prior to use for silane synthesis. We note that (3-chropropyl)trimethoxysilane can be substituted for the (3-iodopropyl)trimethoxysilane by heating for 3 d at 80 °C (all else being the same), resulting in the chloride silanes. To prepare the PINCs, 0.31 g of $MgCl_2 \cdot 6H_2O$ (1.52 mmol) was dissolved in 15 g of absolute EtOH in a 100-mL glass round bottom flask. 0.74 g of [mpim]I silane was dissolved in 10 g of absolute EtOH using brief sonication, forming a solution which was promptly added to the solution of Mg^{2+}. To promote hydrolysis of the silane precursor, 4.0 mL of 0.5 M aqueous NaOH was added to the stirring solution, resulting in the formation of a white precipitate. This cloudy mixture was magnetically stirred at 400 rpm under ambient temperature for 24 h. The contents of the flask were transferred to a 50-mL Falcon centrifuge tube and rinsed three times using absolute EtOH and centrifugation (centrifuge at 10,000 rpm for 15 min, decant the liquid, re-disperse the precipitate in ~20 mL of EtOH via brief shaking, repeat) to obtain a white precipitate of [mpim]I PINC, which was then lyophilized to obtain the dry PINC. The PINC powder was stored at room temperature in a lab drawer until use. This method was also used to synthesize butyl- and octylimidazolium iodide ([b- and [opim]I) PINCs as well as methylimidazolium chloride ([mpim]Cl) PINC using those respective silane precursors. The facile synthesis is not wasteful of expensive IL, and the products possess intrinsic homogeneous surface functionality due to the building-block nature of the bottom-up

nanoclay synthesis. We want to acknowledge that all PINCs produced herein have been assigned nomenclature based on the halide present in the precursor silane IL despite the presence of other anions (e.g., OH^- and Cl^-) in the nanoclay reaction media.

Scheme 4-1: *Proposed PINC Synthetic Routes*

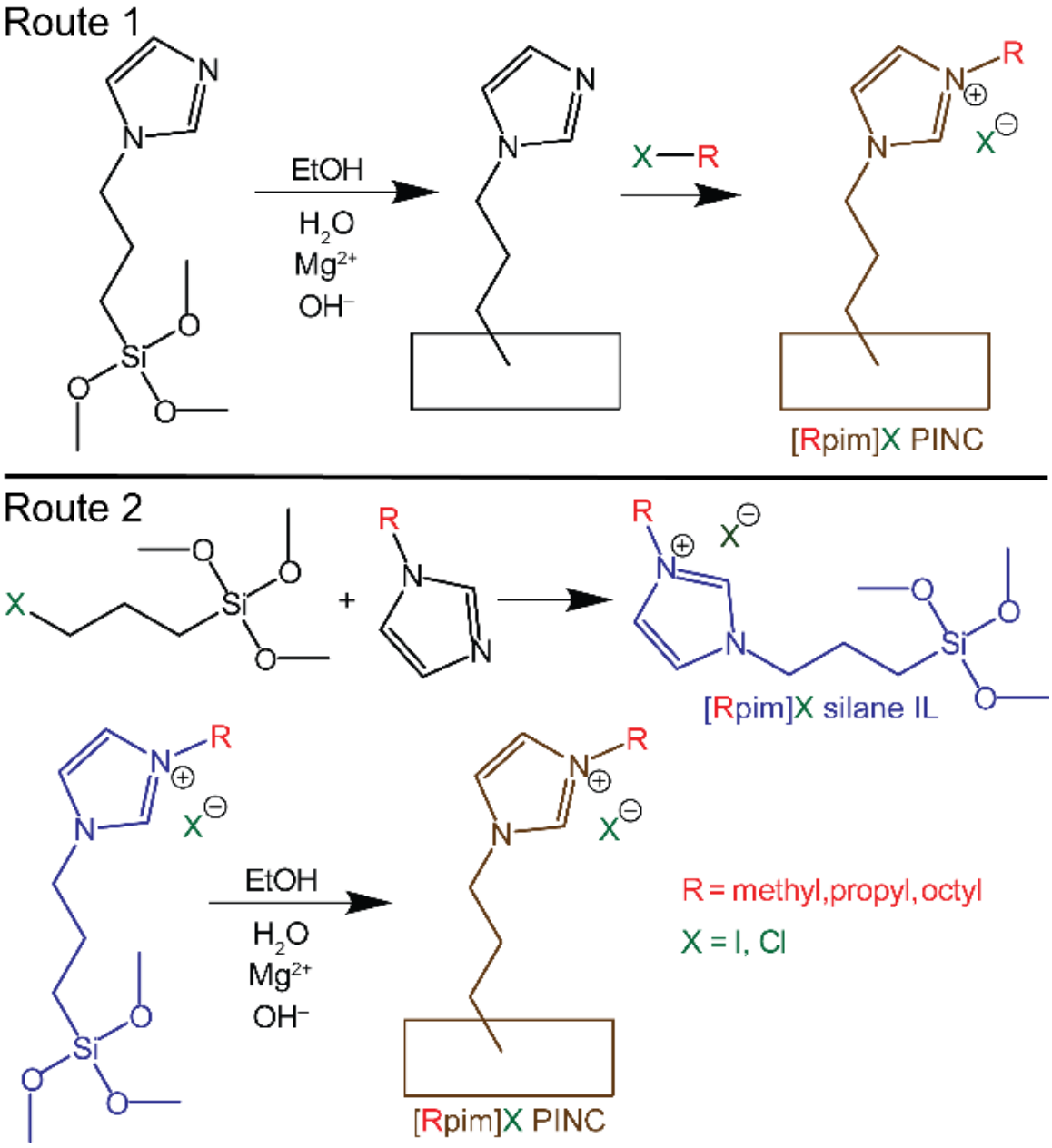

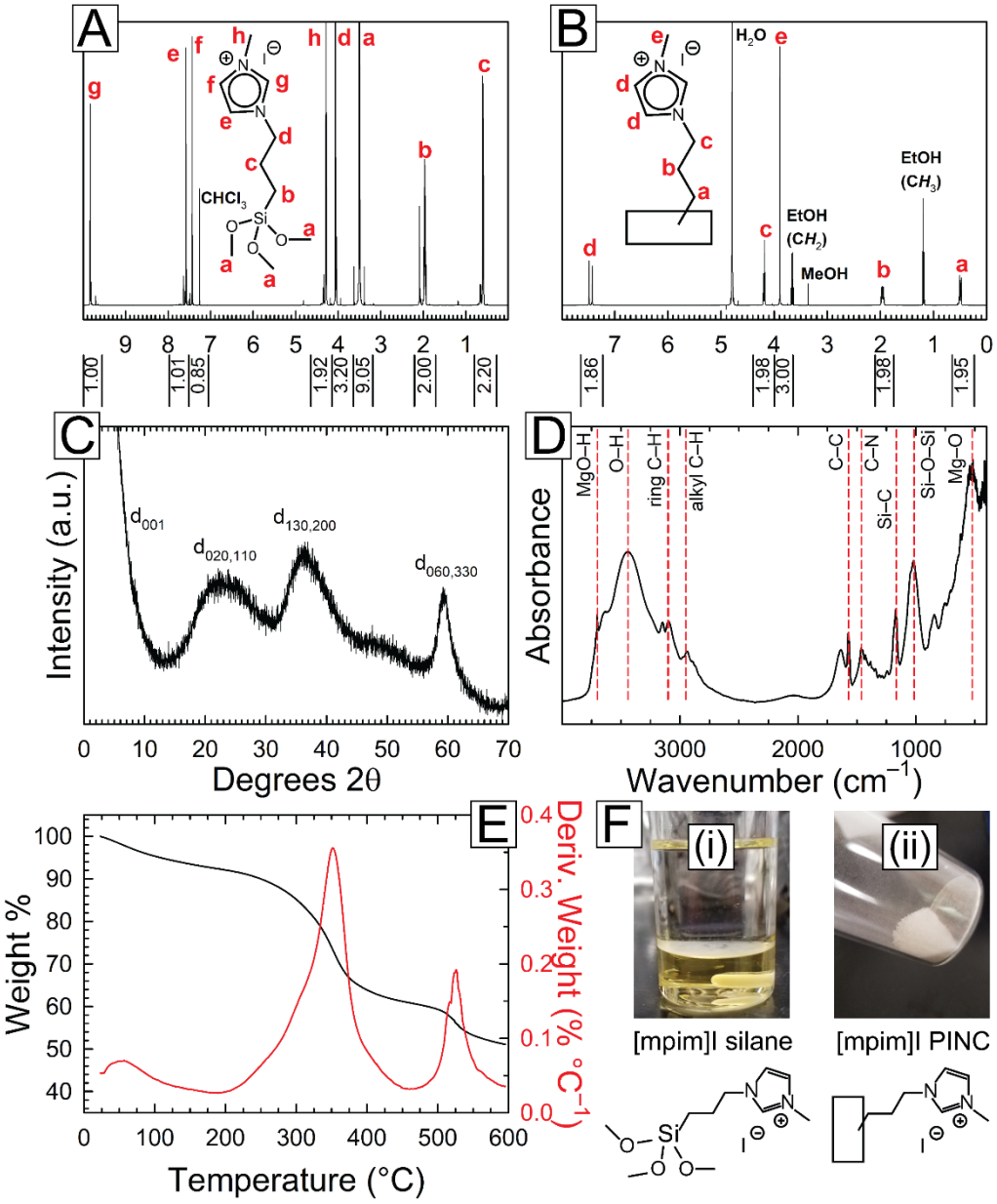

***Figure 4-1**: Characterization of the [mpim]I silane IL and PINC. A) and B) respective ^{1}H NMR spectra; C) XRPD pattern of [mpim]I PINC; D) FTIR spectrum of [mpim]I PINC; E) TGA thermogram of [mpim]I PINC; F) photographs of i) [mpim]I silane IL below ethyl acetate and ii) [mpim]I PINC.*

Solvation of the silane ILs and PINCs can simplify characterization, anion exchange, and purification procedures. We find that the silane ILs are readily soluble in water and chloroform, but not diethyl ether or ethyl acetate (noted as useful purification

solvents to separate the IL from its precursors). Further, the polycationic surfaces of the PINCs cause them to disperse in water, but less so in non-aqueous media (e.g., MeOH, EtOH, acetone, chloroform, hexanes). Mechanistically, this dispersion is similar to the delamination of aminoclay in water below pH 10 (the pK_a for a primary ammonium proton), although we note that our PINCs are always charged (i.e., not pH dependent like aminoclay), and that longer alkyl chains at the imidazolium N2 position contribute to more hydrophobic surfaces, reducing the solubility of those PINCs in water. Indeed, dispersion of the 1-methyl-3-propylimidazolium iodide ([mpim]I) PINC in water results in a clear, colorless solution at concentrations above 100 mg mL^{-1} with light sonication, whereas an aqueous solution of [opim]I PINC has the appearance of a cloudy dispersion. These solubilities should be considered when designing the PINCs or considering their application.

The iodide-based silane ILs and PINCs were characterized using ^{1}H NMR spectroscopy, XRPD, FTIR spectroscopy, and TGA as shown for [mpim]I silane and its respective PINC in Figure 4-1 (further elaboration on characterization of longer alkyl chain silanes/PINCs can be found in Figures 4-2 through 4-8). The ^{1}H NMR spectroscopic assignments and integrations display characteristic peaks for [mpim]I, [bpim]I, and [opim]I silanes and PINCs (Figures 4-1A, 4-2, and 4-5 for silanes, 4-1B and 4-3 for PINCs), with peak broadening in the [bpim]I PINC spectrum attributed to its decreased D_2O solubility. The XRPD diffractograms for the iodide-based PINCs (Figures 4-1C, 4-4, and 4-6) exhibit broader analogs of the talc (020), (110), (130), (200), (060), and (330) reflections (JCPDS card 13-0558), a finding which correlates well with that of Burkett et al. for their organofunctionalized nanoclays.[10] Notably, the (001) reflection, which is representative

of the interlamellar spacing between nanoclays, is difficult to discern in our results. We attribute this observation to exfoliation or steric expansion of the interlayer spacing beyond the working range of the X-ray diffractometer used. The FTIR spectra (Figures 4-1D and 4-7) reveal absorbance peaks corresponding to those of the magneso-silicate backbone and the organic moieties associated with the surface functional groups. The TGA thermograms (Figures 4-1 and 4-8) reveal similar thermal stabilities for each iodide-based PINC, with evaporation of trapped solvent concluding around 150 °C and thermal degradation of the surface organic groups beginning at around 250–300 °C. These results allude to the possibility of using these PINCs for applications at elevated temperatures near 200 °C. Although unfunctionalized aprotic ionic liquids, (e.g., 1-butyl-3-methylimidazolium bis(trifluoromethylsulfonyl)imide) typically produce negligible char residue upon heating in an inert atmosphere,[27] similar thermolysis conducted under confinement within an oxide framework (e.g., silica) afforded significant carbonization yields.[28] Char formation for thermolysis of the [mpim]Cl PINC is evident from the change in appearance from white to black after treatment at 800 °C for 1 h, as shown in Figure 4-9, alluding to the possibility for these PINCs to act as matrices for the entrapment of char.

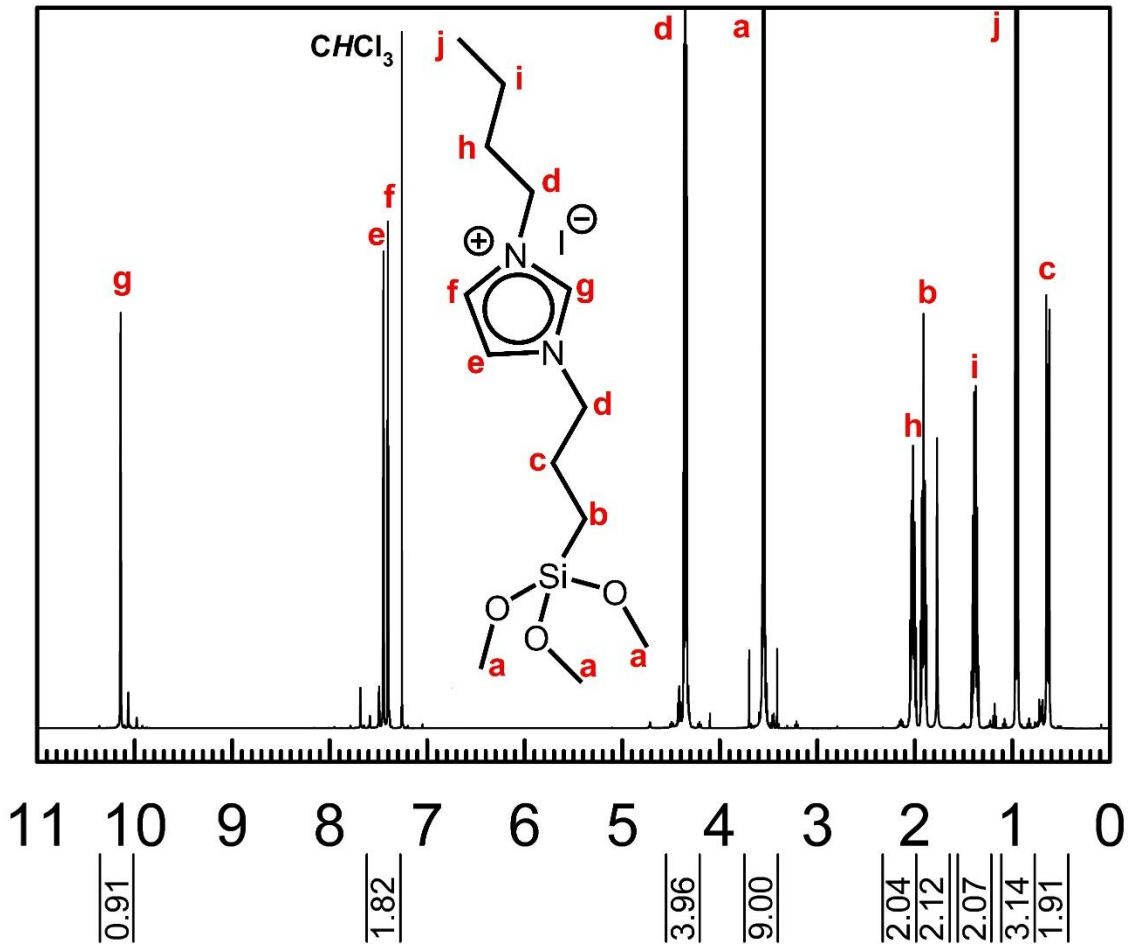

***Figure 4-2**: [1]H-NMR spectrum of butylimidazolium iodide silane IL. Peak assignments show the presence of residual solvent (chloroform) and possibly water (at 1.8 ppm). The following shifts are identified (500MHz; $CDCl_3$): 10.18 (1H, s, N-C**H**-N), 7.45 and 7.40 (1H each, s, CH_2-N-C**H**-C**H**), 4.35 (4H, t, C**H**$_2$-N-CH-N-C**H**$_2$), 3.56 (9H, s, C**H**$_3$-O-Si), 2.03 (2H, m, CH_3-CH_2-C**H**$_2$), 1.91 (2H, m, Si-C**H**$_2$), 1.39 (2H, m, CH_3-C**H**$_2$), 0.96 (3H, t, C**H**$_3$), 0.64 (2H, t, Si-CH_2-C**H**$_2$).*

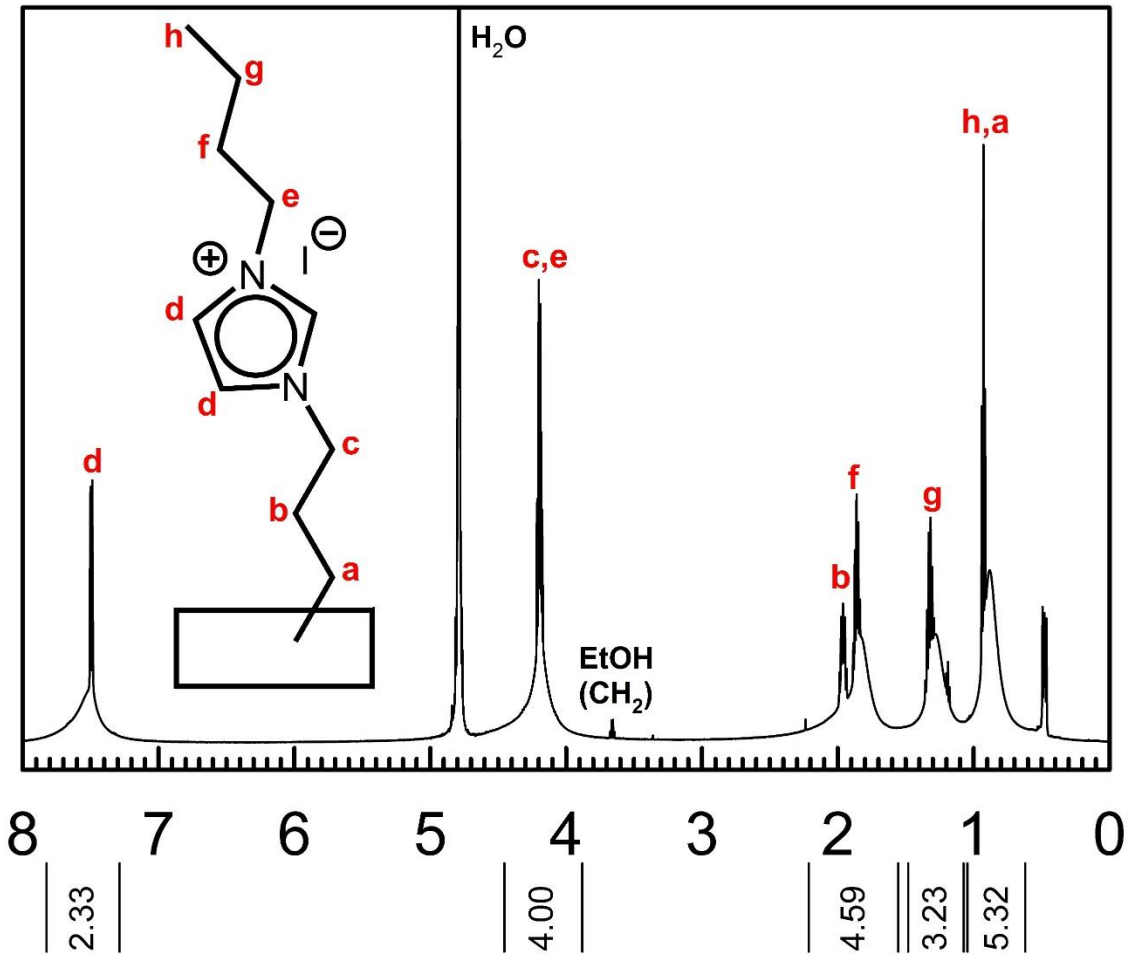

***Figure 4-3**: [1]H-NMR spectrum of the butylimidazolium iodide PINC. Interlocking of the longer alkyl chain branching from the imidazolium ring dissuades delamination of the PINC in water, resulting in broader peaks than those observed in the methylimidazolium iodide PINC. This broadening also reduces peak resolution, producing a significant hurdle for integration. Peak assignments show the presence of residual solvent (ethanol). The following shifts are identified (600MHz; D_2O): 7.49 (2H, s, CH_2-N-C**H**-C**H**), 4.19 (4H, m, C**H**$_2$-N-CH-N-C**H**$_2$), 1.96 (2H, m, Si-CH_2-C**H**$_2$), 1.87 (2H, m, CH_3-CH_2-C**H**$_2$), 1.33 (3H, m, CH_3-C**H**$_2$), 0.94 (3H, s, C**H**$_3$), 0.93 (2H, s, clay-C**H**$_2$). The proton located at the N-C**H**-N location experiences rapid exchange with D_2O, resulting in its absence from the spectrum.*

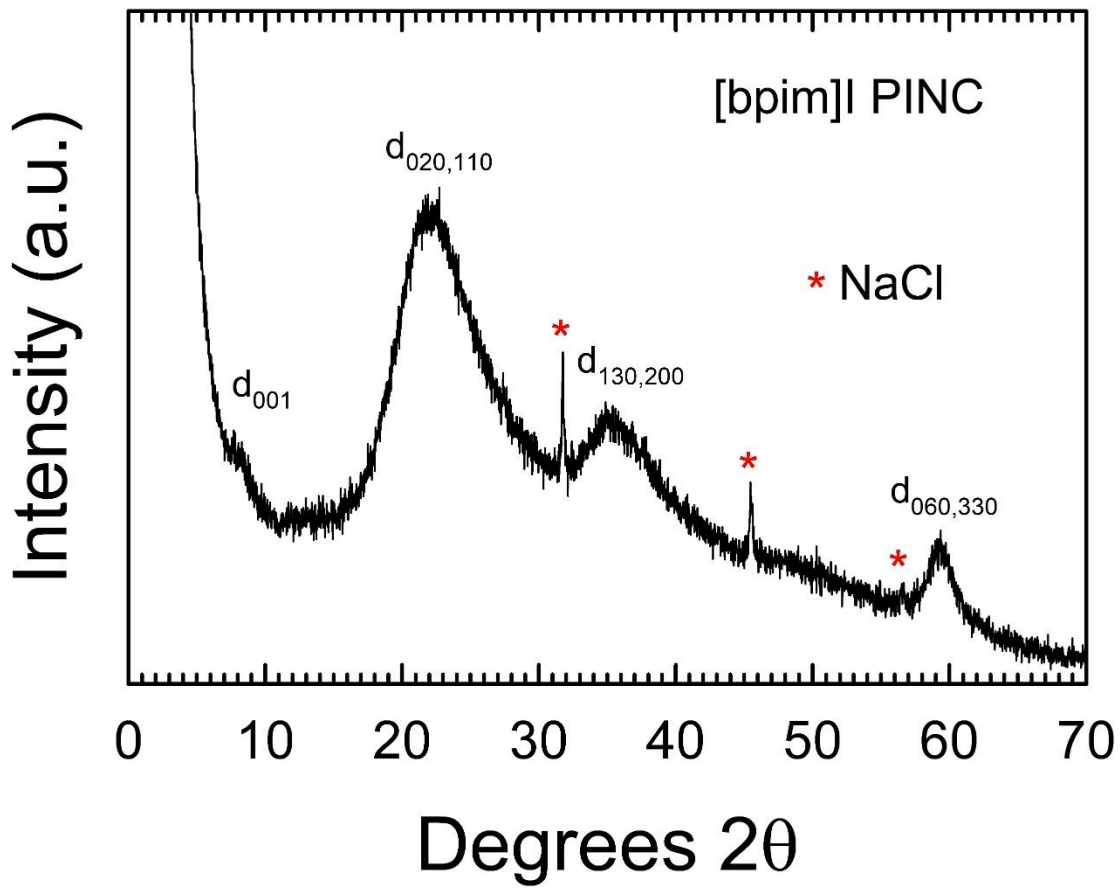

***Figure 4-4**: XRPD diffractogram for the butylimidazolium iodide PINC. Sharp peaks are present at 32°, 45°, and 57° 2Θ, corresponding to the (200), (220), and (222) reflections in NaCl, respectively. All other reflections are indicative of a 2:1 phyllosilicate clay, with peak broadening attributed to the large organic moiety [(1-butyl-(3-propyl)imidazolium] present on the lamella surface.*

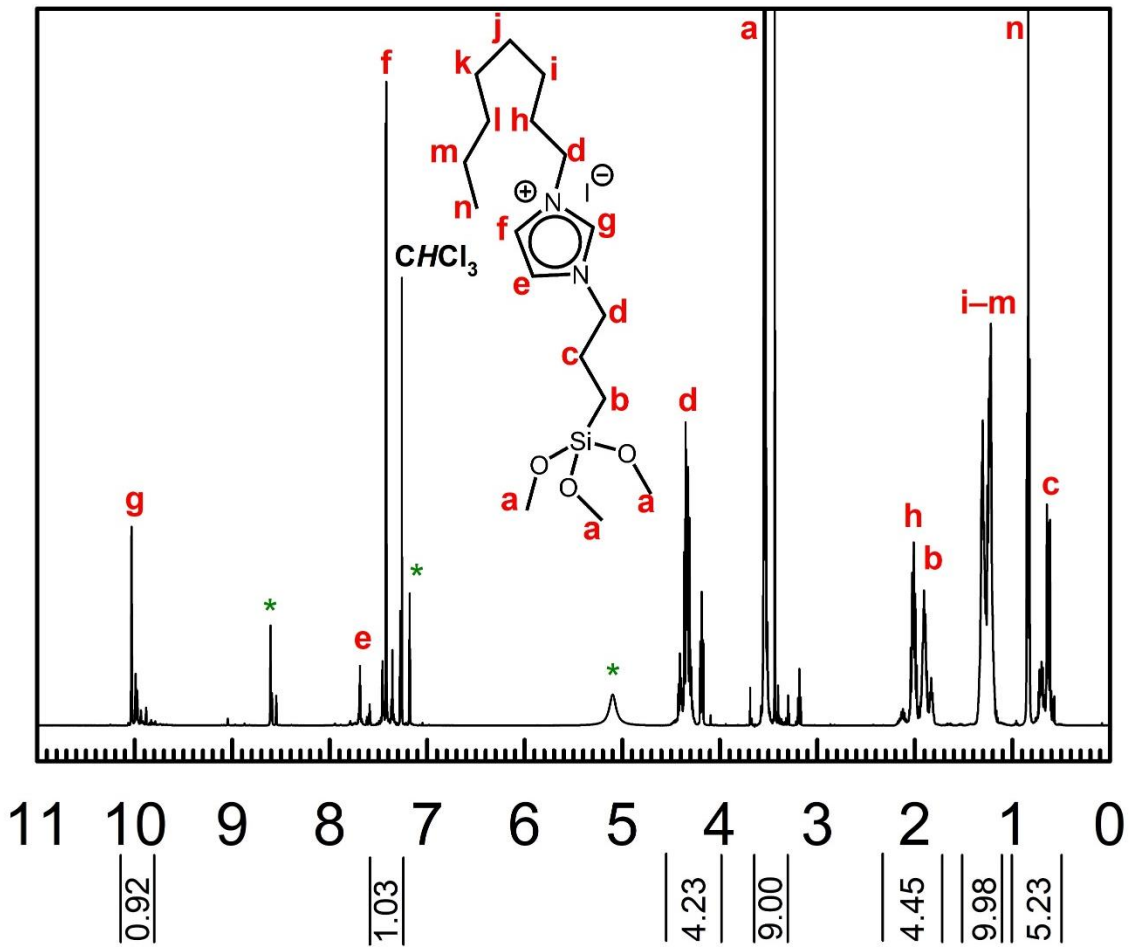

***Figure 4-5**: [1]H-NMR spectrum of octylimidazolium iodide silane IL. Peak assignments show the presence of residual solvent (chloroform) and possibly water (at 1.8 ppm). The following shifts are identified (500 MHz; $CDCl_3$): 10.03 (1H, s, N-C**H**-N), 7.69 and 7.42 (1H each, s, CH_2-N-C**H**-C**H**), 4.34 (4H, m, C**H**$_2$-N-CH-N-C**H**$_2$), 3.54 (9H, s, C**H**$_3$-O-Si), 2.01 (2H, m, Si-…-N-CH_2-C**H**$_2$), 1.90 (2H, m, Si-C**H**$_2$), 1.26 (10H, m, CH_3-C**H**$_2$-C**H**$_2$-C**H**$_2$-C**H**$_2$-C**H**$_2$), 0.84 (3H, t, C**H**$_3$), 0.63 (2H, t, Si-CH_2-C**H**$_2$). Peaks marked with a green asterisk (*) are unidentified but may belong to a degradant of octyimidazole.*

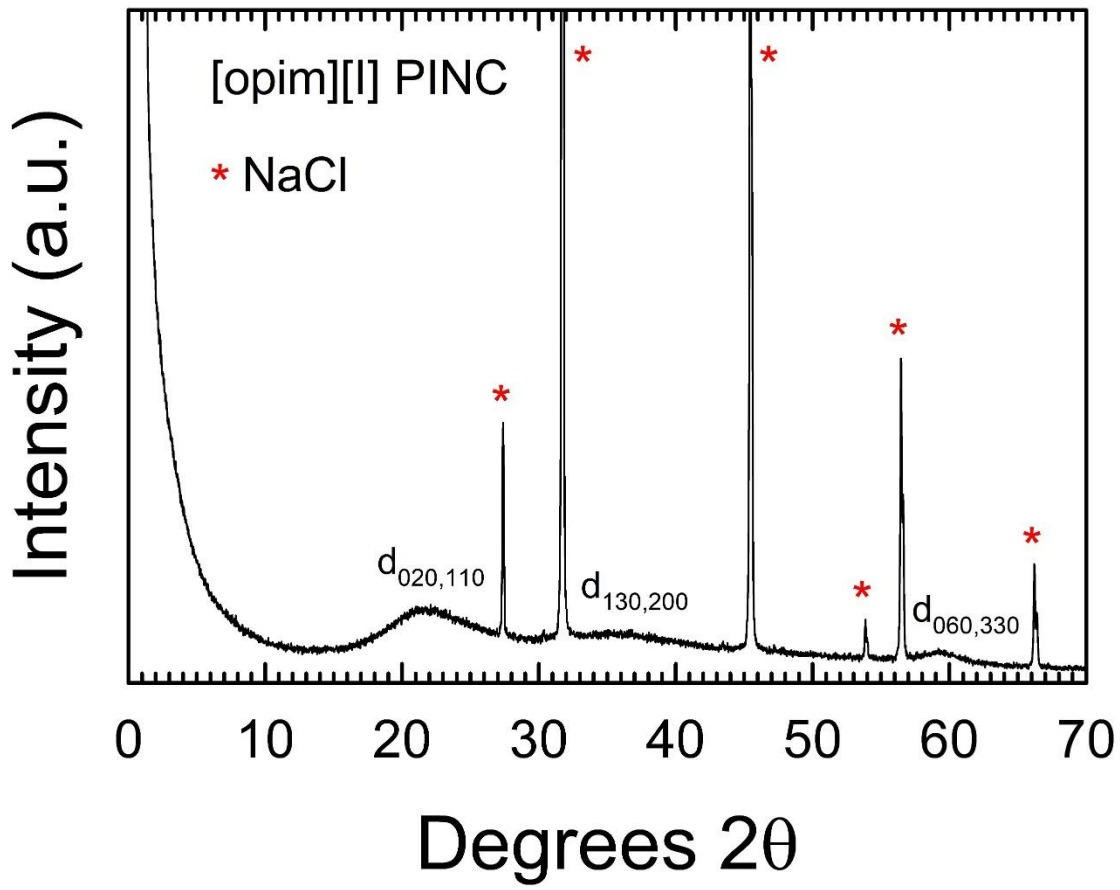

Figure 4-6*: XRPD diffractogram for the octylimidazolium iodide PINC. Sharp peaks are present at 27°, 32°, 45°, 54°, 57°, and 66° 2Θ, corresponding to the (111), (200), (220), (311), (222), and (400) reflections in NaCl, respectively. All other reflections are indicative of a 2:1 phyllosilicate clay, with peak broadening attributed to the large organic moiety [(1-octyl-(3-propyl)imidazolium] present on the lamella surface. It is possible that the absence of the (001) reflection in the PINC, typically found near 8° 2 Θ, is indicative of a large interlayer spacing in the lamellar structure resulting from steric hinderances caused by the large octyl chain.*

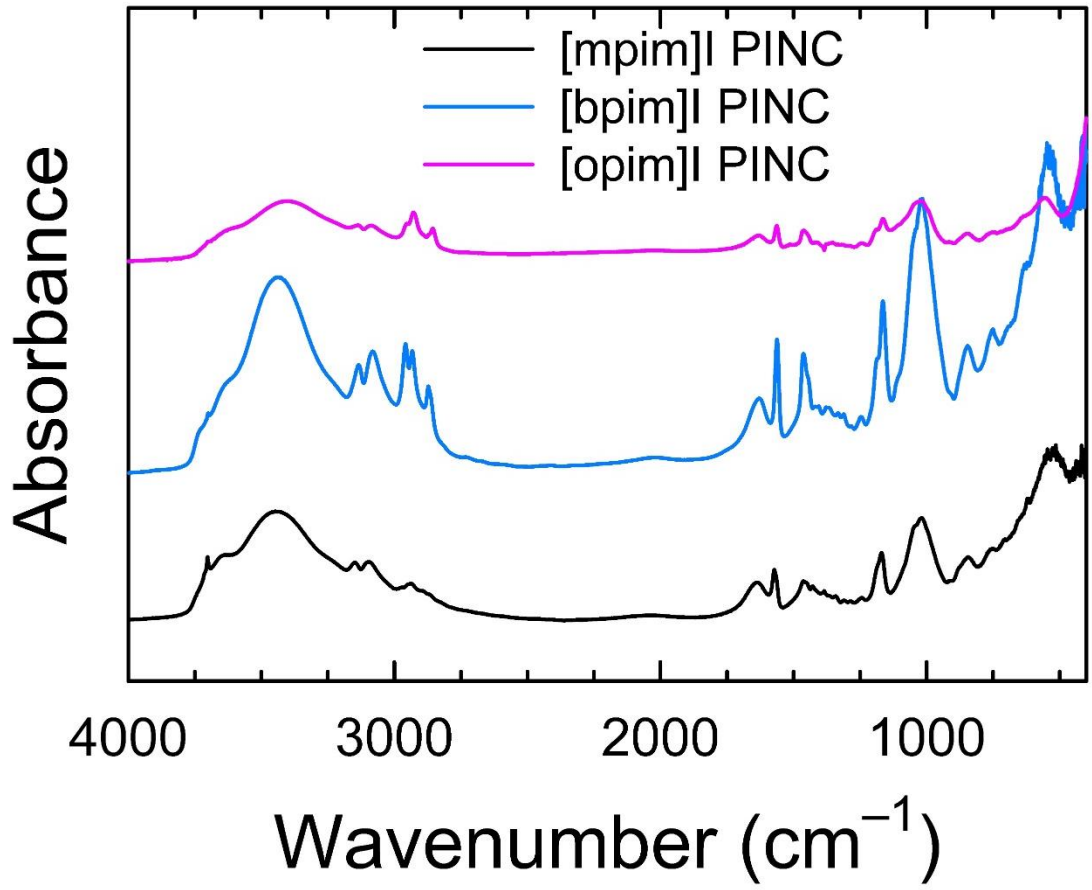

***Figure 4-7**: Transmission FTIR spectra of the [m-, [b, and [opim]I PINCs. Magneso-silicate peaks are observed at ~520 cm^{-1} for Mg–O, 1015-1020 cm^{-1} for Si–O–Si, 1165-1170 cm^{-1} for Si–C, 3430-3450 cm^{-1} for O–H, and 3700 cm^{-1} for MgO–H. Organic moieties display characteristic peaks at 1380-1480 cm^{-1} for C–N, 1560-1575 cm^{-1} for C–C, 2930-2960 cm^{-1} for alkyl C–H, and 3000-3150 cm^{-1} for ring C–H.*

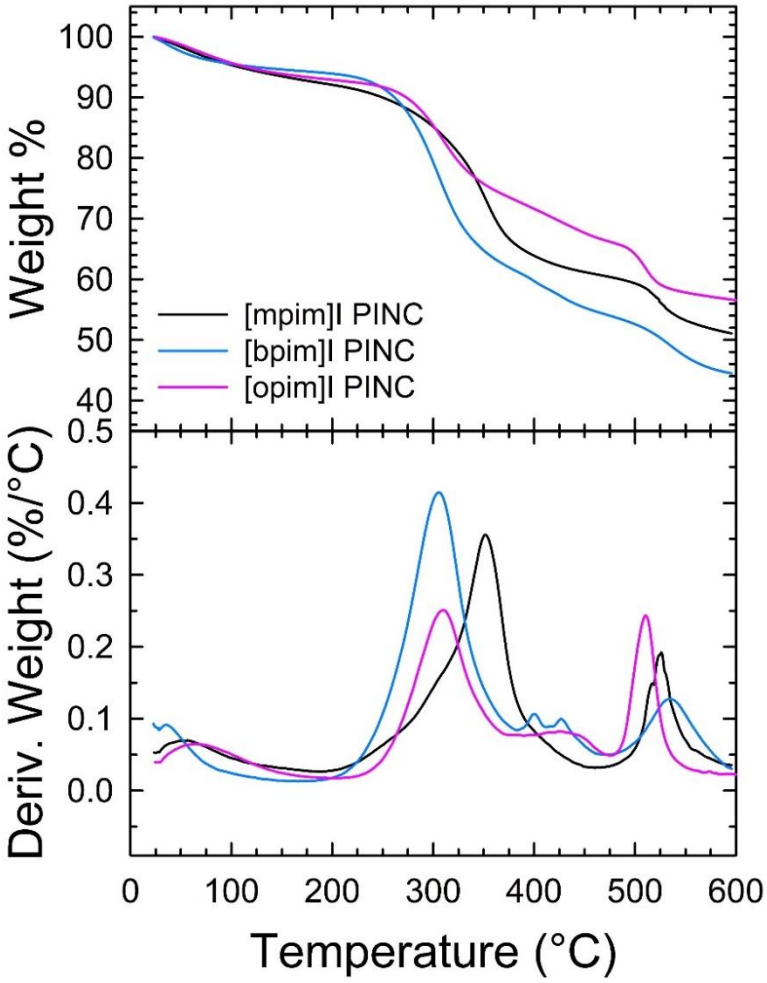

***Figure 4-8**: TGA thermogram (top) and 1st derivative plot (bottom) for the methylimidazolium and butylimidazolium iodide PINCs. For [mpim]I PINC, the following mass losses are noted: 9% loss before 200 °C attributed to gradual release and evaporation of water, EtOH, and MeOH; 31% mass loss from 250 to 450 °C attributed to degradation of the methylimidazolium functionality; 8% mass loss from 475 to 600 °C attributed to degradation of the propyl chain. For the [bpim]I PINC, the following mass losses are noted: 6% loss before 200 °C attributed to gradual release and evaporation of water, EtOH, and MeOH; 30% mass loss from 225 to 375 °C attributed to degradation of the butylimidazolium functionality; 20% mass loss from 375 to 600 °C attributed to degradation of the propyl chain. For [opim]I PINC, the following mass losses are noted: 7% loss before 200 °C attributed to gradual release and evaporation of water, EtOH, and MeOH; 21% mass loss from 250 to 450 °C attributed to degradation of the octylimidazolium functionality; 10% mass loss from 475 to 600 °C attributed to degradation of the propyl chain. Note that the disproportionate mass losses observed for the organic components in [opim]I PINC are tentatively attributed to residual NaCl (presence evident in XRPD).*

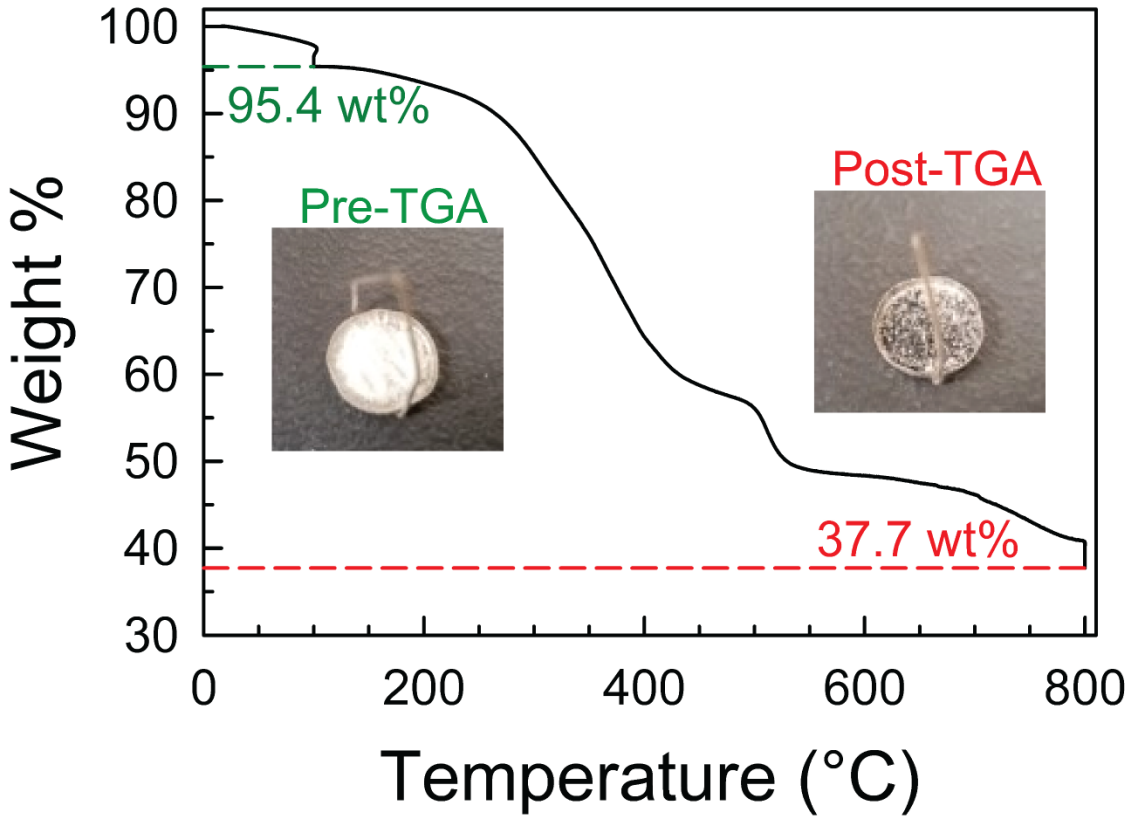

***Figure 4-9**: A TGA profile for [mpim]Cl PINC which was, prior to analysis, cleaned repeatedly with ethanol and thoroughly dried to remove as much solvent and interlamellar salt and reactants as possible. Using a heating rate of 10 °C min^{-1}, the white sample was heated from room temperature to 100 °C, where it remained for 1 h, and then continued to 800 °C, where it remained for 1 h. Subtracting the wt% after drying at 100 °C for 1 h (95.4 wt%) and after run completion (37.7 wt%) yields a total mass loss due to degradation of organic moieties (i.e., the covalently-bound IL) of 57.7 wt%. Using the molecular weight of the [mpim]Cl IL moiety (159.64 g mol^{-1}), we calculate an IL loading of 3.8 mmol g^{-1}. We note that the presence of residual salt and char, the latter of which can be seen in the "post-TGA" picture, can cause error in this estimation.*

The monetary and temporal cost of bulk IL (and by extension SIL) production is a common barrier to their application. Therefore, the expensive, week-long ambient synthesis using the iodine-based precursor silane (3–7 U.S.$ mL^{-1}) was replaced with a cheaper, three-day, 80 °C synthesis using 3-chloropropyltrimethoxysilane (0.20–0.40 U.S.$ mL^{-1}). This alteration to the method produces [mpim]Cl silane IL and PINC, which

notably shows similar solvation properties and characterization results to those of [mpim]I PINC (Figure 4-10) while reducing the reagent cost of the resulting composite by almost an order of magnitude. This [mpim]Cl PINC was used for all following experiments and was further characterized using scanning electron microscopy (SEM) and transmission electron microscopy (TEM) to discern average platelet size and stacking (Figure 4-11).

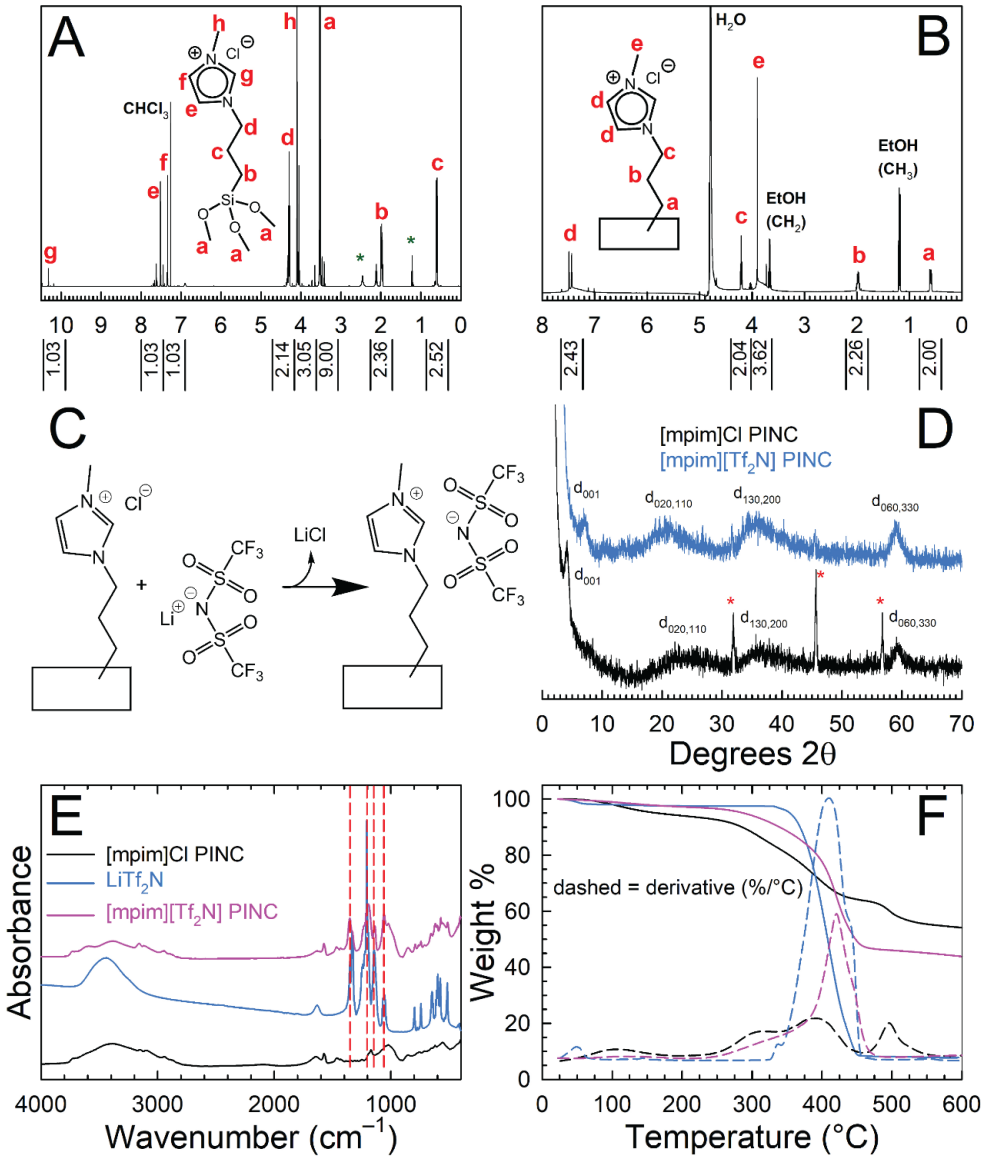

***Figure 4-10**: Characterization of [mpim]Cl silane IL/PINC and [mpim][Tf2N] PINC. A) and B) [mpim]Cl silane IL and PINC ^{1}H-NMR spectra. Green asterisks (*) denote impurities tentatively attributed to degraded methyl imidazole. C) Scheme showing the anion exchange between [mpim]Cl PINC and [mpim][Tf2N]. D) PXRD diffractograms for both [mpim]Cl and [mpim][Tf2N] PINCs, with red asterisks (*) denoting the NaCl (200), (220), and (222) impurity peaks. The higher diffraction angle for the (001) peak in [mpim][Tf2N] PINC when compared to [mpim]Cl PINC is attributed to the hydration of Cl⁻, which expands the interlayer region. E) FTIR spectra, with the denoted ν_aS=O (1350 cm^{-1}), ν_aC–F (peak at 1147 cm^{-1} and shoulder at 1230 cm^{-1}), and ν_aS–N–S (1060 cm^{-1}) bands arising from the [Tf2N]⁻ anion. F) TGA thermogram (solid lines) and first derivative plot (dashed lines) for each analyte from panel E, with characteristic mass losses from Tf2N⁻ in the corresponding [mpim][Tf2N] PINC. The legend in panel E also applies to panel F.*

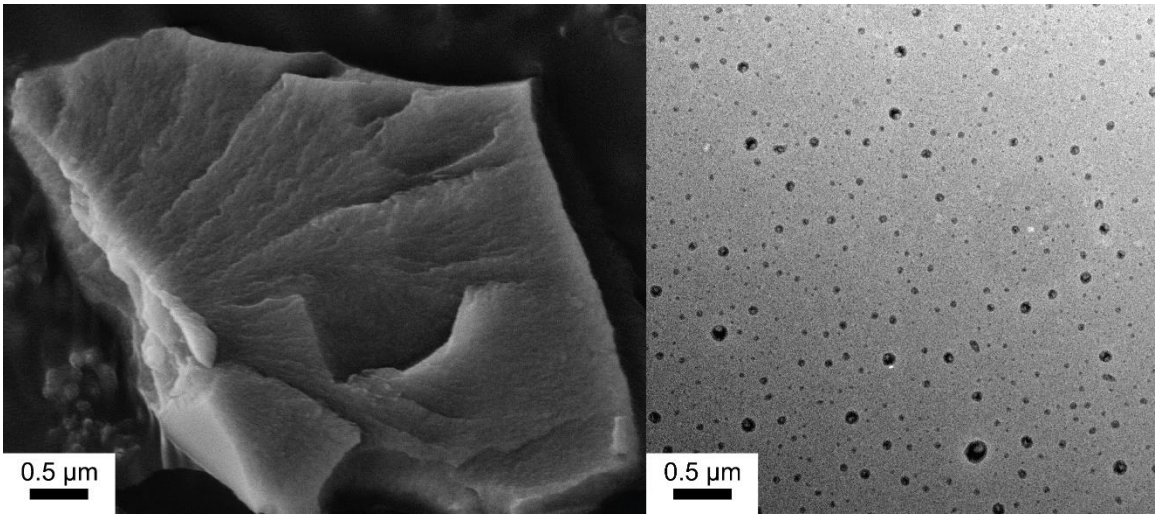

Figure 4-11*: (Left) SEM and (right) TEM images of [mpim]Cl PINC. The stacked PINCs in the SEM image allude to a layered structure, and the TEM image presents an average platelet size of 59.2 ± 26.8 nm (the smallest and largest measured platelets are 12 and 176 nm, respectively).*

Our claim of complete surface functionalization requires conscientious reporting of IL loading and surface charge. Utilizing TGA, we have calculated an IL loading of approximately 3.8 mmol g^{-1} for our [mpim]Cl PINC (Figure 4-9). We wish to note that neat [mpim]Cl IL comprises an "IL loading" of 6.2 mmol g^{-1} when calculated using the molar mass of 160.64 g mol^{-1}. Discrepancies between the calculated and theoretical IL loadings can be due to residual interlamellar salt (likely NaCl) and char formed during TGA (as evidenced by the black appearance of the calcined product in Figure 4-9), and we delved deeper into the backbone structure to determine the presence of other error by way of surface defects. Our initial assumption is that our PINCs possess a talc-like backbone comprising a hexagonal distribution of fully condensed surface silicon (talc JCPDS card 13-0558), which would yield a theoretical maximum single-layer IL loading of 4.2 mmol g^{-1} (3 IL moieties per nm^2).[29] Interestingly, the solid-state ^{29}Si NMR spectrum for [mpim]Cl PINC (Figure 4-12) reveals a polycondensation of 55%, as calculated using

Equation 1, for the Si layer (41% T1, 53% T2, and 6% T3 by area, where T1, T2, and T3 correspond to the singly-, doubly-, and triply-condensed Si atoms, respectively), likening the PINC backbone to that of aminoclay rather than fully-condensed talc (i.e., aminoclay is known to possess a small T3 peak).[23]

$$polycondensation = \frac{(\%T1 + 2\%T2 + 3\%T3)}{3} \quad (1)$$

For the curious reader, we point to an excellent recent publication by M. Bruneau et al. wherein the authors discuss tailoring the reaction conditions to adjust the degree of clay condensation.[30] Unfortunately, the low degree of polymerization complicates our surface-bound IL estimation, though we propose that our bottom-up approach intrinsically leads to complete functionalization of the clay surface. Regardless, our estimated IL loading of 3.8 mmol g^{-1} is over double that of other materials in the literature,[18, 31] and is, to our knowledge, the closest of any SIL phase to the previously mentioned IL density of neat, unsupported [mpim]Cl IL (6.2 mmol g^{-1}). As a final characterization of the charged IL surface, zeta potential measurements of [mpim]Cl PINC colloid reveals a potential difference of +44 mV and +30 mV for [mpim]Cl and [bpim]I PINCs, respectively, which are comparable with the value of +35 mV for aminoclay in an acidic medium.[32]

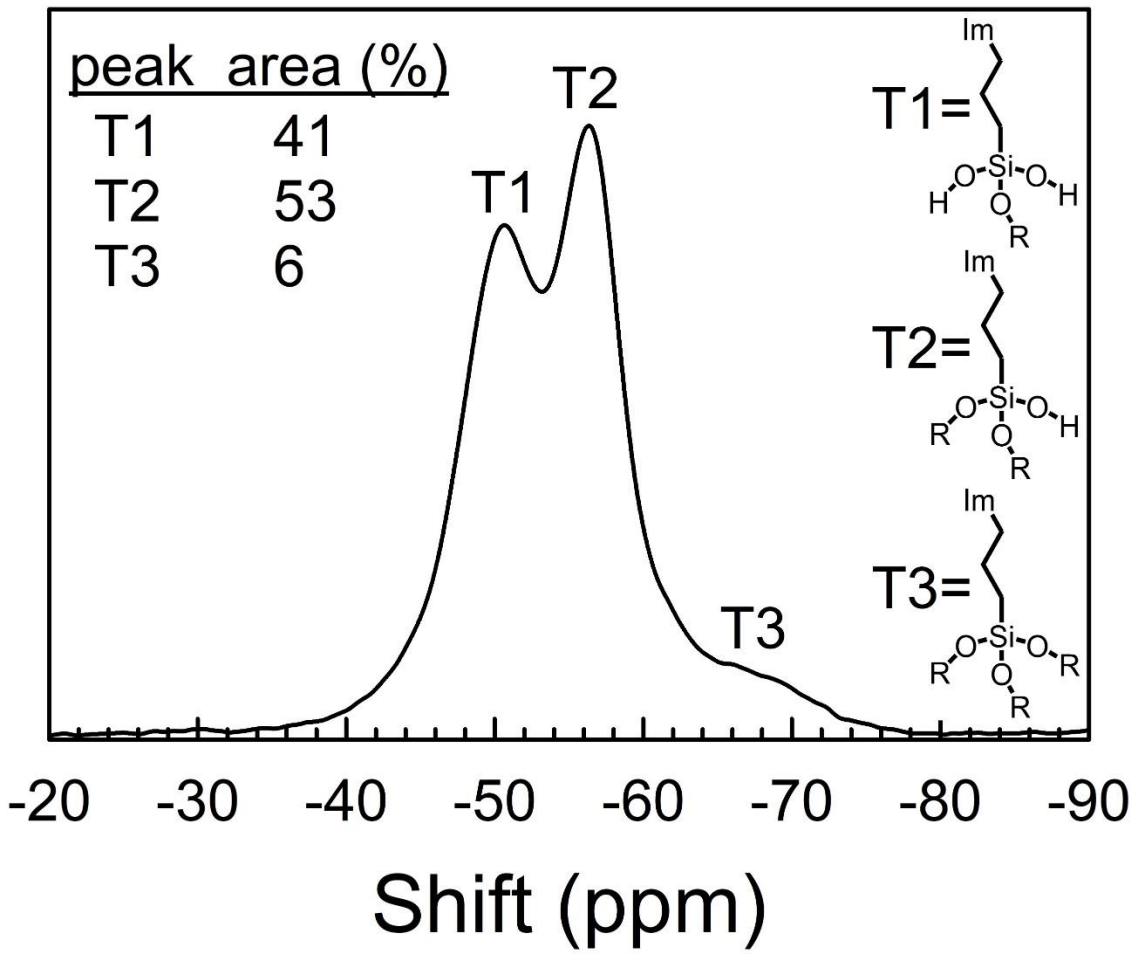

***Figure 4-12**: Solid-state ^{29}Si NMR spectrum for [mpim]Cl PINC. We additionally provide structure representation for each condensation degree, where "Im" represents the imidazolium group and "R" represents either Mg or Si atoms. The area % for each peak is based on the deconvoluted data, which inherently possesses a maximum error of 5%.*

ILs are labeled as designer solvents due to the exchangeability of cations or anions toward a specific application. While we speculate that the cation can be exchanged during synthesis of the silane (indeed, PINCs with pyridinium and pyrrolidinium functionality are interesting topics for a future study), anion exchange of the halide present on the PINC can be readily demonstrated through metathesis in aqueous solution. Addition of excess aqueous $LiTf_2N$ to an aqueous dispersion of [mpim]Cl PINC precipitates the white solid

[mpim][Tf_2N] PINC (Figures 4-10C and 4-13), characterized using XRPD, FTIR spectroscopy, and TGA (Figure 4-10D–F), whereas addition of aqueous $HAuCl_4$ produces a yellow precipitate of [mpim][$AuCl_4$] PINC, which can be re-dispersed through sonication (Figure 4-13). While this simple exchange alludes to many exciting applications in catalysis and separations, the formation of [mpim][$AuCl_4$] PINC incentivizes investigation into substrate-stabilized AuNPs and heterogeneous catalysis. In this regard, reduction of the aqueously-dispersed [mpim][$AuCl_4$] species occurred through the dropwise addition of a molar excess of aqueous sodium borohydride ($NaBH_4$), producing an orange-red solution with an extinction peak at ~500 nm (Figure 4-14). Experimentally, a typical preparation involves solvation of 100 mg of [mpim]Cl PINC in 8.0 mL of H_2O followed by addition of a 1.0 mL aliquot of aqueous 10 mM $HAuCl_4$ while stirring vigorously to form a yellow solution. After 1 min, 1.0 mL of aqueous 1.0 M $NaBH_4$ was added rapidly to the stirring solution form an orange colloid of PINC@AuNPs. This colloid was stored at room temperature in a lab drawer until use. The solution color alludes to the formation of sub-5 nm gold nanoparticles (AuNPs) supported on the PINC surface (PINC@AuNPs), which is confirmed by TEM analysis (Figure 4-13). Significantly, the AuNPs appear to be sufficiently stabilized by surface ligands and the conjugated π electrons from the PINC imidazolium groups,[33] such that aggregation is prevented even after storage in a lab drawer for 2 months (Figure 4-14). As such, these supported AuNPs exhibit good long-term aqueous stability (indeed, the colloidal stability of these PINC@AuNPs was assessed using zeta potential, yielding a surface charge of +26 mV). As a control, a solution of [mpim]Cl IL was prepared and used at a similar molar quantity in the place of PINC to make AuNPs. The resulting solution, prepared identically to that with the PINC, turned blue upon

addition of $NaBH_4$ and, within 1 min, black as the Au^0 aggregates precipitated from solution. This control indicates that the structured PINC is required for the IL to act as an effective stabilizing ligand, and that bulk IL is insufficient to prepare similar AuNPs.

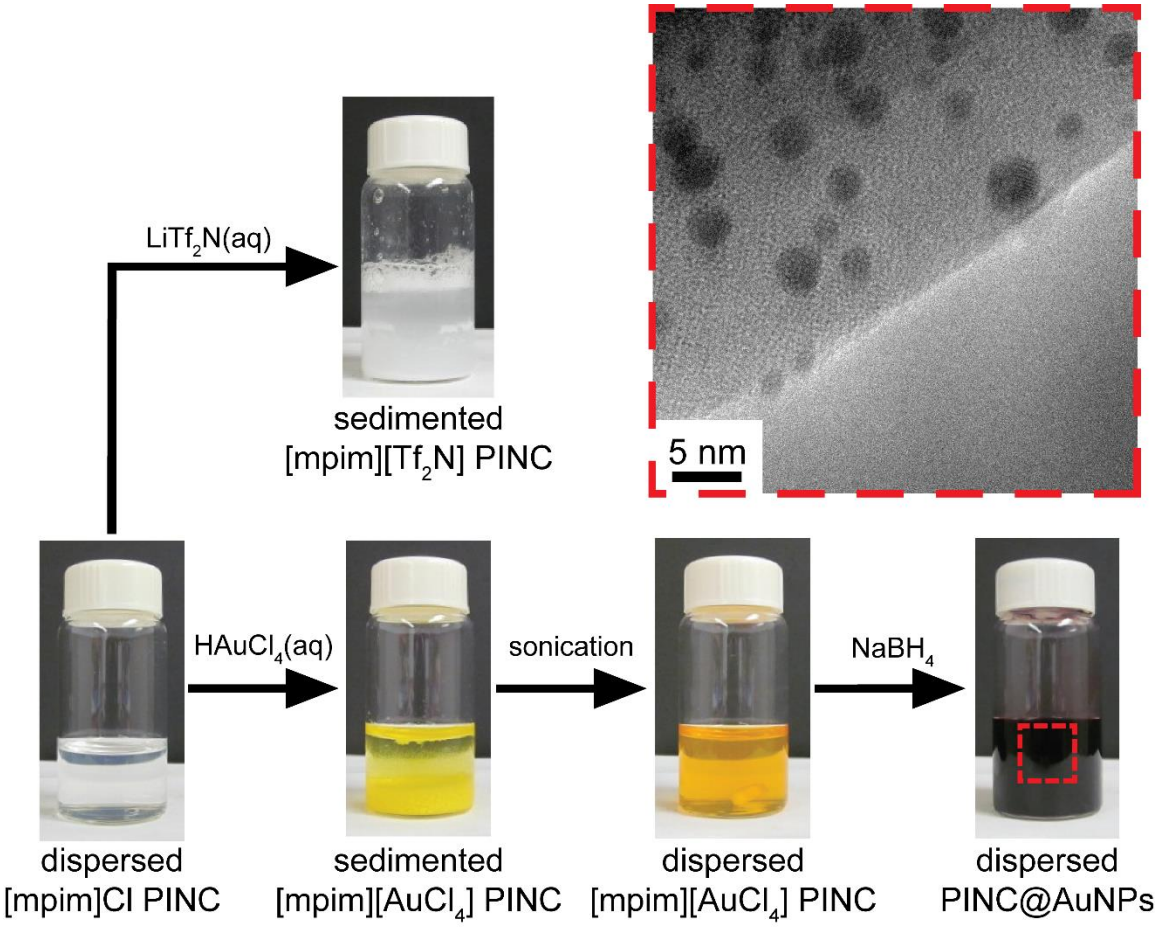

***Figure 4-13**: Aqueous anion exchange of Cl^- for Tf_2N^- (top left) to form an insoluble SIL precipitate [mpim][Tf_2N] PINC, and $AuCl_4^-$ (bottom) to form a sediment of [mpim][$AuCl_4$] PINC, followed by sonication and reduction via sodium borohydride ($NaBH_4$) to create sub-5 nm AuNPs supported on the PINC substrate (top right; image is from the 1.0 mM PINC@AuNPs solution and consists of 2.5 ± 0.7 nm AuNPs).*

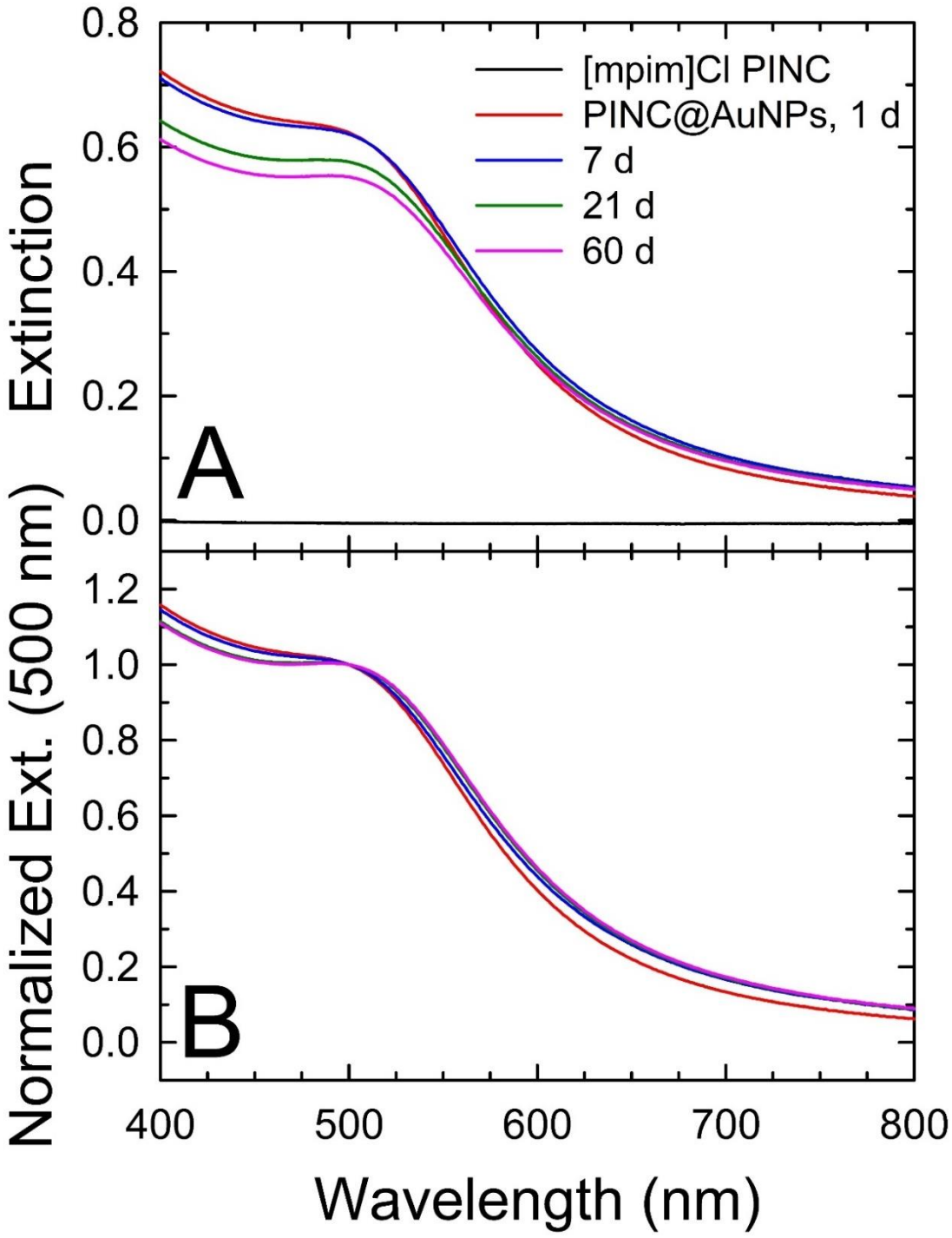

***Figure 4-14**: Stability analysis showing A) the UV–vis spectra showing PINC@AuNP (1.0 mM Au sample, diluted to 0.25 mM for measurement) stability and B) the corresponding normalized spectra. A very slight red shift (~2 nm) was observed in the spectra for samples aged for 21 and 60 d, indicating slight growth in the AuNPs over time.*

Due to the dual role of $NaBH_4$ as reducing/capping agent, it is presumed that these AuNPs should possess a similar surface chemistry to those produced by Deraedt et al.,[34] albeit supported on a PINC surface; accordingly, these AuNPs should perform quite well as heterogeneous catalysts for the model reduction of 4-nitrophenol (4-NP) to 4-aminophenol (4-AP) using $NaBH_4$. In a typical reaction, 2.10 mL of 0.20 mM aqueous 4-NP (0.42 μmol) and 0.90 mL of freshly prepared 100 mM aqueous $NaBH_4$ (90 μmol) were combined in a 4-mL PMMA cuvette (1-cm path length) to yield a yellow solution of 4-nitrophenolate (λ_{max} = 400 nm). Catalysis was initiated by adding 168 μL of 0.025 mM PINC@AuNPs solution (0.0042 μmol Au; diluted from a 1.0 mM PINC@AuNPs stock) to the system (1.0 mol% Au relative to 4-NP), followed by capping and rapid inversion to initiate the reaction. This reaction was performed in triplicate, and further trials were performed using 84-μL, 33.6-μL, and 16.8-μL aliquots of 0.025 mM PINC@AuNPs solution (0.0021, 0.00084, and 0.00042 μmol of Au, respectively) to simulate 0.5, 0.2, and 0.1 mol% Au to 4-NP, respectively. A control experiment was performed using the corresponding concentration of gold-free [mpim]Cl PINC. The reaction kinetics were analyzed via UV–vis spectroscopy by monitoring the decrease in solution absorbance at 400 nm, corresponding to reduction of the 4-nitrophenolate ion. The initial results were astounding: addition of catalyst, equal to 1.0 mol% Au with respect to 4-NP, to the yellow 4-NP/$NaBH_4$ solution resulted in a colorless solution within seconds. We propose that π-π stacking between the imidazolium and 4-NP entities ensures proximity between the reagents and the AuNP surface.[35] The reduction was performed in triplicate using PINC@AuNPs solutions aged for 1 d using 1.0, 0.5, 0.2, and 0.1 mol% Au with respect to 4-NP. The linear correlation of $\ln(A_0/A_t)$, where A_0 is the initial absorbance and A_t is the

time-dependent absorbance, vs. time was plotted (pseudo-first-order) for each catalyzed reaction (Figure 4-15 and 4-16) and the corresponding slopes, representing apparent rates (k_{app}), were calculated. Further, turnover frequencies (TOFs) were calculated by dividing the moles of 4-NP ($n_{4\text{-NP}}$) by the product of moles of Au (n_{Au}) and reaction time (t_{rxn}), corrected for the reaction completion (see equation 2). Note that reaction time is defined here as the time from reaction initiation to the time when the value for $\ln(A_0/A_t)$ equals 3, and that the reaction completion percentage at $\ln(A_0/A_t)$ equals 3 is 95%.

$$\mathbf{TOF} = \frac{\boldsymbol{n}_{\mathbf{4\text{-}NP}}}{(\boldsymbol{n}_{\mathbf{m}})(\boldsymbol{t}_{\mathbf{rxn}})} \times \frac{\mathbf{completion\ \%}}{\mathbf{100}} \quad (2)$$

Similar reductions were performed using 2-month-old PINC@AuNPs, with little change in the catalytic activity. Further, a 10-day-old stock and a 2-month-old stock were separately used to test the recyclability of these PINC@AuNPs as catalysts. As above, 2.10 mL of 0.20 mM aqueous 4-NP and 0.90 mL of freshly prepared 100 mM aqueous $NaBH_4$ were mixed in a 4-mL PMMA cuvette, followed by addition of 2.1 μL of 1.0 mM PINC@AuNPs (representing 0.5 mol% Au with respect to 4-NP). The sample was mixed via inversion and the reduction was monitored at 400 nm using UV–vis spectroscopy. Once the absorbance reached ≥95% completion, 84 μL of 5.0 mM 4-NP was rapidly added and the solution was quickly mixed with inversion and replaced in the instrument. Due to the slight dilution and the reaction progress during mixing, these spectra begin at absorbances below the initial absorbance, which lends some error to the catalytic rate assessment. Three such reduction cycles proceeded without a noticeable decrease in catalytic rate, with the fourth and fifth cycles possessing significantly retarded rates. Therefore, 90 μL of 1.0 M $NaBH_4$ was added in addition to the 4-NP for the sixth and seventh cycles, resulting in a

return of the catalyzed rate to almost the initial values. This implies that the PINC@AuNPs can be recycled at least seven times for this reaction. A control experiment using [mpim]Cl PINC showed no change in absorbance at 400 nm over a 10 min monitoring period, ruling out contribution of Au-free PINC to the catalytic activity.

Our reaction consisting of 0.1 mol% Au possessed a k_{app} of 3.58×10^{-2} s^{-1} and a TOF of 25,000 h^{-1}, the latter of which is, to our knowledge, significantly higher than that of any previously reported gold catalyst. Comparably, a solution of $NaBH_4$-AuNPs produced by the Astruc group in the aforementioned manuscript showed an optimal k_{app} of 9.0×10^{-3} s^{-1} (TOF of 9,000 h^{-1}) when applying a mol% Au of 0.2% and an assumed reaction completion time corresponding to the end of the induction time until $\ln(A_0/A_t) = 2$ (~86.5% completion, although they do not correct for this when calculating TOF). It is worth noting that, using their TOF calculation and reaction completion criteria for our 0.1 mol% Au reaction, we attain a TOF value of 45,000 h^{-1}; however, we do not feel that 86.5% reaction completion is sufficient for this calculation and are instead reporting the TOF at 95% completion with a mathematical correction for the remaining, unreacted 4-NP. In fact, all of the TOFs reported herein greatly exceed the highest catalytic activity reported to date (TOF of just over 12,000 h^{-1}) for bimetallic gold-silver nanoparticles.[36] Our results for these analyses are tabulated in Table 4-1 for comparison purposes, and we also provide examples of literature k_{app} and TOF values in Table 4-2. Catalyst stability is also shown to be quite good, as the loss in catalytic activity for 2-month-old PINC@AuNPs is minimal (Figure 4-16). As an additional control, PINC@AuNPs were prepared using a final [$NaBH_4$] of 10 mM (2 orders of magnitude lower than our typical experimental), resulting in a colloid which expresses similar spectroscopic properties and catalytic efficacy,

indicating that the excess borohydride in our colloid does not impact the catalytic rate. Further study using this PINC@AuNPs solution for other catalytic applications is ongoing.

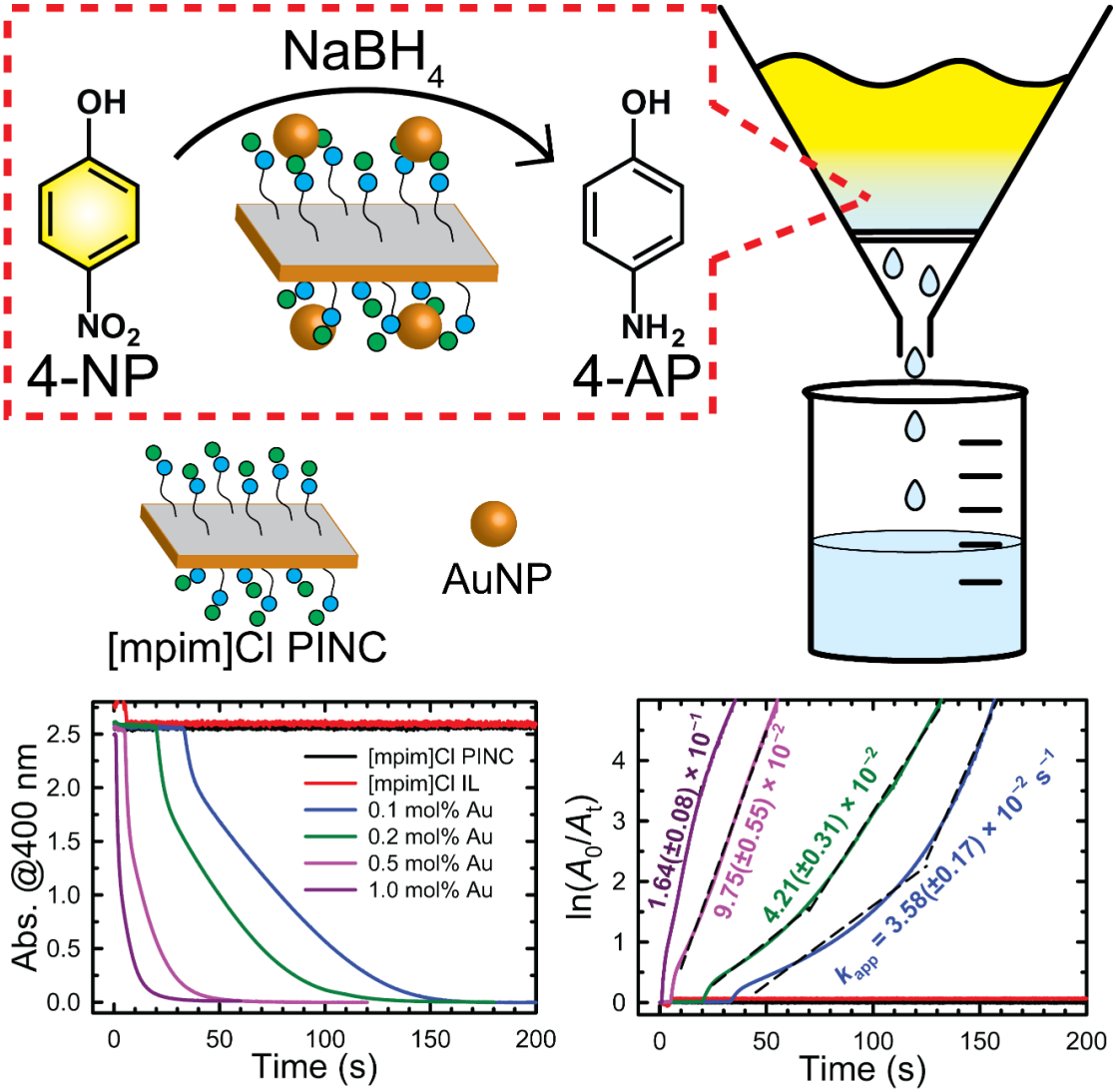

***Figure 4-15**: Top) Schematic of the catalyzed reduction of 4-NP to 4-AP using PINC@AuNPs and $NaBH_4$. Bottom left shows the decrease in absorbance at 400 nm over time, corresponding to loss of the 4-nitrophenolate anion intermediate. At bottom right is a plot of $ln(A_0/A_t)$ vs. time, extracting the slope (k_{app}). Notably, the 0.1 and 0.2 mol% Au reactions appear to be bilinear in nature, and as a result their respective k_{app} values were calculated as an average of the two slopes. The turnover frequency (TOF) of the 0.1 mol% Au reaction is calculated to be 25,000 h^{-1}, which, at the time of publication, is faster than any other Au catalyst reported in literature. All PINC@AuNPs used in these reductions were aged for 1 d prior to use.*

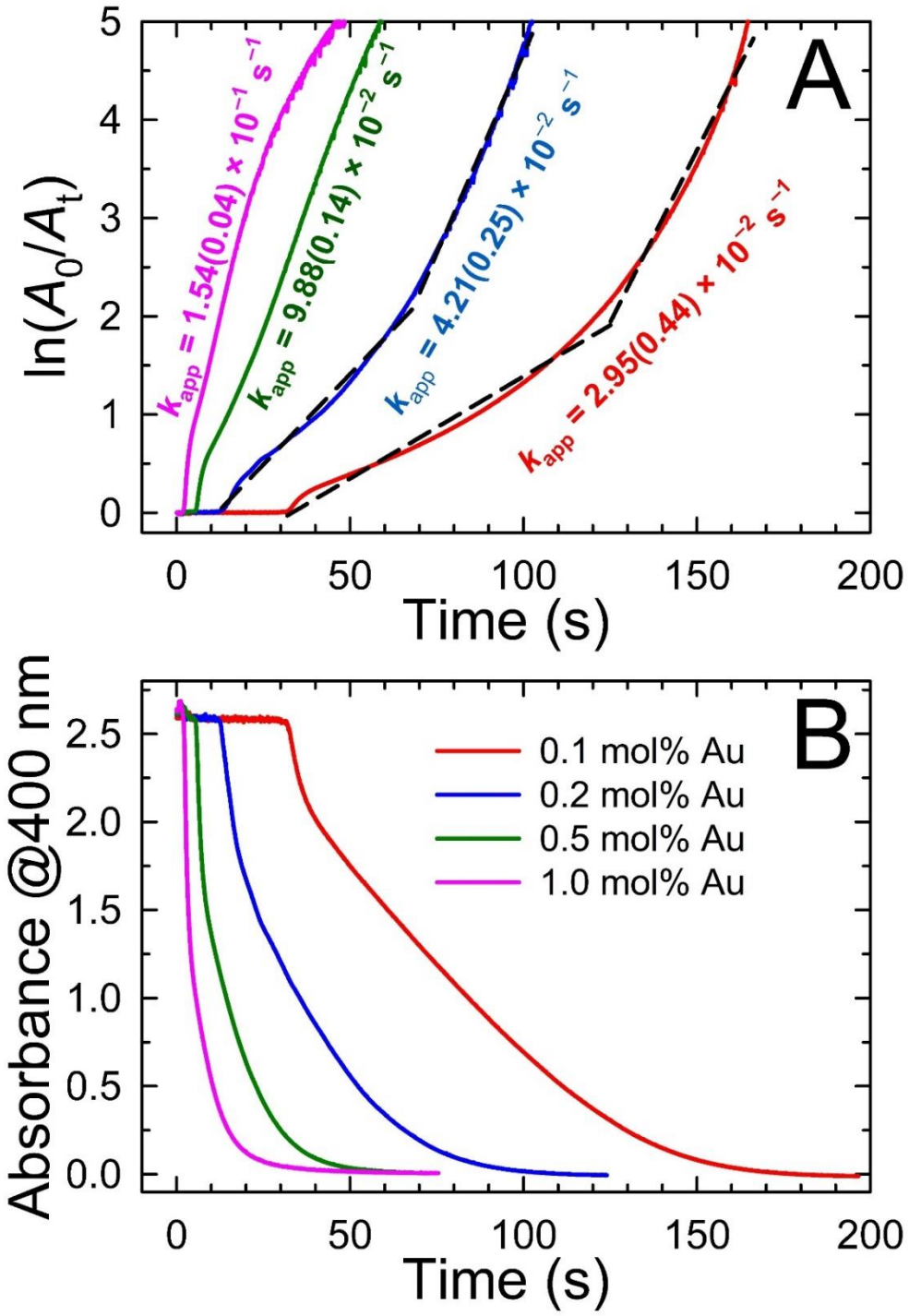

Figure 4-16*: A) Rate plot and B) spectra showing the reduction of 4-NP to 4-AP using $NaBH_4$ and 2-month-old PINC@AuNPs as the catalyst. The apparent rates indicated in A) show good agreement with those obtained from 1-day-old PINC@AuNPs, indicating good catalyst stability.*

The rise in nanoparticle synthesis and application coincides with a concomitant increase in nanowaste, making the recyclability of nanocatalysts of obvious environmental and financial importance. The recyclability of these PINCs@AuNPs was assessed by performing multiple cycles of 4-NP reduction, with each cycle introducing a fresh aliquot of 4-NP to restart the reaction. The catalyzed reduction of 4-NP was performed as above using PINC@AuNPs aged for 10 d (0.5 mol% Au to 4-NP as the reduction using this loading of catalyst exhibited linear reduction kinetics with minimal induction time), except upon reaction completion (assumed when the time-dependent absorbance is <5% of the initial absorbance), 84 μL of 5.0 mM 4-NP was added, the solution was mixed quickly with inversion, and the spectroscopic analysis was continued. What we observed was that the catalytic rate was essentially unchanged for the first 3 cycles, whereas the 4th and 5th cycles showed a large decrease in the catalytic rate (Figure 4-17A). For the 6th and 7th cycles we added 90 μL of 1.0 M $NaBH_4$ alongside the aliquot of 4-NP and observed an increase in the reaction rate, indicating that the rate retardation observed during the 4th and 5th cycles was attributed to a lack of $NaBH_4$. Overall, the excellent recyclability of these PINC@AuNPs catalysts (indeed, a boon shared by many heterogeneous catalysts[37-38]), with a drop in the k_{app} of 26% after 7 cycles (Figure 4-17), is a testament to the use of PINCs for *in situ* AuNP synthesis and stabilization. Further, this recycling study was performed again in its entirety using 2-month-old PINC@AuNPs (Figure 4-17B) with a similar conclusion.

Table 4-1: *Comparison of the apparent catalytic rate (k_{app}), reaction time (t_{rxn}) and turnover frequency (TOF) for each tested mol% Au when performing 4-NP reduction using PINC@AuNPs aged for 1 day (1 d) or 2 months (60 d) as the catalyst.*

mol% Au	k_{app} (s^{-1})	t_{rxn} (h)[a]	TOF (h^{-1})[b]
1.0 (1 d)	$1.64(\pm0.08) \times 10^{-1}$	9.61×10^{-3}	21,000±2,000
1.0 (60 d)	$1.54(\pm0.04) \times 10^{-1}$	$1{,}23 \times 10^{-2}$	18,000±1,000
0.5 (1 d)	$9.75(\pm0.55) \times 10^{-2}$	1.39×10^{-2}	20,000±1,000
0.5 (60 d)	$9.88(\pm0.14) \times 10^{-2}$	1.46×10^{-2}	19,000±1,000
0.2 (1 d)	$4.21(\pm0.31) \times 10^{-2}$	3.11×10^{-2}	18,000±1,000
0.2 (60 d)	$4.21(\pm0.25) \times 10^{-2}$	2.49×10^{-2}	21,000±2,000
0.1 (1 d)	$3.58(\pm0.17) \times 10^{-2}$	3.43×10^{-2}	25,000±2,000
0.1 (60 d)	$2.95(\pm0.44) \times 10^{-2}$	3.69×10^{-2}	24,000±1,000

[a] t_{rxn} is defined here as the time required to achieve 95% substrate turnover.
[b] TOF is calculated as previously reported.[39]

Table 4-2: *Examples of spherical 4-NP catalysts from the literature.*

catalyst	stabilizer	size (nm)	metal (% mol)	k_{app} (s^{-1})	TOF (h^{-1})	Ref.
AuNPs	boron nitride	8.2	635	0.000833	0.00158	[40]
AuNPs	Breynia rhamnoides	25	30	0.00766	0.175	[41]
AuNPs	chitosan	20-24	31.7	0.0561	212	[42]
AuNPs	cellulose nanofibers	5	0.67	0.0059	563	[43]
AuNPs	*Cylindrocladium floridanum*	25	5	0.0267	641	[44]
AuNPs	poly(ethylenimine)	4–13	0.68	0.0070	1,200	[45]
$Au_{0.7}Ag_{0.3}$NPs	[*closo*-$B_{10}H_{10}]^{2-}$	4.2	5	0.200	4,672	[46]
AuNPs	borohydride	3	0.2	0.009	9,000	[34]
AuNPs	[mpim]Cl PINC	2.5	0.1	0.0358	25,000	[a]

[a] This work

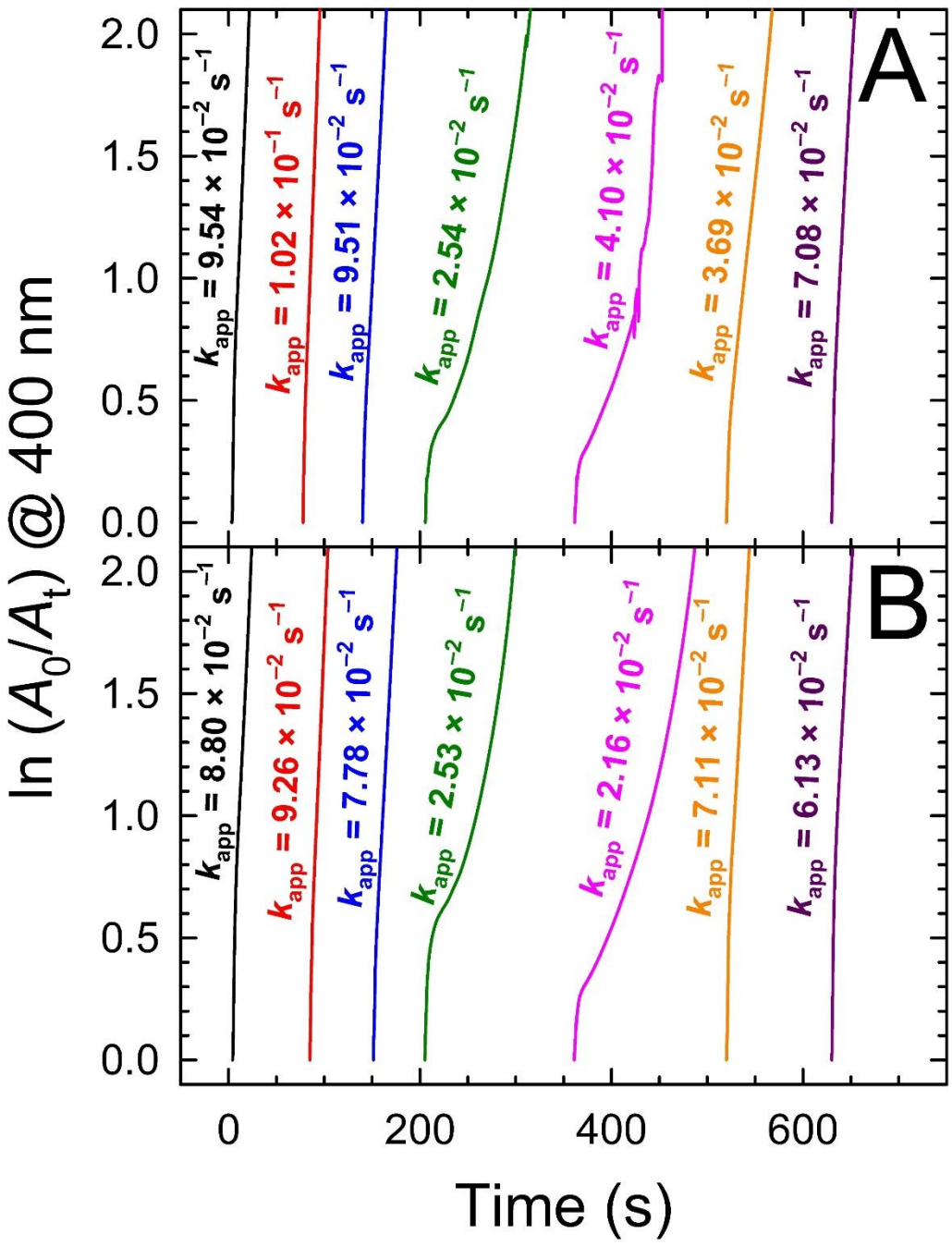

Figure 4-17*: Rate plots showing the change in the apparent rate (k_{app}) imposed by recycling A) 10-day-old PINC@AuNPs and B) 2-month-old PINC@AuNPs for the catalyzed reduction of 4-NP. Both reductions were performed using 0.5 mol% Au to 4-NP. Notably, extra $NaBH_4$ was not added until cycles 6 and 7, resulting in a noticeable increase in the apparent rate. Rate retardations of 26% and 30% were observed for the 10-day-old and 2-month-old PINC@AuNPs after 7 cycles, respectively, attributed in part to the large increases to both ionic character and product concentration in the latter cycles.*

Finally, there is a drive toward bulk production of AuNPs, primarily catalytically active AuNPs, with emphasis on highly-concentrated AuNP solutions to reduce the waste of solvent and reaction time.[47-49] We noticed during TEM analysis of the PINC@AuNPs that much of the PINC surfaces were devoid of AuNPs when [Au] = 1.0 mM and [PINC] = 10.0 mg mL^{-1} in the reaction solution. Thus, we prepared solutions with higher [Au] to increase the number of AuNPs formed. What we observed was quite interesting: AuNP formation and stabilization was obtained up to [Au] = 21.9 mM and [PINC] = 27.4 mg mL^{-1}, with a mild increase in average AuNP diameter, from 2.5(0.7) to 3.9(1.0) nm, evidenced by minor red-shifting of the resulting plasmon band and larger particle sizes observed during TEM analysis (Figures 4-18 and 4-19). While this is not proposed to be the upper concentration limit of Au for stable formation of PINC@AuNPs, it should be noted that the yellow [mpim][$AuCl_4$] PINC precipitate (Figure 4-13) becomes increasingly more difficult to disperse, requiring extensive sonication times (≥30 min) to return to a clear, yellow-orange solution. Simple tuning of the reaction parameters could alleviate these issues, possibly allowing for ultraconcentrated synthesis of extremely catalytically-active supported PINC@AuNPs. We also show that the plasmon band of lyophilized and reconstituted PINC@AuNPs from the 21.9 mM Au solution is nearly identical to that of the parent solution (Figure 4-18), with even a bit of band narrowing, indicating the suitability of these PINC@AuNPs for dry storage. This study is ongoing but contributes significantly to the usefulness of these PINCs for metal nanoparticle synthesis.

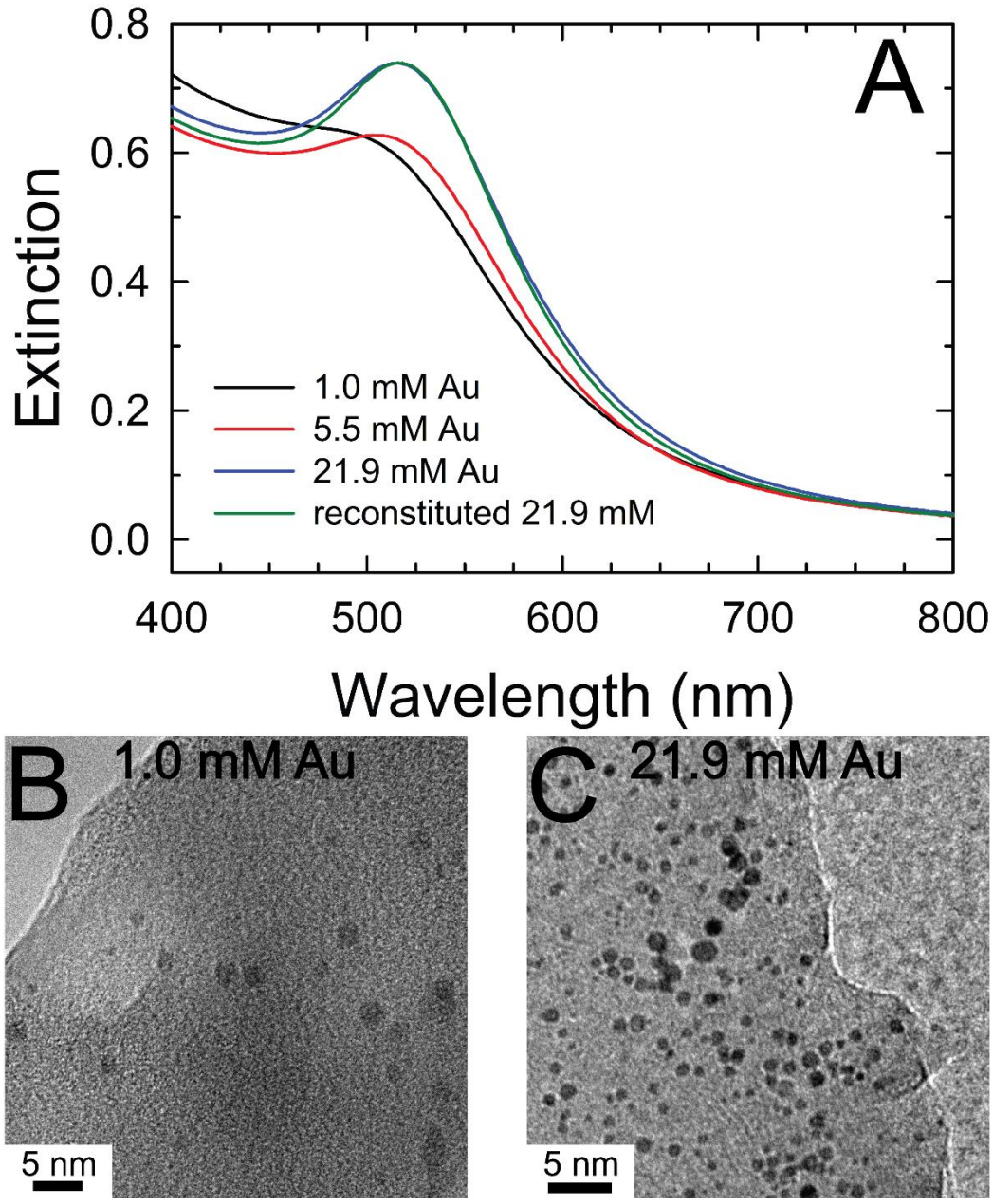

***Figure 4-18**: A) UV–vis spectroscopic analysis of PINC@AuNPs synthesized using several Au concentrations (all diluted to 0.25 mM for measurement) as well as the spectrum of a reconstituted aliquot of previously lyophilized 21.9 mM PINC@AuNPs. A red shift in the LSPR is evident as [Au] increases, indicating an increase particle size. Further, the reconstituted PINC@AuNPs solution is nearly identical to its parent solution, indicating that dry storage followed by aqueous dispersion prior to use is an attractive feature of these supported AuNPs. B) and C) TEM images of 1.0 and 21.9 mM PINC@AuNPs, showing Au-free areas in the former image and possible particle aggregation in the latter. The average particle sizes for each sample are below 5 nm.*

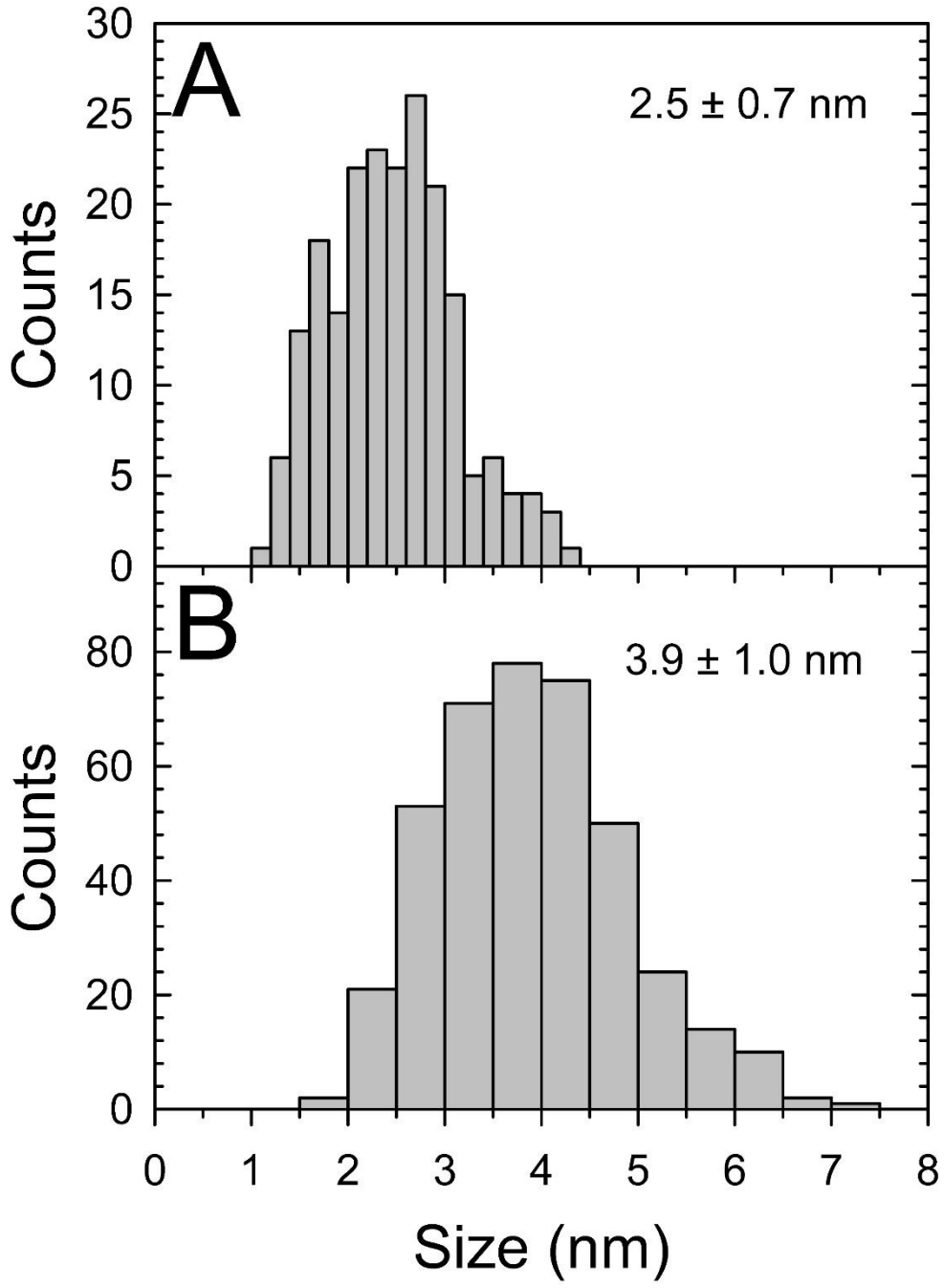

***Figure 4-19**: Histograms representing TEM size analysis of A) 1.0 mM PINC@AuNPs and B) 21.9 mM PINC@AuNPs. As observed in the corresponding UV–vis spectral analysis, particles produced at the lower Au concentration are smaller on average, with no observed particles with diameters larger than 5 nm. Conversely, particles synthesized using a Au concentration of 21.9 mM are about 64% larger, indicating slight aggregation. Both solutions primarily consist of particles smaller than 5 nm in diameter, and no particles with diameters larger than 10 nm were observed.*

In conclusion, we report on the first bottom-up approach toward two-dimensional alkylimidazolium halide-based polyionic nanoclays (PINCs). Through simple metathesis, the halides present on these water-soluble PINCs can exchange with aqueous Tf_2N^- or $AuCl_4^-$ to precipitate white or yellow [mpim][Tf_2N] and [mpim][$AuCl_4$] PINCs, respectively, reinforcing the designer property of these SILs. Further, $NaBH_4$-induced reduction of Au^{3+} in an aqueous dispersion of [mpim][$AuCl_4$] PINC led to the formation of quasi-spherical 2.5±0.7 nm AuNPs supported on the PINC (PINC@AuNPs). These supported PINC@AuNPs, which readily disperse and are colloidally stable for at least 2 months in water, are the most efficient Au catalysts for the borohydride-induced reduction of 4-nitrophenol to 4-aminophenol reported to date, with the added benefit of showing good recyclability for at least 7 cycles of this reaction. The PINC synthesis technique presented herein is a facile approach for creating a myriad of two-dimensional SILs and is integral to the progression of this rapidly expanding field.

Chapter 4 Supplementary Information

Chemicals and Reagents. 1-methylimidazole (M50834, 99%), 1-butylimidazole (348414, 98%), 1-bromooctane (152951, 99%), imidazole (I202, 99%), sodium hydride (223441, 95%), magnesium chloride hexahydrate (M2670, ≥99.0%), 3-chloropropyltrimethoxysilane (440183, ≥97%), potassium bromide (P-5912, ≥99.0%), deuterium oxide (151882; 99.9 atom% D), sodium hydroxide (306576, 99.99%), tetrachloroauric acid (520918, ≥99.9%), and sodium borohydride (213462, 99%) were purchased from Sigma-Aldrich (St. Louis, MO). Ethyl acetate (E195-4, 99.9%) was purchased from Fischer Scientific (Hampton, NH). (3-iodopropyl)trimethoxysilane (SII6452.0) was purchased from Gelest (Morrisville, PA). Absolute ethanol (2716) was purchased from Decon Labs (King of Prussia, PA).

Characterization. X-ray powder diffraction (XRPD) was performed using a Scintag X2 diffractometer with a monochromatic Cu kα (λ=1.5406 Å) source operated at 45 kV and 40 mA with a 2Θ angle pattern. Scanning was done in the region of 3°–70°. Nuclear magnetic resonance (NMR) analysis was performed using either a Bruker Avance-500 MHz spectrometer or a Bruker Avance-600 MHz spectrometer operated at 500 or 600 MHz, respectively (frequencies are appropriately denoted in the related figure captions). Transmission Fourier transform infrared (FTIR) spectroscopy was performed using a Nicolet Nexus 670 FTIR with potassium bromide (KBr) pellets, averaging 32 scans with a resolution of 2 cm^{-1}. Thermogravimetric analysis (TGA) was performed using a TA Instruments Q50 TGA, with a Pt sample pan under 40 mL min^{-1} nitrogen purge. Transmission electron microscopy (TEM) imaging was conducted on carbon-coated

copper grids (Ted Pella, Inc. 01814-F, carbon type-B, 400 mesh copper grid) using a FEI Tecnai F20 microscope operating at a 200 keV accelerating electron voltage. 300-400 individual AuNPs were analyzed for the generation of the particle size histograms. Scanning electron microscopy (SEM) imaging was conducted using a FEI Helios NanoLab 600 FIB/FESEM. Zeta potential measurements were performed in aqueous media using a Malvern Zetasizer Nano ZS in folded capillary zeta cells. An assumed refractive index of 1.6 (talc) was used for all calculations.

Characterization: NMR. ^{1}H nuclear magnetic resonance (NMR) spectra of each silane and PINC produced in this manuscript are presented. For brevity, peak assignments relating to the primary spectra (methylimidazolium iodide silane IL and PINC) are presented in the text here while those relating to other spectra are presented in the text below their respective figures.

The ^{1}H NMR spectrum for methylimidazolium iodide silane (Figure 4-1A) shows peaks for the residual solvent (chloroform) and water (at 2.1 ppm). The following shifts are identified (600 MHz; $CDCl_3$): 9.93 (1H, s, N-C*H*-N), 7.58 (1H, s, CH_3-N-C*H*-CH), 7.43 (1H, s, CH_3-N-CH-C*H*), 4.29 (2H, t, N-CH_2), 4.07 (3H, s, CH_3-N), 3.51 (9H, s, CH_3-O-Si), 1.97 (2H, m, Si-CH_2-CH_2), 0.60 (2H, t, Si-CH_2).

The ^{1}H NMR spectrum for methylimidazolium iodide PINC (Figure 4-1B) shows the presence of residual solvent (ethanol) and reaction byproduct (methanol). The following shifts are identified (500 MHz; D_2O): 7.48 (1H, s, CH_3-N-C*H*-CH), 7.42 (1H, s, CH_3-N-CH-C*H*), 4.19 (2H, t, N-CH_2), 3.89 (3H, s, CH_3-N), 1.96 (2H, m, Si-CH_2-CH_2), 0.50 (2H,

t, Si-CH_2). The proton located at the N-C*H*-N location experiences rapid exchange with D_2O, resulting in its absence in the spectrum.

The ^{29}Si NMR spectrum for [mpim]Cl PINC possesses T1, T2, and T3 peaks at -50.7, -56.5, and -66.5 ppm, respectively.

Characterization: XRPD. It is known that during the formation of 2:1 phyllosilicate clays (such as talc), coordination of silanes around the octahedral Mg complex is limited by the hydrophobicity of the organosilane moieties, resulting in a lamellar structure, stacking of individual clay platelets, and characteristic reflections when analyzed using X-ray powder diffraction (XRPD). Therefore, analysis of the layered structure within the solid [mpim]I PINC was performed (Figure 4-1C), exhibiting reflections which are consistent with the parent Mg silicate (talc; JCPDS card 13-0558), albeit broader, with reflections at 3.93, 2.47, and 1.56 Å corresponding to the clay (020)(110), (130)(200), and (060)(330) reflections, respectively. These peak broadenings are attributed to interlayer disorder caused by the organic moieties present on the PINC surface, a feature which is consistent with the findings of Burkett et al.[23] Furthermore, the d_{001} reflection, which is indicative of interlayer spacing, is not present when measured with a starting angle of 3° 2Θ (29.43 Å), indicating that the interlayer spacing has been increased by steric hindrance and, likely, repulsive surface charges as compared to the spacing and similar reflection in a smaller organic moiety, such as the propyl amine found on aminoclay. These results lend credence to the formation of a lamellar 2:1 phyllosilicate clay with a sterically hindered surface functionality. Comparatively, the butylimidazolium PINC exhibits all of the above reflections with the addition of a (001) reflection at 3.76° 2Θ (23.48 Å) and two sharp

peaks (and an additional small peak) attributed to NaCl at 31.76° and 45.50° 2Θ (and ~56.5° 2Θ).

Characterization: FTIR. Surface and framework vibrational modes within the alkylimidazolium PINC were analyzed using transmission Fourier transform infrared (FTIR) spectroscopy and were found to be consistent with those of a typical magneso-silicate structure, with absorption peaks observed at ~515 cm^{-1} for Mg–O, 1020 cm^{-1} for Si–O–Si, 1170 cm^{-1} for Si–C, 3450 cm^{-1} for O–H, and 3700 cm^{-1} for MgO–H. Furthermore, the organic moieties within IL portion of the alkylimidazolium halide PINCs displayed characteristic peaks resembling those of similar ILs[50] at 1380-1480 cm^{-1} for C–N, 1572 cm^{-1} for C–C, 2937 cm^{-1} for alkyl C–H, and 3000-3150 cm^{-1} for ring C–H. Further, the anion exchange precipitate proposed to be [mpim][Tf2N] PINC showed peaks belonging to both the cation moiety and the Tf_2N^- anion, indicating that metathesis did indeed occur.

Characterization: TGA. Thermogravimetric analysis (TGA) was performed (10 °C min^{-1} from RT to 600 °C; 40 mL min^{-1} N_2 gas flow) to determine the degradation temperatures of the organic moieties in our PINC composites. For [mpim]I PINC (Figure 4-1E), an approximate 9% mass loss while heating to 200 °C is attributed to gradual release and evaporation of water, EtOH, and MeOH trapped within the interlayer structure of the foliated PINCs. Degradation of the methylimidazolium functionality occurs between 250 °C and 450 °C, and accounts for approximately 31% of the overall sample mass, followed by degradation of the propyl chain (~8% mass loss) from 475 °C to 600 °C. The remaining material, accounting for ~52% of the original mass, consists of the Mg silicate backbone

and residual char. The [bpim]I PINC exhibited similar thermogravimetric degradation, with an approximate 6% mass loss before 200 °C attributed to gradual release and evaporation of water, EtOH, and MeOH, 30% mass loss from 225 to 375 °C attributed to degradation of the butylimidazolium functionality, and 20% mass loss from 375 to 600 °C attributed to degradation of the propyl chain. For [opim]I PINC, 7% mass loss before 200 °C is attributed to gradual release and evaporation of water, EtOH, and MeOH while 21% mass loss from 250 to 450 °C is attributed to degradation of the octylimidazolium functionality and 10% mass loss from 475 to 600 °C is attributed to degradation of the propyl chain. Note that the disproportionate mass losses observed for the organic components in [opim]I PINC are tentatively attributed to residual NaCl (presence evident in XRPD, Figure 4-6).

References

1. Baker, G. A.; Baker, S. N.; Pandey, S.; Bright, F. V., An Analytical View of Ionic Liquids. *Analyst* **2005,** *130* (6), 800-808.

2. Zhao, H.; Baker, G. A.; Wagle, D. V.; Ravula, S.; Zhang, Q., Tuning Task-Specific Ionic Liquids for the Extractive Desulfurization of Liquid Fuel. *ACS Sustain. Chem. Eng.* **2016,** *4* (9), 4771-4780.

3. Berthod, A.; Ruiz-Ángel, M. J.; Carda-Broch, S., Ionic Liquids in Separation Techniques. *J. Chromatogr. A* **2008,** *1184* (1), 6-18.

4. Han, X.; Armstrong, D. W., Ionic Liquids in Separations. *Acc. Chem. Res.* **2007,** *40* (11), 1079-1086.

5. Ito, A.; Yasuda, T.; Ma, X.; Watanabe, M., Sulfonated Polyimide/Ionic Liquid Composite Membranes for Carbon Dioxide Separation. *Polym. J.* **2017,** *49*, 671.

6. Dupont, J.; de Souza, R. F.; Suarez, P. A. Z., Ionic Liquid (Molten Salt) Phase Organometallic Catalysis. *Chem. Rev.* **2002,** *102* (10), 3667-3692.

7. Wasserscheid, P.; Keim, W., Ionic Liquids - New 'Solutions' for Transition Metal Catalysis. *Angew. Chem. Int. Ed.* **2000,** *39* (21), 3773-3789.

8. He, Z.; Alexandridis, P., Nanoparticles in Ionic Liquids: Interactions and Organization. *Phys. Chem. Chem. Phys.* **2015,** *17* (28), 18238-18261.

9. Antonietti, M.; Kuang, D.; Smarsly, B.; Zhou, Y., Ionic Liquids for the Convenient Synthesis of Functional Nanoparticles and Other Inorganic Nanostructures. *Angew. Chem. Int. Ed.* **2004,** *43* (38), 4988-4992.

10. Bhawawet, N.; Essner, J. B.; Atwood, J. L.; Baker, G. A., On the Non-Innocence of the Imidazolium Cation in a Rapid Microwave Synthesis of Oleylamine-Capped Gold Nanoparticles in an Ionic Liquid. *Chem. Commun.* **2018,** *54* (54), 7523-7526.

11. Monge-Marcet, A.; Pleixats, R.; Cattoen, X.; Wong Chi Man, M., Imidazolium-Derived Organosilicas for Catalytic Applications. *Catal. Sci. Techol.* **2011,** *1* (9), 1544-1563.

12. Boris, V. R.; Irina, G. T., Supported Ionic Liquids in Catalysis. *Russ. Chem. Rev.* **2017,** *86* (5), 444.

13. Riisagera, A.; Fehrmanna, R.; Haumannb, M.; Wasserscheidb, P., Supported Ionic Liquids: Versatile Reaction and Separation Media. *Top. Catal.* **2006,** *40* (1), 91-102.

14. Xin, B.; Hao, J., Imidazolium-Based Ionic Liquids Grafted on Solid Surfaces. *Chem. Soc. Rev.* **2014,** *43* (20), 7171-7187.

15. Riisager, A.; Fehrmann, R.; Flicker, S.; van Hal, R.; Haumann, M.; Wasserscheid, P., Very Stable and Highly Regioselective Supported Ionic-Liquid-Phase (SILP) Catalysis: Continuous-Flow Fixed-Bed Hydroformylation of Propene. *Angew. Chem. Int. Ed.* **2005,** *44* (5), 815-819.

16. Lemus, J.; Palomar, J.; Gilarranz, M. A.; Rodriguez, J. J., Characterization of Supported Ionic Liquid Phase (Silp) Materials Prepared from Different Supports. *Adsorption* **2011,** *17* (3), 561-571.

17. *Supported Ionic Liquids. Fundamentals and Applications*. Wiley-VCH Verlag GmbH & Co. KGaA: 2014.

18. Ferre, M.; Pleixats, R.; Wong Chi Man, M.; Cattoen, X., Recyclable Organocatalysts Based on Hybrid Silicas. *Green Chem.* **2016,** *18* (4), 881-922.

19. Bauer, T.; Stepic, R.; Wolf, P.; Kollhoff, F.; Karawacka, W.; Wick, C. R.; Haumann, M.; Wasserscheid, P.; Smith, D. M.; Smith, A.-S.; Libuda, J., Dynamic Equilibria in Supported Ionic Liquid Phase (SILP) Catalysis: *In Situ* IR Spectroscopy Identifies [Ru(Co)Xcly]N Species in Water Gas Shift Catalysis. *Catal. Sci. Techol.* **2018,** *8* (1), 344-357.

20. Castillo, M. R.; Fousse, L.; Fraile, J. M.; García, J. I.; Mayoral, J. A., Supported Ionic-Liquid Films (SILF) as Two-Dimensional Nanoreactors for Enantioselective Reactions: Surface-Mediated Selectivity Modulation (SMSM). *Chem.–Eur. J.* **2007,** *13* (1), 287-291.

21. Ha, J. U.; Xanthos, M., Functionalization of Nanoclays with Ionic Liquids for Polypropylene Composites. *Polym. Compos.* **2009,** *30* (5), 534-542.

22. Takahashi, N.; Hata, H.; Kuroda, K., Anion Exchangeable Layered Silicates Modified with Ionic Liquids on the Interlayer Surface. *Chem. Mater.* **2010,** *22* (11), 3340-3348.

23. Burkett, S. L.; Press, A.; Mann, S., Synthesis, Characterization, and Reactivity of Layered Inorganic−Organic Nanocomposites Based on 2:1 Trioctahedral Phyllosilicates. *Chem. Mater.* **1997,** *9* (5), 1071-1073.

24. Datta, K. K. R.; Achari, A.; Eswaramoorthy, M., Aminoclay: A Functional Layered Material with Multifaceted Applications. *J. Mater. Chem. A* **2013,** *1* (23), 6707-6718.

25. Ravula, S.; Essner, J. B.; La, W. A.; Polo-Parada, L.; Kargupta, R.; Hull, G. J.; Sengupta, S.; Baker, G. A., Sunlight-Assisted Route to Antimicrobial Plasmonic Aminoclay Catalysts. *Nanoscale* **2015,** *7* (1), 86-91.

26. Wang, Q.; Baker, G. A.; Baker, S. N.; Colon, L. A., Surface Confined Ionic Liquid as a Stationary Phase for Hplc. *Analyst* **2006,** *131* (9), 1000-1005.

27. Lee, J. S.; Wang, X.; Luo, H.; Baker, G. A.; Dai, S., Facile Ionothermal Synthesis of Microporous and Mesoporous Carbons from Task Specific Ionic Liquids. *J. Am. Chem. Soc.* **2009,** *131* (13), 4596-4597.

28. Wang, X.; Dai, S., Ionic Liquids as Versatile Precursors for Functionalized Porous Carbon and Carbon–Oxide Composite Materials by Confined Carbonization. *Angew. Chem. Int. Ed.* **2010,** *49* (37), 6664-6668.

29. Kallury, K. M. R.; Macdonald, P. M.; Thompson, M., Effect of Surface Water and Base Catalysis on the Silanization of Silica by (Aminopropyl)Alkoxysilanes Studied by X-Ray Photoelectron Spectroscopy and 13c Cross-Polarization/Magic Angle Spinning Nuclear Magnetic Resonance. *Langmuir* **1994,** *10* (2), 492-499.

30. Bruneau, M.; Brendle, J.; Bennici, S.; Limousy, L.; Pluchon, S., Talc-Like Hybrids: Influence of the Synthesis. *New J. Chem.* **2020,** *44* (25), 10326-10333.

31. Miller, P. J.; Shantz, D. F., Covalently Functionalized Uniform Amino-Silica Nanoparticles. Synthesis and Validation of Amine Group Accessibility and Stability. *Nanoscale Adv.* **2020**.

32. Achari, A.; Datta, K. K. R.; De, M.; Dravid, V. P.; Eswaramoorthy, M., Amphiphilic Aminoclay–RGO Hybrids: A Simple Strategy to Disperse a High Concentration of RGO in Water. *Nanoscale* **2013,** *5* (12), 5316-5320.

33. Miyamura, H.; Matsubara, R.; Miyazaki, Y.; Kobayashi, S., Aerobic Oxidation of Alcohols at Room Temperature and Atmospheric Conditions Catalyzed by Reusable Gold

Nanoclusters Stabilized by the Benzene Rings of Polystyrene Derivatives. *Angew. Chem. Int. Ed.* **2007,** *46* (22), 4151-4154.

34. Deraedt, C.; Salmon, L.; Gatard, S.; Ciganda, R.; Hernandez, R.; Ruiz, J.; Astruc, D., Sodium Borohydride Stabilizes Very Active Gold Nanoparticle Catalysts. *Chem. Commun.* **2014,** *50* (91), 14194-14196.

35. Hou, C.; Zhao, D.; Chen, W.; Li, H.; Zhang, S.; Liang, C., Covalent Organic Framework-Functionalized Magnetic $CuFe_2O_4$/Ag Nanoparticles for the Reduction of 4-Nitrophenol. *Nanomaterials* **2020,** *10* (3), 426.

36. Larm, N. E.; Thon, J. A.; Vazmitsel, Y.; Atwood, J. L.; Baker, G. A., Borohydride Stabilized Gold–Silver Bimetallic Nanocatalysts for Highly Efficient 4-Nitrophenol Reduction. *Nanoscale Adv.* **2019,** *1* (12), 4665-4668.

37. Hu, H.; Xin, J. H.; Hu, H.; Wang, X.; Miao, D.; Liu, Y., Synthesis and Stabilization of Metal Nanocatalysts for Reduction Reactions – a Review. *J. Mater. Chem. A* **2015,** *3* (21), 11157-11182.

38. Zhang, K.; Suh, J. M.; Choi, J.-W.; Jang, H. W.; Shokouhimehr, M.; Varma, R. S., Recent Advances in the Nanocatalyst-Assisted Nabh4 Reduction of Nitroaromatics in Water. *ACS Omega* **2019,** *4* (1), 483-495.

39. Larm, N. E.; Bhawawet, N.; Thon, J. A.; Baker, G. A., Best Practices for Reporting Nanocatalytic Performance: Lessons Learned from Nitroarene Reduction as a Model Reaction. *New J. Chem.* **2019,** *43* (46), 17932-17936.

40. Roy, A. K.; Park, S. Y.; In, I., Mussel-Inspired Synthesis of Boron Nitride Nanosheet-Supported Gold Nanoparticles and Their Application for Catalytic Reduction of 4-Nitrophenol. *Nanotechnology* **2015,** *26* (10), 105601.

41. Gangula, A.; Podila, R.; M, R.; Karanam, L.; Janardhana, C.; Rao, A. M., Catalytic Reduction of 4-Nitrophenol Using Biogenic Gold and Silver Nanoparticles Derived from Breynia Rhamnoides. *Langmuir* **2011,** *27* (24), 15268-15274.

42. Qiu, Y.; Ma, Z.; Hu, P., Environmentally Benign Magnetic Chitosan/Fe_3O_4 Composites as Reductant and Stabilizer for Anchoring Au NPs and Their Catalytic Reduction of 4-Nitrophenol. *J. Mater. Chem. A* **2014,** *2* (33), 13471-13478.

43. Koga, H.; Tokunaga, E.; Hidaka, M.; Umemura, Y.; Saito, T.; Isogai, A.; Kitaoka, T., Topochemical Synthesis and Catalysis of Metal Nanoparticles Exposed on Crystalline Cellulose Nanofibers. *Chem. Commun.* **2010,** *46* (45), 8567-8569.

44. Narayanan, K. B.; Sakthivel, N., Synthesis and Characterization of Nano-Gold Composite Using Cylindrocladium Floridanum and Its Heterogeneous Catalysis in the Degradation of 4-Nitrophenol. *J. Hazard. Mater.* **2011,** *189* (1), 519-525.

45. Ballarin, B.; Cassani, M. C.; Tonelli, D.; Boanini, E.; Albonetti, S.; Blosi, M.; Gazzano, M., Gold Nanoparticle-Containing Membranes from *in Situ* Reduction of a Gold(Iii)−Aminoethylimidazolium Aurate Salt. *J. Phys. Chem. C* **2010,** *114* (21), 9693-9701.

46. Larm, N. E.; Madugula, D.; Lee, M. W.; Baker, G. A., Polyhedral Borane-Capped Coinage Metal Nanoparticles as High-Performing Catalysts for 4-Nitrophenol Reduction. *Chem. Commun.* **2019,** *55* (55), 7990-7993.

47. Kim, R.; Park, H. S.; Yu, T.; Yi, J.; Kim, W.-S., Aqueous Synthesis and Stabilization of Highly Concentrated Gold Nanoparticles Using Sterically Hindered Functional Polymer. *Chem. Phys. Lett.* **2013,** *575*, 71-75.

48. Ray, D.; Aswal, V. K.; Kohlbrecher, J., Synthesis and Characterization of High Concentration Block Copolymer-Mediated Gold Nanoparticles. *Langmuir* **2011,** *27* (7), 4048-4056.

49. Adhikari, L.; Larm, N. E.; Baker, G. A., Argentous Deep Eutectic Solvent Approach for Scaling up the Production of Colloidal Silver Nanocrystals. *ACS Sustain. Chem. Eng.* **2019,** *7* (13), 11036-11043.

50. Jeon, Y.; Sung, J.; Seo, C.; Lim, H.; Cheong, H.; Kang, M.; Moon, B.; Ouchi, Y.; Kim, D., Structures of Ionic Liquids with Different Anions Studied by Infrared Vibration Spectroscopy. *J. Phys. Chem. B* **2008,** *112* (15), 4735-4740.

Chapter 5: Advancing the Catalytic Activity of Heterogeneous [mpim]Cl PINCs@NPs and Furthering Their Application for Dye Sequestration

4-Nitrophenol (4-NP) is a harmful environmental contaminant and mutagenic found in the waste streams of pesticide, dye, polymer, and pharmaceutical production facilities.[1-4] As a visible light absorbing molecule, 4-NP pollution has a devastating impact on aquatic biomes where visible light-capture can impede floral photosynthesis.[5] Further, The US Environmental Protection Agency labels 4-NP as harmful to human health, assigning an allowable limit of 0.43 μM in drinking water.[6] Several common methods for removal of 4-NP and other similar contaminants involve destruction or conversion via catalyzed reactions,[7-10] sequestration by filtration, absorption, or extraction,[11-13] or oxidative destruction.[14] Notably, separation and destruction are typically wasteful or energy intensive, and so catalytic conversion of 4-NP to an environmentally benign derivative is often preferred. Noble metal nanoparticles, particularly gold and silver nanoparticles (Au- and AgNPs), are excellent examples of electron reservoir redox catalysts capable of accelerating the reduction of 4-NP into the environmentally benign 4-aminophenol (4-AP) using sodium borohydride.[15] In fact, this reduction is a common model reaction for examining and comparing the catalytic efficiency of Au- and AgNPs.[16-19]

In addition to the monometallic Au- and AgNPs, alloyed AuAgNPs are frequently reported to express enhanced catalytic efficiencies for this model reaction.[20] Indeed,

bimetallic nanocrystals are important vehicles for optics, magnetism, and nanocatalysis, including photo- and electrocatalysis.[21-22] Preparing bimetallic NPs also has the benefit of replacing an expensive metal (Au) with a comparatively less expensive component (Ag), thereby increasing the economic value of the catalyst (estimated as molecular turnover frequency per unit cost). These qualities directly benefit the application of these catalysts toward environmental pacification of contaminants, such as dyes and other light-absorbing species, on an industrial scale.

Our group recently reported an exceedingly effective heterogeneous AuNP catalyst for the 4-NP reduction reaction.[23] This heterogenous catalyst comprises borohydride-stabilized AuNPs adsorbed on a two-dimensional 1-methyl-3-propylimidazolium chloride ([mpim]Cl) polyionic nanoclay (PINC), a novel support first reported in the same study. The structure of this support, a 2:1 magnesium phyllosilicate with pendant [mpim]Cl surface moieties connected by the propyl chain à la aminoclay,[24] is permanently charged across the clay surface, making it perpetually dispersible in aqueous environments sans dramatic environmental changes. In addition, the support is known to protect AuNPs even in high concentration synthetic environments (over 25 mM Au and 1 M $NaBH_4$, conditions where many aqueous stabilizing ligands falter) and during lyophilization and reconstitution, making it a notable new material. Further, the PINC imparts an interesting stereoelectronic effect which amplifies the catalytic capabilities of the AuNPs by an order of magnitude over those of similar, unsupported AuNPs. While these heterogeneous catalysts are already admirable in their catalytic capabilities, we aim to investigate the implementation of a bimetallic AuAgNP system to elucidate the most effective and cost-efficient heterogeneous catalyst for nitroarene reduction yet reported. Further, the dense

polycationic two-dimensional surface of unmodified PINCs provides an interesting opportunity for the sequestration of other absorbing molecules, particularly anionic dyes. As this application has not yet been explored for cationic PINCs, we aim to bolster their environmental usability by demonstrating their use for dye sequestration.

Herein, we first combine the novel [mpim]Cl PINC support with a bimetallic synthesis methodology to prepare [mpim]Cl PINC@AuAgNPs. The PINC was prepared as previously reported,[23] and we describe the experimental details regarding the synthesis of PINC and PINC@AuAgNPs below. The as-prepared heterogeneous catalysts are evaluated for their colloidal stability and surface plasmon resonance and are subsequently applied as catalysts for the reduction of 4-NP to 4-AP using sodium borohydride. We evaluate the catalytic activity by means of the apparent rate of reaction (k_{app}) and turnover frequency (TOF), and additionally provide economical assessment of the catalysts in the form of TOF per $US cost of the commercial metal salt precursors and market value of pure metals. Second, we provide impetus for the use of PINCs as dye sequestration platforms by demonstrating their use in the removal of Congo Red (CR), a mutagenic dianion dye, from aqueous solution. Dye adsorption capacity (q_e) is estimated, and the data is fitted to a Langmuir isotherm (loosely linear, complicated in part by the aqueous dispersibility of the PINCs).

The [mpim]Cl silane was prepared by combining 5.0 grams (25.2 mmol) of (3-chloropropyl)trimethoxysilane and 2.3 grams (28.0 mmol) of 1-methylimidazole in a clean, dry 20-mL glass scintillation vial, stirring the mixture (PTFE coated stir bar, 750 rpm) at 75 °C for 5 days. The resulting yellow liquid was rinsed with dry ethyl acetate three times

to extract excess reactants followed by rotary evaporation at 50 °C to obtain the viscous yellow liquid 1-methyl-3-(trimethoxysilylpropyl)imidazolium chloride ([mpim]Cl silane). We provide an in-depth characterization of this product in our previous report.[23] The [mpim]Cl PINC was then prepared by dissolving 0.31 g of $MgCl_2 \cdot 6H_2O$ (1.52 mmol) in 15 g of absolute EtOH in a 100-mL glass round bottom flask, followed by the addition of 0.74 g of [mpim]Cl silane in 10 mL of EtOH. 4.0 mL of 0.5 M aqueous NaOH was added dropwise to the stirring solution, resulting in the formation of a white precipitate of [mpim]Cl PINC. This cloudy mixture was magnetically stirred at 400 rpm, at room temperature and protected from light, for 24 h to ensure reaction completion. The contents of the flask were transferred to a 50-mL Falcon centrifuge tube and rinsed three times using absolute EtOH and centrifugation (9,000 rpm for 15 min, decant the liquid, re-disperse the precipitate in ~20 mL of EtOH via brief shaking, repeat) to obtain the wet [mpim]Cl PINC. The rinsed PINC was lyophilized to obtain a white, dry powder which was stored at room temperature in a lab drawer until use. Detailed characterization of this PINC is provided in our previous report.[23]

Preparation of monometallic Au- and Ag nanoparticles (Au- and AgNPs) and bimetallic Au_xAg_{1-x}NPs (where x = 0.0–1.0 in increments of 0.1) in the presence of [mpim]Cl PINC was performed according to Table 5-1. 100 mg of PINC was dispersed in 8 mL of water in a 20-mL scintillation vial equipped with a magnetic stir bar. While stirring at 750 rpm, an aliquot of 10 mM aqueous $HAuCl_4$ (see Table 5-1 for aliquot volumes) was rapidly added and the resulting yellow solution was left to stir for 1 min. Next, an aliquot of 10 mM aqueous $AgNO_3$ was rapidly added, followed by a 10 s stir period, then rapid addition of 1.0 mL of 0.10 M aqueous $NaBH_4$. The resulting solution quickly turned dark

orange (AuNPs), faint yellow (AgNPs), or light orange (all other Au:Ag ratios, see Figure 5-1). The solution was left to stir for 1 min before being moved to a lab drawer for storage. The final 10 mL solutions contain 1.0 mM metal, 10 mg mL^{-1} (100 mg) [mpim]Cl PINC, and 10 mM $NaBH_4$.

Table 5-1: *Solution preparation methodology for [mpim]Cl PINC@Au_xAg_{1-x}NPs.*

x, where Au_xAg_{1-x}	12.5 mg mL^{-1} PINC (mL)	10 mM $HAuCl_4$ (mL)	10 mM $AgNO_3$ (mL)	0.10 M $NaBH_4$ (mL)
1.0	8.0	1.0	0.0	1.0
0.9	8.0	0.9	0.1	1.0
0.8	8.0	0.8	0.2	1.0
0.7	8.0	0.7	0.3	1.0
0.6	8.0	0.6	0.4	1.0
0.5	8.0	0.5	0.5	1.0
0.4	8.0	0.4	0.6	1.0
0.3	8.0	0.3	0.7	1.0
0.2	8.0	0.2	0.8	1.0
0.1	8.0	0.1	0.9	1.0
0.0	8.0	0.0	1.0	1.0

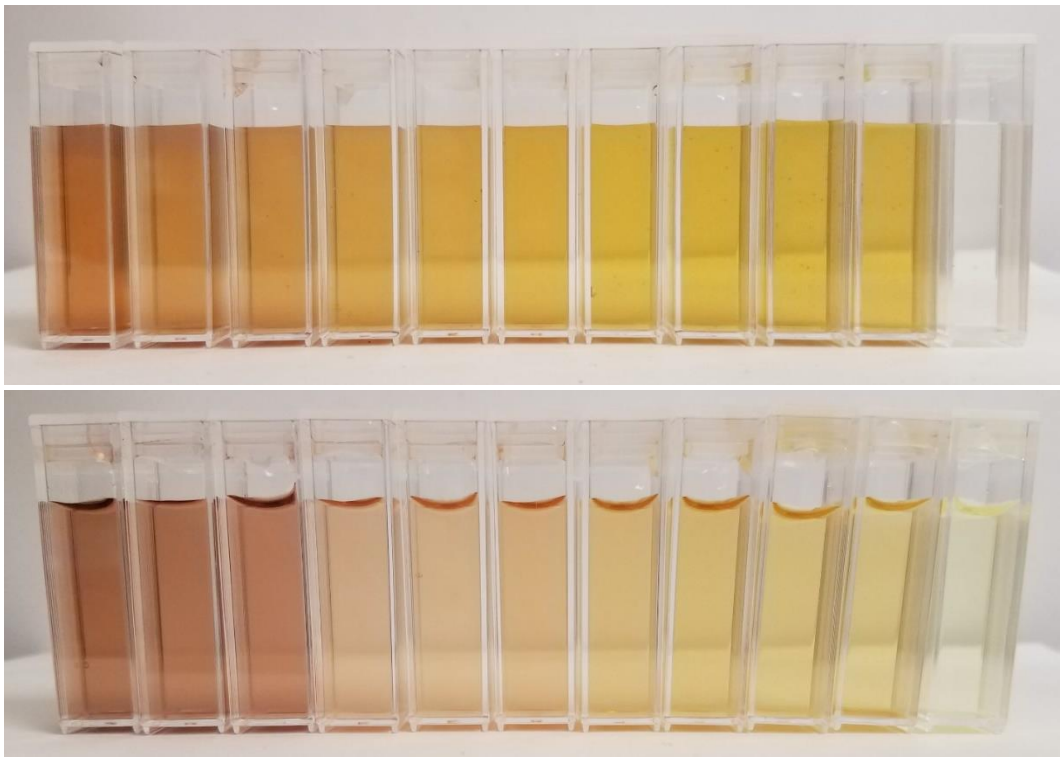

Figure 5-1*: Bimetallic [mpim]Cl PINC@Au_xAg_{1-x}NPs colloids ([metal] = 0.25 mM) at the 1 d (top) and 7 d (bottom) time points. Solutions are ordered based on their x value; from left to right, x = 1.0 (AuNPs) to x = 0.0 (AgNPs).*

The catalytic activity of these [mpim]Cl PINC@Au_xAg_{1-x}NPs was assessed using the model $NaBH_4$-assisted reduction of 4-NP. Specifically, 2.10 mL of 0.20 mM aqueous 4-NP was mixed with 0.90 mL of freshly prepared 0.10 M aqueous $NaBH_4$ in a 4-mL PMMA cuvette (1-cm pathlength) to obtain a yellow solution containing the 4-nitrophenolate ion (λ_{max} = 400 nm). The reaction was initiated upon addition of 2.1 μL of the 1.0 mM aqueous Au_xAg_{1-x}NPs@PINC catalyst (0.5 mol% catalyst to 4-NP), followed promptly by manual inversion to mix before being placed in a UV–vis spectrometer. The final solution concentration was as follows: [4-NP] = 0.14 mM; [$NaBH_4$] = 30 mM; [metal] = 0.00070 mM. The Cary Kinetics program was used to monitor the solution absorbance at 400 nm over time, collecting 10 data points per second. Apparent rates were calculated

using a plot of $\ln(A_0/A_t)$ vs. time, where the slope is the apparent rate k_{app}. A lag time, known as the induction period (t_{ind}), occurs at the beginning of the catalysis runs where dissolved oxygen is used up in a back reaction. We note that the t_{ind} is exceedingly short in analyses when utilizing faster catalysts. In addition, reaction turnover frequency (TOF) was calculated using equation 1, where $n_{4\text{-NP}}$ and n_{cat} are the moles of 4-NP and metal, respectively, t_{rxn} is the reaction time (h) and 0.95 represents our correction for reaction completion. As discussed below, we define t_{rxn} as the time from the end of t_{ind} to the time when the value for $\ln(A_0/A_t)$ equals 3, corresponding to a completion percentage of 95%.

$$\text{TOF} = \frac{n_{4\text{-NP}}}{(n_{cat})(t_{rxn})} \times 0.95 \quad (1)$$

Catalytic activity was assessed as described above after aging each colloid for 3 and 7 d.

While the capability for dye adsorption was evaluated using a variety of anionic, cationic, and neutral dyes in aqueous media, quantification of dye sequestration was performed solely for Congo Red (CR). Calculation of the dye adsorption capacity at equilibrium (q_e) was performed using equation 2, where C_0 and C_e are the initial and equilibrium dye concentrations (mg L^{-1}), respectively, V is the solution volume (L), and m is the mass of sorbent (g).

$$\boldsymbol{q_e} = \frac{(\boldsymbol{C_0 - C_e})\boldsymbol{V}}{m} \quad (2)$$

The localized surface plasmon resonance (LSPR) band for each colloid was measured using UV–vis spectroscopy. As expected, the $LSPR_{max}$ for PINC@AuNPs (x = 1.0) and PINC@AgNPs (x = 0.0) reside near 500 nm and 410 nm (Figure 5-2), respectively,

which agrees with literature values for similar, borohydride-stabilized Au- and AgNPs.[25] For AuAgNPs, the LSPR shifts toward the red with increasing Au content, and presence of single, broad plasmon bands intermediate those of monometallic Au- and AgNPs (or, rather, the absence of the discrete LSPR bands of Au and Ag) indicates the formation of alloyed AuAg bimetallic nanoparticles rather than a physical mixture of AuNPs and AgNPs or an alternate (e.g., core-shell[26]) structure. This outcome is expected based on the nearly identical lattice constants for Au (4.08 Å) and Ag (4.09 Å) which have a difference smaller than the amplitude of the thermal vibrations of the atoms, favoring complete alloy formation. As shown in Figure 5-2C, the LSPR maximum (λ_{max}) is observed to vary in an essentially linear manner with an increase in the Au content, red shifting from about 405 nm for AgNPs to 500 nm for a gold mole fraction of 0.7 (x = 0.7). Indeed, for AuAg alloy NPs, a linear variation of the LSPR peak with compositional fraction has previously been observed and suggested as a general expectation,[27-29] although some nonlinearity (third-order polynominal) has recently been proposed based on models accounting for alloy composition as well as particle size by applying Mie theory.[30-31] Red-shifting and a decrease in extinction of the plasmon band is observed over time in all spectra, a common phenomenon attributed to particle ripening. Select samples (x = 0.7, 0.5, 0.3, and 0.0) were dipped on carbon-coated copper grids and imaged using transmission electron microscopy (TEM), visualizing the PINC substrate coated in small, sub 5 nm NPs (Figure 5-3 and 5-4). At least 300 NPs were counted for each sample to create the representative histograms. Average NP sizes were measured to be 2.8 ± 0.7 nm, 3.7 ± 1.0 nm, 4.2 ± 1.1 nm, and 3.1 ± 0.7 nm for the x = 0.7, 0.5, 0.3, and 0.0 samples, respectively. We note that these sizes are

universally larger than those of the monometallic [mpim]Cl PINC@AuNPs (2.5 ± 0.7 nm as discussed in our recent report[23]).

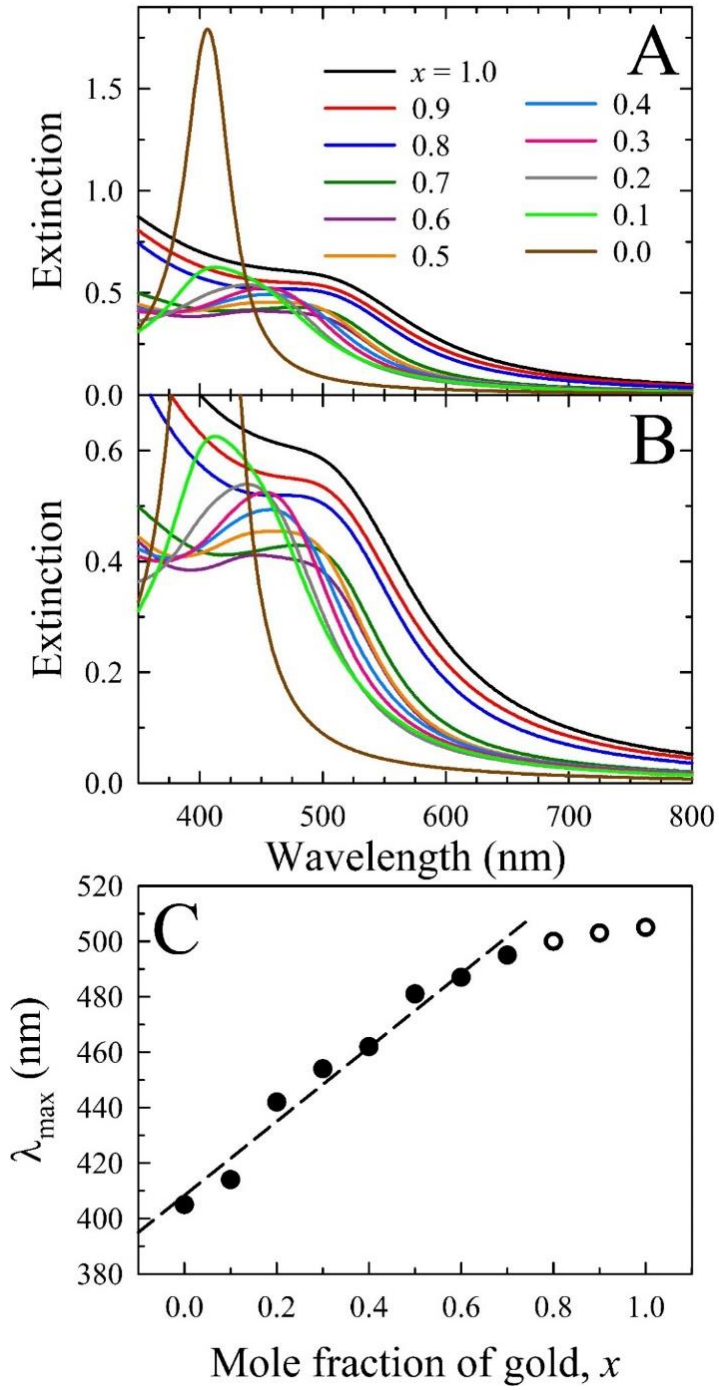

***Figure 5-2**: UV–vis spectroscopic assessment of the LSPR band for [mpim]Cl PINC@Au$_x$Ag$_{1-x}$NPs colloids after 7 d of aging, where (A) shows the full spectra and (B) is more focused to show spectral differences between x values. The legend in panel A also*

applies to panel B. In panel C, we show the LSPR max (λ_{max}) for each x value, where closed circles represent defined peaks and open circles represent an estimation of the LSPR due to the presence of a broad shoulder.

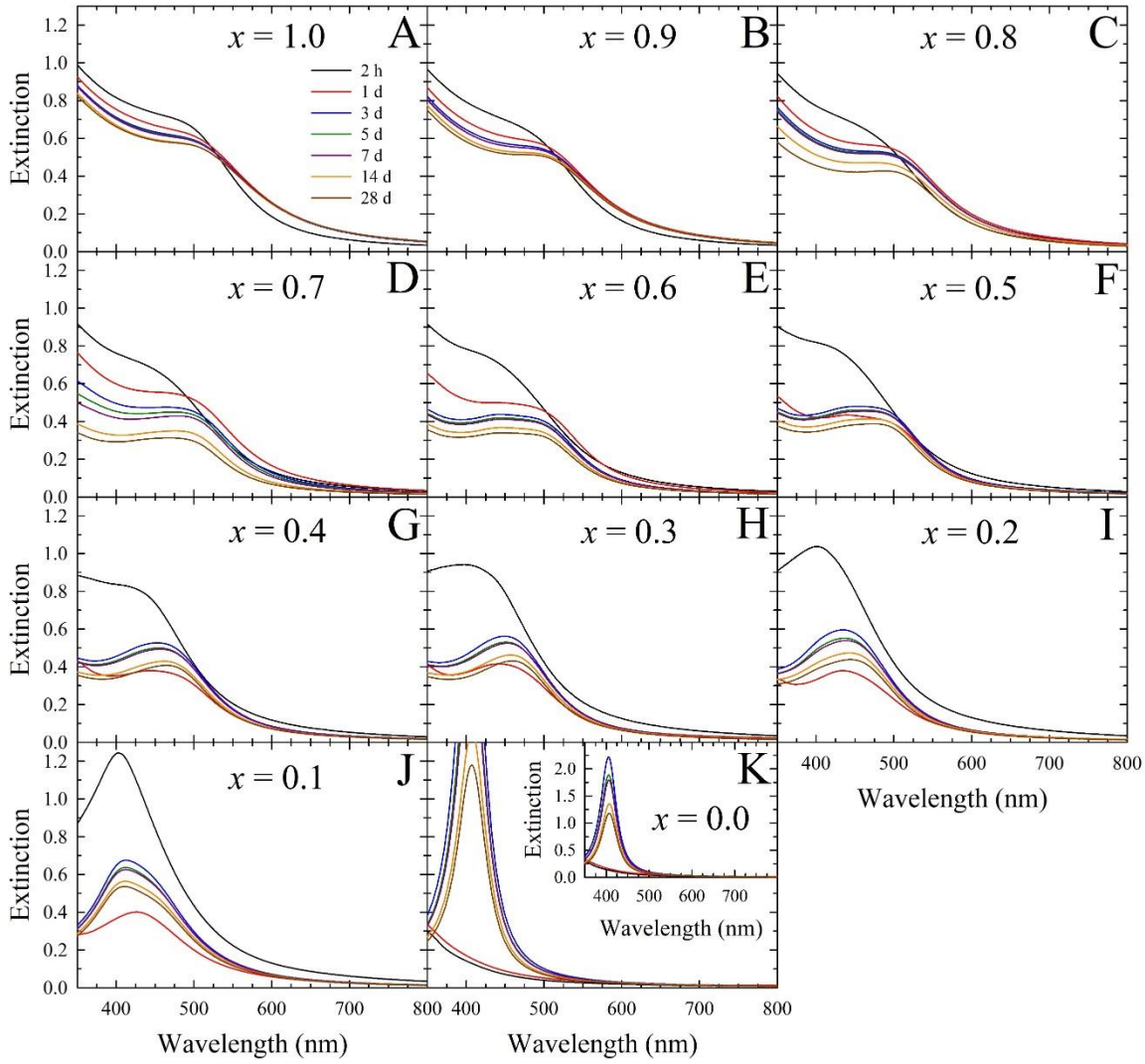

***Figure 5-3**: UV–vis spectroscopic stability assessment of [mpim]Cl PINC@Au_xAg_{1-x}NPs. The legend in panel A applies to all panels. The [mpim]Cl PINC@AgNPs in panel K exhibit a large plasmon growth after storage for 1 d, necessitating the use of an inset to properly show the plasmon band. LSPR band evolution is more pronounced for colloids containing higher ratios of Ag, and most samples experience particle ripening across a 1-month time frame.*

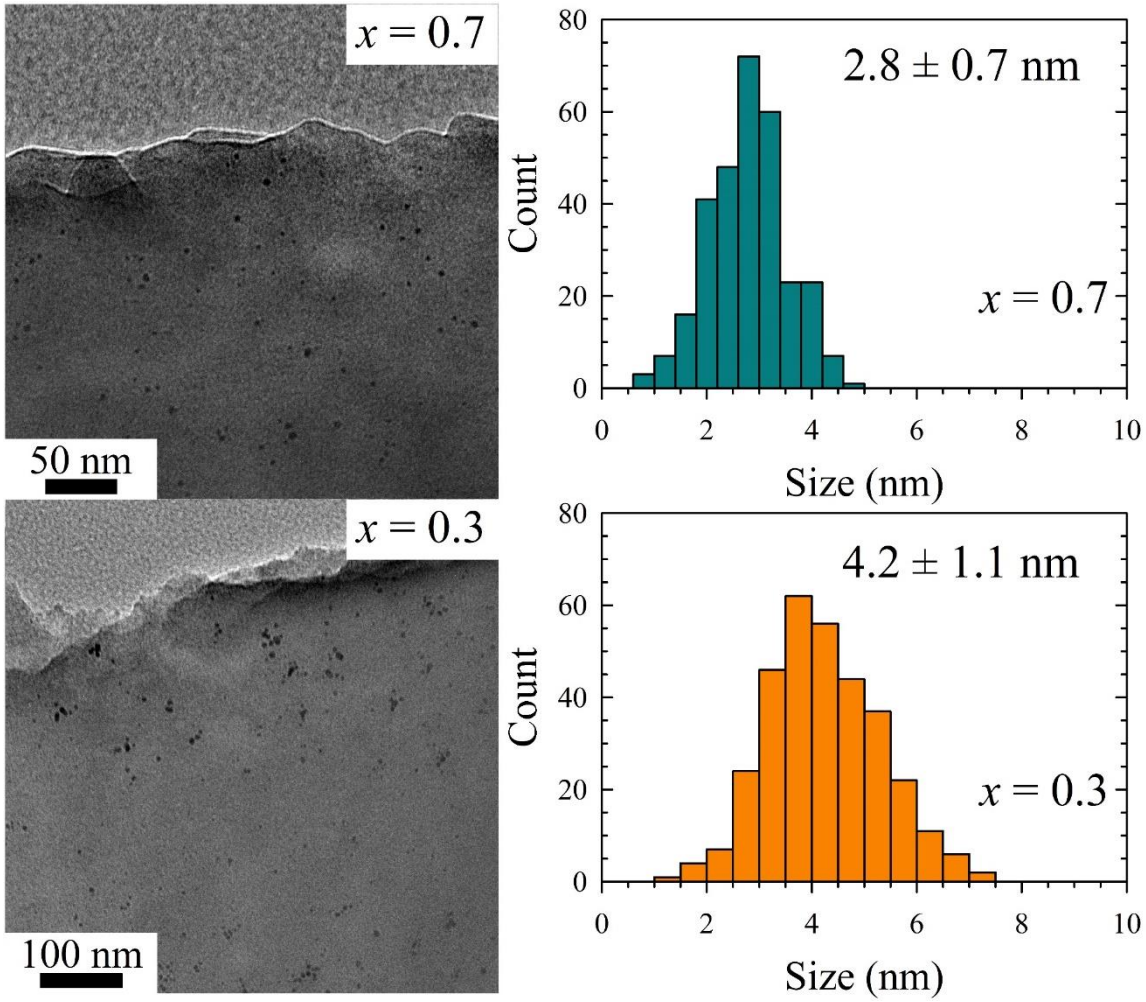

***Figure 5-4**: Representative TEM images and particle size histograms of the x = 0.7 (top panels) and x = 0.3 (bottom panels) bimetallic [mpim]Cl PINC@Au_xAg_{1-x}NPs solutions.*

The atomic composition of the $x = 0.7$ bimetallic NPs was elucidated using energy-dispersive X-ray spectroscopy (EDS) spot analysis, and the Au and Ag contents were determined to be 76.5 and 23.5 atom%, respectively (Figure 5-5). The minor discrepancy between the as-measured and expected Au : Ag atomic ratio of 70 : 30 is attributed to low X-ray counts due to the diminutive size of the NPs.

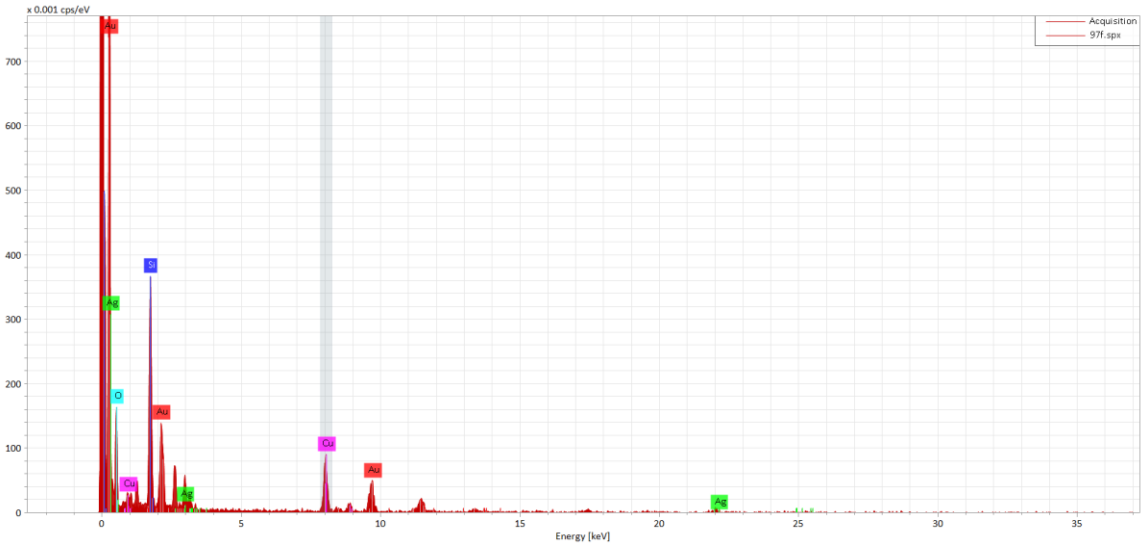

***Figure 5-5**: EDS spectrum for the x = 0.7 intermetallic sample confirming the presence of Au and Ag in a 76.5 : 23.5 atom% ratio, respectively. The inset is expanded to show the area of interest (Au and Ag).*

The reduction of 4-nitrophenol (4-NP) to 4-aminophenol (4-AP) by $NaBH_4$ in the presence of a noble metal catalyst is a well-established model reaction for assessing the catalytic activity of noble metal NPs. This pseudo-first-order reaction provides a linear relationship when comparing $\ln(A_0/A_t)$ versus time, where A_0 and A_t are the initial and time-dependent absorbance values, respectively. The slope of this correlation is equal to the apparent catalytic rate (k_{app}). While many researchers report k_{app} as a comparator, we additionally report reaction turnover frequency (TOF) for each catalyst, a value which provides a simple route for comparing catalysts from different studies. Here, we calculate TOF as previously described in our other report[16]: by dividing the moles of the reaction precursor (4-NP) by the product of the moles of catalyst (noble metal) and the reaction time (h), then correcting for reaction completion as shown in equation 1. The TOF calculation invites discrepancy in the literature as to the definition of "reaction time"; here, we use the time required to attain a $\ln(A_0/A_t)$ value of 3, which is equivalent to 95% reaction

completion. We have previously reasoned that this criterion provides a suitable comparison benchmark for future work while alleviating problems emanating from instrument noise.[16] We note that the t_{ind} is excluded when measuring t_{rxn}, a practice which we have adopted as it ignores the exceedingly long and irreproducible t_{ind} values observed for AgNPs (noting that these long induction periods are absent from recycles where dissolved O_2 is in short supply).

The 4-NP reduction reaction was performed using PINC@Au_xAg_{1-x}NPs colloids aged for both 3 and 7 d to assess short-term catalyst stability (Figures 5-6 through 5-8), revealing similar TOF values at each time point (usually within a standard deviation; Table 5-2). Measurable differences larger than a standard deviation between these TOF values are attributed to particle ripening over time, and we note that all catalysts, aside from the monometallic AgNPs and x = 0.1 colloid, possess greater TOF values at both time points than any reported unsupported noble metal catalyst that we are aware of (examples of several other published catalysts are provided in Table 5-3). Indeed, the reaction is complete within 30 s for colloids where x = 1.0–0.3, within 50 s when x = 0.2, and within 90 s when x = 0.1. We also wish to point out that the very long induction period for the x = 0.0 sample preludes a rapid reduction of the 4-NP (Figure 5-8), though the overall reaction time is almost 4 min with a TOF value of 3,000 h^{-1}. In Figure 5-9A, we plot the calculated TOF values as a function of x value at both the 3d and 7d time points. Notably, x values from 0.7–0.4 possess similar or higher TOF values than that of monometallic Au (x = 1.0), with the best performer at both time points being the x = 0.7 sample with a TOF of over 33,000 h^{-1} (Table 5-2), higher than any other reported noble metal nanocatalyst to date.

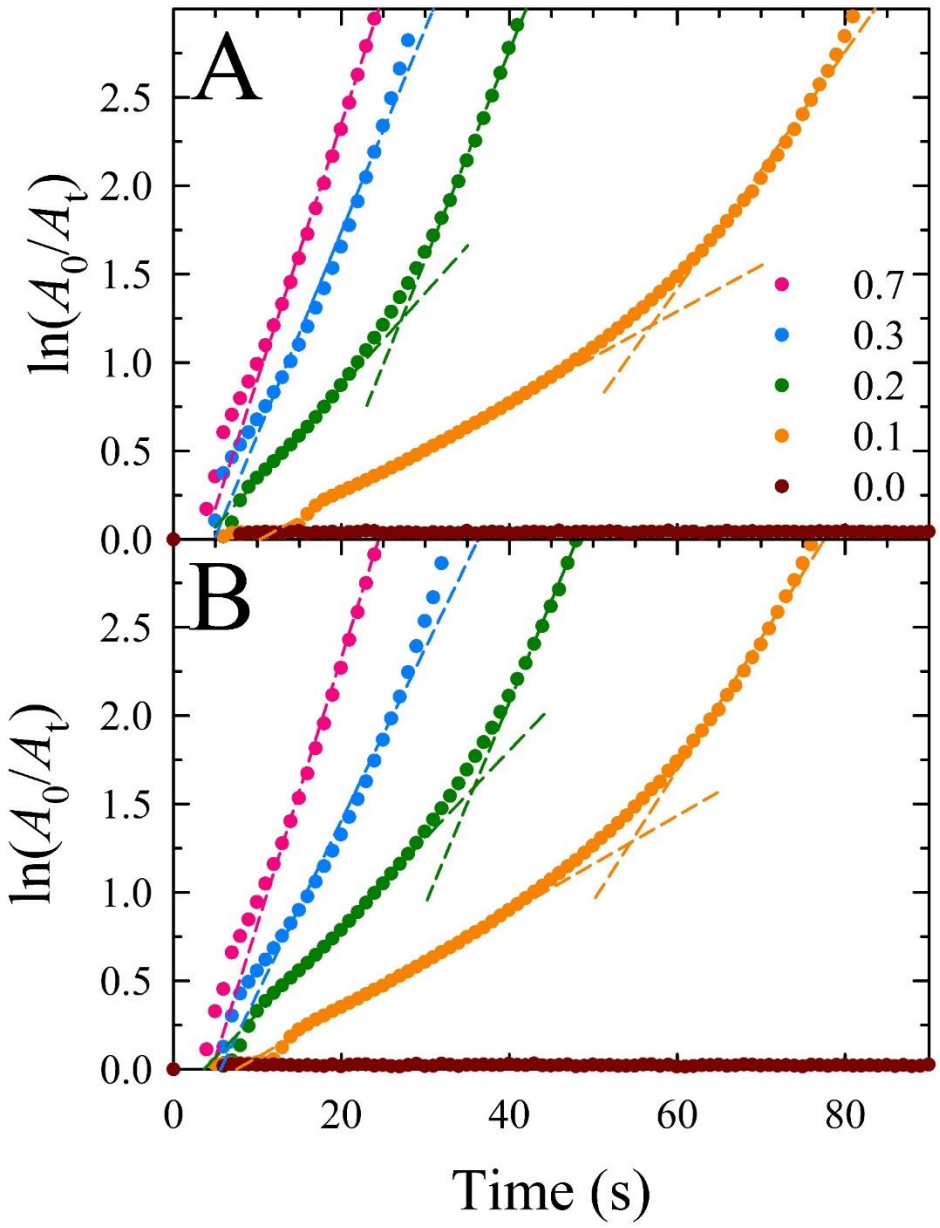

***Figure 5-6**: Rate plots illustrating the catalytic conversion of 4-NP to 4-AP in the presence of [mpim]Cl PINC@Au_xAg_{1-x}NPs and $NaBH_4$. The rate kinetics are determined by plotting $ln(A_t/A_0)$ vs. time, and panels A and B represent colloids aged for 3 d and 7 d, respectively. The legend in A applies to both plots. All colloids where x = 1.0–0.3 fall intermediate within the cyan and magenta plots. For ease of viewing, we exclude the first 5 s of the reaction from these plots due to copious bubble formation. Dashed lines indicate the linear portions used to calculate k_{app}.*

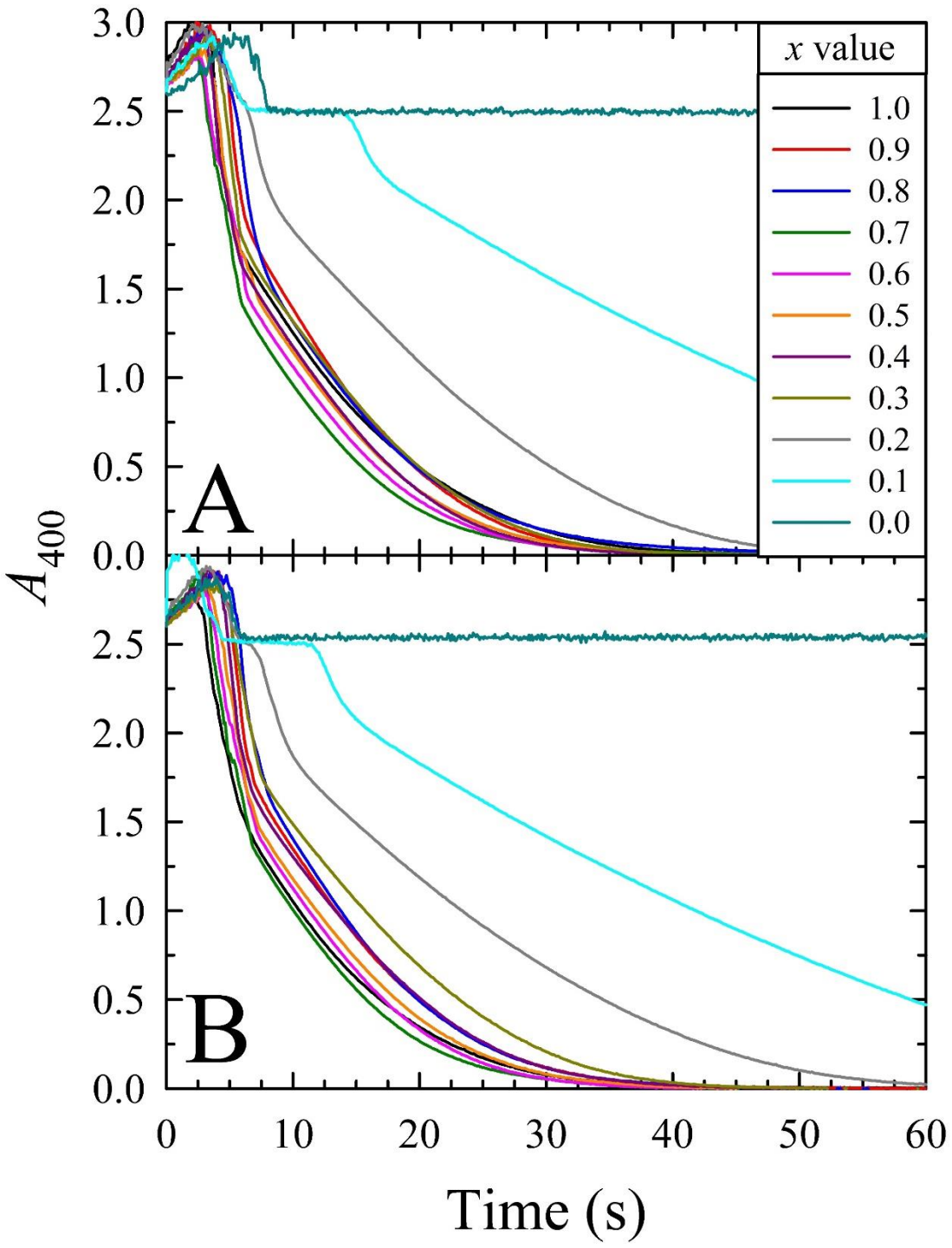

***Figure 5-7**: Plots illustrating the catalytic conversion of 4-NP to 4-AP in the presence of [mpim]Cl PINC@Au_xAg_{1-x}NPs and $NaBH_4$. Panels A and B illustrate the decrease in solution absorbance at 400 nm (400 nm is the characteristic peak of the 4-nitrophenolate intermediate) when utilizing PINC@NPs aged for 3 and 7 d, respectively, as measured using UV–vis spectrometry. The legend in A applies to both panels.*

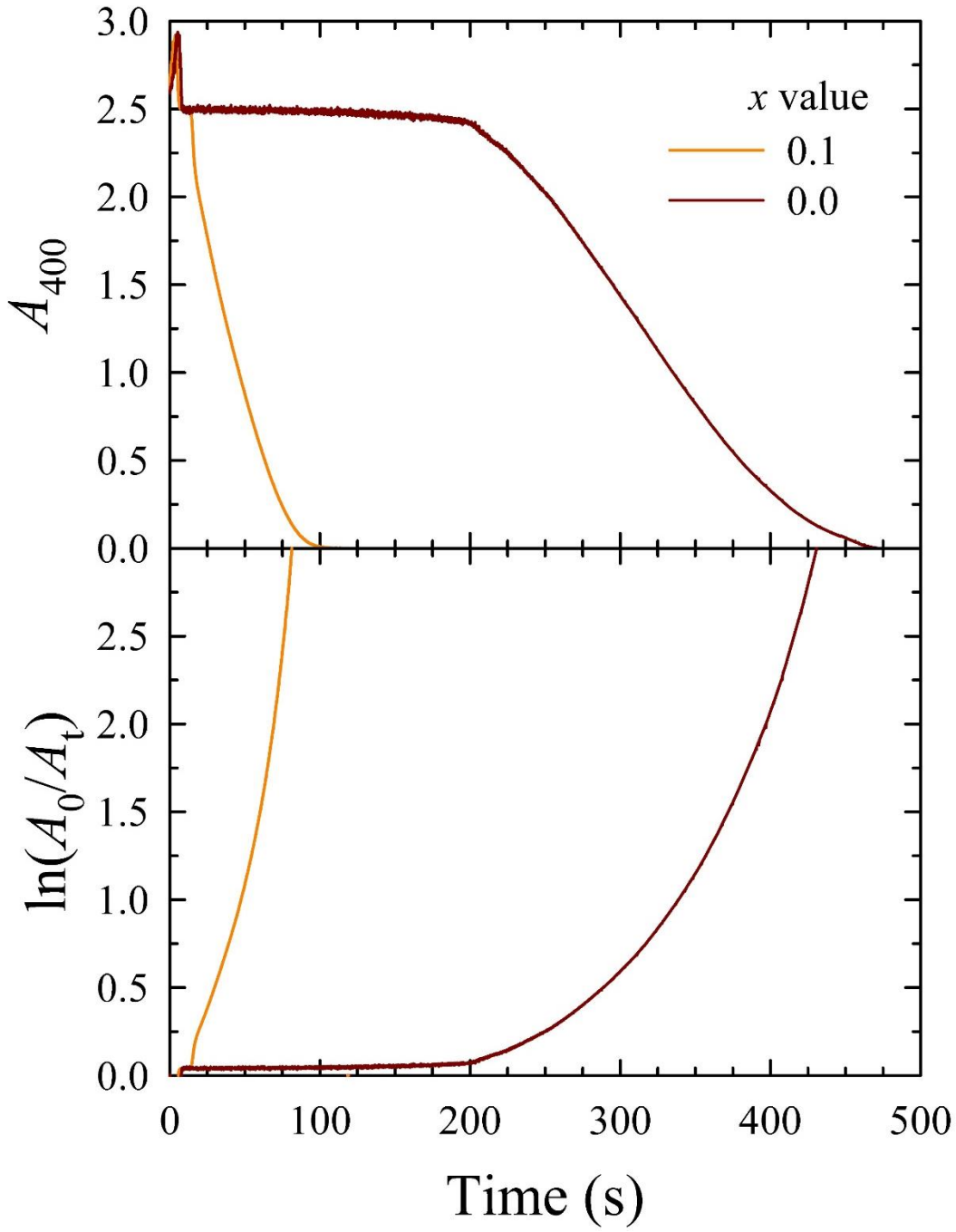

***Figure 5-8**: UV–vis spectra illustrating the much slower catalytic conversion of 4-NP to 4-AP when using PINC@AgNPs aged for 3 d. The top panel and bottom panel display the 4-NP conversion by monitoring absorbance at 400 nm and the $\ln(A_0/A_t)$ rate plot, respectively, with the x = 0.1 sample provided for comparison purposes. The legend in A applies to both panels.*

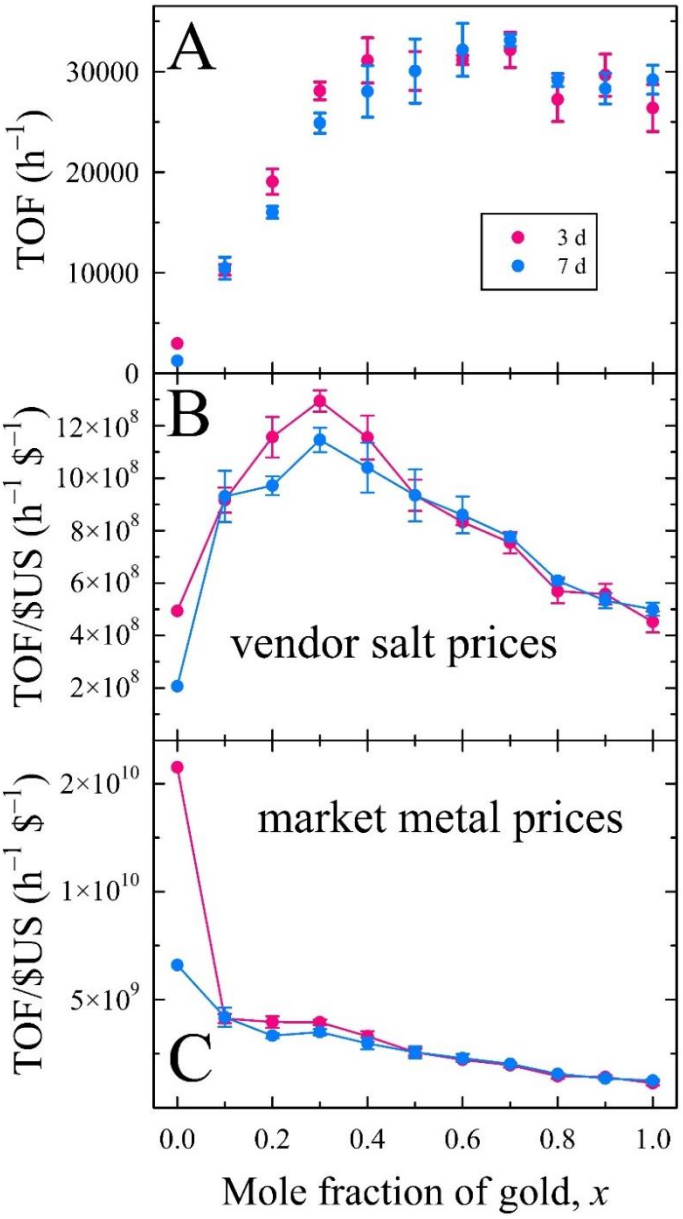

Figure 5-9*: Panel A shows the correlation between TOF and x value in the [mpim]Cl PINC@Au$_x$Ag$_{1-x}$NPs after aging for either 3 or 7 d when using 0.5 mol% metal to 4-NP (excluding t_{ind} from the TOF calculation). Notably, the PINC@Au$_{0.7}$Ag$_{0.3}$NPs possess the highest yet recorded TOF for noble metal nanocatalysts at roughly 33,000 h^{-1}. Panel B provides the TOF per $US (based on the metal salt precursors) versus the x value for each [mpim]Cl PINC@Au$_x$Ag$_{1-x}$NPs solution, while panel C provides a similar assessment using the values of pure metal. Metal salt prices were obtained from Millipore Sigma for one-gram bottles of the respective metal precursors (HAuCl$_4$·3H$_2$O, cat. no. 520918, $US 141.00 for 1 g; AgNO$_3$, cat. no. 204390, $US 26.50 for 1 g), while market metal prices ($US 56.23 per g for Au, $US 0.83 per g for Ag) were obtained from https://www.nasdaq.com/market-activity/commodities/gc%3Acmx (accessed on March 22, 2021).*

Table 5-2: *Induction and reaction time (t_{ind} and t_{rxn}, respectively), apparent catalytic rate (k_{app}), and turnover frequency (TOF) for the reduction of 4-NP using Au_xAg_{1-x}NPs@PINC aged for 3 or 7 d. Note that t_{rxn} is the time from the end of t_{ind} until an $\ln(A_0/A_t)$ value of 3 is achieved.*

x	t_{ind} / s (3 d)	t_{rxn} / s (3 d)	10^1 k_{app} / s^{-1} (3 d)	TOF / h^{-1} (3 d)	t_{ind} / s (7 d)	t_{rxn} / s (7 d)	10^1 k_{app} / s^{-1} (7 d)	TOF / h^{-1} (7 d)
1.0	4.00	26.08	1.11(±0.15)	26,400(±2,300)	3.25	23.48	1.30(±0.07)	29,200(±1,400)
0.9	5.00	23.15	1.25(±0.14)	29,600(±2,100)	5.00	24.23	1.22(±0.07)	28,300(±1,500)
0.8	5.25	25.23	1.15(±0.11)	27,200(±2,200)	5.75	23.47	1.26(±0.06)	29,200(±600)
0.7	3.00	21.32	1.45(±0.09)	32,100(±1,800)	3.75	20.67	1.51(±0.05)	33,100(±600)
0.6	3.25	21.97	1.50(±0.05)	31,100(±500)	4.00	21.38	1.55(±0.14)	32,200(±2,600)
0.5	4.00	22.82	1.38(±0.16)	30,100(±1,900)	4.25	22.93	1.38(±0.23)	30,100(±3,200)
0.4	3.75	22.07	1.37(±0.16)	31,100(±2,300)	4.85	24.58	1.23(±0.18)	28,000(±2,600)
0.3	4.50	24.38	1.25(±0.04)	28,100(±900)	5.25	27.53	9.78(±0.64)	24,900(±1,000)
0.2	5.50	36.02	0.52(±0.05), 1.16(±0.18)[a]	19,000(±1,300)	5.25	42.78	0.50(±0.03), 1.15(±0.19)[a]	16,000(±600)
0.1	15.0	66.55	0.26(±0.02), 0.65(±0.07)[a]	10,300(±500)	11.2	65.90	0.27(±0.04), 0.61(±0.05)[a]	10,500(±1,100)
0.0	200	230.9	[b]	3,000	300	551.0	[b]	1,200

[a] These colloids each give rise to bilinear rate plots at both time points, yielding two k_{app} values (represented as dashed lines in Figure 5-6).
[b] This reaction possessed a long induction period which makes k_{app} difficult to discern.

Table 5-3: *Examples of 4-NP catalysts from the literature.*

catalyst	stabilizer	shape	size (nm)	metal (% mol)	k_{app} (s^{-1})	TOF (h^{-1})	ref.
AuNPs	graphene oxide (GO)	spherical	15–40	2.6	0.19	126	[32]
AuNPs	GO/SiO_2	spherical	3	2.7	0.0051	212	[33]
AuNPs	caffeic acid	spherical	38.6	50	0.0057	13[a]	[34]
AuNPs	PVP; encapsulated	spherical	2.3	2,500	0.0025	0.12	[35]
AuNPs	catechin	variety	16.6	220	0.0015	0.79[a]	[36]
AuNPs	*Aspergillus*	spherical	4.4	8.7	0.0252	329[a]	[18]
AuNPs	GO/tannic acid	spherical	4–20	2.6	0.0031	137[a]	[37]
Au clusters	S-c-C_6H_{11}	spherical	~1 nm	4.2	0.0370	820[a]	[38]
$Au_{0.7}Ag_{0.3}$NPs	[*closo*-$B_{10}H_{10}$]$^{2-}$	spherical	4.2	5	0.200	4,672	[39]
AuNPs	[mpim]Cl PINC	spherical	2.5	0.1	0.0358	25,000	[23]
$Au_{0.7}Ag_{0.3}$NPs	[mpim]Cl PINC	spherical	2.8	0.5	0.151	33,100	this work

[a] These TOF values were calculated using information provided within the referenced work.

In an earlier study, we noted a similar catalytic enhancement for unsupported bimetallic borohydride-stabilized Au_xAg_{1-x}NPs at intermediate compositions.[25] It is important to highlight that the nanosynthetic parameters employed in the current work are

identical to those used earlier, aside from the presence of the dispersed PINC support. The boost in catalytic activity for 4-NP reduction observed for the supported bimetallic nanoparticles compared to the free (unsupported) AuAgNPs dispersed in water suggests a clear synergy between the AuAgNPs and the imidazolium PINC support. Figure 5-10 provides a comparison of the TOF displayed by free AuAgNPs and the corresponding bimetallic nanoparticles supported on the imidazolium PINCs. Aside from monometallic AgNPs, all PINC@AuAgNPs showed enhanced activity over their free counterparts for any given value of *x*. Specifically, we can easily compare the $x = 0.3$ samples due to similarities in NP size between studies (4.6 nm for free NPs, 4.2 nm for PINC-supported NPs). For this sample, we observe a 134% increase in TOF between PINC@$Au_{0.3}Ag_{0.7}$NPs (28,100 h^{-1}) and free $Au_{0.3}Ag_{0.7}$NPs (12,000 h^{-1}). More broadly, AuAgNPs where $x \geq 0.4$ all exhibit an enhancement of over 200% when incorporating PINCs, while monometallic AuNPs show a staggering enhancement of over 4,500%. We note that a clear but much weaker synergistic effect was observed earlier for AuNPs supported on graphene oxide (GO), with the GO support giving rise to a 54% increase in the rate of 4-NP reduction.[37] We reason that surface interactions between Au and the PINC imidazolium π-electrons offer a synergy which is absent when Ag is dominant.[40]

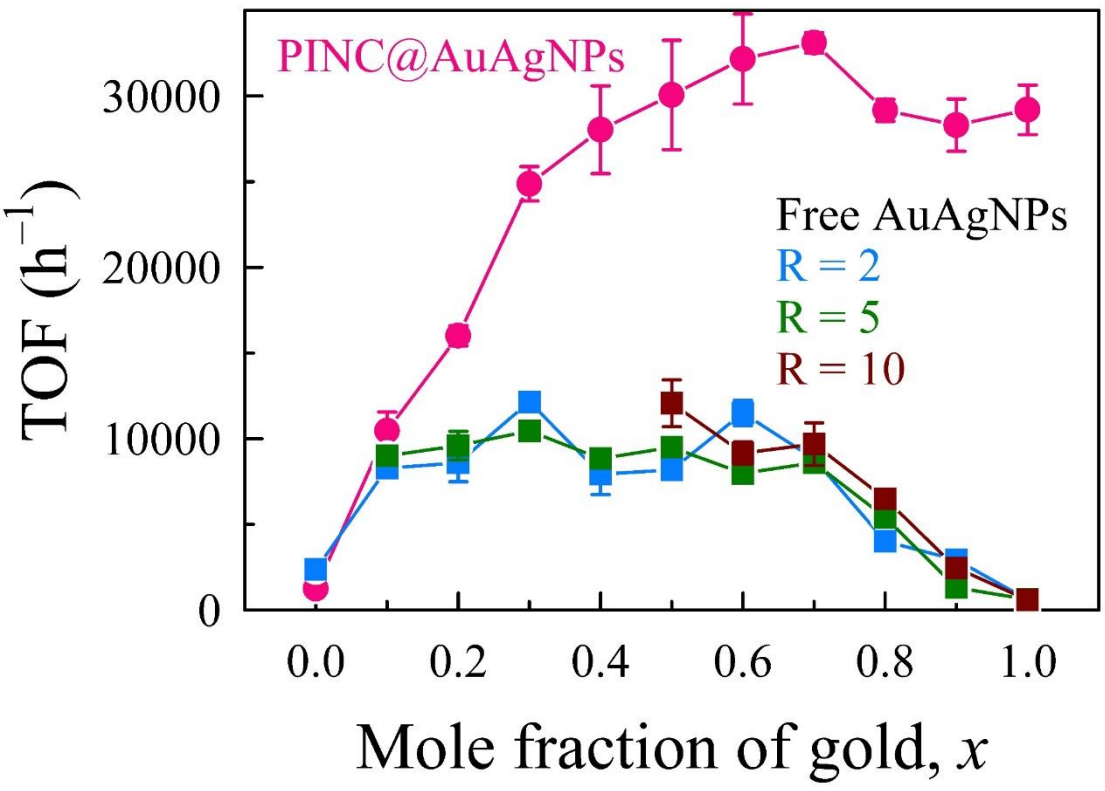

***Figure 5-10**: Plot comparing the TOF values observed for free, borohydride-stabilized AuAgNPs and those generated in situ and supported directly on the [mpim]Cl PINCs. A distinct synergistic effect arising from the PINC support leads to an extreme enhancement in nanocatalytic activity, particularly at higher Au mole fractions. The R value represents the borohydride-to-metal (i.e., Au + Ag) molar ratio; for PINC-supported AuAgNPs, R = 10.*

The exceptional catalytic activities of these supported catalysts are certainly noteworthy (higher activities directly translate to lower quantities of catalyst required to reduce the same quantity of 4-NP in a given time frame), but we also want to compare the economic value of the metal components of the catalyst as a function of TOF per unit cost. Therefore, we have acquired the price for 1-g bottles of both $HAuCl_4 \cdot 3H_2O$ and $AgNO_3$ from Millipore Sigma (accessed in February 2021) and market values for pure metal from Nasdaq (accessed in March 2021) to compare the TOF per $US for the monometallic and bimetallic [mpim]Cl PINC@Au_xAg_{1-x}NPs (Figure 5-9, panels B and C). The highest

activity for the price is exhibited by the x = 0.3 solution, replacing 70% of Au with the much cheaper Ag while maintaining a notable activity of about 28,000 h^{-1} when used 3 d after preparation. With regards to nitroarene reduction (and tangentially, dye pacification and an assortment of other, similar reactions), these catalysts perform at levels far above any other reported noble metal catalyst and at a fraction of the cost, rendering them an immense economical interest for industrial waste cleanup and preservation of aquatic biomes.

Recyclability is a staple of sustainable materials, and herein we demonstrate this property for our x = 0.7 (Figure 5-11) and x = 0.0 (Figure 5-12) catalysts by performing iterative cycles of 4-NP reduction using the same aliquot of catalyst and observing changes in reaction rate. An initial catalyzed reaction was performed to completion as described previously, followed by rapid addition of 84 μL of 5.0 mM 4-NP and 90 μL of 1.0 M $NaBH_4$ to restart the reaction. This restart was repeated for seven recycles (i.e., eight total cycles). In each case, t_{ind} is absent during recycles due to the removal of solubilized O_2 during the initial cycle. Later recycles experience a loss in catalytic activity, down to a minimum of 16,400 h^{-1} for the eighth cycle of the x = 0.7 sample (Figure 5-11). This loss is commonly observed during recycling and is attributed to gradual overloading and poisoning of the nanocatalyst due to excessive quantities of reaction product remaining in solution.[25] The x = 0.0 sample also experiences an enhanced activity upon the removal of the induction period during iterative cycles, achieving a maximum TOF of 9,800 h^{-1} after five catalyst cycles (Figure 5-12). Interestingly, the slowest TOF observed during the eight cycles was that of the initial run (1,900 h^{-1}), which was the only cycle with a notable t_{ind} (nearly 250 s).

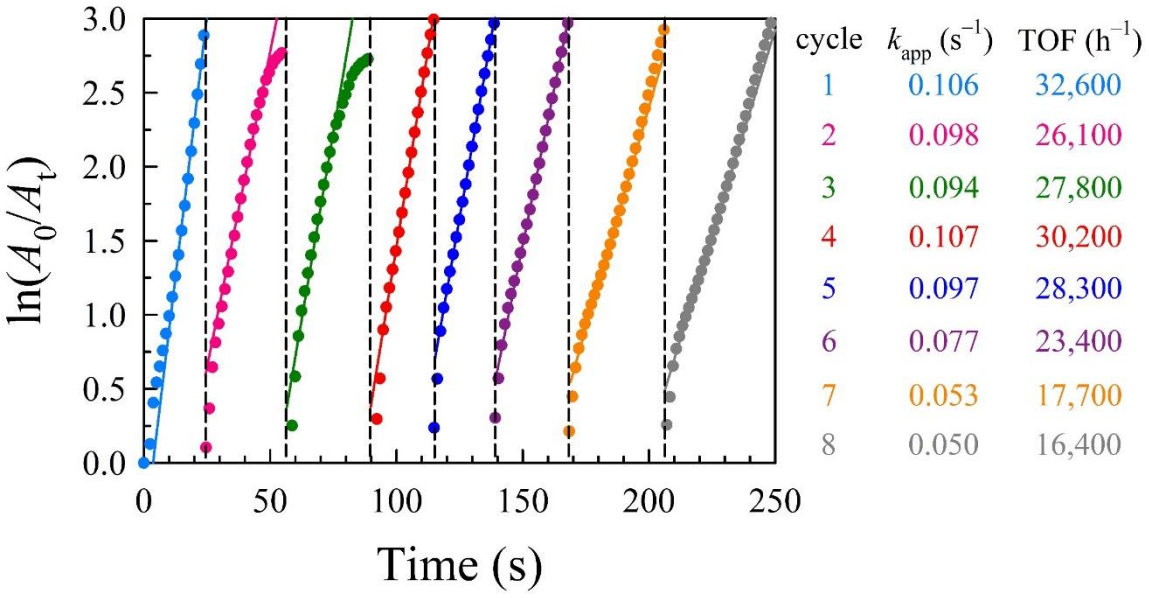

***Figure 5-11**: Rate plot showing recycling of the PINC@Au$_{0.7}$Ag$_{0.3}$NPs catalyst performed by restarting the 4-NP reduction reaction. Relative k_{app} and TOF values are color-coded to their respective rate plots. Cycle four expresses a TOF value of 30,190 h^{-1}, the highest value observed for this study, alluding to the capabilities of this catalyst when utilized under conditions which suppress the induction period (e.g., inert gas flow). The trailing kinetics in cycles 2 and 3 are caused by bubble formation in the light pathway.*

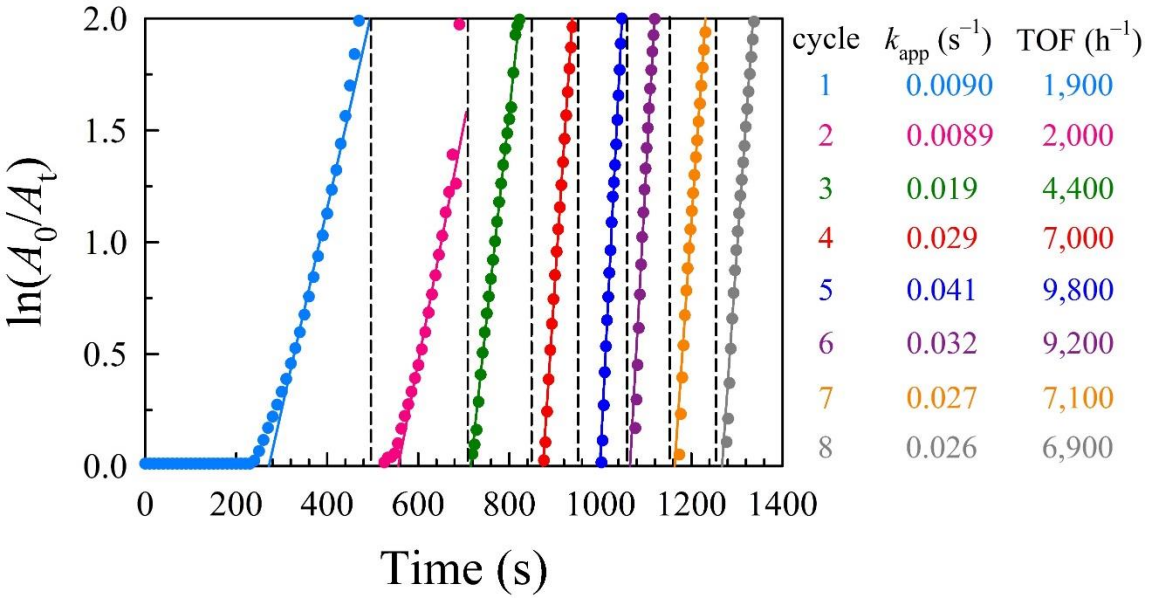

***Figure 5-12**: Rate plot showing recycling of the PINC@AgNPs catalyst performed by restarting the 4-NP reduction reaction. Relative k_{app} and TOF values are color-coded to their respective rate plots. The induction time decreases with each iterative cycle and is absent for cycles 4–8, which are also cycles with the fastest TOF values.*

The robustness of these PINC@NPs nanocatalysts is also demonstrated herein by showing their application for bulk 4-NP reduction. A 0.14 g (1.0 mmol) bolus of 4-NP was dissolved in ~500 mL of water, followed by the addition of 7.57 g (200 mmol) of $NaBH_4$ while stirring to obtain a bright yellow solution. This mixture was treated with 1.0 mL of 1.0 mM PINC@AuNPs (0.0010 mmol Au) solution and magnetically stirred until rendered colorless (~4 min), resulting in a TOF of approximately 15,000 h^{-1}. This reaction represents 0.1 mol% Au to 4-NP and demonstrates the capacity for PINC@AuNPs to perform in environments with a high-concentration of substrate.

Having established an exceptional capacity for reduction of 4-nitrophenol, we expanded the application of PINCs@AuNPs to the catalyzed reduction of an anionic carcinogenic dye, Congo Red (CR), by sodium borohydride. The x = 1.0, 0.7, and 0.0 configurations were compared to their free counterparts, namely borohydride-stabilized AuNPs[41] and salmalia malabarica gum-stabilized AuNPs.[42] We note that neither publication explicitly calculates reaction TOF, so to compare we have extrapolated the provided rate plots (assumed pseudo-first-order linearity through $\ln(A_0/A_t) = 3$ as stated in the referenced material[42]) to estimate TOF values (95% reaction completion). The reduction reaction utilized concentrations comparable to those within the aforementioned studies (specifically, 2.1 mL of 50 μM CR and 0.9 mL of 0.10 mM $NaBH_4$ were added to a PMMA cuvette, followed by 52.5 μL of 1.0 mM catalyst to initiate reduction and achieve a catalyst loading of 50 mol% metal to CR). Upon reduction, the vibrant red solution (monitored at a λ_{max} of 498 nm) becomes visually colorless as CR degrades to 3,4-diaminonaphthalene-1-sulfonate and benzidine. Interestingly, the free borohydride-stabilized AuNPs (TOF = 230 h^{-1}) outperformed all PINC-based composites, with the

PINC@AuNPs possessing a TOF of 27 h^{-1} and the x = 0.7 NPs possessing a TOF of 37 h^{-1} (Figure 5-13), though the gum-stabilized AuNPs possess a lower TOF of ~5 h^{-1}. Further, the x = 0.0 sample (PINC@AgNPs) rapidly precipitated as red flakes in a colorless solution (Figure 5-14). Fluctuations in the reaction spectrum for the x = 0.7 sample imply similar precipitation as PINC-CR complexes pass through the light pathway, though we could not visibly identify the precipitate in this sample. A control of unmodified PINC (i.e., no nanoparticles) was applied under similar reaction conditions to yield a colorless solution with a red precipitate of the PINC-CR complex (Figure 5-14), alluding to the use of the cationic PINC as a dye removal substrate.

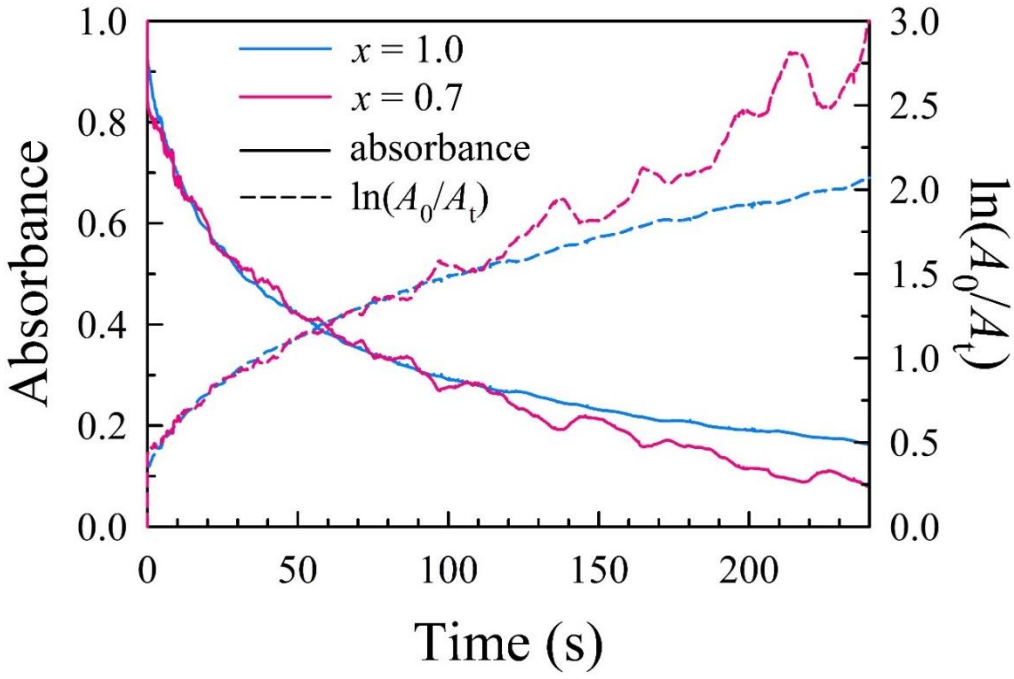

***Figure 5-13**: Absorbance spectra (solid lines) and rate plots (dashed lines) showing reduction of Congo Red by $NaBH_4$ when using PINC@AuNPs and PINC@$Au_{0.7}Ag_{0.3}$NPs as catalysts. The spectra, particularly for the x = 0.7 sample, show fluctuations as the Congo Red is both reduced and adsorbed to the PINC surface. While no precipitation was visually confirmed for these samples, sorption and precipitation does occur with mixtures of Congo Red and PINC (i.e., absent metal nanoparticles) as well as mixtures with Congo Red and PINC@AgNPs.*

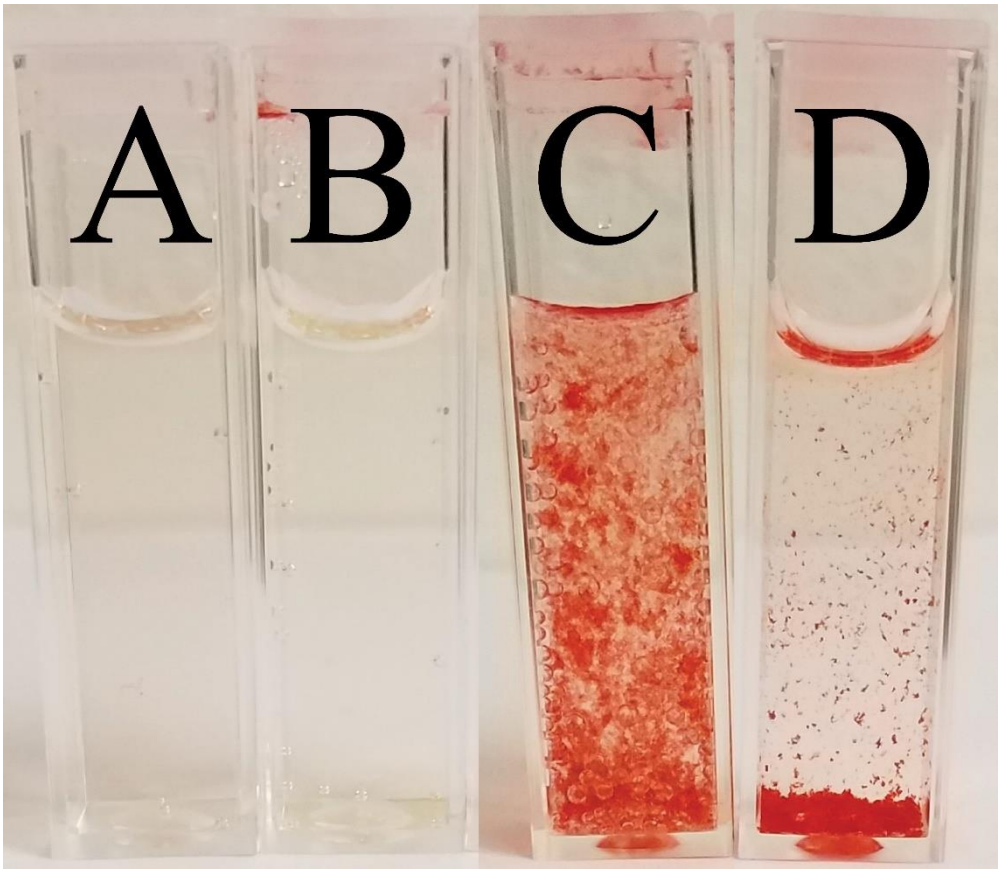

***Figure 5-14**: Photographs of Congo Red reduction solution aged for 30 min in PMMA cuvettes. These solutions were catalyzed by A) PINC@AuNPs B) PINC@$Au_{0.7}Ag_{0.3}$NPs, C) PINC@AgNPs, and D) unmodified PINC (control). Sorption of anionic Congo Red by the cationic PINC causes the emergence of a distinct red precipitate; while this precipitation likely occurs in all samples, we propose that the reduction of Congo Red occurs rapidly in the presence of PINC@AuNPs and PINC@$Au_{0.7}Ag_{0.3}$NPs catalysts such that no visible precipitation is observed before reaction completion. The PINC@AgNPs sample (C) becomes colorless after about 2 h, indicating a continuation of reduction in the precipitate.*

A preliminary investigation was conducted to elucidate the dye adsorption capabilities of the cationic PINC. First, several stocks of 5.0 mM aqueous anionic and cationic dyes were prepared. 100 μL of 10 mg mL^{-1} aqueous [mpim]Cl PINC was combined with 30 μL of 5.0 mM aqueous dye stock (anionic: Congo Red, Rose Bengal, Naphthol Blue Black, Biebrich Scarlet, and Methyl Orange; cationic: Malachite Green, Methylene Blue, Phenosafranin, Crystal Violet, and Mordant Orange 1) in 10-mL glass

vials. The solutions were gently mixed, then 5 mL of acetone was added as an antisolvent to precipitate the PINCs. Control samples were prepared for each dye solution, with a 100 μL aliquot of water acting as a substitute for the PINC solution. In Figure 5-15, we observe dye complexation for solutions comprising PINC and each anionic dye, though Methyl Orange (a carboxylic acid-containing dye) shows only partial complexation. As expected, all cationic dyes do not noticeably adsorb to the cationic PINC due to repulsion between charged moieties (Figure 5-16). All dye chemical structures are provided in Figure 5-17 as a reference. The aqueous dye adsorption rate was further investigated using CR as a model anionic dye. 3.0 mL of 50 μM aqueous CR (0.10 mg) was added to a 4-mL PMMA cuvette, followed by the rapid addition of 100 μL of 10 mg mL^{-1} aqueous [mpim]Cl PINC (1.0 mg). The cuvette was capped, inverted several times to mix, and placed in a UV–vis spectrometer programmed to scan from 400–600 nm every 5 min for 16 h (2 nm resolution) while maintaining a temperature of 25.0 °C using a Peltier accessory. The absorbance profile for CR is relatively stable for the first 5 h of analysis with only minor shifting (Figure 5-18). However, a rapid decrease in absorption occurs at the 5 h mark, indicating the precipitation of the PINC-CR complex. After ~6 h, the solution appears colorless aside from isolated floating red flakes of precipitated PINC-CR complex. While similar in appearance, the profile for a similar analysis at 50 °C occurs in half of the time (Figure 5-18), indicating acceleration of dye adsorption at elevated temperatures. Dye adsorption capacity at equilibrium (q_e) for these samples was estimated as 66.7 mg g^{-1} (that is, mg of CR per g of PINC) using equation 2 above.

***Figure 5-15**: Photograph depicting the anionic dyes in acetone solutions, either in the absence of PINC (left vial) or in the presence of PINC (right vial). Dyes from left to right: Congo Red, Rose Bengal, Naphthol Blue Black, Biebrich Scarlet, and Methyl Orange.*

***Figure 5-16**: Photograph depicting the cationic dyes in acetone solutions, either in the absence of PINC (left vial) or in the presence of PINC (right vial). Dyes from left to right: Malachite Green, Methylene Blue, Phenosafranin, Crystal Violet, and Mordant Orange 1.*

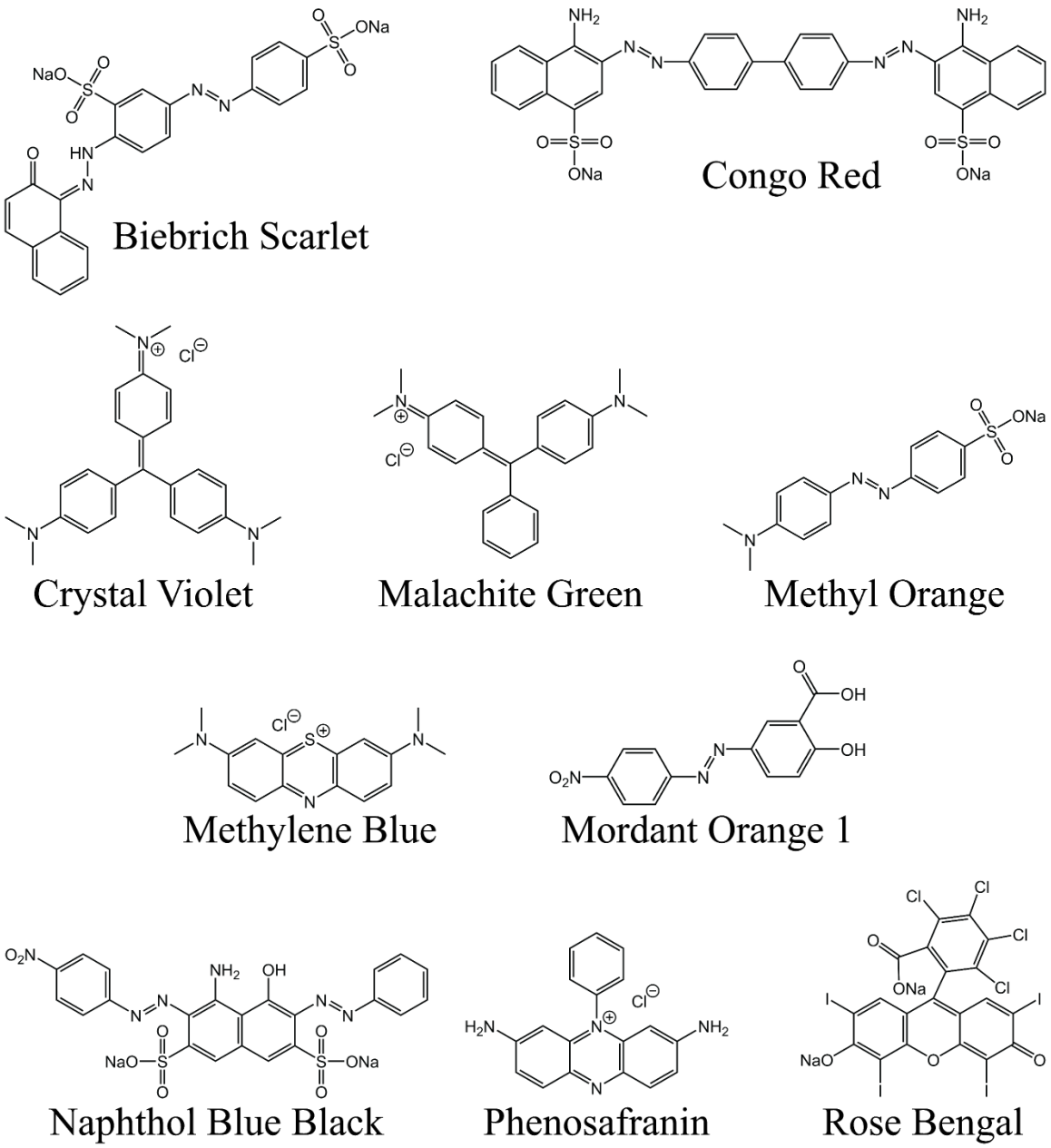

***Figure 5-17**: Chemical structures of all dyes used in the dye sequestration study.*

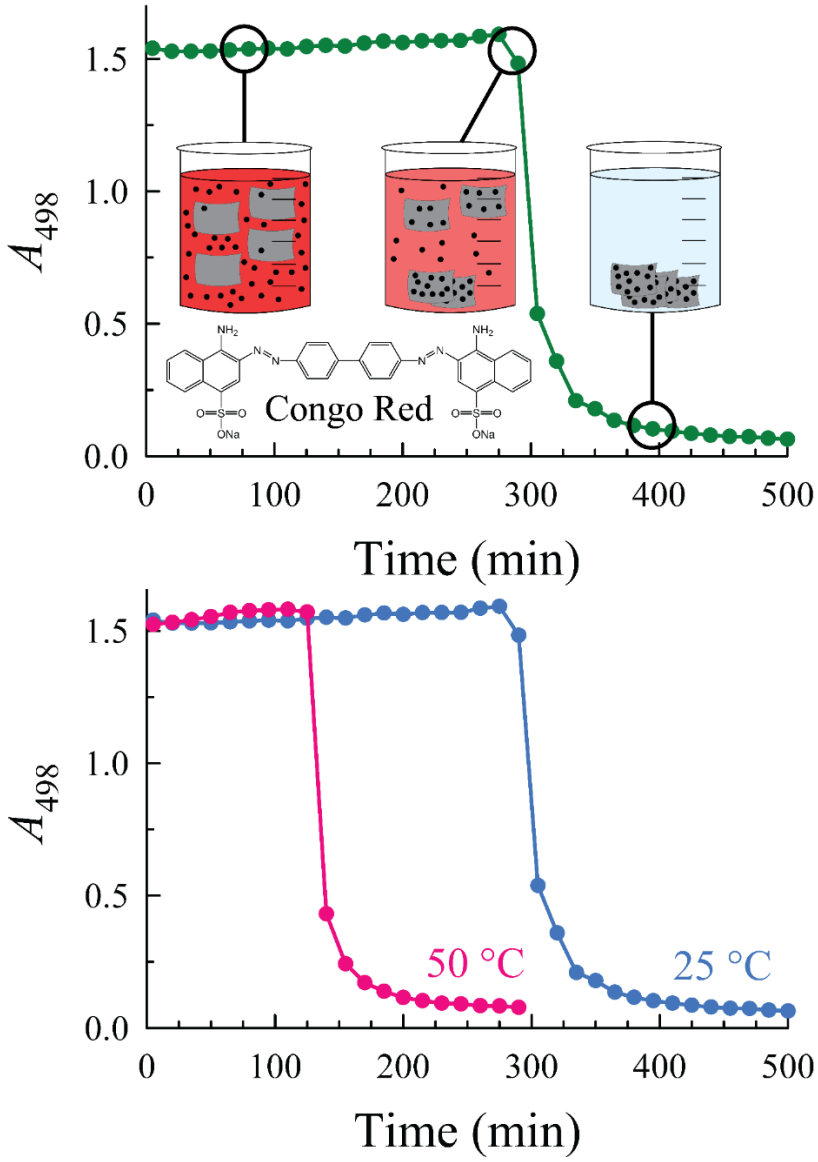

***Figure 5-18**: (Top) Schematic illustrating the adsorption of Congo Red (CR, black dots) onto [mpim]Cl PINCs (grey sheets) over 8 h. The left beaker represents dispersed CR and PINCs, while the center beaker shows extensive interactions and the initial precipitation as the solution absorbance at 498 (λ_{max} for CR) begins to decrease. Finally, the beaker on the right represents a fully precipitated PINC-CR complex, yielding a colorless solution. (Bottom) Temperature-dependent precipitation of the PINC-CR complex, based on absorbance at 498 nm, presented at 25 °C and 50 °C, with accelerated precipitation observed at higher temperature.*

To further elucidate q_e as a function of [CR], we performed an adsorption study by combining aqueous solutions of CR in a range of concentrations while maintaining a

constant PINC concentration. In short, aliquots of 10 mg mL^{-1} aqueous CR were combined with 100 μL of 10 mg mL^{-1} aqueous PINC in 10-mL glass vials followed by dilution to 5.0 mL with water. The recipes for these solutions are provided in Table 5-4. All diluted solutions were shaken by hand for 5 min and then allowed to rest without stirring for 48 h at room temperature or 50 °C (Figure 5-19), after which 1.0 mL of the supernatant was removed and diluted to 3.0 mL for UV–vis analysis. Further, q_e was calculated for each sample (Tables 5-5 and 5-6), revealing a maximum adsorption capacity of 1,180 mg g^{-1} at room temperature (Table 5-5) and 2,620 mg g^{-1} at 50 °C (Table 5-6). A comparison between the q_e results for [mpim]Cl PINC and several literature results (in the form of estimated maximum adsorption capacities, or q_m) is provided as Table 5-7. Unfortunately, the dispersibility of the PINCs complicates attempts to fit the data to a model isotherm for the estimation of q_m (indeed, ideal adsorbents are insoluble in their testing media), though we provide fits to both a Langmuir and Freundlich isotherm to illustrate this poor behavior (Figure 5-20). Figure 5-21 illustrates the effect of initial dye concentration (C_0) on both q_e and the % dye removed at each temperature, and we note the pronounced linearity of the C_0 and q_e correlation at 50 °C (r^2 of 0.998). It is reasonable to assume that this linearity will continue beyond 3,000 mg CR g^{-1} PINC, and these higher concentrations (along with solution-state variables, such as pH and electrolyte density) will be investigated in a forthcoming, in-depth dye sequestration study.

Table 5-4: *Experimental parameters for preparing high-concentration CR solutions.*

sample ID	10 mg mL^{-1} PINC (µL)	10 mg mL^{-1} CR (µL)	H_2O (µL)	CR (mg)	PINC (mg)
CR1	100	10	4890	0.10	1.00
CR2	100	20	4880	0.20	1.00
CR3	100	30	4870	0.30	1.00
CR4	100	40	4860	0.40	1.00
CR5	100	50	4850	0.50	1.00
CR6	100	75	4825	0.75	1.00
CR7	100	100	4800	1.00	1.00
CR8	100	125	4775	1.25	1.00
CR9	100	150	4750	1.50	1.00
CR10	100	200	4700	2.00	1.00
CR11	100	250	4650	2.50	1.00
CR12	100	300	4600	3.00	1.00

Figure 5-19*: Photographs of the array of PINC-CR complexation samples stored for 48 h at room temperature (top photo) or 50 °C (bottom photo). In each photograph, the left-to-right sample identifications (IDs) are CR1–CR12.*

Table 5-5: *Congo Red adsorption capacity on [mpim]Cl PINC estimated using a range of CR solution loadings and storage at room temperature for 48 h.*

sample ID	[dye] (mg g^{-1})[a]	C_0 (mg L^{-1})	C_e (mg L^{-1})	V (L)	m (g)	q_e (mg g^{-1})	% adsorbed
CR1	100	20.0	8.75(±0.34)	0.005	0.001	56.3(±1.7)	56.3(±1.7)
CR2	200	40.0	1.73(±0.93)	0.005	0.001	191(±5)	95.7(±2.3)
CR3	300	60.0	0.45(±0.05)	0.005	0.001	298(±1)	99.3(±0.1)
CR4	400	80.0	0.87(±0.08)	0.005	0.001	396(±1)	98.9(±0.1)
CR5	500	100	0.58(±0.01)	0.005	0.001	497(±1)	99.4(±0.1)
CR6	750	150	1.52(±0.57)	0.005	0.001	742(±3)	99.0(±0.4)
CR7	1000	200	65.3(±11.2)	0.005	0.001	674(±56)	67.4(±5.6)
CR8	1250	250	110(±11)	0.005	0.001	700(±54)	56.0(±4.3)
CR9	1500	300	108(±1)	0.005	0.001	960(±4)	64.0(±0.3)
CR10	2000	400	164(±55)	0.005	0.001	1180(±280)	58.9(±13.8)
CR11	2500	500	268(±78)	0.005	0.001	1160(±390)	46.3(±15.6)
CR12	3000	600	396(±23)	0.005	0.001	1020(±120)	34.1(±3.8)

[a] Dye concentrations are recorded as mg CR per g of [mpim]Cl PINC in the initial solution.

Table 5-6: *Congo Red adsorption capacity on [mpim]Cl PINC estimated using a range of CR solution loadings and storage at 50 °C for 48 h.*

sample ID	[dye] (mg g^{-1})[a]	C_0 (mg L^{-1})	C_e (mg L^{-1})	V (L)	m (g)	q_e (mg g^{-1})	% adsorbed
CR1	100	20.0	1.02	0.005	0.001	94.9	94.9
CR2	200	40.0	0.26	0.005	0.001	199	99.4
CR3	300	60.0	0.17	0.005	0.001	299	99.7
CR4	400	80.0	0.32	0.005	0.001	399	99.8
CR5	500	100	2.19	0.005	0.001	489	97.8
CR6	750	150	3.50	0.005	0.001	732	97.7
CR7	1000	200	7.88	0.005	0.001	961	96.1
CR8	1250	250	19.1	0.005	0.001	1150	92.4
CR9	1500	300	24.1	0.005	0.001	1380	92.0
CR10	2000	400	23.6	0.005	0.001	1880	94.1
CR11	2500	500	37.6	0.005	0.001	2310	92.5
CR12	3000	600	76.9	0.005	0.001	2620	87.2

[a] Dye concentrations are recorded as mg CR per g of [mpim]Cl PINC in the initial solution.

Table 5-7: *Comparison of maximum adsorption capacities (q_m) for CR from the literature.*

sorbent	q_m (mg g^{-1})	temperature (°C)	reference
guar gum/activated carbon	832	40	[43]
cotton stalks biochar (CSB)	250	25	[44]
CSB/ZnO nanoparticles	556	25	[44]
litchi peel biochar	404	45	[45]
hydroxyapatite/chitosan	769	20	[46]
activated carbon	449	30	[47]
Fe_3O_4 nanoparticles	630	20	[43]
Aloe vera leaf shells activated carbon	1,850	25	[44]
[mpim]Cl PINC	1,180[a]	20	this work
[mpim]Cl PINC	2,620[a]	50	this work

[a] Due to the poor Langmuir isotherm fit, this value is the equilibrium adsorption capacity (qe), not the estimated maximum adsorption capacity (q_m).

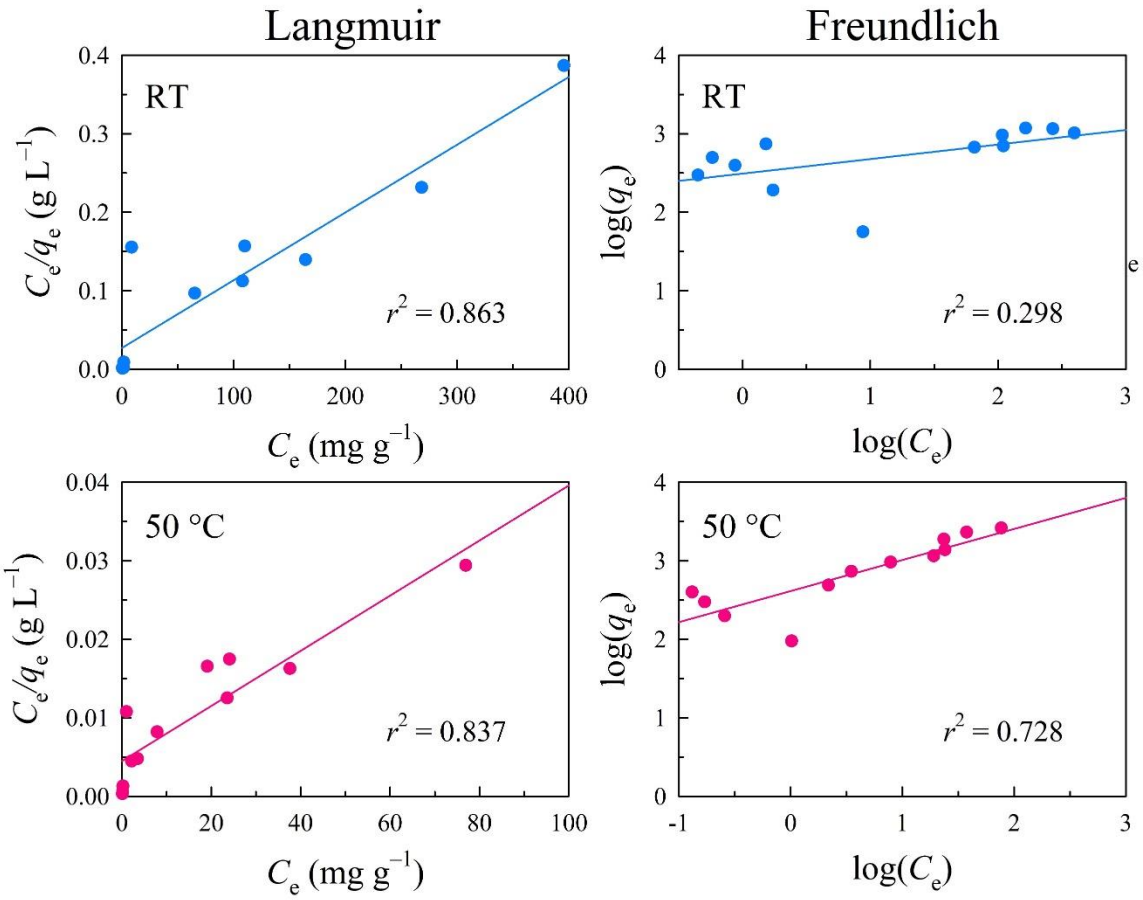

Figure 5-20*: Langmuir (left) and Freundlich (right) isotherms for CR adsorption onto [mpim]Cl PINC at room temperature (RT; top) and 50 °C (bottom). Neither isotherm model demonstrates a strong linear correlation at either temperature.*

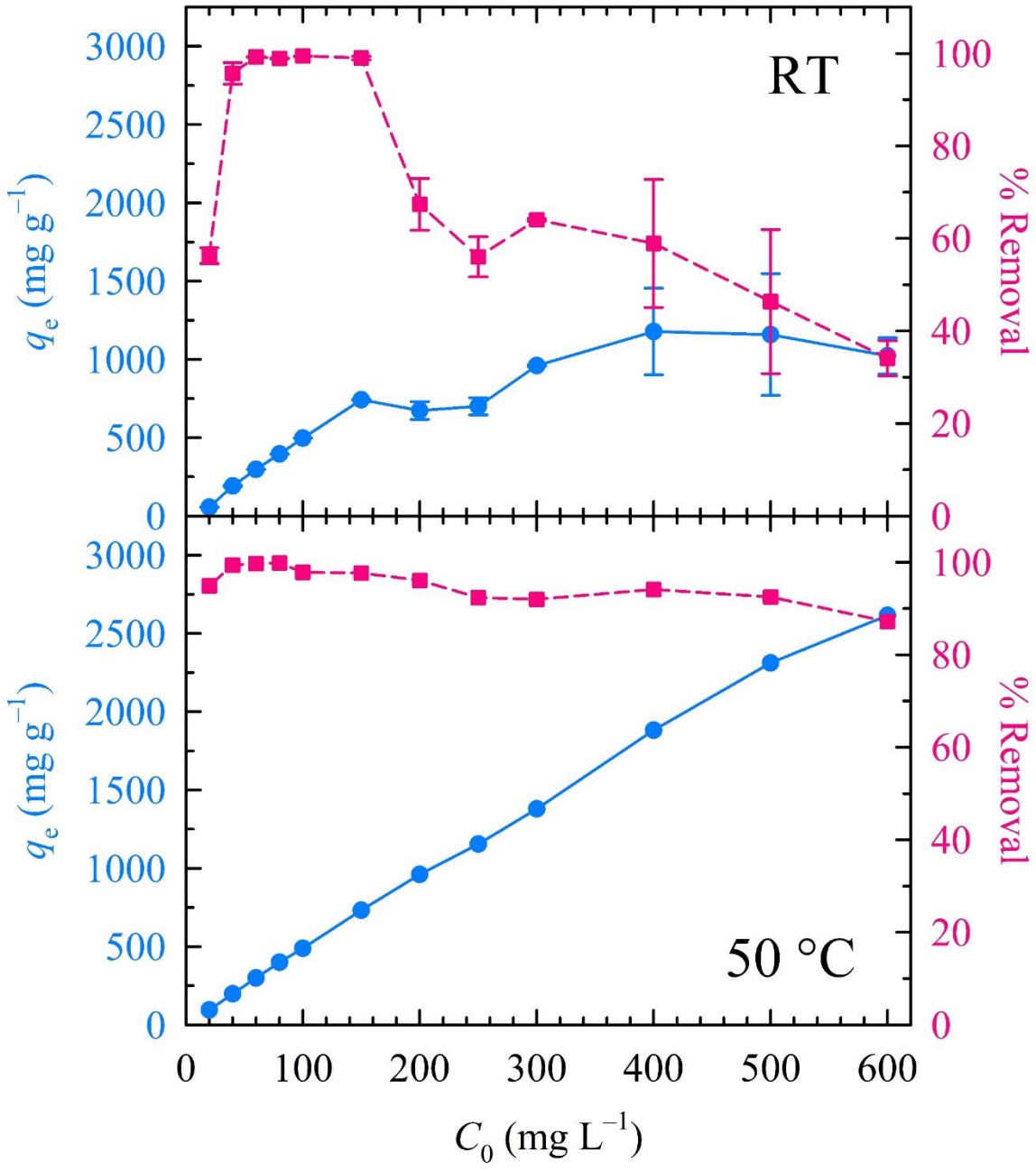

***Figure 5-21**: Effect of initial concentration (C_0) on the equilibrium adsorption capacity (q_e) and % removal when performing dye sequestration at room temperature (RT, top panel) versus 50 °C (bottom panel). Blue circles connected by solid lines denote q_e, whereas pink squares connected by dashed lines denote % removed.*

In a final set of experiments, PINC adsorption selectivity was investigated by attempting to remove the anionic CR species from an equimolar mixture of CR and the cationic dye Methylene Blue (MB). In this experiment, 1.5 mL volumes of 100 μM aqueous CR and MB stocks were combined within a PMMA cuvette, followed by the rapid addition of 100 μL of 10 mg mL^{-1} aqueous PINC solution, capping of the cuvette, and rapid manual mixing. Upon mixing, an apparent decrease in absorbance (hypochromism) was observed for both dyes (particularly for MB), signifying their electrostatic interaction. The λ_{max} for CR blue shifts from 498 nm to 490 nm in the presence of MB and shifts further to 484 nm in the presence of MB and PINC, with a concurrent decrease in absorbance of 7% and 17%, respectively. Similarly, the λ_{max} for MB (665 nm) increases to 675 nm in the presence of CR but only to 670 nm when both CR and PINC and present. However, MB shows marked hypochromism in the presence of CR and CR/PINC (77% and 40% decrease in absorbance, respectively), as summarized in Figure 5-22. Hypochromism has been noted previously for MB upon electrostatic binding with DNA or t-RNA.[48-49] Interestingly, when an equimolar mixture of CR (anionic) and MB (cationic) is challenged with PINC, both dyes are quantitatively precipitated to yield a colorless supernatant after 2 days at room temperature (Figure 5-22, inset photograph). We propose that the CR dianion acts to bridge the cationic PINC surface and the cationic MB dye, thereby promoting the electrostatic complexation of all three species and their eventual precipitation from aqueous solution, offering a potential strategy for the cleanup of dye-contaminated waters.

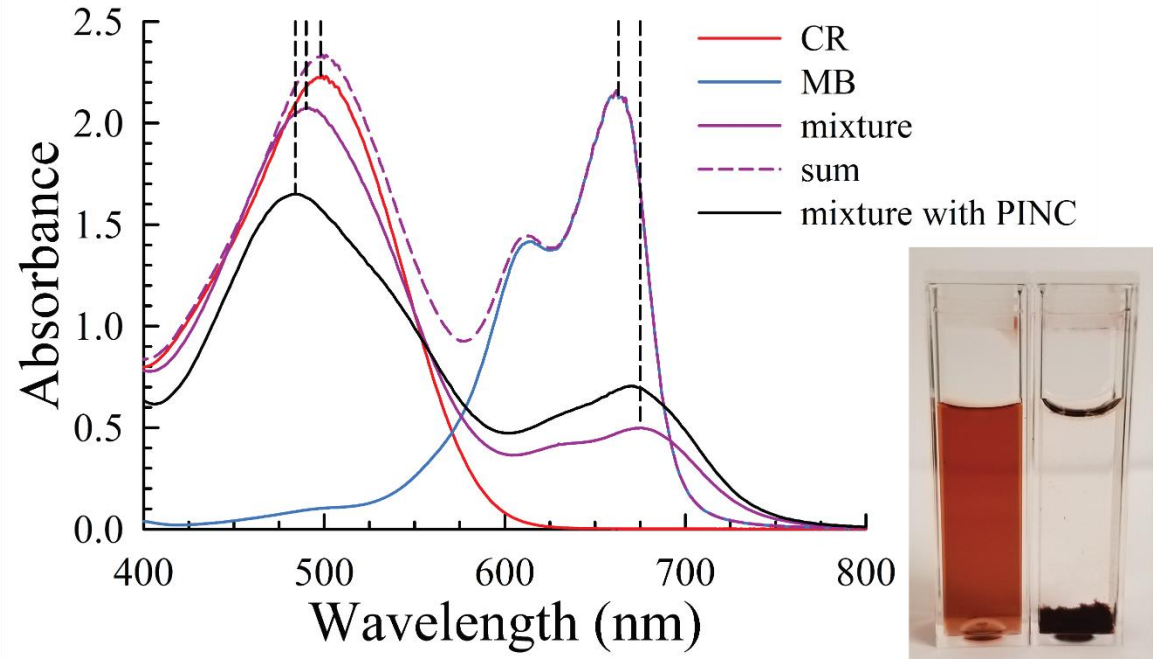

***Figure 5-22**: UV–vis spectra for 50 mM aqueous CR, 50 mM aqueous MB, a mixture of the dyes, the artificially summed spectra for each neat dye solution, and the mixture of dyes in the presence of PINC. Dashed black vertical lines track the shifting λ_{max} for CR and MB. The inset photograph displays the initial CR/MB dye solution prior to the addition of PINC (left cuvette) and after adding PINC and allowing the solution to rest for 48 h (right cuvette), resulting in a colorless solution.*

In conclusion, we report a new best-in-class catalytic system for 4-NP reduction using heterogeneous bimetallic noble metal catalysts. The [mpim]Cl PINC acts as a novel support structure to elevate the catalytic activities of appended bimetallic Au_xAg_{1-x}NPs far beyond those of any reported unsupported or monometallic noble metal catalyst, achieving a record turnover frequency (TOF) of 33,100 h^{-1} for the $x = 0.7$ configuration. Further, we show the robustness of these heterogeneous catalysts over multiple recycles and explore their economic value by calculating TOF per $US for each [mpim]Cl PINC@Au_xAg_{1-x}NPs system, a metric which is under-reported but crucial for comparing the industrial viability of catalysts. Finally, we extend the applicability of these cationic supports by demonstrating their use as dye adsorbents for anionic dyes using Congo Red as a model

dye, attaining an impressive adsorption capacity, q_e, of 2,620 mg CR per g of PINC. Altogether, the investigations reported herein thoroughly demonstrate the catalytic enhancement and dye sequestration capabilities of these novel PINCs and provide impetus for their further application as catalyst supports and dye adsorption platforms.

Chapter 5 Supplementary Information

Materials. All experiments were carried out using ultrapure Millipore water (18.2 MΩ cm). Reagents were purchased commercially and used without further purification. 1-methylimidazole (M50834, 99%), magnesium chloride hexahydrate (M2670, ≥99.0%), 3-chloropropyltrimethoxysilane (440183, ≥97%), sodium hydroxide (306576, 99.99%), gold chloride (520918, ≥99.9%), silver nitrate (204390, 99.9999%), sodium borohydride (213462, 99%), 4-nitrophenol (241326, ≥99%), Mordant Orange 1 (19,507-3, 80%), Malachite Green (M9015, 93%), Rose Bengal (330000, 95%), Phenosafranin (199648, 80%), Crystal Violet (C6158, ≥90.0%), and Naphthol Blue Black (195243, 80%) were purchased from Sigma-Aldrich (St. Louis, MO). Ethyl acetate (E195-4, 99.9%), Congo Red (C-580, 95%), Methylene Blue (M9140, 89%), Biebrich Scarlet (J65603.22, 70%), and Methyl Orange (M-216, certified ACS) were purchased from Fischer Scientific (Hampton, NH). Absolute ethanol (2716) was purchased from Decon Labs (King of Prussia, PA).

Characterization. UV–vis absorbance spectra were recorded on a Varian Cary 50 Bio spectrophotometer using standard 1-cm PMMA cuvettes. Temperature-dependent UV–vis experiments were performed using a Peltier attachment for fine temperature control. Spectral characterization of the PINC@Au_xAg_{1-x}NPs colloids was performed to assess stability after aging for 2 h, 1 d, 3 d, 5 d, 7 d, 14 d, and 28 d (Figures 5-2 and 5-3). For TEM analysis, 8-μL sample aliquots were deposited onto carbon-coated copper grids (Ted Pella, Inc.; 01814-F, support films, carbon type-B, 400 mesh copper grid) by drop-casting, followed by drying in open air. TEM micrographs were obtained on an FEI Tecnai (F20) microscope operated at 200 keV. ImageJ software was used to analyze the resulting

micrographs, and at least 300 particles were counted to create the corresponding size histograms.

References

1. Han, L.; Liu, S. G.; Liang, J. Y.; Ju, Y. J.; Li, N. B.; Luo, H. Q., Ph-Mediated Reversible Fluorescence Nanoswitch Based on Inner Filter Effect Induced Fluorescence Quenching for Selective and Visual Detection of 4-Nitrophenol. *J. Hazard. Mater.* **2019,** *362*, 45-52.

2. Zhou, Q.; He, H. P.; Zhu, J. X.; Shen, W.; Frost, R. L.; Yuan, P., Mechanism of P-Nitrophenol Adsorption from Aqueous Solution by Hdtma+-Pillared Montmorillonite—Implications for Water Purification. *J. Hazard. Mater.* **2008,** *154* (1), 1025-1032.

3. Zhou, Y.; Liu, X.; Tang, L.; Zhang, F.; Zeng, G.; Peng, X.; Luo, L.; Deng, Y.; Pang, Y.; Zhang, J., Insight into Highly Efficient Co-Removal of P-Nitrophenol and Lead by Nitrogen-Functionalized Magnetic Ordered Mesoporous Carbon: Performance and Modelling. *J. Hazard. Mater.* **2017,** *333*, 80-87.

4. Dai, H.; Deng, Z.; Zeng, Y.; Zhang, J.; Yang, Y.; Ma, Q.; Hu, W.; Guo, L.; Li, L.; Wan, S.; Liu, H., Highly Sensitive Determination of 4-Nitrophenol with Coumarin-Based Fluorescent Molecularly Imprinted Poly (Ionic Liquid). *J. Hazard. Mater.* **2020,** *398*, 122854.

5. Lellis, B.; Fávaro-Polonio, C. Z.; Pamphile, J. A.; Polonio, J. C., Effects of Textile Dyes on Health and the Environment and Bioremediation Potential of Living Organisms. *Biotechnol. Res. Innov.* **2019,** *3* (2), 275-290.

6. Wei, Y.; Kong, L.-T.; Yang, R.; Wang, L.; Liu, J.-H.; Huang, X.-J., Single-Walled Carbon Nanotube/Pyrenecyclodextrin Nanohybrids for Ultrahighly Sensitive and Selective Detection of P-Nitrophenol. *Langmuir* **2011,** *27* (16), 10295-10301.

7. Khataee, A. R.; Pons, M. N.; Zahraa, O., Photocatalytic Degradation of Three Azo Dyes Using Immobilized TiO_2 Nanoparticles on Glass Plates Activated by UV Light Irradiation: Influence of Dye Molecular Structure. *J. Hazard. Mater.* **2009,** *168* (1), 451-457.

8. Zhao, B.; Mele, G.; Pio, I.; Li, J.; Palmisano, L.; Vasapollo, G., Degradation of 4-Nitrophenol (4-NP) Using Fe–TiO_2 as a Heterogeneous Photo-Fenton Catalyst. *J. Hazard. Mater.* **2010,** *176* (1), 569-574.

9. Payra, S.; Challagulla, S.; Bobde, Y.; Chakraborty, C.; Ghosh, B.; Roy, S., Probing the Photo- and Electro-Catalytic Degradation Mechanism of Methylene Blue Dye over Zif-Derived Zno. *J. Hazard. Mater.* **2019,** *373*, 377-388.

10. Wang, Y.; Hou, Y.; Wang, Q.; Wang, Y., The Elucidation of the Biodegradation of Nitrobenzene and P-Nitrophenol of Nitroreductase from Antarctic Psychrophile Psychrobacter sp. ANT206 under Low Temperature. *J. Hazard. Mater.* **2021**, 125377.

11. Malik, P. K., Dye Removal from Wastewater Using Activated Carbon Developed from Sawdust: Adsorption Equilibrium and Kinetics. *J. Hazard. Mater.* **2004,** *113* (1), 81-88.

12. Bhatia, D.; Sharma, N. R.; Singh, J.; Kanwar, R. S., Biological Methods for Textile Dye Removal from Wastewater: A Review. *Crit. Rev. Env. Sci. Tech.* **2017,** *47* (19), 1836-1876.

13. Bayomie, O. S.; Kandeel, H.; Shoeib, T.; Yang, H.; Youssef, N.; El-Sayed, M. M. H., Novel Approach for Effective Removal of Methylene Blue Dye from Water Using Fava Bean Peel Waste. *Sci. Rep.* **2020,** *10* (1), 7824.

14. Chong, M. N.; Sharma, A. K.; Burn, S.; Saint, C. P., Feasibility Study on the Application of Advanced Oxidation Technologies for Decentralised Wastewater Treatment. *J. Clean. Prod.* **2012,** *35*, 230-238.

15. Ciganda, R.; Li, N.; Deraedt, C.; Gatard, S.; Zhao, P.; Salmon, L.; Hernández, R.; Ruiz, J.; Astruc, D., Gold Nanoparticles as Electron Reservoir Redox Catalysts for 4-Nitrophenol Reduction: A Strong Stereoelectronic Ligand Influence. *Chem. Commun.* **2014,** *50* (70), 10126-10129.

16. Larm, N. E.; Bhawawet, N.; Thon, J. A.; Baker, G. A., Best Practices for Reporting Nanocatalytic Performance: Lessons Learned from Nitroarene Reduction as a Model Reaction. *New J. Chem.* **2019,** *43* (46), 17932-17936.

17. Larm, N. E.; Essner, J. B.; Pokpas, K.; Canon, J. A.; Jahed, N.; Iwuoha, E. I.; Baker, G. A., Room-Temperature Turkevich Method: Formation of Gold Nanoparticles at the Speed of Mixing Using Cyclic Oxocarbon Reducing Agents. *J. Phys. Chem. C* **2018,** *122* (9), 5105-5118.

18. Shen, W.; Qu, Y.; Pei, X.; Li, S.; You, S.; Wang, J.; Zhang, Z.; Zhou, J., Catalytic Reduction of 4-Nitrophenol Using Gold Nanoparticles Biosynthesized by Cell-Free Extracts of Aspergillus sp. Wl-Au. *J. Hazard. Mater.* **2017,** *321*, 299-306.

19. Aditya, T.; Pal, A.; Pal, T., Nitroarene Reduction: A Trusted Model Reaction to Test Nanoparticle Catalysts. *Chem. Commun.* **2015,** *51* (46), 9410-9431.

20. Gamler, J. T. L.; Ashberry, H. M.; Skrabalak, S. E.; Koczkur, K. M., Random Alloyed Versus Intermetallic Nanoparticles: A Comparison of Electrocatalytic Performance. *Adv. Mater.* **2018,** *30* (40), 1801563.

21. Zhou, M.; Li, C.; Fang, J., Noble-Metal Based Random Alloy and Intermetallic Nanocrystals: Syntheses and Applications. *Chem. Rev.* **2021,** *121* (2), 736-795.

22. Gilroy, K. D.; Ruditskiy, A.; Peng, H.-C.; Qin, D.; Xia, Y., Bimetallic Nanocrystals: Syntheses, Properties, and Applications. *Chem. Rev.* **2016,** *116* (18), 10414-10472.

23. Larm, N. E. A., Laxmi; McKee, Samantha; Baker, Gary A,, Polyionic Nanoclays: Tailorable Hybrid Organic-Inorganic Catalytic Platforms. *Chem. Mater.* **2021**.

24. Burkett, S. L.; Press, A.; Mann, S., Synthesis, Characterization, and Reactivity of Layered Inorganic−Organic Nanocomposites Based on 2:1 Trioctahedral Phyllosilicates. *Chem. Mater.* **1997,** *9* (5), 1071-1073.

25. Larm, N. E.; Thon, J. A.; Vazmitsel, Y.; Atwood, J. L.; Baker, G. A., Borohydride Stabilized Gold–Silver Bimetallic Nanocatalysts for Highly Efficient 4-Nitrophenol Reduction. *Nanoscale Adv.* **2019,** *1* (12), 4665-4668.

26. Haldar, K. K.; Kundu, S.; Patra, A., Core-Size-Dependent Catalytic Properties of Bimetallic Au/Ag Core–Shell Nanoparticles. *ACS Appl. Mater. Interfaces* **2014,** *6* (24), 21946-21953.

27. Link, S.; Wang, Z. L.; El-Sayed, M. A., Alloy Formation of Gold−Silver Nanoparticles and the Dependence of the Plasmon Absorption on Their Composition. *J. Phys. Chem. B* **1999,** *103* (18), 3529-3533.

28. Mallin, M. P.; Murphy, C. J., Solution-Phase Synthesis of Sub-10 nm Au−Ag Alloy Nanoparticles. *Nano Lett.* **2002,** *2* (11), 1235-1237.

29. Essner, J. B.; Laber, C. H.; Baker, G. A., Carbon Dot Reduced Bimetallic Nanoparticles: Size and Surface Plasmon Resonance Tunability for Enhanced Catalytic Applications. *J. Mater. Chem. A* **2015,** *3* (31), 16354-16360.

30. Verbruggen, S. W.; Keulemans, M.; Martens, J. A.; Lenaerts, S., Predicting the Surface Plasmon Resonance Wavelength of Gold–Silver Alloy Nanoparticles. *J. Phys. Chem. C* **2013,** *117* (37), 19142-19145.

31. Rajendra, R.; Bhatia, P.; Justin, A.; Sharma, S.; Ballav, N., Homogeneously-Alloyed Gold–Silver Nanoparticles as Per Feeding Moles. *J. Phys. Chem. C* **2015,** *119* (10), 5604-5613.

32. Jana, D.; Dandapat, A.; De, G., Anisotropic Gold Nanoparticle Doped Mesoporous Boehmite Films and Their Use as Reusable Catalysts in Electron Transfer Reactions. *Langmuir* **2010,** *26* (14), 12177-12184.

33. Zhu, C.; Han, L.; Hu, P.; Dong, S., *In Situ* Loading of Well-Dispersed Gold Nanoparticles on Two-Dimensional Graphene Oxide/SiO_2 Composite Nanosheets and Their Catalytic Properties. *Nanoscale* **2012,** *4* (5), 1641-1646.

34. Seo, Y. S.; Ahn, E.-Y.; Park, J.; Kim, T. Y.; Hong, J. E.; Kim, K.; Park, Y.; Park, Y., Catalytic Reduction of 4-Nitrophenol with Gold Nanoparticles Synthesized by Caffeic Acid. *Nanoscale Res. Lett.* **2017,** *12* (1), 7-7.

35. Wu, H.; Liu, Z.; Wang, X.; Zhao, B.; Zhang, J.; Li, C., Preparation of Hollow Capsule-Stabilized Gold Nanoparticles through the Encapsulation of the Dendrimer. *J. Colloid Interf. Sci.* **2006,** *302* (1), 142-148.

36. Choi, Y.; Choi, M.-J.; Cha, S.-H.; Kim, Y. S.; Cho, S.; Park, Y., Catechin-Capped Gold Nanoparticles: Green Synthesis, Characterization, and Catalytic Activity toward 4-Nitrophenol Reduction. *Nanoscale Res. Lett.* **2014,** *9* (1), 103.

37. Zhang, Y.; Liu, S.; Lu, W.; Wang, L.; Tian, J.; Sun, X., *In Situ* Green Synthesis of Au Nanostructures on Graphene Oxide and Their Application for Catalytic Reduction of 4-Nitrophenol. *Catal. Sci. Techol.* **2011,** *1* (7), 1142-1144.

38. Zhao, S.; Das, A.; Zhang, H.; Jin, R.; Song, Y.; Jin, R., Mechanistic Insights from Atomically Precise Gold Nanocluster-Catalyzed Reduction of 4-Nitrophenol. *Pro. Nat. Sci.-Mater.* **2016,** *26* (5), 483-486.

39. Larm, N. E.; Madugula, D.; Lee, M. W.; Baker, G. A., Polyhedral Borane-Capped Coinage Metal Nanoparticles as High-Performing Catalysts for 4-Nitrophenol Reduction. *Chem. Commun.* **2019,** *55* (55), 7990-7993.

40. Kumar, A.; Mandal, S.; Mathew, S. P.; Selvakannan, P. R.; Mandale, A. B.; Chaudhari, R. V.; Sastry, M., Benzene- and Anthracene-Mediated Assembly of Gold Nanoparticles at the Liquid−Liquid Interface. *Langmuir* **2002,** *18* (17), 6478-6483.

41. Larm, N. E.; Essner, J. B.; Thon, J. A.; Bhawawet, N.; Adhikari, L.; St. Angelo, S. K.; Baker, G. A., Single Laboratory Experiment Integrating the Synthesis, Optical Characterization, and Nanocatalytic Assessment of Gold Nanoparticles. *J. Chem. Educ.* **2020,** *97* (5), 1454-1459.

42. Ganapuram, B. R.; Alle, M.; Dadigala, R.; Dasari, A.; Maragoni, V.; Guttena, V., Catalytic Reduction of Methylene Blue and Congo Red Dyes Using Green Synthesized Gold Nanoparticles Capped by Salmalia Malabarica Gum. *Int. Nano Lett.* **2015,** *5* (4), 215-222.

43. Gupta, V. K.; Agarwal, S.; Ahmad, R.; Mirza, A.; Mittal, J., Sequestration of Toxic Congo Red Dye from Aqueous Solution Using Ecofriendly Guar Gum/ Activated Carbon Nanocomposite. *Int. J. Biol. Macromol.* **2020,** *158*, 1310-1318.

44. Iqbal, M. M.; Imran, M.; Hussain, T.; Naeem, M. A.; Al-Kahtani, A. A.; Shah, G. M.; Ahmad, S.; Farooq, A.; Rizwan, M.; Majeed, A.; Khan, A. R.; Ali, S., Effective Sequestration of Congo Red Dye with ZnO/Cotton Stalks Biochar Nanocomposite: Modeling, Reusability and Stability. *J. Saudi Chem. Soc.* **2021,** *25* (2), 101176.

45. Wu, J.; Yang, J.; Feng, P.; Huang, G.; Xu, C.; Lin, B., High-Efficiency Removal of Dyes from Wastewater by Fully Recycling Litchi Peel Biochar. *Chemosphere* **2020,** *246*, 125734.

46. Hou, H.; Zhou, R.; Wu, P.; Wu, L., Removal of Congo Red Dye from Aqueous Solution with Hydroxyapatite/Chitosan Composite. *Chem. Eng. J.* **2012,** *211-212*, 336-342.

47. Sewu, D. D.; Boakye, P.; Woo, S. H., Highly Efficient Adsorption of Cationic Dye by Biochar Produced with Korean Cabbage Waste. *Bioresource Technol.* **2017,** *224*, 206-213.

48. Antony, T.; Atreyi, M.; Rao, M. V. R., Interaction of Methylene Blue with Transfer RNA — a Spectroscopic Study. *Chem.-Biol. Interact.* **1995,** *97* (3), 199-214.

49. Li, W.-Y.; Xu, J.-G.; He, X.-W., Characterization of the Binding of Methylene Blue to DNA by Spectroscopic Methods. *Anal. Lett.* **2000,** *33* (12), 2453-2464.

Conclusion

The research presented herein outlines our goal to prepare polyionic nanoclays (PINCs), an aminoclay-like nanomaterial possessing permanent surface cations. These aqueously dispersing two-dimensional nanomaterials exfoliate readily in water (regardless of pH) and short-chain alcohols. In addition, we demonstrate their application as nanocatalyst supports and dye removal agents and highlight their exceptional performance in both roles. Indeed, heterogeneous catalysts comprising [mpim]Cl PINC@AuAgNPs perform to a higher degree for 4-nitrophenol reduction than any other noble metal catalyst yet reported in the literature, and naked PINCs remove Congo Red from aqueous media with a greater adsorption capacity than anything we have found in our literature searches.

Looking toward the future, ionic liquids are often known for their ability to be tailored for a given application. Our next endeavor will demonstrate this property in PINCs as we devise silane syntheses which aim to alter the surface cation moiety. Specifically, N-(trimethoxysilylpropyl)pyridinium chloride and 1-methyl-1-(trimethoxysilylpropyl)pyrrolidinium silanes (and their respective PINCs) have already been prepared and used as comparators in elucidating the role of the cation identity in the observed catalytic enhancement during 4-nitrophenol reduction. Impetus also exists in the preparation of anionic and zwitterionic PINCs (sulfonate or carboxylate functionalized anionic PINCs; reaction between imidazole- or amine-based silane with 3-propanesultone to achieve a zwitterionic moiety). Further, functionalization of the surface cation is underway wherein a PINC synthesized using 1-ethoxy-3-(trimethoxysilylpropyl)imidazolium silane is combined with ethylenediaminetetraacetic

acid (EDTA) dianhydride to produce an EDTA-modified PINC for metal ion sequestration or, when modified with Ni^{2+}, protein sequestration via his-tagging. Many routes exist for modification of PINCs (thiol-ene click chemistry being an enticing option) to alter their identities for an assortment of applications in this budding field.

Regarding the current studies, additional nanoparticle compositions (gold-palladium bimetallics, platinum, non-noble or ignoble metals) will be prepared in the presence of these PINCs to assess their application for other, high-value catalyzed reactions, such as Suzuki coupling and alcohol oxidation. Fundamental knowledge regarding catalyst-substrate interactions are needed to push the designer aspect of these catalysts (computational calculations are underway), though such investigations will herald powerful heterogeneous catalysts.

Vita

Nathaniel E. Larm was born in 1988 in Columbia, Missouri to Daniel and Tina Larm. He grew up in Boonville, Missouri and received his primary education in the Boonville R-1 school district, graduating in 2007. Following high school, he attended the University of Central Missouri in Warrensburg, Missouri, where he worked with Drs. Gija Geme and Innocent Pumure on trichloroacetic acid quantification in drinking water and coal fly ash heavy metal analysis. He graduated with a B.S. degree in Chemistry in 2011.

After college, he obtained a job at Acceleration Laboratory Services, Inc., a contract research organization for pharmaceutical products. There, he gained much of his instrumental experience and notebook-keeping skills under good manufacturing practices (GMP) regulations. In 2014, he decided (with guidance from his then girlfriend, Bryanne Cornine) to pursue a degree in higher education at the University of Missouri – Columbia. He joined the group of Dr. Gary A. Baker where he investigated room temperature metal nanoparticle syntheses and the first-ever production of polyionic nanoclays (summarized within this document and for which he jointly holds a patent). He graduated in 2021 with a PhD in Chemistry and will continue his career at the United States Naval Academy in Annapolis, Maryland.